A thesis entitled

Numerical Investigations of ns Laser Induced Shock Waves from Aluminum and Air

Submitted to

University of Hyderabad

Towards partial fulfillment for the degree of

Doctor of Philosophy

in

Physics

by

S. Sai Shiva

(10ACPP13)

Under the supervision of

Dr. P. Prem Kiran

Advanced Centre of Research in High Energy Materials (ACRHEM),

School of Physics, University of Hyderabad, Hyderabad 500046

Telangana, India.

August-2016

Dedicated to...

My Mother (Amma)

Declaration

I**, S. Sai Shiva**, hereby declare that the work presented in this thesis entitled **"Numerical Investigations of ns Laser Induced Shock Waves from Aluminum and Air"**has been carried out by me under the supervision of **Dr. P. Prem Kiran**, Assistant Professor, ACRHEM, School of Physics, University of Hyderabad, Hyderabad, India, as per the Ph.D. ordinances of the University, which is also free from plagiarism. I declare, to the best of my knowledge, that no part of this thesis has been submitted for the award of a research degree of any other University. I hereby agree that my thesis can be deposited in Shodhganga/NFLIBNET.

A report on plagiarism statistics from the University Librarian is enclosed.

(S. SAI SHIVA)

Reg. No: 10ACPP13

Dr. P. Prem Kiran,

AssistantProfessor (Physics)

Thesis Supervisor,

ACRHEM, School of Physics,

University of Hyderabad.

Dr. P. Prem Kiran
Assistant Professor
Tel.: +91-40-23138842
Fax: +91-40-23012800
E-mail: prem@uohyd.ac.in
premkiranuoh@gmail.com

ACRHEM
School of Physics
University of Hyderabad
Prof. C. R. Rao Road,
Gachi Bowli
Hyderabad – 500 046, INDIA

Certificate

This is is to certify that the thesis entitled "**Numerical Investigations of ns Laser Induced Shock Waves from Aluminum and Air**" being submitted to the University of Hyderabad by **S. Sai Shiva** (Reg. No. 10ACPP13), for the award of the degree of Doctor of Philosophy in Physics, is a record of *bonafide* work carried out by him under my supervision and is free of plagiarism.

The matter embodied in this report has not been submitted to any other University or Institution for the award of any degree or diploma.

Dr. P. Prem Kiran
(Supervisor)

Director
ACRHEM

Dean
School of Physics

Acknowledgments

First and foremost, my deepest gratitude to my supervisor Dr. P. Prem Kiran, for his guidance and support through inevitable ups and down during this research and also giving the opportunity to set up the base for modelling the RHD simulations at our center, ACRHEM.

A special thanks to both of my co-supervisors from BARC, Visakhapatnam, Dr. Venkata Ramana Ikkurthi and Dr. C. D. Sijoy for always keeping me focused and giving me sound advice whenever necessary in all aspects, for lending me to fix some of the key issues in the modelling and simulations. Many fruitful discussions with the supervisor and co-supervisors helped me to understand the subject properly and led me to finish the work on time.

I would like to thank the centre ACRHEM for giving the opportunity to carry the research work and DRDO for its financial support without which it would have been very hard to finish the work. I was fortunate to be a part of the collaboration between ACRHEM and BARC. It was a pleasure to thank present director, Dr. K. Venkateshwara Rao, and former director Prof. S. P. Tewari, of ACRHEM for their constant support in all aspects that helped me in successful completion of the work. I am thankful to the Dean, School of Physics (SoP), UoH, for the academic support.

I would also like to thank the CAD director of BARC, S. Chaturvedi for accepting the collaboration and to carry the simulations and the discussions with him was invaluable.

Unforgettable thanks to Dr. Couairon for his wonderful lectures on filamentation during my early research career that led me to understand the complexities involved in the modelling. His lectures really rendered to initiate the progress of the work.

Special thanks to all the teaching staff of ACRHEM, SoP for providing the classes during my course work which really helped me to understand the physics. I thank all the non-teaching staff of ACRHEM and SoP.

I am very grateful for selecting me to SERC School, RRCAT held during 2013, which has helped me to understand the lasers, laser produced plasmas and the simulation aspects. This knowledge gained from this school has helped me to broaden the understanding the plasma physics subject.

I would like to thank my senior Dr. Ch. Leela for having many fruitful discussions, which helped me to clarify many doubts encountered in understanding the experimental observations.

I am lucky to have a good number of friends and I always enjoyed taking to them every, the time spent with them has helped me to refresh. I thank all my friends Manikanta, Rakesh, Phani Sri, Nagaraj, Venkateshwarlu, Vinoth, Tarun, Konda Srinivasa Rao, Ashwin, Venkatesh, Anubham, Ganesh etc. for their support all the way from the early research work.

I am very lucky to have a loving and caring family and I am also lucky of being the youngest of all the siblings, their constant encouragement and blessings all the time had made me to achieve this degree. I am blessed by my mother, four sisters and brother, their patience, hard work and the moral support had taught me to survive in this world.

Finally, I am very much thankful to my wife (Kavitha) for showing constant and uncountable support, love and patience towards me. She deserves a major share of the credit for being with me on all accounts, ever since we met.

Contents

Contents

Contents

List of Figures

List of Figures

List of Figures

List of Figures

List of Figures

List of Figures

List of Figures

List of Tables

Nomenclature

ETR – Electron thermal radiation

No-ETR/NORAD – No electron thermal radiation

SW- Shock wave

LSW – Left shock wave

RSW – Right shock wave

SF – Shock front

RW- Rarefaction wave

LISW – Laser induced shock wave

LASW – Laser ablative shock wave

LDSW – Laser driven shock wave

PAF – Plasma absorption front

AF – Absorption front

PC – Plasma core

POR – Plasma outer region

R-H – Rankine Hugoniot

ALE – Arbitrary Lagrangian Eulerian

HD – Hydrodynamics

HC – Heat conduction

RTE – Radiation heat transfer

Constants

Electro static charge, $q = 4.8\times10^{-10}$ ($g^{1/2}$ $cm^{3/2}s^{-1}$)

Planck constant, $h = 6.64\times10^{-30}$ (erg/g)

Speed of light, $c = 2.99\times10^{-10}$ (cm/s)

Proton mass, $m_p = 1.67\times10^{-24}$ (g)

Electron mass, $m_e = 9.1\times10^{-28}$ (g)

Boltzmann constant, $k_b = 1.38\times10^{-16}$ (erg/K)

Geometry, n = 1, 2, 3 (planar, cylindrical and spherical)

Abstract

The interaction of pulsed lasers with solid targets leads to the ablation of material followed by the generation of shock waves (SW) into an ambient atmosphere. The ablative shockwave expanding into ambient air launches a compression wave through the material due to momentum conservation. Hence, understanding of laser ablative shock wave (LASW) will help get an insight into the shock propagation through target material. As the imaging of shockwaves through an opaque target is challenging, understanding the evolution of ablative SW into the ambient atmospheric medium to estimate the propagation of SW launched into the target of interest is an alternative method. The challenge of the laser induced dynamic loading is to understand the planarity of the SW propagating into the target material. In contrast to the conventional impact experiments, with LISW the investigations may be done for shorter (ns to μs) time scales.

The ablation of materials had proven to be a promising technique for the applications such as deposition of thin films, generation of nanoparticles, and study of elemental and chemical analysis of materials using laser induced breakdown spectroscopy (LIBS). Similarly, the laser generated SW found applications, such as strengthening of material, using laser shock peening test the response of bulk materials to generate Equation-of-State (EOS) using dynamical loading, micro-propulsion, inertial confinement fusion (ICF), and also in medicine. Hence it is essential to understand the spatio-temporal behavior of the plasma and the SW under different ambient conditions.

The expansion dynamics of laser ablated plasma and shock waves depends on various parameters, such as the input laser intensity, wavelength, pulse duration, ablated material properties, and on the pressure and mass concentrations of the ambient atmosphere. Due to transient nature of the laser pulse intensity, various physical processes occur during laser interaction, viz., target heating, melting, evaporation, ionization, phase explosion, and formation of plasma. After the termination of the laser pulse, the plasma expands adiabatically leading to the generation of shock wave (SW) that propagates supersonically into ambient gas. Due to multiple physical processes occurring during and after the laser pulse, the physics of laser generated plasma and SW has become a complex subject to understand. Intensive numerical efforts have been made using models based on thermo-optics or hydrodynamics or the combination of both to understand the fundamentals of laser–

target, laser–plasma interaction, and ablation processes occurring during and after the termination of laser pulse.

In view of the importance of the laser induced shock waves, this thesis primarily focuses on the following:

1. The effect of electron thermal radiation (ETR) on 7 ns laser ablative shock waves from aluminum (Al) plasma into an ambient atmospheric air using a self-consistent, one dimensional, three-temperature (electron, ion, and radiation) radiation hydrodynamic (1D-RHD) MULTI-fs code. The code considers electrons and ions as different species with different energy equations. However, plasma is assumed to have a single fluid velocity (u) and mass density (ρ). A detailed study of the plasma dynamics, SW evolution with and without ETR effects, and its influence on the geometrical transitions of SWs for longer durations of time are studied. The expansion features of the plasma and laser ablative shockwaves (LASW), from aluminum target into ambient atmospheric air, were numerically studied using modified 1D-RHD MULTI-fs code. The temporal evolution of shock velocity Vsw is compared using three geometries by considering with and without ETR effects. This is followed by studying the influence of ETR on the spatial evolution of the flow properties of electron and ion temperatures (Te, Ti), specific energies (Ee, Ei), pressures (Pe, Pi), electron number density (ne), and mass density (ρ). Finally, the temporal evolution of plasma parameters such as ne, Te with and without ETR and the temporal evolution of the mass density in the core plasma and across the shock front (SF) are studied. These are validated with the experimental observations presented elsewhere.

2. Numerical investigation of laser induced shock wave (SW) propagation into bulk aluminum target with and without the effects of electron thermal radiation (ETR and No-ETR) is demonstrated using modified MULTI-fs 1D-code over intensity range 10^{10} – 10^{11} W/cm^2. The radiation emitting from the plasma is observed to show negligible effects on the SW propagating into aluminum target for lower input laser energy (25mJ) and significant effects at higher laser energy (175 mJ) which was found to be dominant up to 50 ns of time. The observations show that two SW have been launched on to the target surface: one during the pulse duration termed as primary SW (PSW) and the other immediately after the laser pulse termination termed as secondary SW (SSW). The effects of ETR were found dominant on SSW compared to that on PSW for 175 mJ. The PSW and SSW found to coalesce at around 30-40 ns and move as a single SW after these time

scales. The resultant pressure after coalesce is higher than the individual ones before coalesce for 175 mJ. The PSW pressures at 25 mJ and 175 mJ were found to be ~1.5 GPa and ~7 GPa, respectively that were launched at 10 ns and 7 ns. The evolution of particle velocities of Al behind the PSW and the SSW are also studied up to 1000 ns.

3. One dimensional numerical simulation of the generation of LASW from quiescent atmospheric air and their propagation into the ambient atmosphere is studied. The interaction of these SWs with a bulk Al target placed at different distances from laser generated spark (plasma in air)

4. Two dimensional numerical simulations of the generation of LASW from quiescent atmospheric air and their propagation into the ambient atmosphere is studied.

   A two dimensional (2D) axis symmetric hydrodynamic model was developed to investigate the laser induced plasma and shock wave dynamics in ambient air. The simulations have been performed using laser absorption models viz., inverse Bremsstrahlung (IB), and photoionization (PI) and with two equations of states (EOS) viz., ideal gas and CEA (EOS). The shock waves (SW) generated by ns Nd: YAG laser whose velocities measured experimentally from the shadowgraphy technique over the time scales of 0.4 – 8 μs for the intensities ranging between 2.3×10^{10} to 1.8×10^{11} W/cm^2 was compared with that of numerical models. The plasma features like the initial tear drop shape and the subsequent expansion into the spherical shape, rolling and splitting of the internal plasma, shock wave detachment from the plasma observed experimentally was able to reproduce with the numerical simulations. Apart, the temporal evolution of electron number density, temperature and specific internal energy obtained in the hot core plasma and across the shock front (SF) numerically over the time scales 0.2 - 8 μs is presented. The measured number density, temperatures, and specific energies in the plasma region were observed to decay from 12×10^{19}-2×10^{19} (cm^{-3}), 14×10^4 - 0.6×10^4 (K), and 1×10^8 -5×10^6 (J/kg), respectively over 0.2 - 8 μs of time. Similarly, the temperatures carried by the SF after the detachment from the plasma was observed to decay from 3500 - 400 (K) over the same time scales. The compared numerical results show that the velocities along the laser direction found to be reasonably matching, whereas opposite to the laser direction were over predicting with the experimental velocities.

Chapter 1

Introduction

In this chapter, introduction to laser generated shock waves (SWs) and its applications in various fields is discussed briefly. The physical processes involved in the nanosecond (ns) laser-matter interaction and the accompanied effects are discussed. The background and motivation followed by the scope of the work and overview of the thesis is presented.

1.1 Introduction

Pressure is a fundamental quantity exists naturally on the earth where its presence can be seen from the atomistic to the giant bodies. Force acting on a body due to the presence of other bodies per unit area is a measure of pressure on the body. Pressure can exist in static or dynamic form. In day-to-day life one can experience the act of pressure by many ways. A tea cup lying on the table can create static pressure on the table similarly a sweet voice of birds, whistling from train can exist in dynamic form that create pressures on ear diaphragm as a result we sense the presence of pressure in the form of sound. The pressure wave propagates through the medium in the form of crests and troughs from the point of source. The propagation of pressure wave in general is expressed in terms of sound waves. In ambient atmospheric air at NTP the sound waves propagates with the speed 340 m/s however the speed normally depends on the thermodynamic variable temperature. High pressures are generated by several naturally occurring phenomena such as explosions created by volcanoes, meteorites impact with earth's surface and earth quakes that release huge amount of energy and pressures that propagate through the medium in the form of seismic, compression or shock waves(SW)[1, 2]. Nevertheless, high pressures are also created by several artificial means such as diamond anvil cell (DAC) that creates high static pressures of few Mbar[3] and shock tubes, gas guns, detonation of chemically reactive elements, ion beams, Z-pinches, flyer plate impacts, nuclear explosions[4] create dynamic pressures of few tens of Mbar or higher. Soon after the invention of lasers in 1960 by Maiman, it became a reliable tool for the generation of very high dynamic pressures up to hundreds of Mbar and temperatures of few tens of eV[5] thus making it an efficient tool relevant for understanding fundamental aspects of materials leading to many technological applications.

1.2 Fundamentals of Laser-Matter Interaction

In the laser-matter interaction (LMI) process the absorption of the laser energy causes the breakdown of the medium leading to the formation and growth of the plasma until the termination of the laser pulse. The plasma thus formed has very high specific internal energy (E_{sp}), pressure (P) and temperature (T) within it, resulting in very high gradients (P, T and E_{sp}) existing across the plasma surrounding atmospheric interface. Due to the high gradients the deposited energy is released suddenly into the surrounding gas leading to the generation of SW. This SW with very high pressure and energy across it propagating through the gas with supersonic speed and rapidly compresses the gas or medium ahead of it.

Figure 1.1 gives the schematic of the optical energy conversion for the ns laser-matter interaction. The optical energy is converted into different forms such as thermal, radiation and mechanical (plasma expansion and generation of shock wave) making it an efficient tool to be employed in different areas of research. These processes become significant depending on the threshold intensity of the laser. At laser intensities lower than the breakdown threshold of the material, the optical energy is mostly converted into thermal energy where the material mostly gets evaporated and partially ionized. However with the increasing laser intensity the thermal effects become dominant and also other effects such as the radiation in the form of free-free, free-bound and bound-bound and mechanical energy in the form of shock wave becomes significant. The strength of SW generated from the ablated plasma increases with the increasing intensity which also depends on the other variables such as laser pulse duration, wavelength, target properties and surrounding gas conditions.

The inverse bremsstrahlung (IB) absorption plays a predominant role in the breakdown of the medium and in the generation of plasma. In gases, apart from IB, the photoionization (PI)[6] process also plays a role in the generation of free electrons and it becomes prominent at moderate temperatures where the atoms existing in the excited states absorb a single photon energy and causes the ionization of the atom.

The absorption strongly depends on the input laser wavelength, and offers different plasma and SW dynamics across ultraviolet (UV), visible (VIS) and infrared (IR) excitation wavelengths[7, 8].

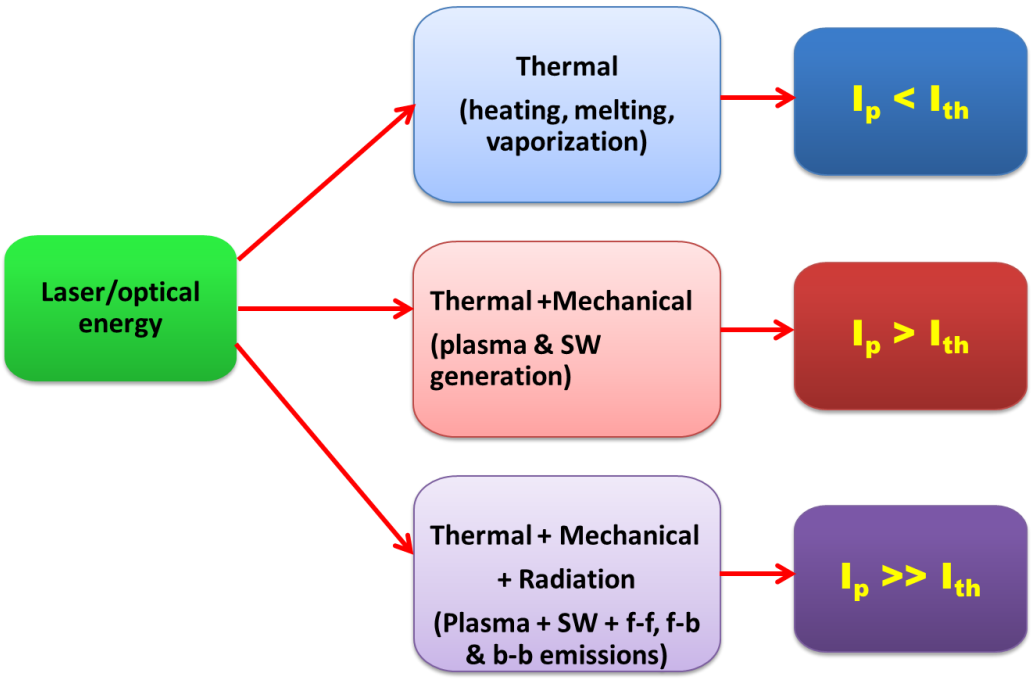

Figure 1.1 Schematic of energy conversion in nanosecond laser-matter interaction at different peak input laser intensities (I_p). I_{th} is the threshold intensities of the material where the breakdown occurs.

The free electrons generated in the plasma by different processes, receive energy from the incoming photons, resulting in the increase of kinetic energy (electron temperatures). However, due to collisions with the surrounding particles (electrons, neutrals and ions) plasma loses its energy which is converted in the form of thermal energy. The process of gaining and losing the electron energy continues because, the nanosecond pulse duration is greater than the excitation and de-excitation times of the electrons leading to the increase in the thermal energy and ionization. The temperatures, ionization, electron number density, pressures, total specific energy of the plasma increases that causes the expansion of the plasma. During the expansion process, a rapid thermal energy transfer between the particles of the hot plasma and

surrounding gas takes place within a thin layer of few orders of mean free path[6, 9] resulting in accumulation of the energy and increasing in entropy. According to Raizer et al.[6] the discontinuity layer in the form of SW leaves the plasma when the area of the background gas (swept gas) becomes equal to the area of the expanding plasma. A hydrodynamic motion of the fluid is set across the SW into the background gas due to the existence of very high pressure gradients that expands independently and quickly with respect to the plasma by highly compressing the surrounding gas. The released SW energy is dissipated due to opposing forces of the background gas. The propagation of the SW continues until the pressure gradients become equal to the ambient pressure. Across the SW, a discontinuity in pressure, density, energy and temperature exists, thus continuous solution does not exist across the SW. Hence the flow conditions and the SW characteristics are described by the Rankine-Hugoniot (R-H) jump conditions [10].

The plasma and the SW formed at the solid target surface preferentially expands in the direction normal to the surface due to the momentum conservation[11]. During this process a recoil momentum is created onto the target surface by the ablated plasma as a result, the SW is launched into the target material also[12]. Similarly in gases the expansion happens both along and towards the laser direction but, mostly it favours in the direction opposite to the laser propagation direction due to the interaction of laser energy with the absorption front surface[6]. After the termination of the laser pulse, the ablated plasma continuously loses its energy that is, dissipated as thermal energy transfer, electron thermal radiation (ETR) in the bremsstrahlung process and the energy carried by the SW. The thermal energy transfer majorly takes place between the high energetic electrons with the constituent particles (electrons, ions and neutrals). Similarly, the energy lost by the free electrons due to the recombination to the atoms is emitted in the form bremsstrahlung radiation shown in fig. 1.2 (a & b) via free-free (f-f), free-bound (f-b) and bound-bound (b-b) transitions. The SW carries some fraction of the absorbed energy and propagates through the surrounding gas.

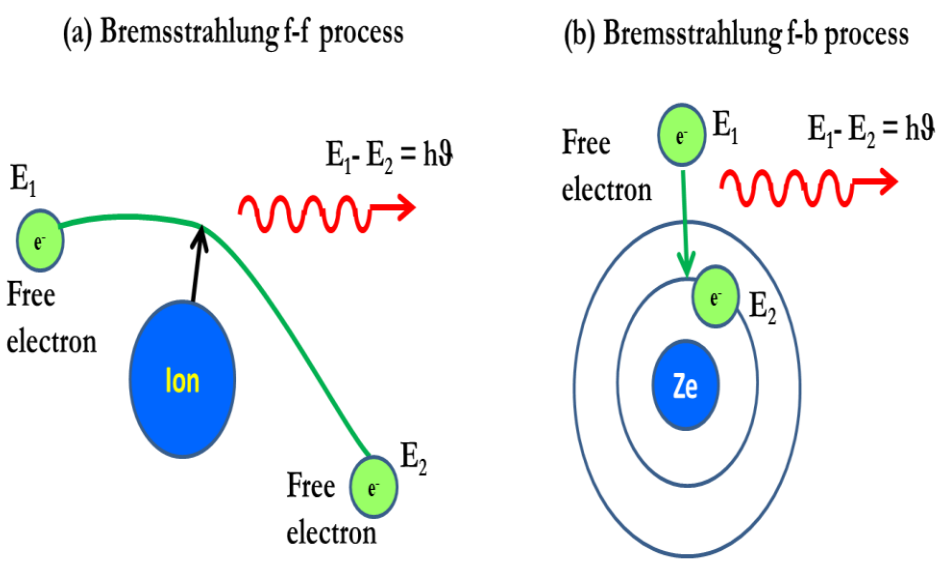

Figure 1.2 Bremsstrahlung radiation emissions by a) free-free (f-f) process and b) free-bound (f-b) process where the electron is bounded to the atom.

1.3 Background and motivation

Extensive research has been carried out to understand the basic phenomena occurring at initial times of nanosecond laser-matter interaction and the accompanied convoluted effects both from gases and solid targets. The material undergoes several simultaneous physical processes like: heating, melting, evaporation[13], phase explosion[14] and ionization leading to breakdown followed by the plasma formation[11, 13]. The expansion of the plasma into low ambient gas pressures leads to plume splitting and sharpening that is associated with the ejection and separation of high and low mass particles into the background gas due to different paths followed by the particles depending on their masses[15]. The expansion of plasma at moderate background pressures leads to the generation of SW due to the thermal energy transfer between the ablated particles and ambient gas due to confinement of the plume by the background gas. The plasma and SW expansion into different ambient gases like He[16], N, Ar and air[17] over pressure range of 1 – 10^5 Pa has shown a significant difference in the plume dynamics and

revealed that the ambient gas conditions severely influence the plasma and SW dynamics. Similarly at higher pressure of background gas, the SW confinement increases[9] due to increase in opposite force acting on the SW evolution. Bogaerts et al.[16] and Hussein et al.[8] investigated the plasma dynamics and the associated effects using UV, visible and infrared wavelengths and observed the dependence of wavelength and pulse duration on plasma evolution into ambient gases [8]. The shape and structure of the ablated plasma and the subsequent SW is examined and found to be dependent on the background gas and laser wavelength[8]. Porneala et al.[14] observed the phase explosion of the material at laser intensities higher than the breakdown threshold of the material. In the phase explosion process, the material undergoes a direct transition from solid to gas phase.[14] Singh et al.[18] studied the physical phenomena involved in the laser-target interaction process and demonstrated that the ablated material undergoes isothermal and adiabatic processes during and after the termination of the laser pulse. Few reports examined the plasma expansion, shape and size of the plasma with varying intensities and pulse durations[9, 19, 20]. Yoh et al.[19] had given a trivial solution to the expansion of SW such as planar (hemi-spherical) expansion during the initial times and spherical expansion at later times. The importance of the electron thermal radiation (ETR) and the amount of radiation emitting and different types of emissions occurring from laser produced plasma is studied[21] which shows that the ETR from ablated plasma increases proportionally with increasing laser energy. The studies of radiation emissions from the laser ablated plasma (LAP) show that, the electron temperatures of the plasma with ETR is found to have lower values compared to that without ETR (No-ETR) effects considered[20, 22]. The ETR increases with increasing input laser intensity due to increase in the free electron number density[20-22].

1.4 Applications

Lasers based technique has gained considerable interest in many areas of research. The applications of it broadly may fall within the four categories depending on the intensity and pulse duration.

Laser with low intensities of $<10^8$ W/cm^2 and energies < mJ, with pulses ranging from micrometer - nanosecond are widely used in the medicinal applications such as in the biological tissue ablation[23], eye retina[13] etc.,

At intensities ranging between $10^8 – 10^{12}$ W/cm^2 are used in the the ablation of materials which had proven to be a promising technique for the applications such as deposition of thin films[24], generation of nanoparticles[25], and study of elemental and chemical analysis of materials using laser induced breakdown spectroscopy (LIBS)[26], ignition of gases. The laser generated SWs from the ablated materials found applications, such as strengthening of material using laser shock peening[27]. In the recent times, the laser also gained special interest in the ignition of combustible fuels in rocket engine as it has numerous many advantages over the conventional electrical spark ignition methods. Recently very intense research work has been carried to employ lasers for the propulsion of space vehicles into deep space where the thrust for lifting the vehicle is achieved by ignition of fuel by the high power lasers[28]. The LISW from gases has also gained interest in wave drag reduction of blunt bodies during the re-entry of space vehicles into earth's atmosphere.

At very high intensities of $>10^{13}$ W/cm^2 are used to test the response of bulk materials, generation of Equation-of-State (EOS) using dynamical loading[29], micro-propulsion[28], inertial confinement fusion (ICF)[5].

In all these applications it is essential to understand the spatio-temporal behavior of the plasma and the SW under different ambient conditions. Though very complex processes are involved in the laser interaction process, due to its rapid advancing in various fields has motivated in carrying the present work.

1.5 Scope of the work

The present work is aimed at numerical investigation of the ns laser ablated plasma and the consequent shock wave propagation from Al and air into the surrounding quiescent air at atmospheric pressures and the SW propagation into bulk Al target. The experimental work has been carried out by Leela et al.[30] using Nd:YAG laser operating at second harmonic wavelength of 532 nm with 7 ns pulse duration (FWHM). The energies in the range of 25 mJ – 175 mJ are focused to a focal diameter of approximately 140±10 μm and the intensities in the range 2.0×10^{10} - 1.6×10^{11} W/cm^2 are generated. The spatio-temporal evolution of shockwaves into quiescent air from Al and air are captured using shadowgraphic imaging technique with a temporal resolution of 1.5 ns[30].

A considerable amount of work both experimentally and theoretically have been devoted towards understanding the fundamental aspects of initial laser target interaction and the accompanied processes such as breakdown phenomena[31, 32], plasma formation, ablation and plasma dynamics[11], SW generation and expansion[8], radiation emissions and relaxation of the plasma[21, 22], energy conversion ratio into ambient gas[7]. However, some of the following issues with the nanosecond laser produced plasma and SWs are sparsely discussed

- the influence of the ETR from the ablated plasma and its effects on the plasma itself and the resulting shock wave dynamics,
- the minimum fraction of energy absorption where the radiation effects become dominant,
- the time scales up to which the radiation effects influence the SW propagation,
- the existence times of planarity of the SW with respect to the intensity,
- the transition of the SW structure from planar to cylindrical and to spherical during its evolution,
- radiation effects on the SW propagating into Al target

- dynamics of the plasma and SW interaction with the solid targets,
- Modelling of laser-air interaction and the associated processes during and after the laser interaction such as the plasma formation, growth, asymmetric expansion, plasma rolling, plasma splitting and SW propagation into ambient air.

It is difficult to visualize and capture all the processes in one set of experiment, as it involves deploying of large number of diagnosing tools which are very expensive and difficult to handle. Moreover, the spatio-temporal evolution of the ablated plasma and SW occur over few mm of length and few tens of microseconds. Spanning such a spatial and temporal length is very difficult in experimental perspective. This is where the scope of modelling and numerical simulation comes in as a useful tool. The simulation of the laser ablated plasma and the accompanying effects on computers will help one in understanding the processes efficiently over few mm lengths and few ns to ms time scales. Variety of approaches used numerically to study the behaviour of the plasma flow fields and the associated physical processes. The direct Monte-Carlo simulation (DMCS)[33] is one method applicable if the interest lies in understanding the microscopic behaviour of the particles where the fluid flows are understood from the motion and collisions of the particles present in the gas. The particle-in-cell (PIC)[34] method is another approach widely used for plasma simulations where the kinetics of the charged particles in the electromagnetic fields are investigated. The plasma behaviour is understood from the system of equations applied to the particles (electrons, ions, neutrals, molecules, dust particles etc.) with Lorentz force. Both these approaches are extensively used in understanding the microscopic behaviour of the system of particles and the processes occurring at the microscopic level. However these approaches become computationally expensive with the increasing number of particles, and also the computational time increases incredibly due to coupling of one particle to the rest of particles.

The radiation hydrodynamic (RHD)[35-38] simulation is another approach which offer excellent features if the interest lies in studying the macroscopic behaviour of the system. This approach provides useful information of the spatio-temporal behaviour of the macroscopic quantities of the plasma such as electron number density, mass density, temperature, pressure, specific internal energy contribution of electron and ions. Similarly, the plasma flow and SW propagation can be investigated over large length and time scales (few tens of mm and upto few milliseconds) with higher resolution (ns). Moreover, the physical processes like thermal energy transfer due to collisions between electrons-ions (e-i) and electrons-neutrals (e-n), radiation emissions from the plasma, SW generation time scales and its propagation through background gas can be well traced by the RHD simulations using Lagrangian, Eulerian, Arbitrary Lagrangian-Eulerian (ALE) formalism. Another great advantage with these simulations is that they are in-expensive in terms of computational requirements and simulation times compared to DMCS and PIC methods. In RHD simulations, the spatio-temporal evolution of the plasma and SW is assumed to behave as a fluid whose properties are governed by the conservation equations of mass, momentum and energy. These system of equations are closed by taking the equation-of-state (EOS) of the material. An ideal gas EOS with charge state ionization may be used at low temperatures where the ionization effects are negligible or at very high temperatures where the plasma is fully ionized[6]. The ideal EOS has certain limitations as it does not consider the atomic effects. Despite the ideal EOS, other EOS namely SESAME[39] and QEOS[40] are widely used in the RHD simulations to consider the effect of the processes occurring at atomic scales. The thermodynamic variables (pressure, specific internal energy and specific entropy) are derived from the specific Helmholtz free energy that composes of contributions from electrons, ions and phenomenological bonding correction[40]. The EOS of the material is calculated from the specified atomic number, atomic weight and number of atoms per molecule. These EOS (SESAME and QEOS) cover wide range of data from very low to very high values of temperatures, densities and pressures.[39,40]

Figure 2.3 shows the schematic of the EOS used for Al and air medium in the simulations.

A wide variety of RHD numerical codes are available in the research community where most of the codes are based on Lagrangian formalism. Some of the codes are MULTI[41] and MULTI-fs[35] developed by Ramis et al., MEDUSA developed by Christiansen et al.[36], FLASH developed by the group at University of Chicago[37] and so on. These codes are widely used by many researchers world-wide for the plasma and SW dynamics. In the present work two different codes have been used to carry out the numerical simulations of nanosecond laser ablative plasmas and the accompanied processes.

1) MULTI-fs 1D-RHD developed by Ramis et al.[35]: This code was modified according to the experimental conditions by taking into account the background air effects[22]. The background air is treated as ideal gas hence, the charge state ideal EOS is considered[6]. The total pressure of the EOS is split into two parts as the contribution of electron and ion pressure. The charge state ionization is evaluated from Saha relation[6] assuming singly ionization state of the gas. Since the simulations are carried for multi-material (Al & air), the QEOS data and ideal EOS is used separately for Al and air to evaluate the thermodynamic variables.
2) 2D-hydrodynamic code developed by Sijoy et al.[38] was used to perform the numerical simulations of laser-air interaction and the accompanied effects. In this code, two separate EOS were used to close the system of equations, first the ideal gas EOS[6] with ionization effects and the second Chemical Equilibrium and Applications (CEA) EOS[42].

1.6 Organization of thesis

Chapter-2: Numerical Methodology and Basic Analysis

In this chapter, an introduction to the conservation (hydrodynamic) equations and the relevance of RHD in modeling the fluid dynamics are discussed. Based on the blast model, the role of thermal conduction due to the electron-ion[35] and electron-neutral[6] collisions and electron thermal radiation (ETR) effects on SW evolution is investigated.

Chapter 3: 1D-Numerical Simulation of Laser Ablative SWs (LASW) from Aluminum Target into Ambient Atmospheric Air: Effects of ETR

The effects of ns laser ablative shock wave (LASW) from Al target expanding into ambient air is numerically analysed where the laser is directly focused on to the target surface. The processes are simulated using modified one-dimensional radiation hydrodynamic (1D-RHD) MULTI-fs code[22] using planar, cylindrical and spherical geometries. The experimentally measured shock velocities were compared with the values obtained using this model.

Chapter 4: 1D-Numerical study of Laser driven SWs into bulk Al target: Effects of ETR

In this chapter, the SW launched into bulk aluminium target[30,43] (thickness 2 – 3 mm) by the laser ablated plasma in ambient air is numerically investigated with ETR and No-ETR effects for 25 mJ and 175 mJ input laser energies. The spatio-temporal evolution of different variables such as total pressure (P), particle velocity (u_p), mass density (ρ), total specific energy (E_{sp}) is compared with and without ETR for both the energies.

Chapter 5: 1D-Numerical study of Laser Ablative plasma and SW dynamics in air and their interaction with Al target

This chapter has two parts: in Part-I, the laser induced under-plasma (UD) and SW dynamics in air is numerically investigated[44, 45] using modified MULTI-fs[22] 1D-RHD code where the radiation effects are taken into consideration. The spatio-temporal evolution of SW variables such as electron number density (n_e), electron temperature (T_e), mass density (ρ), total pressure (P) and total specific energy (E_{sp}) was compared with 25 mJ and 175 mJ.

In Part-II, the interaction of the laser induced under-dense (UD) air plasma with the Al target[44] was analysed as a function of the separation between the UD air plasma and target surface (termed as D) is varied from 5 μm to 40 μm. The analysis has been carried as two sub-sections: In the first sub-section of part-II, the spatio-temporal evolution of the reflected plasma and SW propagating into ambient air was analysed for varying D. In the second sub-section, the SW dynamics in bulk Al target is analysed for varying D for both the energies. Since the plasma ablation dynamics change with respect to D and due to backward and forward motion the air plasma near the target surface, multiple SWs (termed as PSW, SSW and third SW (TSW)) were observed to be launched into the Al target. The peak pressures of these shocks were observed to vary with D and laser energy. The time scales at which the PSW, SSW and TSW launched into the Al target and their coalescence (PSW with SSW and SSW with TSW) during propagation is tabulated for varying D for both laser energies.

Chapter 6: Numerical Investigation of Laser Induced Shock Waves (LISW) from air using 2D-radiation hydrodynamic code.

In this chapter, experimental observations such as the internal plasma core dynamics, formation of two independent point sources in the plasma and spatio-temporal evolution of the SW for different input laser energies[30,46] is modeled using the 2D-numerical simulations. As the 1D simulations presented in the chapter 5 are not able to highlight the essential experimental observations, 2D numerical simulations have been used to understand these features such as asymmetric laser energy deposition in air, the associated plasma (plasma rolling, splitting) and SW dynamics. As the radiation effects

are found to be negligible from the 1D code, these effects are discarded in the 2D code. The 2D-hydrodynamic code developed by Sijoy et al.[38] was used to perform the simulations where different models were used. The model assumes plasma having single temperature (T) where the electrons and ions have same temperature ($T = T_e = T_i$). Hence the plasma is assumed to be at local thermodynamic equilibrium (LTE). The simulations have been carried out using three different models[46]. A brief discussion to different models is given below:

Chapter 7: Summary and Future Scope

This chapter summarizes and concludes the work carried out in the thesis. The future work to be carried is emphasized.

References

[1]A. E. Gates and D. Ritchie, *Encyclopedia of Earthquakes and Volcanoes*. (Facts On File, Incorporated, 2006).
[2]A. Bevan, J. De Laeter and J. R. De Laeter, *Meteorites: A Journey Through Space and Time*. (UNSW Press, 2002).
[3]A. Jayaraman, Reviews of Modern Physics **55** (1), 65-108 (1983).
[4]N. K. Bourne, J. C. F. Millett and G. T. Gray, Journal of Materials Science **44** (13), 3319-3343 (2009).
[5]D. Batani, H. Stabile, A. Ravasio, G. Lucchini, F. Strati, T. Desai, J. Ullschmied, E. Krousky, J. Skala, L. Juha, B. Kralikova, M. Pfeifer, C. Kadlec, T. Mocek, A. Präg, H. Nishimura and Y. Ochi, Physical Review E **68** (6), 067403 (2003).
[6]Y. B. Zel'dovich and Y. P. Raizer, *Physics of Shock Waves and High-Temperature Hydrodynamic Phenomena*. (Dover Publications, 2012).
[7]B. Wang, K. Komurasaki, T. Yamaguchi, K. Shimamura and Y. Arakawa, Journal of Applied Physics **108** (12), 124911 (2010).
[8]A. E. Hussein, P. K. Diwakar, S. S. Harilal and A. Hassanein, Journal of Applied Physics **113** (14), 143305 (2013).
[9]S. S. Harilal, G. V. Miloshevsky, P. K. Diwakar, N. L. LaHaye and A. Hassanein, Physics of Plasmas **19** (8), 083504 (2012).
[10]E. F. Toro, *Riemann Solvers and Numerical Methods for Fluid Dynamics: A Practical Introduction*. (Springer Berlin Heidelberg, 2009).
[11]L. J. Radziemski, *Lasers-Induced Plasmas and Applications*. (Taylor & Francis, 1989).
[12]D. Batani, A. Balducci, D. Beretta, A. Bernardinello, T. Löwer, M. Koenig, A. Benuzzi, B. Faral and T. Hall, Physical Review B **61** (14), 9287-9294 (2000).
[13]D. W. Bäuerle, *Laser Processing and Chemistry*. (Springer Berlin Heidelberg, 2013).
[14]C. Porneala and D. A. Willis, Applied Physics Letters **89** (21), 211121 (2006).
[15]R. F. Wood, J. N. Leboeuf, K. R. Chen, D. B. Geohegan and A. A. Puretzky, Applied Surface Science **127–129**, 151-158 (1998).
[16]A. Bogaerts and Z. Chen, Spectrochimica Acta Part B: Atomic Spectroscopy **60** (9–10), 1280-1307 (2005).
[17]A. Gomes, A. Aubreton, J. J. Gonzalez and S. Vacquié, Journal of Physics D: Applied Physics **37** (5), 689 (2004).
[18]R. K. Singh and J. Narayan, Physical Review B **41** (13), 8843-8859 (1990).
[19]J. J. Yoh, H. Lee, J. Choi, K.-c. Lee and K.-h. Kim, Journal of Applied Physics **103** (4), 043511 (2008).
[20]S. Laville, F. Vidal, T. W. Johnston, M. Chaker, B. Le Drogoff, O. Barthélemy, J. Margot and M. Sabsabi, Physics of Plasmas **11** (5), 2182-2190 (2004).
[21]F. Rezaei and S. H. Tavassoli, Physics of Plasmas **20** (1), 013301 (2013).
[22]S. Sai Shiva, C. Leela, P. Prem Kiran, C. D. Sijoy and S. Chaturvedi, Physics of Plasmas **23** (5), 053107 (2016).
[23]A. Vogel and V. Venugopalan, Chemical Reviews **103** (2), 577-644 (2003).

[24]D. B. Chrisey and G. K. Hubler, *Pulsed Laser Deposition of Thin Films*. (Wiley, 1994).
[25]S. C. Singh and R. Gopal, The Journal of Physical Chemistry C **112** (8), 2812-2819 (2008).
[26]L. J. Radziemski, Spectrochimica Acta Part B: Atomic Spectroscopy **57** (7), 1109-1113 (2002).
[27]H. Chen, *Microscale Laser Shock Peening: Experiment, Modeling and Spatially Resolved Material Characterization*. (2004).
[28]C. Phipps, M. Birkan, W. Bohn, H.-A. Eckel, H. Horisawa, T. Lippert, M. Michaelis, Y. Rezunkov, A. Sasoh, W. Schall, S. Scharring and J. Sinko, Journal of Propulsion and Power **26** (4), 609-637 (2010).
[29]H. C. P. M. Shukla, V. K. Senecha, V. N. Rai, P. Khare, A. K. Verma, R. S. Rao, N. K. Gupta, and B. K. Godwal, CURRENT SCIENCE **85** (6), 802-808 (2003).
[30]C. Leela, Ph. D. thesis, University of Hyderabad, India, 2014.
[31]C. G. Morgan, Reports on Progress in Physics **38** (5), 621 (1975).
[32]C. DeMichelis, IEEE Journal of Quantum Electronics **5** (4), 188-202 (1969).
[33]T. E. Itina, J. Hermann, P. Delaporte and M. Sentis, Physical Review E **66** (6), 066406 (2002).
[34]J. M. Dawson, Reviews of Modern Physics **55** (2), 403-447 (1983).
[35]R. Ramis, K. Eidmann, J. Meyer-ter-Vehn and S. Hüller, Computer Physics Communications **183** (3), 637-655 (2012).
[36]J. P. Christiansen, D. E. T. F. Ashby and K. V. Roberts, Computer Physics Communications **7** (5), 271-287 (1974).
[37]http://flash.uchicago.edu/site/relatedsites/.
[38]C. D. Sijoy and S. Chaturvedi, Computer Physics Communications **190**, 98-119 (2015).
[39]http://www.lanl.gov/org/padste/adtsc/theoretical/physics-chemistry-materials/sesame-database.php.
[40]R. M. More, K. H. Warren, D. A. Young and G. B. Zimmerman, Physics of Fluids **31** (10), 3059-3078 (1988).
[41]R. Ramis, R. Schmalz and J. Meyer-Ter-Vehn, Computer Physics Communications **49** (3), 475-505 (1988).
[42]Sanford Gordon and B. J. McBride, NASA Reference Publication **1311**, 1-58 (1994).
[43]S. Sai Shiva, C. Leela, P. Prem Kiran, C. D. Sijoy and S. Chaturvedi, 10th Asia Plasma and Fusion Association (APFA) Conference-2015, December 14 – 18th, 2015, Gandhinagar, India. Communicated in IOP: Conference Serics, 2016. .
[44]S. Sai Shiva, C. Leela, P. Prem Kiran, C. D. Sijoy, V. Ikkurthi and S. Chaturvedi, in *(Manuscript under preparation)*.
[45]C. Leela, S. Bagchi, V. R. Kumar, S. P. Tewari and P. P. Kiran, Laser and Particle Beams **31** (02), 263-272 (2013).
[46]S. Sai Shiva, C. Leela, P. Prem Kiran, C. D. Sijoy, V. Ikkurthi and S. Chaturvedi, in *(Manuscript under preparation)*.

This page is intentionally left blank

Chapter 2

Numerical Methodology and Basic Analysis

In this chapter, introduction to hydrodynamics and the conservation equations in Eulerian and Lagrangian description along with the necessity of Rankine-Hugoniot jump conditions is discussed. Based on the blast model, the hydrodynamics of the blast evolution and the generation of SW in ambient air are investigated. The distribution of stored energy into air as SW during the blast evolution is presented. The role of thermal conduction and electron thermal radiation (ETR) in the energy distribution to the surroundings is presented.

2.1 Introduction

When an intense pulsed laser is focused to a small volume in a medium, a spark followed by intense sound due to the breakdown of the medium occurs[1]. The optical energy in the form of electro-magnetic field interacts with the medium such that atoms are excited to the higher energy states and further the electrons in it becomes free leading to the ionization of the atom. The number of atoms ionizing increases as the absorption of the laser energy increases which causes rapid growth in the free electron number density and electron temperatures[1-3]. During this process, simultaneously the specific internal energy and pressure of the medium also increases rapidly. The deposited energy thus, is stored as the internal energy which is confined within a small volume of few microns (spot diameter). The sudden micro-explosion of this stored energy into the surrounding atmosphere dumped using the pulsed lasers mimic the explosions occur during the reaction of larger scales of chemically reactive elements. Moreover, the pressure and temperature gradients resulting from the micro-explosions mimic the reactive explosions. The reaction of such elements is characterized by the blast wave whose strength depends on the internal energy stored and on the material properties[4]. During the explosion, a shock wave (SW) is generated which is non-linear in nature owing to high compression of the surrounding gas present ahead of it[4]. The propagation speed of such waves is very high typically few orders of magnitude greater than the local sound speed (Mach number). The SW generated carries the energy and is dissipated to the surroundings. Across the SW, a discontinuity in pressure, density, specific energy and temperature exists thus continuous solution does not exist across the SW. Hence the flow conditions and the SW characteristics are described by the Rankine-Hugoniot (R-H) jump conditions[5].

2.1.1. Conservation equations of mass, momentum and energy

The spatio-temporal evolution of the explosions created by different methods such as optical energy deposition[6], chemical explosions[4, 7] etc. and the associated effects may be

understood from the hydrodynamic equations. The propagation of the SW and its effects through a medium are governed by the three laws: conservation of mass or continuity, conservation of momentum and conservation of energy where the shocked material is considered as a fluid. The conservation equations are the partial differential equations (PDEs) that are generally solved by either Eulerian or Lagrangian or arbitrary Lagrangian-Eulerian[8] formalisms. There exists a variety of numerical techniques implicit[8, 9], explicit[5] that are used to numerically discretize the PDEs where each technique has its own advantage and disadvantage over the other. Hence the numerical technique can be adopted depending on the on the complexity of problem.

2.1.2 Eulerian and Lagrangian formalism

Let V be the arbitrary volume in which the fluid flow takes place and dV is infinitesimal control volume inside V as shown in figure 2.1, ds is the surface of the volume pointed outward normally $\vec{n}$.

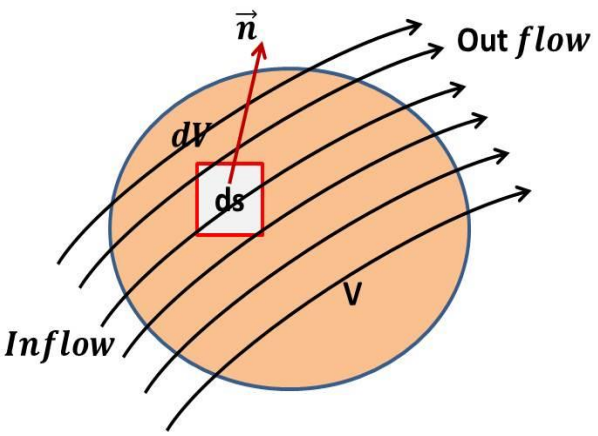

Figure 2.1 Fluid flow through a control volume in the total fluid volume

According to the continuity equation (eq. 2.1), the change in the density in the control volume is due to the mass flux ($\rho\vec{u}$) entering into and leaving the volume[5].

$$\frac{\partial \rho}{\partial t} = -\vec{\nabla}.(\rho\vec{u}), \tag{2.1}$$

The time rate of change of total momentum ($\rho\vec{u}$) of the fluid (eq. 2.2) in the control volume is due to the net momentum inflow over the out flow and due to the surface or volume forces acting on the volume[5], dV

$$\frac{\partial(\rho\vec{u})}{\partial t} = -\vec{\nabla}.(\rho\vec{u}\vec{u}) - \vec{\nabla}P, \tag{2.2}$$

The time rate of change of total energy in the control volume (eq. 2.3) is equal to the influx of energy per unit time plus all the forces acting on the volume

$$\frac{\partial(\rho E)}{\partial t} = -\vec{\nabla}.[(\rho E + P)\vec{u}] \tag{2.3}$$

The variables in equations (2.1) – (2.3) account for ρ - the mass density, $\vec{u}$ - fluid velocity, P is the pressure, e is the internal specific energy, $\frac{1}{2}u^2$ is the kinetic specific energy. The total energy of the fluid in a volume is $E = \rho(e+\frac{1}{2}u^2)$. The set of equations (2.1) – (2.3) are in the Eulerian form where the control volume is fixed and the fluid flows with reference to this fixed volume.

The system of equations can also be expressed in other way known as Lagrangian form, where the control volume also flows with respect to the local fluid flow. The above system of equations (2.1) – (2.3) in the Eulerian form are converted to Lagrangian form[10] as shown in eqs. (2.4) - (2.6) with the help of a material or particle derivative, $\frac{D}{Dt}$.

$$\frac{D\rho}{Dt} = -\rho\vec{\nabla}.\vec{u}, \tag{2.4}$$

$$\rho\frac{D\vec{u}}{Dt} = -\vec{\nabla}P, \tag{2.5}$$

$$\rho\frac{DE}{Dt} = -P\vec{\nabla}.\vec{u} \tag{2.6}$$

where $\frac{D}{Dt} \equiv \frac{\partial}{\partial t} + \vec{u}.\vec{\nabla}$ is the material or particle derivative. The first term $\frac{\partial}{\partial t}$ represent the change (increase or decrease) in the variable (ρ, u, E) at a given fixed point in space with time. The second term $\vec{u}.\vec{\nabla}$ is the advective term of the total derivative which represents the change in the variable (ρ, u, E) during its motion from one region to another[9].

2.1.3 Rankine Hugoniot Jump Conditions

The shock wave (SW) during the propagation through the medium has the discontinuity in the variables because of the steep gradients existing across the front. So the states behind and ahead of the shock wave are given by the Rankine Hugoniot-jump conditions which are derived from the conservation equations. in the Lagrangian form is given

$$\rho_0(U - u_0) = \rho_1(U - u_1) \tag{2.7}$$

$$P_1 - P_0 = \rho_0(u_1 - u_0)(U - u_0) \tag{2.8}$$

$$e_1 - e_0 = (P_1 - P_0)(V_0 - V_1) \tag{2.9}$$

where U is the shock velocity and u_0, P_0, e_0, V_0 are the particle velocity, pressure and specific internal energy and specific volume ahead of the SW, respectively which are the original states of the material before SW propagation. The state variables after the SW propagation are u_1, P_1, e_1, V_1. The particle velocity ahead of the SW is normally u_0 =0. The specific volume, V is defined as $(1/\rho)$.

2.2. Blast Model

2.2.1 Hydrodynamics

As discussed in the introduction (section 2.1), the explosion created by different approaches is characterized by the blast wave that generates the SW into the ambient gas due to the sudden release of the stored energy. In this section, the blast model is

taken in air where the energy is assumed to be deposited by some external source. Here the energy is assumed to be stored in a small region in the ambient air by raising the temperatures. This model helps to analyze its spatio-temporal evolution of the blast and the associated SW propagation into ambient air. The system of equations (2.10) – (2.13) are closed by the ideal gas EOS where the ionization effects are taken into account

$$\frac{D\rho}{Dt} = -\rho\vec{\nabla}.\vec{u}, \tag{2.10}$$

$$\rho\frac{D\bar{u}}{Dt} = -\vec{\nabla}(P_e + P_i + P_v), \tag{2.11}$$

$$\rho\frac{DE_e}{Dt} = -P_e\vec{\nabla}.\vec{u}, \tag{2.12}$$

$$\rho\frac{DE_i}{Dt} = -(P_i + P_v)\vec{\nabla}.\vec{u} \tag{2.13}$$

The variables account for P_v – artificial viscous pressure acting on ions, P_e & P_i - electron and ion pressures, E_e & E_i - electron and ion specific energies and T_e & T_i - electron and ion temperatures, respectively.

The equations (2.10) – (2.13) represented here, essentially a two temperature model as the energy conservation equations is associated with both the electrons and ions. The usage of two separate relations for electrons and ions is advantageous when dealing with the fluid flows associated with the plasmas created by the high intense lasers. The plasma is normally characterized by the electron number density (n_e) and electron temperature (T_e) where the electrons move in the ionic fields and interacts. The two temperature model is essential in order to well understand the behavior of the plasma existing either in the under-dense (UD) or critical dense regimes. The total pressure of the system can be represented by,

$$P = N(1 + z_i)k_bT \tag{2.14}$$

having two contributions, one for the electron pressure P_e and the other for ion pressure P_i given by

$$P_e = Nz_i k_b T_e \tag{2.15}$$

$$P_i = Nk_b T_i \tag{2.16}$$

The electron and ion temperatures (T_e and T_i) of the gas, is obtained respectively, from the electron and ion pressures (P_e and P_i) given by

$$T_e = \frac{P_e}{N\alpha k_b}, \tag{2.17}$$

$$T_i = \frac{P_i}{Nk_b} \tag{2.18}$$

Air is a composition of different molecules where nitrogen molecules is majority in number (78 %) followed by the oxygen (21 %). The rest is occupied by Ar and other molecules whose composition is very small. Among all molecules (Table 2.1) O_2 has lowest ionization potential, it is taken as the first ionization potential of air leading to the generation of seed electrons and plasma. In the model, the ionization or charge state of air is evaluated from the analytical expression given by More. et al[11] and Atzeni et. al[12]. The initial density of air is taken to be 1.29 kg/m^3. Table-2.1 gives the air constituents with first ionization potentials.

Table 2.1 Air constituents at NTP and their corresponding first ionization potentials.

Air Composition	%	First Ionization potential (eV)
Nitrogen (N_2)	78.08	14.53
Oxygen (O_2)	20.95	13.61
Argon (Ar)	0.93	15.76

In Figure 2.2 (a & b) the energy is stored within a small region of ~5 μm in the form of specific internal energy, E_{sp} with the peak energies existing around 12 × 10^7 J/kg and 100 × 10^7 J/kg, respectively which are about two to three orders of magnitude high compared to the ambient conditions whose values typically exist around 2 × 10^5

J/kg. The corresponding peak temperatures of the stored energy typically is found to be ~5 eV (fig. 2.2 a) and ~20 eV (fig. 2.2 b).

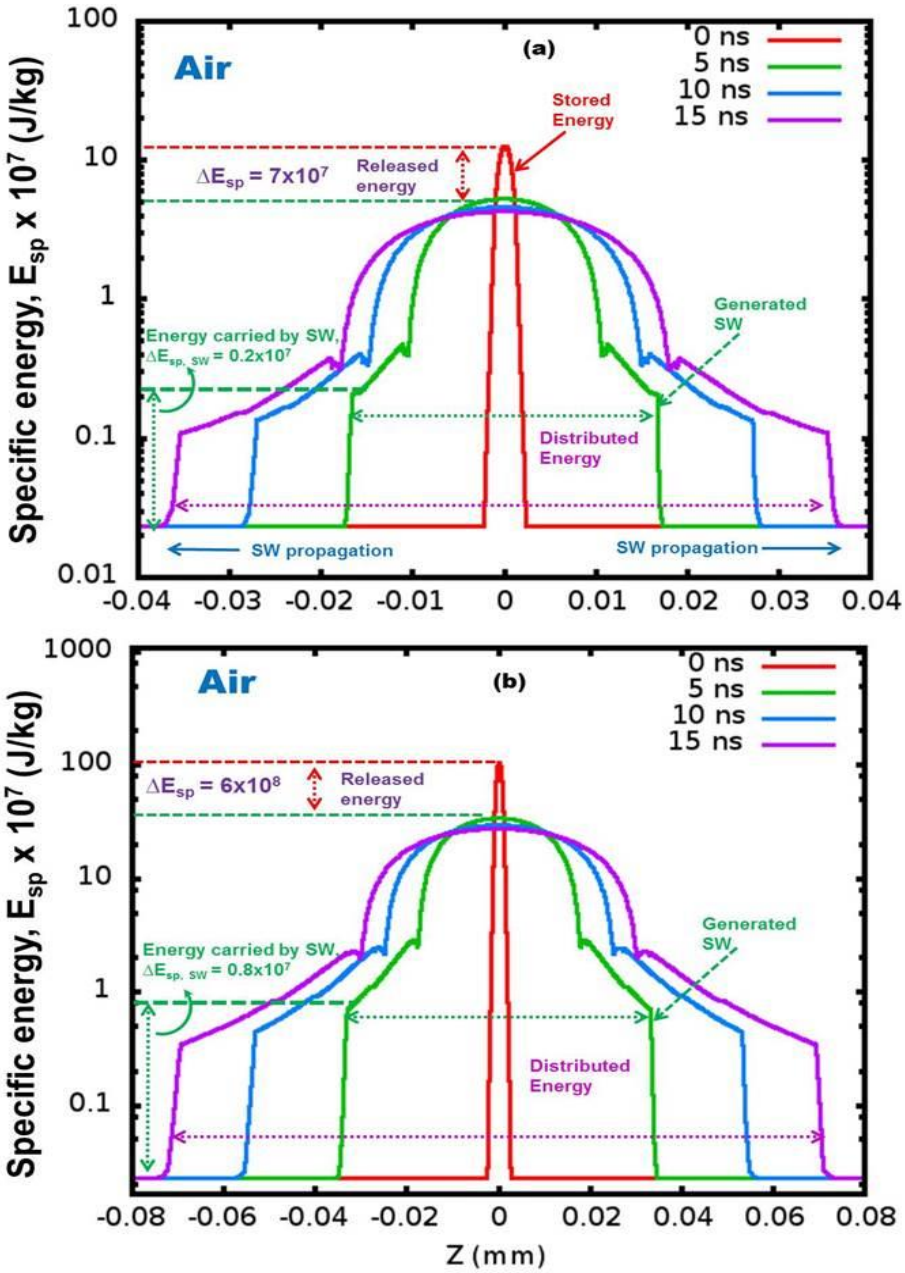

Figure 2.2 Comparison of energy release and shock wave formation from the blast for initial input conditions a) 12 × 10^7 (J/kg)and b) 100×10^7 (J/kg)over the time scales of 5 – 15 ns

The specific energy stored in the small region is assumed as a micro blast that is taken as the initial condition and is allowed to release suddenly in to the surrounding air. The expansion of the blast is simulated for 5 ns, 10 ns, 15 ns is shown in figure (2.2 (a & b)). Since there exist very high energy gradient across the stored energy region and ambient air a hydrodynamic motion is set across this interface resulting in the hydrodynamic expansion of the blast to the surroundings. During this motion, the stored energy is distributed to the surrounding air as a result the peak energy over time. At 5 ns this is decreased to ~5×10^7 J/kg (fig. 2.2 a) and ~40×10^7 J/kg (fig. 2.2 b) that is, less than half that of the initial stored energy. Similarly at latter time scales the peak energy decreases to much lower values. The corresponding regions at 5 ns are observed to be expanded to ~20 μm and ~40 μm, respectively. The sudden release of the energy not only causes the hydrodynamic expansion of the blast, but also generates a wave that is capable of carrying fraction of the stored energy. This wave is non-linear in nature, as it highly compresses and releases the surrounding gas non-linearly and propagates with supersonic velocities. Such waves are termed as the shock wave (SW) whose strength and propagation speed depends on various parameters such as the initial energy deposited, material properties and ambient conditions. Table 2.2 summarizes the peak energy distribution to the surroundings and the energy carried by the SW during its evolution at 5 ns.

Table 2.2 Energy distributed to the surroundings and energy carried by the SW during blast evolution.

Energy distribution	Input conditions(fig. 2.2)	
	(a)	(b)
Initial stored energy × 10^7 (J/kg) (peak)	12	100
Peak energy × 10^7 (J/kg) at 5 ns	5	40
Peak Energy difference, ΔE_{sp}× 10^7 (J/kg)	7	60
Energy of the SW × 10^7 (J/kg) at 5 ns	0.2	0.9

As observed in fig. 2.2 (a) the energy difference, ΔE_{sp} between 0 - 5 ns is found to be ~7×10^7 J/kg (fig. 2.2 (a)) and ~60×10^7 J/kg (fig. 2.2 (a)). This fraction of energy of this released energy is utilized in hydrodynamic expansion of the blast and the generation of the SW that carries the energy of ~0.2×10^7 J/kg (fig. 2.2 (a)) and ~0.9×10^7 J/kg. The shows that the more the energy stored in the system, the higher will be the strength of the SW. At latter time scales (15 ns) the energy of the SW decreases continuously which is found to be of ~0.1×10^7 J/kg and of ~0.4×10^7 J/kg as shown in fig. fig. 2.2 (a) and fig. 2.2 (b), respectively. Similarly the peak energy in the blast region at later times between 5 - 15 ns is observed to decrease to 5×10^7 - 4×10^7 J/kg and 35×10^7 – 25×10^7 J/kg, respectively.

Figure 2.3 (a & b) show the corresponding pressure profiles of the blast given in fig. 2.2 (a & b). The spatial evolution of the pressure profile shows that in the blast region (central part) the pressure is small compared to that across the SW which is due to the high pressure gradient existing between the ambient surrounding air and SW interface. The SW during its propagation highly compresses the air and propagates with supersonic speed. The compression of air takes place within a small region of few orders of mean free paths of molecules and happens very quickly within short durations of time resulting in the increase in the temperature, energy, pressure and entropy. In the blast region since the pressure gradients are small, the blast evolution is slow compared to that of the SW. The compression of the air further behind the SW is released as a rarefaction wave (RW) that propagates in the direction opposite to the SW propagation as shown in fig 2.3 (a & b). The peak SW pressures is observed to decrease from 6 - 3 MPa (fig. 2.3 (a)) and from 25 - 10 MPa (fig. 2.3 (b)) over the time scales of 5 – 15 ns, respectively.

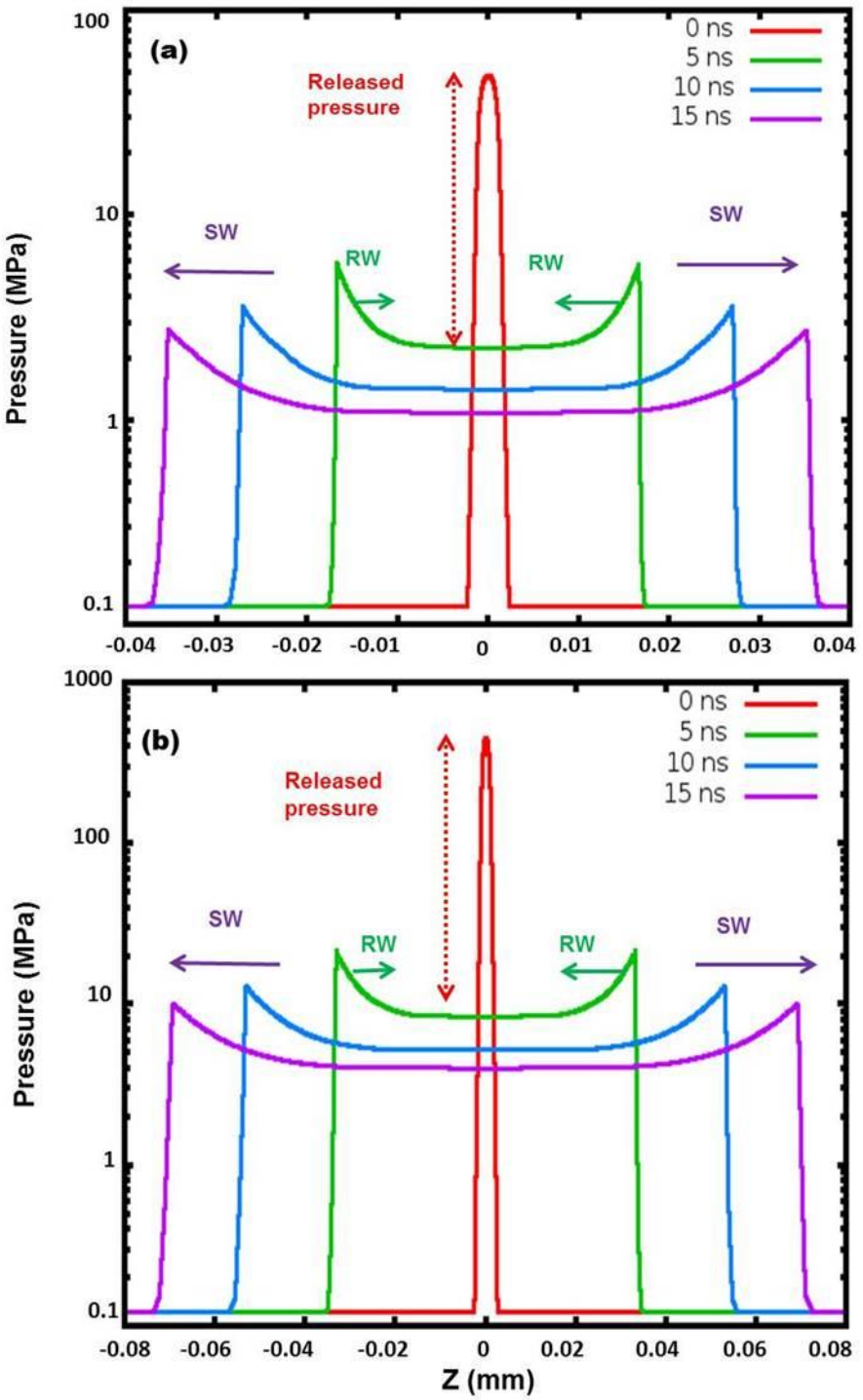

Figure 2.3 Spatial evolution of pressure for the corresponding input stored energies a) 12×10^7 (J/kg) and b) 100×10^7 over the time scales of 5 – 15 ns.

2.3. Role of Source terms and their importance

2.3.1 Thermal conduction

During the energy release time, the stored energy is also dissipated in the form of thermal energy transferred between the particles due to the conduction of the medium. The thermal conduction plays a major role in the distribution of energy to the surroundings. The thermal conduction is added to the electron energy equation given by,

$$\rho \frac{DE_e}{Dt} = -P_e \vec{\nabla}.\vec{u} - K_{th} \nabla T_e, \tag{2.19}$$

The term, $K_{th} \nabla T_e$, is the thermal diffusion where K_{th} is the heat conduction coefficient and ∇T_e is the temperature gradient existing within the system. The negative sign represents the energy transfer by the electrons to the constituent particles ions and neutrals. According to Spitzer-Harm[13], the thermal conduction coefficient with free streaming factor (f) is given by the relation[10],

$$k_{th} = f \frac{n_e {k_b}^2 T_e}{m_e \vartheta_e} \alpha(Z), \tag{2.20}$$

where 'f' value in simulations is taken to be equal to 0.05.k_b is the boltzmann constant, T_e is the electron temperature, m_e is the electron mass, n_e is the electron number density related to the charge state ionization and density of the medium as

$$n_e = \frac{Z_i \rho}{A m_p}, \tag{2.21}$$

ϑ_e is the sum of the electron-ion (ϑ_{ei})[12] and electron-neutral (ϑ_{en})[14] collision frequency given by,

$$\vartheta_{ei} = \frac{4\sqrt{2\pi}\, \ln\Lambda q^4 Z_i n_e}{3\sqrt{m_e}(k_b T_e)^{3/2}}, \tag{2.22}$$

$$\vartheta_{en} = \frac{N_n \sigma_{el} T_e^{1/2}}{W}, \tag{2.23}$$

$$\alpha(Z) = 3.22554\frac{Z_i+0.24}{1+0.24Z_i} \quad (2.24)$$

where A - the atomic mass number, m_p - proton mass, lnΛ - Coulomb logarithm, q- the electro-static charge of the electron, N_n - the neutral number density, σ_{el} - collision cross-section of neutrals, W - atomic weight.

Figure 2.4 (a, c) shows the energy distribution of the blast compared with only hydrodynamics (HD) and with heat conduction (HC) effects at 5 ns and 10 ns, respectively. Similarly figure 2.4 (b, d) are the corresponding pressure comparison for the two initial conditions 5 eV and 20 eV.

As observed when the thermal conduction effects are added, the energy dissipation is occurring very rapidly compared to that with HD. The difference in the specific energy ($\Delta\mathbf{E_{sp}}$) between HD and HC at 5 ns is found to be small ~3×10^7 J/kg with 5 eV compared with 20 eV which is found to be ~28×10^7 J/kg. The smaller difference in specific energy, $\Delta\mathbf{E_{sp}}$ indicates that the thermal conduction effect increases with the energy stored in the system. As the temperature increases, the electron number density increases simultaneously followed by the increase in the e-i collisions resulting in rapid distribution of the thermal energy to the surrounding gas. The e-i collision effectively is the dominant mechanism compared to the e-n collision, because in this mechanism the collision depends on cross-section of the neutral atoms which is very small compared to the ionic field cross-section. The SW pressure comparison with HD and HC is shown in fig. 2.4 (b & d) which shows that the pressure difference is very small. The SW expansion is observed to be same in both the cases.

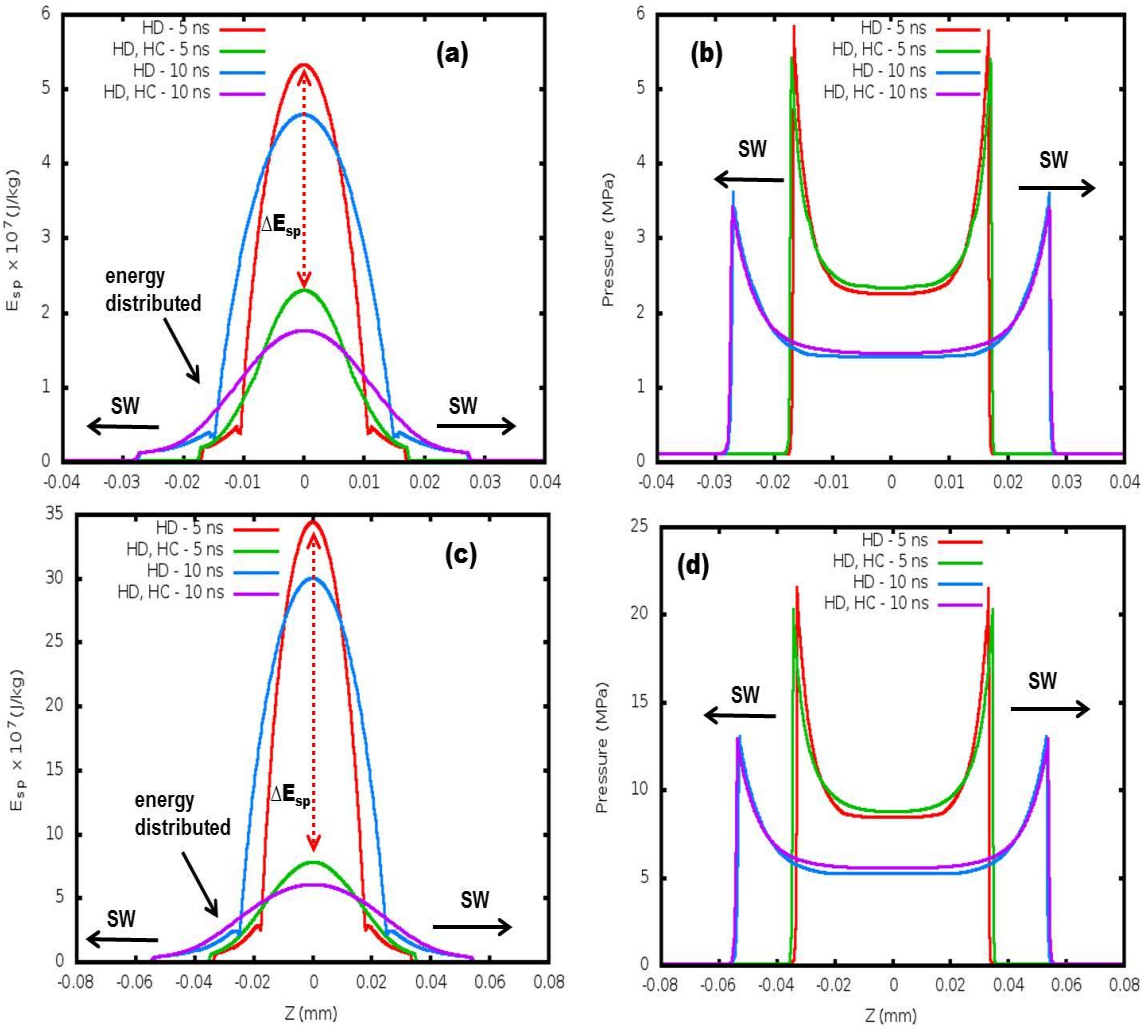

Figure 2.4 Comparison of (a, c) specific energy and (b, d) pressure of the blast with only hydrodynamics (HD) and HD with heat conduction (HC) effects.

2.3.2 Electron thermal radiation (ETR) effects

The system of equations with radiation effects taken into account in general is described as the radiation hydrodynamics (RHD). The radiation emission from the hot body is added to the electron energy equation[10, 15] given in eq. 2.25.

$$\rho \frac{DE_e}{Dt} = -P_e \vec{\nabla}.\vec{u} - K_{th} \nabla T_e - \vec{Q}_{rad}, \qquad (2.25)$$

$\vec{Q}_{rad}$ is the radiation emitted from the hot body which is obtained by solving the radiative transfer equation (RTE) given by 2.26. The radiation emitted from any hot body has wide range of frequency spectrum, solving the RTE for all the frequencies are cumbersome. Hence the frequency spectrum is divided into spectral groups by the multi group approximation method.

$$\frac{1}{c}\frac{\partial I}{\partial t} + \vec{n}.\vec{\nabla} I = \eta - Xi, \tag{2.26}$$

The right hand side (RHS) of the equation is the effective rate of energy emission by the matter per unit of volume, frequency and solid angle. By integrating over all frequencies and directions, the RHS of the equation takes the form

$$\vec{Q}_{rad} = \int_0^\infty \int_{4\pi} (\eta - \chi I)\, d\hat{n}\, d\vartheta, \tag{2.27}$$

where $\eta = \chi I_s$ is the total emissivity, I_s is the source function, I is specific intensity of radiation, χ is the total opacity. In the Lagrangian coordinates, the total opacity is expressed as, $\chi = \kappa\rho$. All these parameters have the functions as:

$$I = I(x, \mu, \vartheta, t);$$

$$I_s = I_s\,(t, \rho, \vartheta, N);$$

$$\chi = \chi\,(T, \rho, \vartheta, N)$$

where μ is the cosine of the angle between the photon direction and x-axis, T, ρ, N are the temperature, density and matter composition which are functions of position and time (x,t).

Eq. 2.27 in terms of energy densities and frequency groups, K is written as:

$$Q(m,t) = c\rho(m,t)\kappa_p^K\,(\rho, T, N)(U_{sk} - U_k), \tag{2.28}$$

$U_{sk} = \epsilon_k U_{pk}$ is the source energy density and U_{pk} is the Planck energy density expressed as:

$$U_{pk} = \frac{4\pi(\mu_b - \mu_a)}{c} \int_{\vartheta_a^K}^{\vartheta_b^K} \mathrm{I_p}(T, \vartheta) d\vartheta \,, \tag{2.29}$$

U_k is the energy density of photons belonging to group K that depends on the photon flux, S and is expressed as:

$$c g_K^2 \frac{dU_k}{dm} = -\kappa_R^K S_k \tag{2.30}$$

The Planck (κ_p^K) and Rosseland (κ_R^K)[10, 15] opacities are related to the material properties and the temperature. For each frequency group the opacities is different as the mean free path of a photon is different for different frequencies. The Planck and Rosseland opacities are given by the relations

$$\kappa_p^K = \frac{\int_{\vartheta_a^K}^{\vartheta_b^K} \kappa \mathrm{I_p} d\vartheta}{\int_{\vartheta_a^K}^{\vartheta_b^K} \mathrm{I_p} d\vartheta}, \tag{2.31}$$

$$\kappa_R^K = \frac{\int_{\vartheta_a^K}^{\vartheta_b^K} \kappa I_p' \, d\vartheta}{\int_{\vartheta_a^K}^{\vartheta_b^K} \frac{I_p'}{\kappa} d\vartheta} \tag{2.32}$$

K=1….. N_G corresponds to the number of frequency group and ϑ_a^K and ϑ_b^K are the lower and higher limit frequencies in the in the group K.

In the present simulations, the Planck and Rosseland opacities of oxygen atom are evaluated from the analytical expression given by Minguez et al.[16] which take the form,

$$X_k^R = 3.78 T^{-2.48} \rho^{0.481} \,, \tag{2.33}$$

$$X_k^P 34.18 T^{-2.415} \rho^{0.483} \tag{2.34}$$

These quantities depend on the mass density and the electron temperature of the gas.

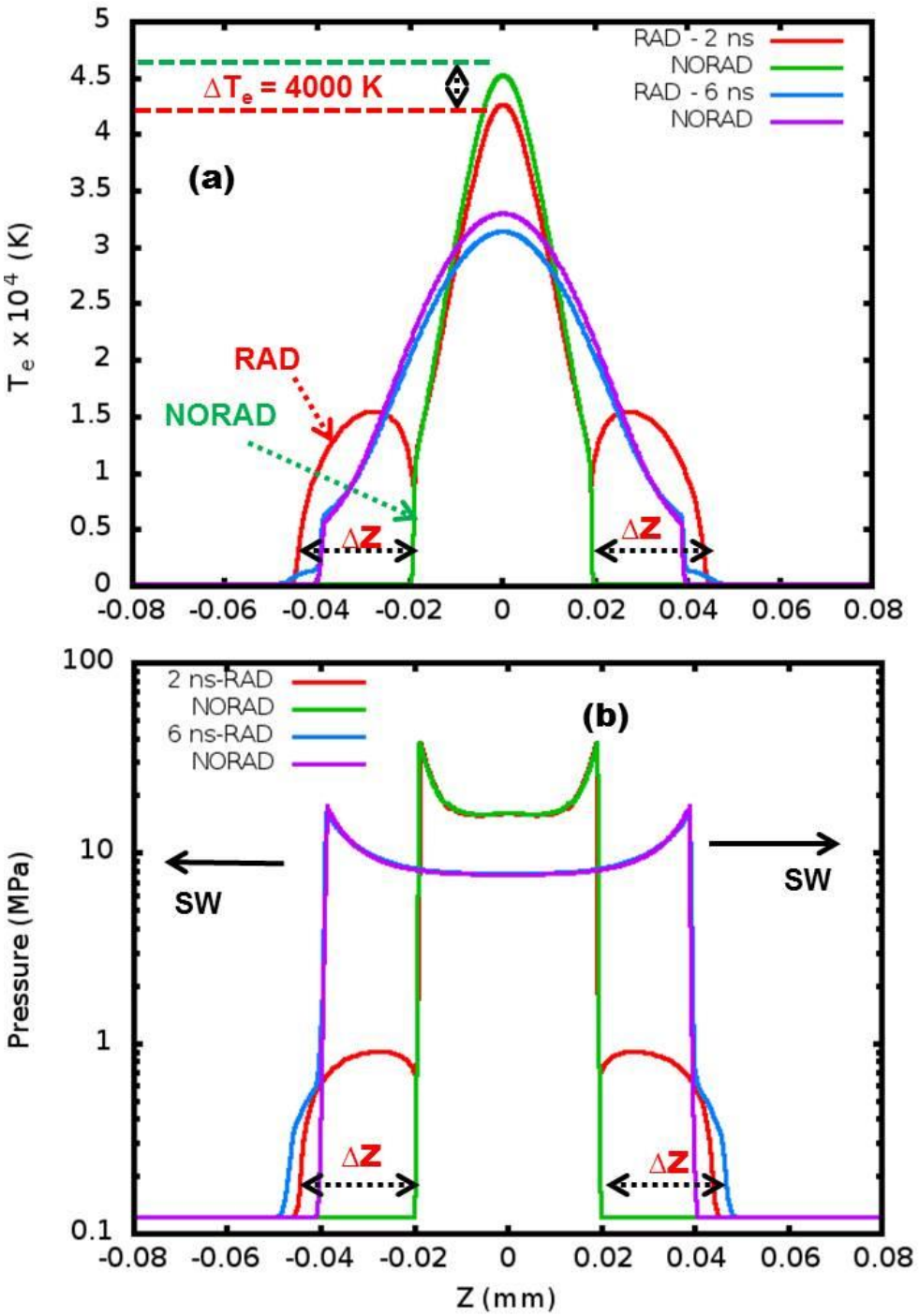

Figure 2.5 Effects of electron thermal radiation on blast wave parameters a) electron temperature and b) total pressure at 20 eV as initial condition

The radiation emissions from laser induced air spark[17] whose typical percentages is observed to be very small with respect to the laser energy absorption. In this section the role of radiation emitting from the hot body and its influence on the blast expansion is investigated. In figure 2.5 the comparison of hydrodynamics with and without radiation effects mentioned as RAD and NORAD, respectively is presented for initial condition of 20 eV. As observed from figure 2.5 (a) there is a small difference in the electron temperature, (ΔT_e) (fig. 2.5 (a)) is seen at time 2 ns at the central region of the blast wave which is found to be ~0.4 × 10^4 K. However, this dissipated temperature in the form of electron thermal radiation pre-heats the surrounding medium present in front of the wave resulting in the increase of the volume. The difference in the spatial length, ΔZ with RAD and NORAD is found to be 2 mm which is the pre-heated air region (ΔZ) region where the electron temperature is found to be ~1.5 × 10^4 K. At 6 ns, the difference in ΔT_e becomes small, resulting in very small radiation emissions. In figure 2.5 (b), the corresponding pressure profile shows that the pressure of the pre-heated region at 2 ns is increased to 1 MPa due to the increase in the temperature. The pressure at 6 ns also decreases due to decrease in the radiation emissions. The results show that the radiation emissions from the blast is observed to be slightly modifying the blast wave dynamics of where its effects were observed to be existing at early time scales of < 10 ns. The radiation emissions from the solid target is observed to increase with intensity[18, 19] significantly modifying the plasma and SW dynamics[20].

2.3.3 Shock velocity comparison with Sedov-Taylor relation

Often the propagation speed of the SW through the medium is compared with the point explosion of the blast wave from the Sedov- Taylor relation given by,

$$V_{sw} = \varphi_0 \left(\frac{E}{\rho_0 t^n}\right)^{\frac{1}{n+2}} \tag{2.34}$$

where $\varphi_0 \approx 1$ for air and is depends on the gas considered, E is the stored or absorbed energy in joules, ρ_0 is the initial density of air taken to be equal to 1.3 kg/m^3, 't' is the time evolution of the SW, 'n' is a number that depends on the geometry, n=3, 2,1 represents the spherical, cylindrical and planar geometries, respectively. The SW velocity, V_{sw} propagation through ambient air for two different input conditions 5 eV and 20 eV is compared from Sedov-Taylor evolution for spherical geometry (eq. 2.34) as is shown in fig. 2.6 (a & b) for the initial stored energies as given in fig. 2.2 (a & b).

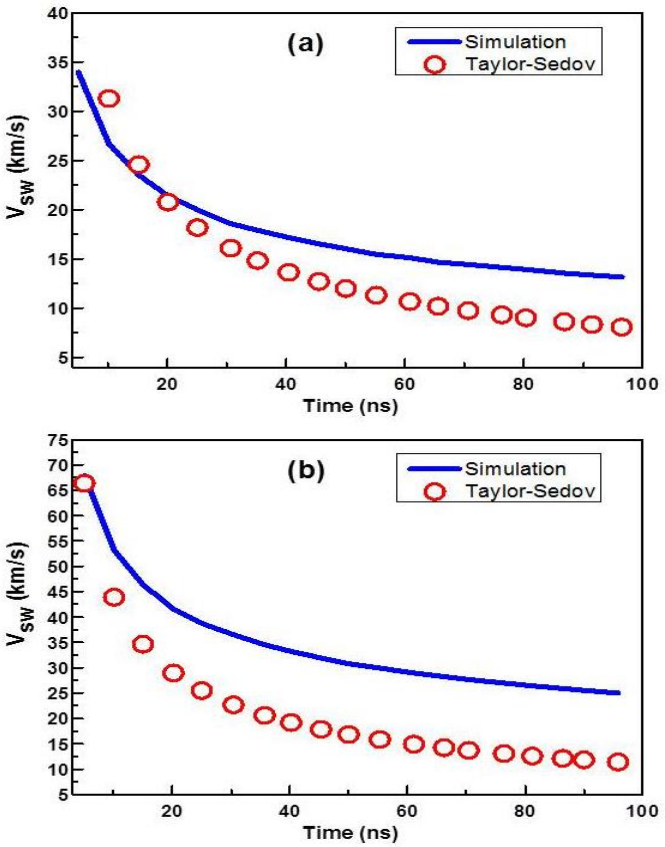

Figure 2.6 Comparison of shock velocity, V_{sw} between simulations and Sedov-Taylor spherical evolution for input conditions of a) 12 × 10^7 (J/kg) (5 eV) and b) 100× 10^7 (20 eV) over the time scales of 5 – 100 ns.

As seen from the fig. 2.6, the highest shock velocity, V_{sw} at 5 ns with simulations (fig. 2.6 (a)) is found to be 32 km/s whereas, with Taylor-Sedov model it is found to be around 34 km/s. Similarly, in fig. 2.6 (b) the highest shock velocity, V_{sw} at 5 ns with

simulations is found to be 65 km/s which is found to be same with Taylor-Sedov model. However, at latter time scales the decrease in the SW velocity with simulations is found to be occurring slowly compared to that of the Sedov-Taylor relation.

In the next chapter-3, the laser ablative shock waves from aluminum target propagating into ambient air will be discussed where the ETR effects were observed to significantly modifying the ablated plasma and SW dynamics.

2.4. Summary

A brief overview of hydrodynamic equations in Eulerian and Lagrangian form is presented. Various sources terms used in the thesis that explain the e-i, e-n collisions and ETR effects in plasma and their role in the energy transfer to the surroundings. From the blast wave analysis the role of thermal conduction in the hot region is analyzed from the simple hydrodynamics and observed that the sudden release of the stored energy generated the SW that propagates through the surrounding air supersonically. The thermal conduction source term when added to the energy equation, the energy is observed to be dissipated in the form of heat transport to the constituent particles. The difference in the energy is found to be high signifying that the thermal conduction plays a significant role in the plasma dynamics and SW evolution. Later on the role of radiation emissions on the blast wave dynamics is analyzed by taking into consideration radiative transfer equation. The emitted radiation is observed to pre-heat the surrounding medium present near the blast wave and ambient air interface. These effects were found to be existing for shorter durations of time typically < 10 ns.

References

[1]C. DeMichelis, IEEE Journal of Quantum Electronics **5** (4), 188-202 (1969).
[2]C. G. Morgan, Reports on Progress in Physics **38** (5), 621 (1975).
[3]C. L. M. Ireland and C. G. Morgan, Journal of Physics D: Applied Physics **6** (6), 720 (1973).
[4]G. Taylor, Proceedings of the Royal Society of London A: Mathematical, Physical and Engineering Sciences **201** (1065), 159-174 (1950).
[5]E. F. Toro, *Riemann Solvers and Numerical Methods for Fluid Dynamics: A Practical Introduction*. (Springer Berlin Heidelberg, 2009).
[6]C. Leela, S. Bagchi, V. R. Kumar, S. P. Tewari and P. P. Kiran, Laser and Particle Beams **31** (02), 263-272 (2013).
[7]P. W. Cooper, *Explosives engineering*. (Wiley-VCH, 1996).
[8]R. W. Anderson, N. S. Elliott, R. B. Pember, L. L. N. Laboratory, U. S. D. o. Energy, U. S. D. o. E. O. o. Scientific and T. Information, *A Dynamically Adaptive Arbitrary Lagrangian-Eulerian Method for Hydrodynamics*. (United States. Department of Energy, 2004).
[9]J. Anderson, *Computational Fluid Dynamics*. (McGraw-Hill Education, 1995).
[10]R. Ramis, K. Eidmann, J. Meyer-ter-Vehn and S. Hüller, Computer Physics Communications **183** (3), 637-655 (2012).
[11]R. M. More, in *Advances in Atomic and Molecular Physics*, edited by D. R. Bates and B. Benjamin (Academic Press, 1985), Vol. Volume 21, pp. 305-356.
[12]S. Atzeni and J. Meyer-ter-Vehn, *The Physics of Inertial Fusion: BeamPlasma Interaction, Hydrodynamics, Hot Dense Matter*. (OUP Oxford, 2004).
[13]L. Spitzer, *Physics of fully ionized gases*. (Interscience Publishers, 1962).
[14]Y. B. Zel'dovich and Y. P. Raizer, *Physics of Shock Waves and High-Temperature Hydrodynamic Phenomena*. (Dover Publications, 2012).
[15]R. Ramis, R. Schmalz and J. Meyer-Ter-Vehn, Computer Physics Communications **49** (3), 475-505 (1988).
[16]E. Mínguez, P. Martel, J. M. Gil, J. G. Rubiano and R. Rodríguez, Fusion Engineering and Design **60** (1), 17-25 (2002).
[17]R. Joarder, G. C. Gebel and T. Mosbach, International Journal of Heat and Mass Transfer **63**, 284-300 (2013).
[18]S. Laville, F. Vidal, T. W. Johnston, M. Chaker, B. Le Drogoff, O. Barthélemy, J. Margot and M. Sabsabi, Physics of Plasmas **11** (5), 2182-2190 (2004).
[19]F. Rezaei and S. H. Tavassoli, Physics of Plasmas **20** (1), 013301 (2013).
[20]S. Sai Shiva, C. Leela, P. Prem Kiran, C. D. Sijoy and S. Chaturvedi, Physics of Plasmas **23** (5), 053107 (2016).

This page is intentionally left blank

Chapter 3

1D-Numerical Simulation of Laser Ablative SWs from Al Target into Ambient Atmospheric Air: Effects of ETR

The effect of electron thermal radiation (ETR) on 7ns laser ablative shock waves (LASW) from aluminum (Al) plasma into an ambient atmospheric air has been numerically investigated using a one-dimensional, three-temperature (electron, ion and radiation) radiation hydrodynamic (RHD) code MULTI. The governing equations in Lagrangian form are solved using an implicit scheme for planar, cylindrical, and spherical geometries. The shockwave velocities (V_{sw}) obtained numerically are compared with our experimental values obtained over intensity range 2.0×10^{10} - 1.4×10^{11} W/cm^2. It is observed that the numerically obtained V_{sw} are significantly influenced by the thermal radiation effects which are found to be dominant in the initial stage up to 2 μs depending on the input laser energy. Also, the results are found to be sensitive to the co-ordinate geometry used in the simulation (planar, cylindrical and spherical). Moreover, it is revealed that shock wave (SW) undergoes geometrical transitions from planar to cylindrical (Pln-Cyl) nature and from cylindrical to spherical (Cyl-Sph) nature with time during its propagation into an ambient atmospheric air. It is also observed that the spatio-temporal evolution of plasma electron and ion parameters like temperature, specific energy, pressure, electron number density, and mass density were found to be modified significantly due to the effects of electron thermal radiation.

3.1 Introduction

The interaction of pulsed lasers with solid targets leads to ablation of material followed by the generation of shock waves (SW) into an ambient atmosphere. The ablation of materials had proven to be promising technique for the applications like deposition of thin films[1], generation of nanoparticles[2], study of elemental and chemical analysis of materials using laser induced breakdown spectroscopy (LIBS)[3]. Similarly, the laser generated shock waves (SW) found applications such as strengthening of material using laser shock peening (LSP)[4], test the response of bulk materials to generate EOS using dynamical loading[5], micro-propulsion[6], inertial confinement fusion (ICF)[7] and also in medicine[8]. In the SW based applications it is very important to understand the spatio-temporal evolution of the shock waves (SW) under different ambient conditions. In contrast to the conventional impact experiments where the material responses are investigated at longer times (>μs), with LISW the investigations may be done for shorter (ns to μs) time scales.

The ablative shockwave expanding into ambient air launches a compression wave through the material due to momentum conservation. Hence understanding of laser ablative shock wave (LASW) will help get an insight into the shock propagation through target material. The challenge of the laser induced dynamic loading is to understand the planarity of the shock wave (SW) propagating into the target material. As the imaging of shockwaves through an opaque target is challenging, understanding the evolution of ablative SWs into the ambient atmospheric medium to estimate the propagation of SW launched into the target of interest is an alternative method. The investigation of shock planarity is important for the generation of EOS of different materials based on which novel materials can be designed for the applications of space science, inertial confinement fusion (ICF), material science etc. In all these applications except in medicine the incident laser energies range over few J to kJ with the intensity > 10^{13} W/cm^2 and the SWs generated are in few MPa – GPa. Due to very high

intensity range the radiation effects may strongly influence the SW propagation. Many authors[9-14] have obtained the scaling laws for ablative pressures that are observed to be largely dependent on the laser Intensity, wavelength and material properties. Such scaling laws proved to be very useful to estimate the laser ablative implosion and explosion pressures of different materials. Of course these studies are based on several assumptions and have certain limitations. For example, the radiation losses and its influence on SW evolution is discussed sparsely. Despite of these a decent agreement of the experiments results with the scaling laws is observed. In medicinal applications for the ns pulse widths and the material considered, laser energies (few mJ) and intensities ($<10^{10}$ W/cm^2) are very low compared to that used for ICF and EOS applications. The SW generated in this case will be weak (few MPa) with almost negligible radiation influence.

The expansion dynamics of laser ablated plasma and shock waves depend on various parameters, such as the input laser intensity, wavelength, pulse duration, ablated target material properties, and on the pressure and mass concentrations of the ambient atmosphere. Due to transient nature of the laser pulse intensity various physical processes occur during laser interaction viz., target heating, melting, evaporation, ionization[15], phase explosion[16-18], formation of plasma. After the termination of the laser pulse the plasma expands adiabatically leading to the generation of shock wave (SW) that propagates supersonically into ambient gas. Due to multiple physical processes occurring during and after the laser pulse, the physics of laser generated plasma and SW has become a complex subject to understand. Numerous reports have demonstrated the ablated plasma dynamics experimentally in vacuum, and by taking into account the effects of different background gases (He, N, O_2, Ar, air)[19-23] over pressure range of 1 – 10^5 Pa[24-38]. These experiments revealed some of the important physical phenomenon such as the free or adiabatic expansion[39] of the plume into vacuum, splitting and sharpening [23, 24, 40] of plume into different species at moderate pressures (low pressures) with low and high mass particles moving with

different velocities, generation and confinement of SW and plume[29-32, 34] at ambient pressures due to collisions between the plasma particles and ambient gas.

Intensive numerical efforts have been made using models based on the thermo-optics or hydrodynamics or the combination of both[38, 39, 41-44] to understand the fundamentals of laser-target, laser-plasma interaction and ablation processes occurring during and after the termination of laser pulse. Bogaerts et al[38] had numerically investigated the influence of laser parameters on target melting, evaporation, plume dynamics and compared with the experimental results. Jeong et al[44] studied the effects of the ambient pressure and the laser fluence on the vapor expansion. Singh et al[39] studied the physical phenomena involved in the laser-target interaction process and demonstrated that the ablated material undergo isothermal and adiabatic processes during and after the termination of laser pulse. Amoruso[42] had investigated the ablation of material by taking into consideration of photo-ionization and inverse bremsstrahlung (IB). Gragossian et al.[18] had revealed that at intensities higher than the breakdown thresholds the ablated material undergoes phase explosion[18]. Overall, the initial laser-target-plasma interaction, plasma dynamics was observed to be strongly dependent on the laser wavelength, laser fluence, and ambient gas conditions. Few reports[30-32] examined the plasma expansion and Yoh et al. has provided a trivial solution to the expansion of SW such as planar (hemi-spherical) expansion during the initial times and spherical expansion at later times. The importance of the electron thermal radiation (ETR), the amount of radiation emitting and different types of emissions occurring from laser produced plasma show that the ETR from ablated plasma increases proportionally with increasing laser energy. Moreover due to radiation emissions the plasma temperature was found to decrease to that without ETR effects[30, 37, 45-49]. Though, the effects of ETR on the plasma parameters like the electron number density and temperature (n_e and T_e) are explained, but the deeper insight of the spatial and temporal behavior of the plasma dynamics and the influence of electron thermal radiation (ETR) on SW evolution for longer durations of time was not reported so far.

In this chapter, a detailed study of the plasma dynamics, SW evolution with and without ETR effects and its influence on the geometrical transitions of SWs upto 10 μs will be discussed. The expansion features of the plasma and laser ablative shockwaves (LASW), from aluminum target into ambient atmospheric air was numerically studied using modified 1D-RHD MULTI-fs[50] code. This Lagrangian code is widely used for laser ablation studies from nanosecond to femtosecond duration of pulses which has the option to perform simulations in three different geometries viz., planar, cylindrical and spherical. Hence simulations have been carried out using three geometries for the intensities ranging from 2.0×10^{10} to 1.4×10^{11} W/cm^2 and time durations of up to 8.0 μs. The temporal evolution of shock velocity V_{sw} is compared using three geometries by considering with and without ETR effects. This is followed by studying the influence of ETR on the spatial evolution of the flow properties of electron and ion temperatures (T_e, T_i), specific energies (E_e, E_i), pressures (P_e, P_i), electron number density (n_e), and mass density (ρ). Finally, the temporal evolution of plasma parameters such as n_e, T_e with and without ETR and the temporal evolution of the mass density in the core plasma and across the SF are presented.

3.2 Numerical Model and Simulation Methodology

The schematic of laser-target and laser-plasma interaction (fig. 3.1 (a)) shows the expansion of internal plasma core and outer region, contact front (CF), shock wave (SW) into ambient air, radiation emission from the ablated plasma and its interaction with SWs. The sequential order of different physical processes occurring during the laser pulse (upto15 ns) and post the laser pulse upto 10 μs is depicted in fig. 3.1(b).

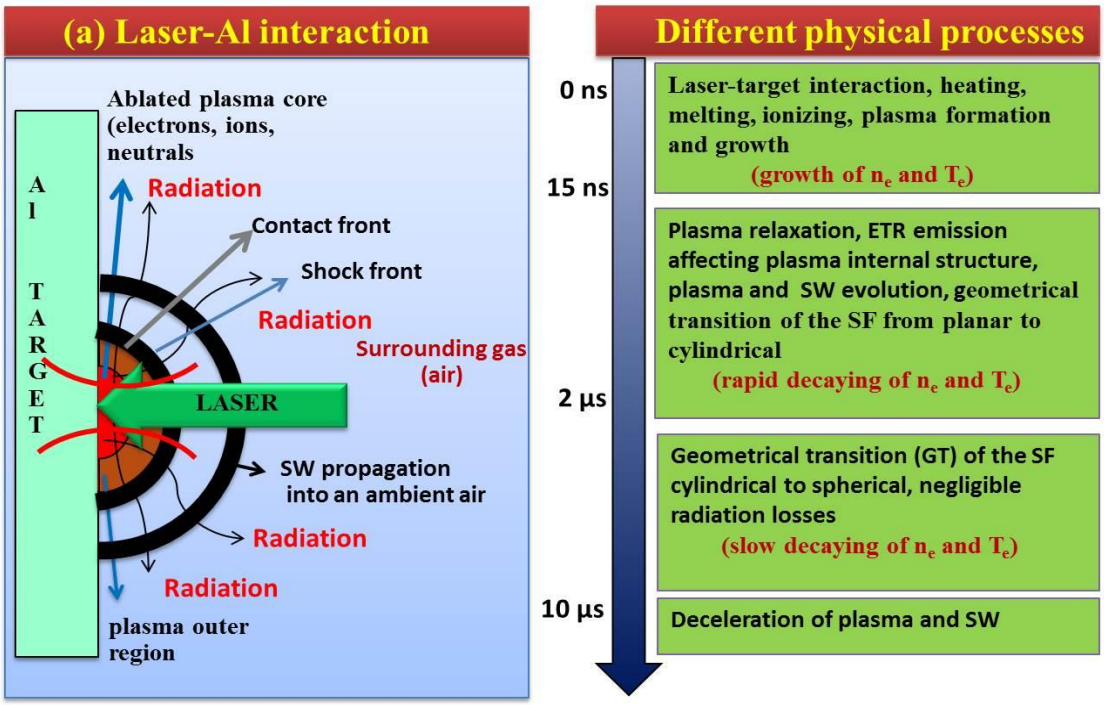

Figure 3.1 a) Schematic of laser-target interaction and SW propagation in ambient air and b) different processes occurring during and following the laser pulse leading to geometrical transitions in SW during its evolution.

For a self-consistent simulation of these physical processes we have used a one dimensional, Lagrangian, three temperature (electron, ion and radiation) radiation hydrodynamic (1D –RHD) MULTI-fs[50] code. The code considers electrons and ions as different species with different energy equations. However plasma is assumed to have a single fluid velocity ($\vec{u}$) and mass density (ρ)[50].

3.2.1 Governing RHD equations

The governing RHD equations to describe the temporal evolution of laser ablated plasma and SW is given by,

$$\frac{D\rho}{Dt} = -\rho\vec{\nabla}.\vec{u}, \tag{3.1}$$

$$\rho\frac{D\bar{u}}{Dt} = -\vec{\nabla}(P_e + P_i + P_v), \tag{3.2}$$

$$\rho\frac{DE_e}{Dt} = -P_e\vec{\nabla}.\vec{u} - K_{th}\nabla T_e + \varphi_{ei} + k_{IB}I_L - \vec{Q}_{rad}, \quad (3.2)$$

$$\rho\frac{DE_i}{Dt} = -(P_i + P_v)\vec{\nabla}.\vec{u} - \varphi_{ei} + k_{IB}I_L \quad (3.4)$$

The variables in equations (1) – (4) account for mass density (ρ), fluid velocity ($\vec{u}$), viscous pressure (P_v) acting on ions, electron and ion pressures (P_e & P_i), electron and ion specific energies (E_e & E_i) and electron and ion temperatures (T_e & T_i). Different physical mechanisms involved during the laser-matter interaction and after termination of laser pulse are incorporated in energy equations (3) & (4). k_{IB} accounts for laser absorption coefficient due to inverse-bremsstrahlung of electron-ion (e-i) collisions, K_{th} is the heat conduction coefficient due to electron-ion (e-i) [50] and electron to neutrals (e-n) collisions ($K_{th} = K_{ei}+K_{en}$)[42, 51, 52], $\vec{Q}_{rad}$ accounts for radiation losses and φ_{ei} the energy relaxation between electron and ion. The radiation term is solved by the multi-group approximation method. The Planck and Rosseland mean opacities, charge state and QEOS data of Al[50, 53] target provided in the original code are used. The initial mass density (ρ) and total electron number density (n_e) of Al are taken as 2700 kg/m^3 and 1.39 $\times 10^{29}$ m^3, respectively.

3.2.2 Modifications to MULTI-fs code

The original MULTI-fs code was developed for laser ablation studies of different materials in vacuum. As our experiments were carried out in ambient atmospheric air the code has been modified according to the experimental conditions and a separate routine for air is introduced as the background medium. We have assumed air as ideal gas with charge state ionization taking into account. So the EOS is given by[51],

$$P = N(1 + Z_i)k_bT, \quad (3.5)$$

The equation will have two contributions one for the electron pressure P_e and the other for ion pressure P_i,

$$P_e = NZ_ik_bT_e, \quad (3.6)$$

$$P_i = Nk_bT_i, \tag{3.7}$$

Assuming air to be ionized thermally and singly ionized we have adopted Saha[51] relation to obtain the charge state, Z_i given by,

$$\frac{{Z_i}^2}{1-Z_i} = \frac{1}{N} 2AT_e^{3/2} exp\left(\frac{-I_p}{k_B T_e}\right), \tag{3.8}$$

where N is the local neutral number density, $A = \left(\frac{2\pi m_e k_b}{h^2}\right)^{3/2}$ is a constant, I_p is the first ionization potential of oxygen taken to be equal to 14.56 eV[51] by assuming the contribution of nitrogen atoms is negligible. The electron and ion temperatures (T_e and T_i) of the gas, is obtained respectively, from the electron and ion pressures (P_e and P_i).

$$T_e = \frac{P_e}{N\alpha k_b}, \tag{3.9}$$

$$T_i = \frac{P_i}{Nk_b} \tag{3.10}$$

The deposition of laser energy into Al is modeled following WKB approximation[50].

3.3 Experimental data and Results

The experimental setup for capturing spatio-temporal evolution of plasma plume and LASW from laser ablation of aluminum is described elsewhere[54-56]. The target is ablated using 7 ns (FWHM) second harmonic of Q-switched Nd:YAG at 532 nm. The beam was focused on to the target surface using a plano-convex lens with f/10 focusing geometry. The experiments were carried out for laser energies varied in the range of 25 mJ - 175 mJ that are focused to a diameter of approximately 140±10 μm giving rise to intensities in the range 2.0×10^{10} - 1.4×10^{11} W/cm^2. All experiments were carried out in ambient air at room temperature and atmospheric pressure.

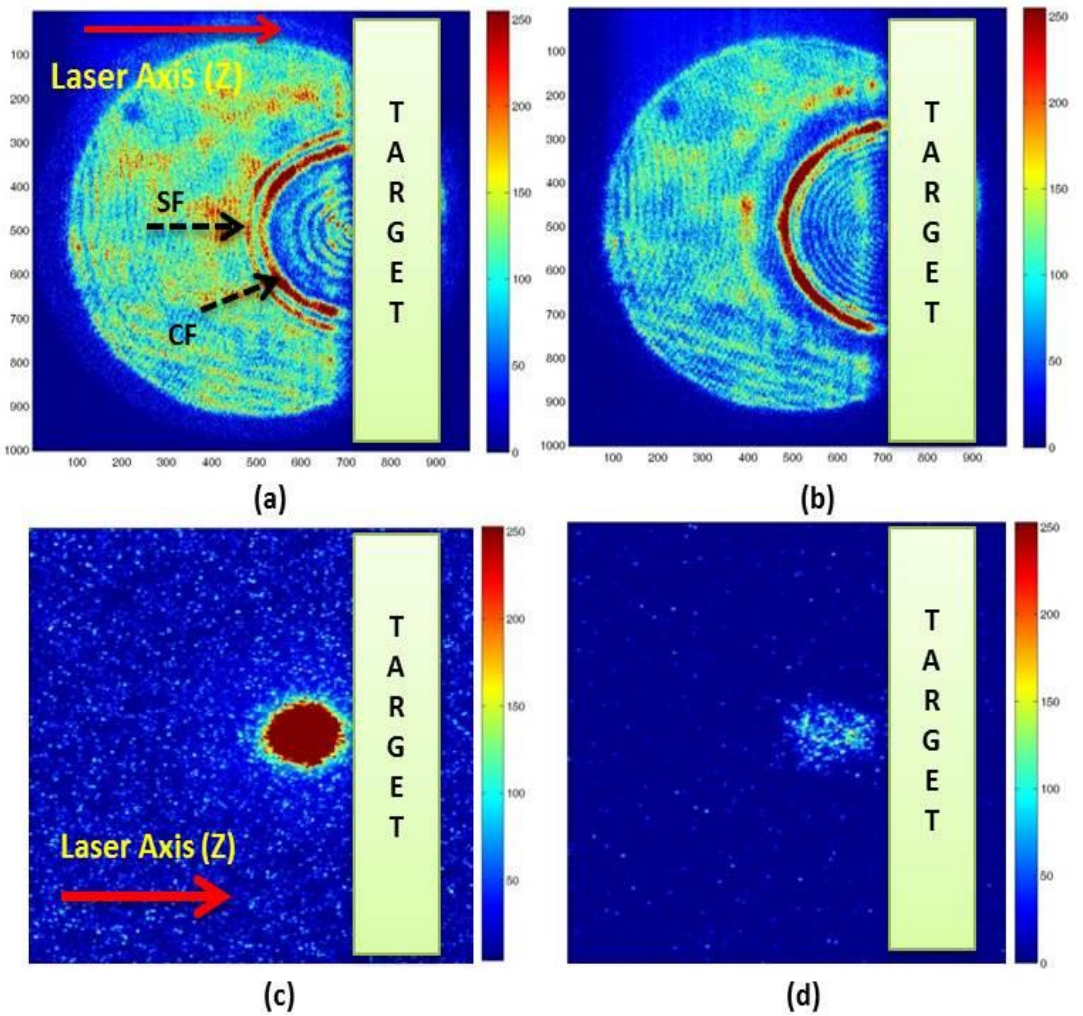

Figure 3.2 (a, b) Shadowgrams of spatio-temporal evolution of shock front (SF), contact front (CF) at 2.2 μs and 5.4 μs, respectively. (c, d) 2D Self-emission images of Al II (466.3) species at 50 ns and 2 μs delay for input laser energy of 25 mJ. Figure courtesy Ch. Leela et al.[55, 56]. Solid arrow represents the laser propagation direction and dashed arrow represents the SF and CF.

Figure 3.2 (a,b) show the shadowgraph images of the spatio-temporal evolution of the shock front (SF) along normal to the target and in the perpendicular direction into ambient air at 2.2 μs and 5.4 μs, respectively after the laser pulse interaction at 25 mJ. The velocity (V_{sw}) of the SF with respect to the target position was measured over the time scales 0.4 μs – 8.0 μs. The 2D self-emission representing the expansion of ablative plasma into ambient atmospheric air at 50 ns and 2 μs are shown in fig 3.2 (c, d). The

correlation between the evolution of the SW and the decay of Al II emissions from the Al ablative plasma is shown in fig. 3.2.

3.4 Effects of ETR on SW evolution into ambient air

3.4.1 Shock wave evolution without ETR effects

Figure 3.3 (a) shows the comparison of experimentally obtained V_{sw} values with planar, cylindrical and spherical geometry for the times scales of 0.4μs – 8.0 μs for the input laser energy of 25 mJ. With the intensity used in the experiment the plasma is under dense and collisional absorption plays a major role and is used to set initial conditions[57].

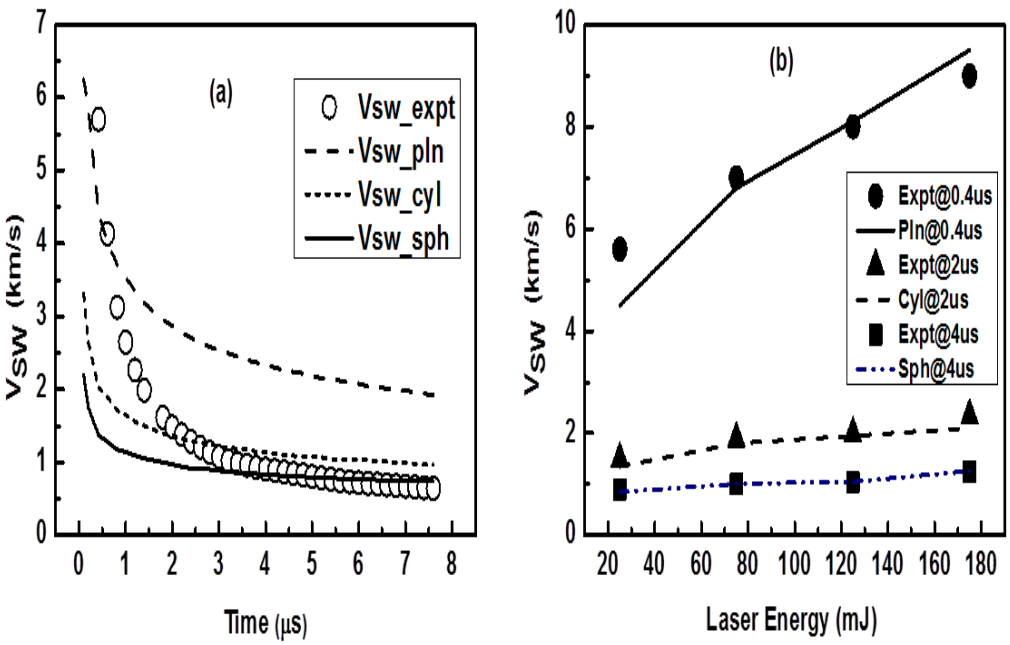

Figure 3.3 Comparison of experimentally obtained V_{sw} with a) simulations using planar, cylindrical and spherical geometries for times scales of 0.4 μs – 8.0 μs for the input laser energy of 25mJ, b) planar and spherical geometries at 0.4 μs and 4.0 μs respectively, for laser energies of 25 mJ, 75 mJ, 125 mJ and 175 mJ respectively.

The numerical results compared are the best fits of the experimental data. It is observed that for the initial times of up to 0.8 μs the SW follows a planar nature. From 0.8 – 1.6 μs it is in between planar and cylindrical shape. Between times scales 1.6 – 3.0

μs it follows the cylindrical nature. Finally, after 3.0 μs it is observed to follow spherical nature. The transition from planar to cylindrical is not instantaneous and is observed to take certain time to convert from planar to cylindrical nature. Similarly the transition from cylindrical to spherical is observed to be instantaneous. The time gap between planar to cylindrical may be due to transfer of SW expansion from one dimensional to three dimensional. The SW front have to push larger areas of the surrounding gas ahead of it, hence the transition takes certain time to evolve from planar to cylindrical. Figure 3.3 (b) shows the comparison of V_{sw} with planar geometry at 0.4 μs and with spherical geometry at 4.0 μs for range of input laser energies used. At 0.4 μs, V_{SW} for 25 mJ have lower value~4.5 km/s compared to experimental 6.0 km/s. For 75 mJ, 125 mJ and 175 mJ the experimental and simulation values were found to be in good agreement. The spherical nature was observed to exist early with the increasing laser energy. For example, for 25 mJ this nature is observed to exist after 3.0 μs and with the increasing energy this is observed to exist from 2.0 μs onwards. In fig. 3.3 (b) shows that the SW evolution completely follows the spherical nature from 4.0 μs for all the input laser energies used in the study.

3.4.2 Ablated plasma expansion with planar, cylindrical and spherical geometries

The laser ablated plasma expanding in ambient air is shown in fig. 3.4 is compared with planar, cylindrical and spherical geometries for the input laser energy 125 mJ at 24 ns. The laser absorption is taken to be same with all the three geometries. Regions I &2 in fig. 3.14 (a) represent the plasma core (PC) and plasma outer region (POR). The expansion length of the plasma is found to be larger with the planar (0.68 mm), simultaneously followed by the cylindrical (0.2 mm) and spherical (0.1 mm). Similarly, the corresponding electron number density and the total pressure is also found be more with planar followed by the other two geometries.

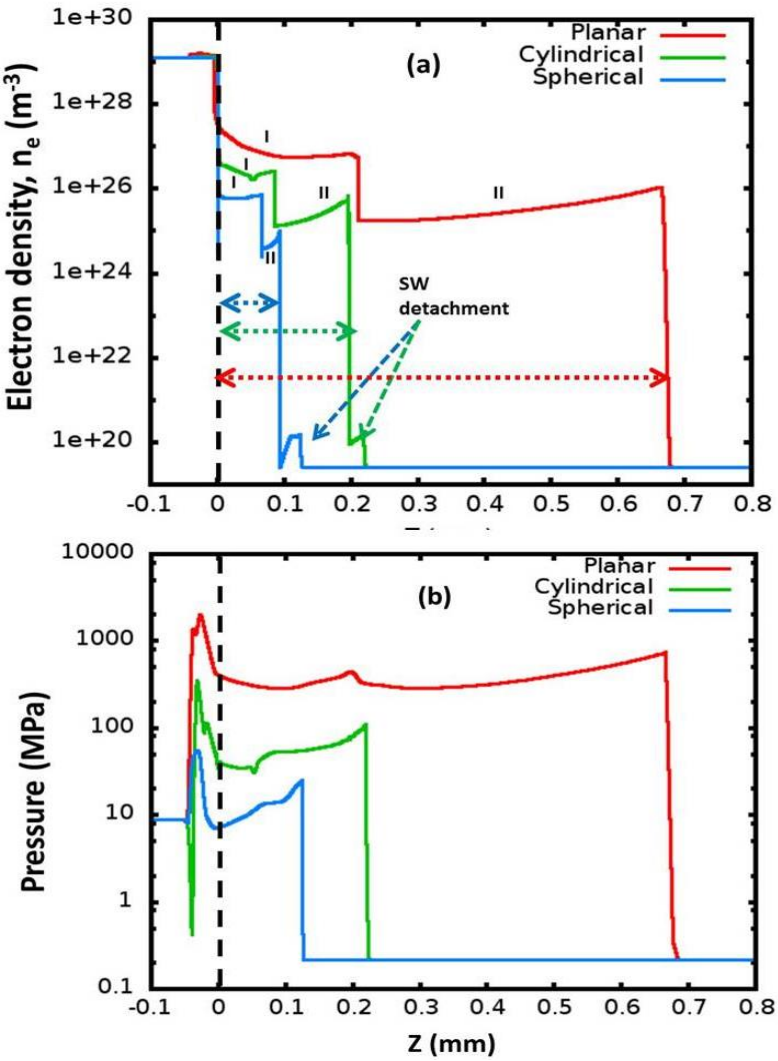

Figure 3.4 Comparison of the ablated plasma dimension and SW detachments at 24 ns with planar, cylindrical and spherical geometries for 125 mJ with ETR effects a) electron number density and b) total pressure (electron and ion) of the plasma.

The mass of the computational cells has higher values in the case of spherical and is followed by the cylindrical and planar geometries. So the ablated plasma with the spherical geometry has to push the higher area ahead of it. Due to this, the expansion is slow in the case of spherical. Similar is the case with the cylindrical geometry where the expansion is found to be smaller than that of planar since the mass of the cylindrical cell is higher than the planar the ablated plasma expands slowly than that of the planar

case. The SW is observed to detach early in the case of cylindrical and spherical geometries whereas, with planar no SW detachment is observed for the present time scale. This shows that the SW detachment times depend on the geometry considered.

3.4.3 Effects of ETR on SW evolution and geometrical transitions

Figure 3.5 (a-d) compares the shock front (SF) velocity, V_{sw} of experiments with numerical simulations with and without ETR effects for lower (25 mJ and 75mJ), and higher (125 mJ and 175 mJ) laser energies used in our study.

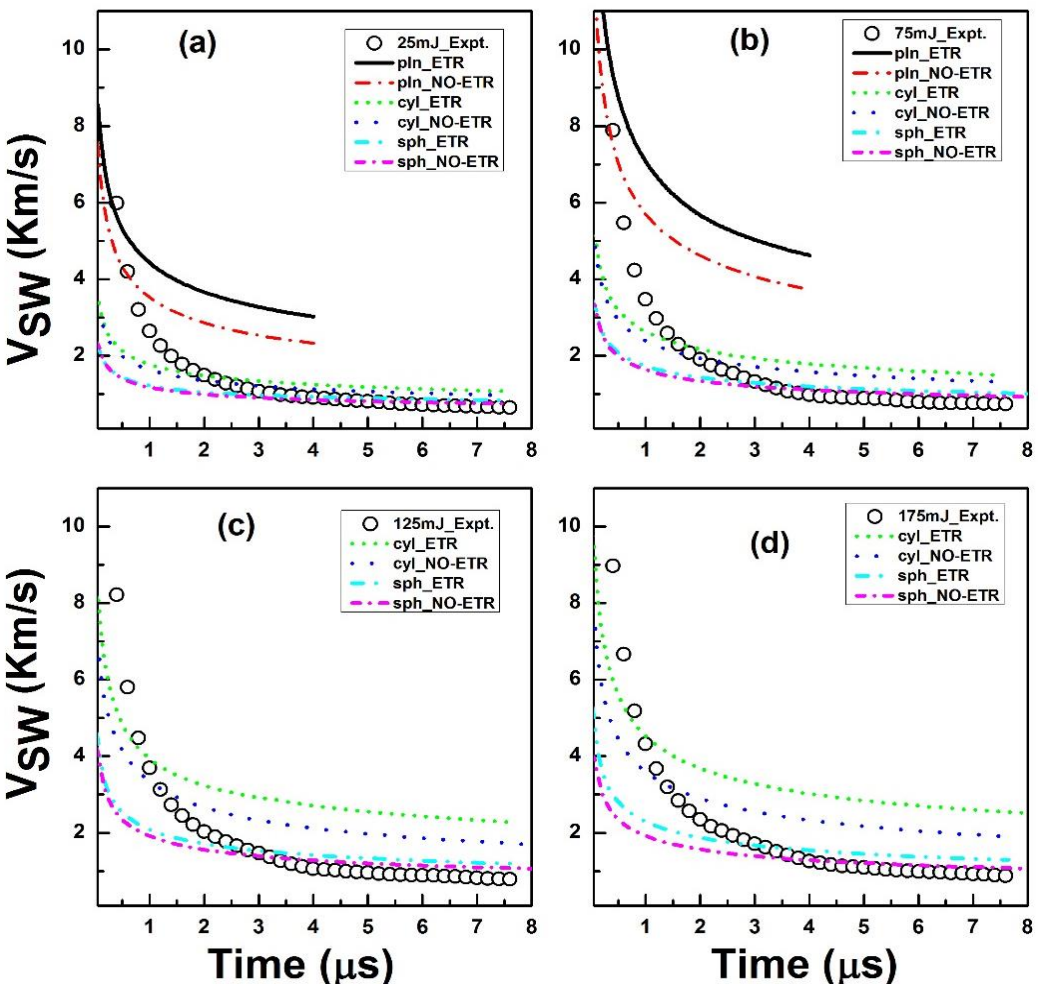

Figure 3.5 Comparison of experimentally obtained shock wave velocity(open circles) with numerical data with and without ETR effects for the input laser energies of a) 25 mJ, b) 75 mJ, c) 125 mJ and d) 175 mJ using planar, cylindrical and spherical geometries.

The compared velocities show that the SF undergoes geometrical transitions from planar to cylindrical (Pln-Cyl) and from cylindrical to spherical nature (Cyl-Sph) during its evolution. Table-1 summarizes the times scales SF undergoes transition from Pln-Cyl and from Cyl-Sph during the evolution. The existence of planar is observed dominantly up to ~ 0.8 μs for 25 mJ and ~ 0.6 μs for 75 mJ without electron thermal radiation (ETR) effects whereas, with ETR, PN existed up to ~0.6 μs for 25 mJ and ~0.4 μs for 75 mJ. The shock velocity (V_{sw}) for 25 mJ at 1 μs with ETR is found to be higher ~4.5 km/s than that of without ETR ~3.5 km/s. Similarly, at 75 mJ this is observed to be ~7.0 and ~5.5 km/s, respectively. This significant difference in the shock velocity shows that ETR plays a crucial role in driving the SW into ambient air during its evolution. The existence of planar nature at higher energies was not observed for the longer times (> 0.4 μs). This nature may exist at even lower time scales[31].

The planar nature of the SF is followed by the cylindrical nature which is observed to exist for both lower (fig. 3.5 (a & b) and higher (fig. 3.5 (c & d)) energies. At lower energies the cylindrical exists between 1-1.5 μs while at higher energies it exists up to ~2.0 μs. The difference in the shock velocity with and without ETR at lower energies is observed to be very small indicating that the radiation losses have become negligible. However, at higher energies a clear difference in the V_{sw} is seen with and without ETR effects. At 2μs, V_{sw} values for 125 mJ with and without ETR have ~3.5 and ~2.7 km/s, respectively. Whereas, for 175 mJ the V_{sw} ~4.0 and ~ 3.0 km/s, respectively. With increasing laser energy the difference in shock velocities shows that radiation plays a crucial role even upto longer time scales (up to 2.0 μs). The influence of ETR up to longer times results in the increase of laser energy absorption by the ablated plasma[44]. The cylindrical nature of the SF is observed to instantaneously become spherical nature for all the laser energies considered. This nature is found to originate around 2 μs for lower energies and around 1.5 - 1.6 μs for higher energies. The difference in V_{sw} during this nature is observed to be small at higher and lower energies indicating that the radiation becoming negligible after 2 μs. The SN of the SF signifies

that the plasma and SF evolution has become symmetric and expands with uniform velocity in all the directions.

The existence of planar at lower energies is due to low absorption of laser energy by the ablated plasma as a result the plasma occupies small volume and mostly resides on the target surface. Moreover, due to high expansion speed towards normal to the target direction, the SF appears to be of planar. The plasma and SF expansion may be assumed as the 1D flow. However, at later times due to confinement of the plasma and SF by the ambient gas, the expansion speed normal to the target becomes comparable to the radial direction and expands uniformly in 2D and 3D giving rise to cylindrical and spherical.

At higher energies due to increase in the laser energy absorption, the ablated plasma occupies higher volume compared to that of lower energies. Due to this, the expansion of the SF becomes significant in both directions as a result the SF appears to follow cylindrical nature from 0.4 – 1.6 μs and spherical nature after 2 μs. The plasma and SF expansion will have 2D or 3D flow. The similar flow field conditions is also observed from shadowgraph images (not given in this chapter) taken experimentally[56]. Due to increase in the laser energy absorption, the ETR also increases and lasts for long time scales (up to 2 μs). The increase in the shock velocity with ETR is due to increase in the temperature of the surrounding gas which results from the pre-heating of the gas. The radiation emitting from the plasma interacts with the surrounding air resulting in pre-heating of the gas. Due to this process, the SF moves quickly because the propagation speed of the SF is proportional to the temperature. This process continues as long as the radiation is dominant.

3.4.4 Effects of ETR on SW at Minimum Fraction of Absorption

The fraction of laser energy absorbed (A_{abs}) to the total laser energy (E_L) taken in the simulations is summarized in Table-3.1 for incident laser energies 25 – 175 mJ. These values were in agreement with the values given by Kundu[57] where the time dependent

electron-ion collision frequency of under-dense plasma (closer to our experimental conditions) is observed to affect the mass ablation rate and its scaling.

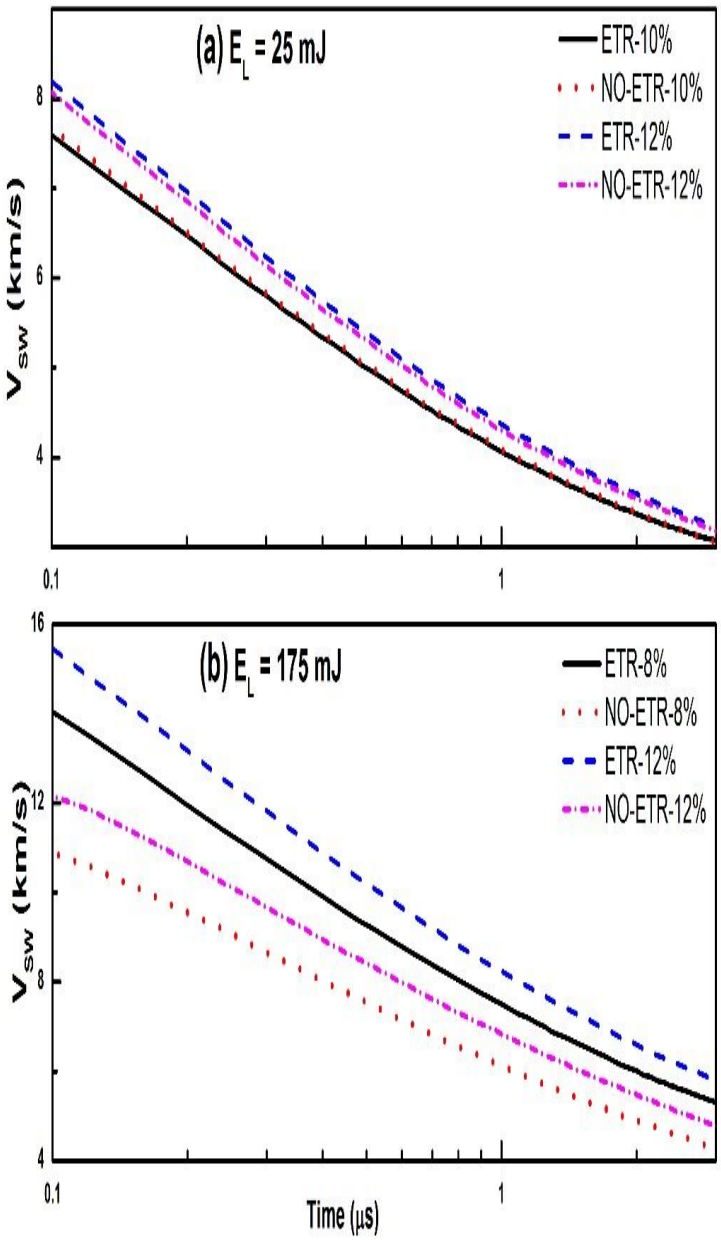

Figure 3.6 Shock velocity comparison at and above threshold fraction of laser absorption for a) 25 mJ and b) 175 mJ laser energies for planar geometry.

Table-3.1 also summarizes the fraction of threshold absorptions (A_{th}) where, the radiation heating starts affecting the SW propagation. Fig. 3.6 (a & b) show the comparison of shock velocities (V_{SW}) for planar geometry with and without radiation effect for 25 and 175 mJ energies, respectively. At 25 mJ, for 10 % absorption the radiation is not observed to influence the shock velocity (V_{sw}), but as the absorption is increased to 12 % a slight increase in the V_{sw} with radiation can be seen (fig. 3.6 a). Similarly, for 175 mJ the radiation heating starts affecting from 8 % onwards, and with the increased absorption (12 %) the radiation heating becoming dominant (fig. 3.6 b).

Table 3.1 SW transition times from Pln-Cyl and from Cyl-Sph with ETR effects.

E_L (mJ)	t_{PN} (ns)	t_{PN}-t_{CN} (ns)	t_{CN} (µs)	t_{CN}-t_{SN} (µs)	t_{SN} (µs)	A_{abs} %	A_{th} %
25	~600	~600	~1.2-2.2	Instantaneous	≥ 2.2	15-18	12
75	~400	~600	~1.2-2.0	Instantaneous	≥ 2.0	23-25	9
125	<100	~400	< 1.2	Instantaneous	≥ 1.2	35-38	8
175	<100	~400	< 1.2	Instantaneous	≥ 1.2	45-48	8

t_{PN} – existence time of Pln nature, t_{PN}- t_{CN} – time taken to transit from pln-Cyl nature, t_{CN} – existence time of Cyl nature, t_{CN}- t_{SN} – time taken to transit from Cyl-Sph nature, t_{CN} – existence time of Sph. nature.

At 25 mJ the radiation heating show its influence on the shock velocity at > 12 % of absorption. At 75 mJ, the radiation affects can be seen from 9 % onwards. Similarly at higher laser energies (125 and 175 mJ) this can be seen at even low absorptions ≤ 8 %. This is obvious because with increasing laser energy the peak intensity also increases and the breakdown threshold of the target material occurs at very initial part of the laser pulse. Hence, with the increasing laser energy the radiation heating affects starts occurring at lower threshold absorptions. The radiation effects for

As given in Table-3.1, the transition in SF from planar to cylindrical nature is not continuous at lower laser energies that is, SW has taken certain time to convert from planar to cylindrical while the transition from cylindrical to spherical is observed to be instantaneous for all the energies considered. Overall, the effect of ETR has played a

crucial role in the evolution of SF. This effect is predominant at higher laser energies and lasts up to longer time scales (2 μs). The ETR effect on the evolution of the SF was found to be dominant for planar evolution compared to that of cylindrical and spherical evolution. The influence of radiation on SF evolution is dominant as long as the radiation emissions are dominant.

3.4.5 Existence of Planarity of the SW

The shift of SW from planar to spherical nature can be explained using the (i) The ratio of characteristic plasma length (L) to the laser spot size[12] ($2\omega_0$), (ii) The dependence of laser absorption coefficient on the excitation wavelength[29] and (iii) Lateral transport of thermal energy and the lateral flow of mass[14]. According to Mora et al.[12] the initial plasma expansion is decided by the absorbed laser energy, pulse duration and the focal spot diameter. For a plane self-similar expansion of isothermal plasma in vacuum is determined by the characteristic scale length (L) with the condition that, L less than the spot diameter ($2\omega_0$).

$$L = C_s\tau = \left(\frac{ZT_e}{m_i}\right)^{\frac{1}{2}}\tau \qquad (3.11)$$

where C_s is the ion acoustic velocity, T_e is the electron temperature in eV, m_i is the ion mass, A is the mass number, m_p is the proton mass, and τ is the laser pulse width.

In the simulations the electron temperatures (T_e) and charge state (Z) for 25 mJ were found to be ~12 eV and Z ~ 1, respectively. These values give an estimated plasma length, L ~ 0.09 mm which is less than the spot diameter ($2\omega_0$) 0.14 mm used in our experiments. The characteristic length L in this case, may be even small because the expansion is considered in ambient air at atmospheric pressure. Similar, for 125 mJ, T_e ~80 eV and Z ~ 8 gives the plasma length of ~ 0.7 mm which is greater than $2\omega_0$. So as the energy increases the expansion becomes cylindrical or spherical. The similar expansion features with respect to the increasing laser energy was reported by Yoh et

al. where instantaneous transition of SW from planar to spherical nature is observed during 1064 nm wavelength excitation[31].

Hussein et al.[29] investigated the plasma and shock wave evolution with 1064 nm, 532 nm and 266 nm and found that the expansion is dependent on the excitation wavelength. The laser absorption coefficient is observed to play a major role in the SW evolution with three different laser excitation wavelengths due to cubic proportionality to the wavelength, $k_{IB} \propto \lambda^3$. The ablative pressure P_{abl} in turn varies with laser intensity and the wavelength[14] as $P_{abl} \propto (I_L)^{2/3}\ \lambda^{-2/3}$. With longer wavelength excitation (1064 nm) the expansion is spherical while at lower wavelength (532 nm) excitation planar SW expansion is observed. Moreover for a given excitation wavelength higher laser energies have resulted in cylindrical SW expansion.

Batani et al.[14] has given the scaling for the time dependent mass ablation rate and showed that the mass ablation rate increases up to the critical number density of the plasma is reached. In our case, the electron densities for the highest laser energy (175 mJ) were found to be $n_e \sim 10^{26}$ m^{-3} that is low compared to the critical number density, $n_c = 4\times10^{27}$ m^{-3}. So, the mass ablation rate increases with increasing laser energy. Hence lateral transport of thermal energy and lateral flow of mass into ambient air will determine the planar to spherical nature which is given by the condition $L/2\omega_0 > 1$. With 25 mJ, the condition L< spot diameter is valid hence, the plasma expansion can be treated as planar in the initial times. Due to the self-similar nature the expansion continues to be in the planar for some time of the order of 10 τ_p.

After the planar nature the SW attains the cylindrical and finally spherical nature. During the transition from planar to cylindrical and to spherical the kinetic energy of the SW decreases rapidly. This decreased energy is utilized in expanding the SW through the ambient air. The expansion takes place due to the collision between particles at the shock front and ambient air interface, as a result, the energy is transferred to the ambient air. Since the kinetic energy of the SW at the initial stages is very high it is capable of pushing large areas ahead of it as a result it lost most of its

energy, hence the energy drops suddenly (shown in fig. 3.3 shock velocity) during the transition from planar to cylindrical and then to spherical. Thus the change in the kinetic energy and momentum is equal to the change in the total volume of the SW expansion. Once the expansion becomes spherical in nature it means that the SW has achieved equal velocity in all the directions hence the expansion becomes spherical self-similar. One of the interesting aspects observed from the numerical simulations is that the SW expansion is following the cylindrical expansion in between planar and spherical expansions. Moreover, the transition from planar to cylindrical is not instantaneous, but there exists certain time gap in contrast to Yoh et al's report[31].

3.5 Effects of ETR on Spatial Evolution of Plasma Parameters and SW

The influence of ETR on the plasma and SW evolution is explained by comparing spatial evolution of different variables like electron and ion specific energies (E_e and E_i), temperatures (T_e and T_i), electron number density (n_e) and mass density (ρ) and electron and ion pressures (P_e and P_i) with and without ETR. The evolution is considered for 125 mJ using cylindrical geometry at 50 and 1000 ns to see the effects of ETR at different times.

3.5.1 Spatial evolution of E_e, E_i, T_e, and T_i

The spatial expansion of electron and ion specific energies (E_e and E_i) are given in fig. 3.7 (a & b). Similarly the corresponding electron and ion temperatures (T_e and T_i) are given in fig. 3.7 (c & d). the arrows in the fig. 3.7 and fig. 3.8 indicates the PC, POR, SF, CF, shocked air and rarefaction wave (RW), respectively.

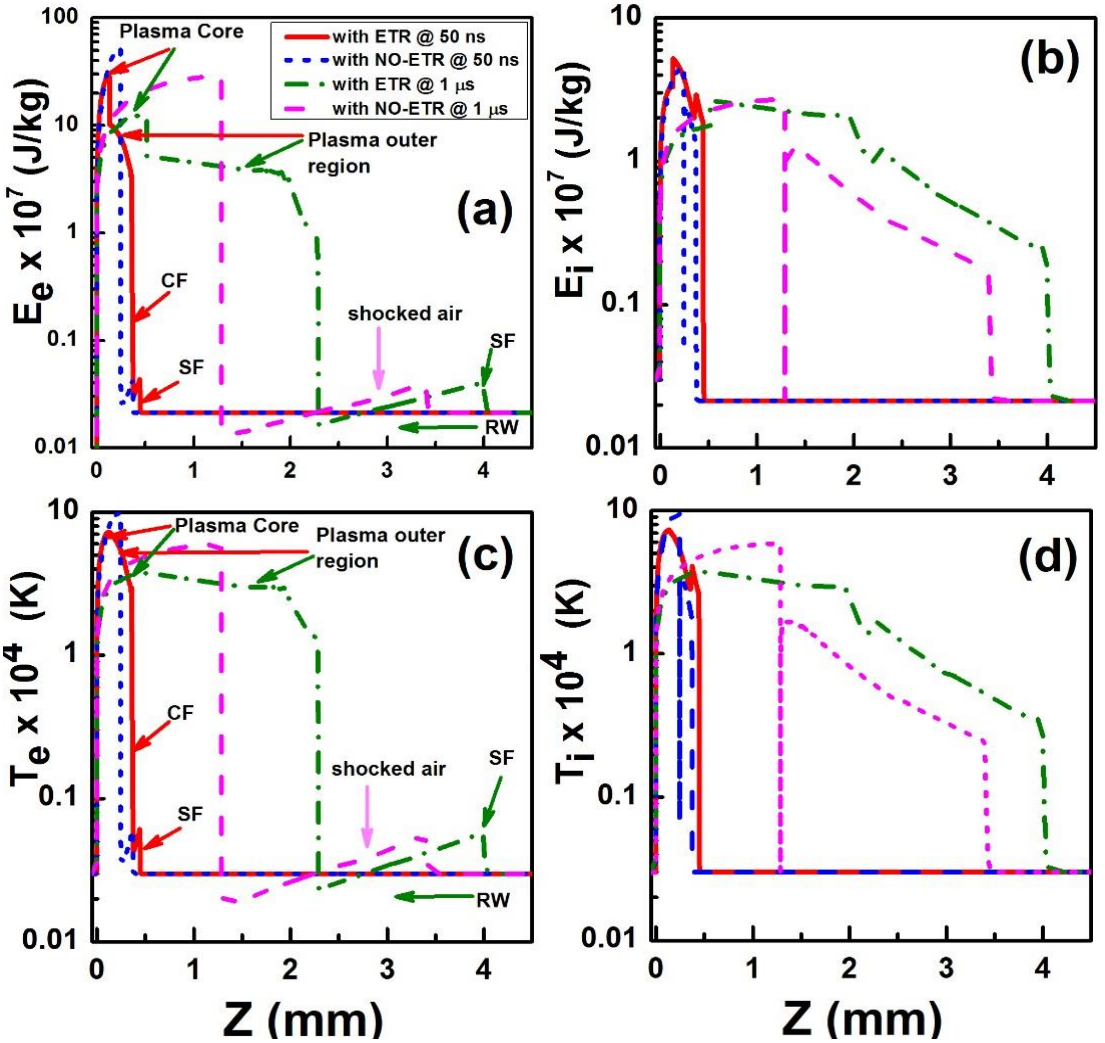

Figure 3.7 Comparison of spatial evolution of a) electron specific energy, b) ion specific energy, c) electron pressure, and d) ion pressure at 50 ns and 1000 ns with and without ETR effects for the input laser energy of 125 mJ using cylindrical geometry

An interesting feature of the plasma dynamics is observed with ETR effects. That is, the internal structure of the plasma is observed to split into two parts: the plasma core (PC) and the plasma outer region (POR). The PC region at 50 and 1000 ns exist around 0.15 mm and 0.5 mm from target surface. Similarly, the POR exist between 0.15 - 0.4 mm and 0.5 - 2.3 mm, respectively for the same time scales. Various regions formed in the plasma and in the shocked region are shown in fig. 3.7 (a).

3.5.2 Spatial evolution of n_e, ρ, P_e, and P_i

The spatial evolution of electron number density (n_e) and mass density (ρ) (fig. 3.8 (a, b)) and electron and ion pressures (P_e and P_i) (fig. 3.8 (c, d)) is given.

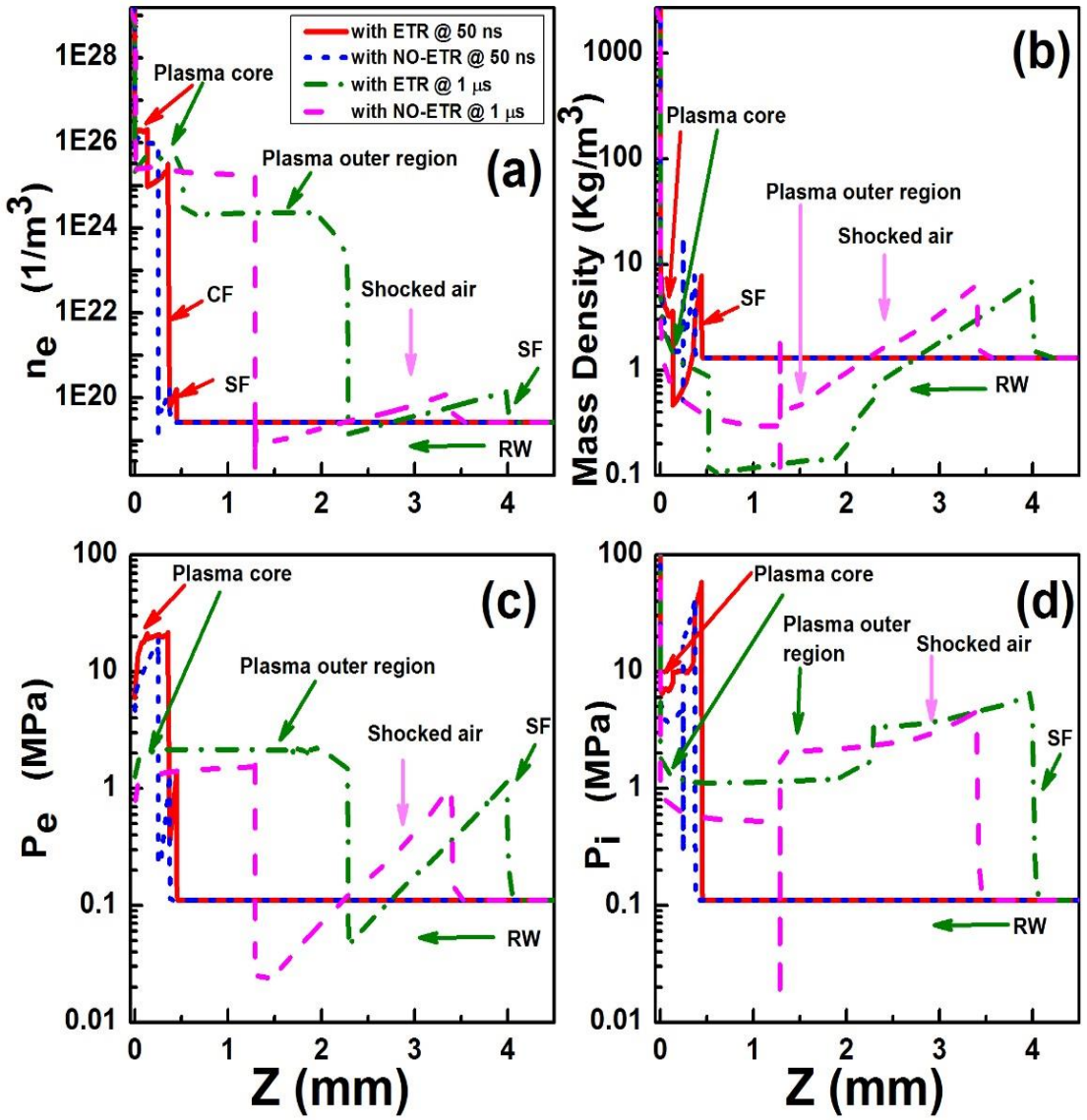

Figure 3.8 Comparison of spatial evolution of a) electron number density (n_e), b) mass density (ρ), c) electron (P_e) and d) ion pressures (P_i) at 50 ns and 1000 ns with and without ETR using cylindrical geometry for the input laser energy of 125 mJ.

A similar splitting of plasma into core and outer region is observed in all the profiles given in figures 3.7 (a-d) and 3.8 (a-d). The plasma nearer to the target surface is the core part and at positions slightly away from the target surface the POR is formed. The SW generated from the plasma moves quickly by compressing surrounding ambient air. The front portion of the SW is the SF that moves with high velocity. Behind the SF, the compressed gas relaxes and tries to come back to its normal ambient conditions. During the relaxation a rarefaction wave (RW) is formed that moves opposite to the SF direction (fig. 3.8). The region between the POR and SF is the shocked region in which the CF and POR propagates (fig. 3.8). The interface between the shocked air and the POR is the CF that moves with lower velocities compared to SF. The higher value of all the variables in the PC is due to majority of the laser energy absorption taking place in that region. Without ETR effects the splitting of the plasma is not observed. The ablated plasma is found to have only one region which may be treated as the PC. The PC regions exist around 0.25 and 1.3 mm at 50 and 1000 ns, respectively.

Table 3.2 Positions and velocities of SF and CF at 50 ns and 1000ns observed with and without ETR effects at 125 mJ with cylindrical geometry.

t (ns)	Z_{SF} (mm)	V_{SF} (km/s)	Z_{CF} (mm)	V_{CF} (km/s)	EFFECT
50	0.48	9.6	0.4	5.25	ETR
50	0.40	8.0	0.3	4.5	NO-ETR
1000	4.0	4.0	2.3	2.3	ETR
1000	3.4	3.4	1.3	1.3	NO-ETR

Table-3.2 summarizes the position and velocities of SF and CF at 50 ns and 1000 ns with and without ETR, respectively. Since the position of SF with ETR is ahead to that of without ETR, the corresponding shock velocities have higher values. The velocity V_{sw} with ETR drops from 9.6 to 4.0 km/s while without ETR drops from 8.0

to 3.5 km/s over the time 50 – 1000 ns, respectively. The fast decay in the SF suggests that the radiation support to the SF evolution decreases with the time evolution.

The higher E_e (fig. 3.7 (a)) is due to absorption of laser energy by the free electrons generated during the initial laser interaction process. The electrons gain energy by absorbing the laser energy and become free from the neutral atom. These free electrons acquire very high kinetic energies and moves freely with very high velocities in the ion field. During this process, they transfer the energy to the surrounding ions and neutrals by collisions resulting in decrease in the kinetic energy. The process of gaining and losing of the kinetic energy continues until the laser is on. However, after the laser pulse terminates, due to electron-ion (e-i) collisions, plasma expansion and radiation emissions, the plasma cools down and reaches local thermal equilibrium (LTE). The electron and ion temperature is found to have same values at 50 ns indicating that the plasma is at LTE. The recombination of electron and ions during this process will lead to the emission of high amount of ETR from ablated plasma. Though the plasma attains the LTE but, the electron specific energy E_e (fig. 3.7 (a)) both in the PC and POR have higher values than ionic specific energy E_i (fig. 3.7 (b)) due to the electrons being the lighter particles and having higher concentrations (number density) than ions. Fig. 3.8 (a) shows the existence of higher electron number density in the PC. This number is achieved due to multiple ionization of neutral atom during the laser interaction. That is, the atom gives up maximum number of electrons depending on its interaction with the laser energy and e-i collision rate. The electron and ion pressure (P_e, P_i) (fig. 3.8 (c & d)) in the plasma region follows proportionality relation to their corresponding energies. Once the LTE is reached within the plasma, the electrons across the POR and ambient air interface interacts with the surrounding air particles resulting in generation of the SW into ambient air. During this process, the electrons transfer their energy to the gas particles by thermal conduction and electron thermal radiation (ETR). Simultaneously, the ions in the shocked region gains energy

due to contribution from the viscosity. The variables E_i, T_i, P_i in the shocked region have higher values than variables E_e, T_e, P_e.

Table 3.3 Plasma parameters compared in the PC region with and without ETR effects at 125 mJ using cylindrical geometry.

t (ns)	$E_e \times 10^8$ (J/kg)	$E_i \times 10^8$ (J/kg)	$T_e \times 10^4$ (K)	$T_i \times 10^4$ (K)	P_e (MPa)	P_i (MPa)	$n_e \times 10^{26}$ (m^{-3})	ρ ($kg.m^{-3}$)	EFFECT
50	3.0	0.4	7.0	7.0	20.0	9.0	1.2	5.0	ETR
50	5.0	0.4	10.0	10.0	16.0	5.0	1.0	2.0	NO-ETR
1000	1.0	0.15	3.8	3.8	2.0	1.5	0.5	1.0	ETR
1000	3.0	0.25	6.0	6.0	1.3	0.8	0.4	0.4	NO-ETR

Table-3.3 summarizes the numerical values of electron and ion parameters such as specific energies (E_e, E_i), temperatures (T_e, T_i), pressures (P_e, P_i), electron number density (n_e) and mass density (ρ) in the PC region at 50 ns and 1000 ns, respectively with and without ETR effects. The electron temperature and specific energy with ETR effects is found to have lower values compared to that of without ETR effects. For example, at 50 ns T_e with ETR have ~ 7×10^4 K whereas, without ETR ~ 10×10^4 K. Similarly, E_e with ETR have ~ 3×10^8 J/kg and without ETR ~ 5×10^8 J/kg. The decrease in these values indicates that, a fraction of internal energy stored within the plasma region converts in to radiation that escapes from the plasma region. The radiation escaping from the PC may be utilized in driving the plasma. Similarly, the radiation escaping from POR will drive the SF into ambient air. As a result, the expansion of the plasma and SW is found to have advanced spatially that is, occupying higher volumes for the same times considered without ETR effects. Due to this advancement, the velocities of the SF compared in fig. 3.5 (a-d) are found to have higher values with the ETR effects. Due to high electron number density in the PC the radiation emissions from the core region will be dominant compared to that of the POR. Though T_e in the PC with ETR, have low value, the n_e is found to have almost equal values with and without ETR effects. For example, at 50 ns, T_e values with and

without ETR is found to have ~ 7×10^4 K and 10×10^4 K, but n_e is found to have same values ~ 1.0×10^{26}. So it could be expected that the radiation emissions from the PC is continuously occurring due to free-free (f-f) transitions of the electrons. Rezaei et al. has reported that the plasma residing near the target surface[37] will emit continuous radiation during plasma expansion in inert gas atmosphere. During the f-f transitions the electrons lose their kinetic energy in the form of radiation as they approach close to the ionic field. So during the process of f-f transitions the electrons lose their kinetic energy without recombining to the ions hence, the number density is found to have remained same. Though the electron, ion specific energies and temperature in the PC with ETR have lower values but, the mass density (ρ) is found to have higher values (fig. 3.8 (b)). At 50 ns, ρ has higher value ~5 kg/m^3 with ETR than ~2 kg/m^3 than without ETR. The higher mass density is due to the low T_e and T_i existing and due to less volume occupied by PC region. The mass density in the PC region evolves inversely with temperatures and volume. The electron and ion pressures in the PC region follow the proportionality relation with the corresponding energies. The similar feature is also observed at 1000 ns of time scales as summarized in Table-3.3.

Table 3.4 Plasma variables in the POR with ETR effects at 125 mJ with cylindrical geometry.

t (ns)	$E_e\times10^8$ (J/kg)	$E_i\times10^8$ (J/kg)	$T_e\times10^4$ (K)	$T_i\times10^4$ (K)	P_e (MPa)	P_i (MPa)	$n_e\times10^5$ (m^{-3})	ρ ($kg.m^{-3}$)
50	1-0.4	0.5-0.2	7.0-3.0	7.0-3.0	20	10-40	1.0-5.0	0.5-5.0
1000	0.5-0.1	0.3-0.1	3.8-1.5	3.8-1.5	2.0	1.5-5.0	0.3-0.5	0.1-0.8

Table-3.4 summarizes the range of the variables existing in the POR. Since the ablated plasma outer region is away from the target surface the variables n_e, T_e, E_e and E_i is found to have lower values compared to PC region. Due to the formation of the POR the overall plasma expansion was observed to be higher compared to that without ETR effects. Hence the SF expansion was also observed to be higher with ETR effects. One may infer from the above observations that, the loss in the plasma

internal energy is converted into the radiation which in turn utilized in driving the plasma and SF. Due to this mechanism the plasma was observed to occupy larger dimensions with radiation. Hence it is confirmed that the radiation significantly modifies the internal plasma structure, plasma, and SF dynamics during its evolution.

Table 3.5 Mass density at the SF and PC region with and without ETR effects for 125 mJ with cylindrical geometry.

t (ns)	ρ at SF ($kg.m^{-3}$)	ρ at PC ($kg.m^{-3}$)	EFFECT
50	8.5	5.0	ETR
50	8.5	1.5	NO-ETR
1000	6.0	1.0	ETR
1000	6.0	0.4	NO-ETR

Table-3.5 compares the mass density (ρ) in the PC, and across the SF at 50 ns and 1000 ns, respectively. Across the SF, ρ is found to have higher values compared to that in the PC due to high compression of the background air by the SF. Similarly, lower ρ values occurring in the PC are due to the existence of very high T_e and T_i values. Behind the SF, a rarefaction wave (RW) is generated that counter propagates in the shocked air and releases the compressed gas to come back to its ambient condition. So in region behind the SF, the mass density, P_e and P_i was observed fall off linearly up to the POR due to RW propagation. The propagation direction of the RW is indicated (fig. 3.8 (b)) with arrow directed towards POR. In the region ahead of the PC (fig. 3.8 (b)), the mass density was observed to rise up linearly towards the SF direction up to CF region. This nature is due to decay of T_e and T_i in the POR.

3.5.3 Evolution of plasma, generation and detachment of SF and CF from the ablated plasma

In fig. 3.9 (a-c) the detachment of SF and CF from ablated plasma into an ambient air is shown for 25 mJ, 125 mJ and 175 mJ laser energies.

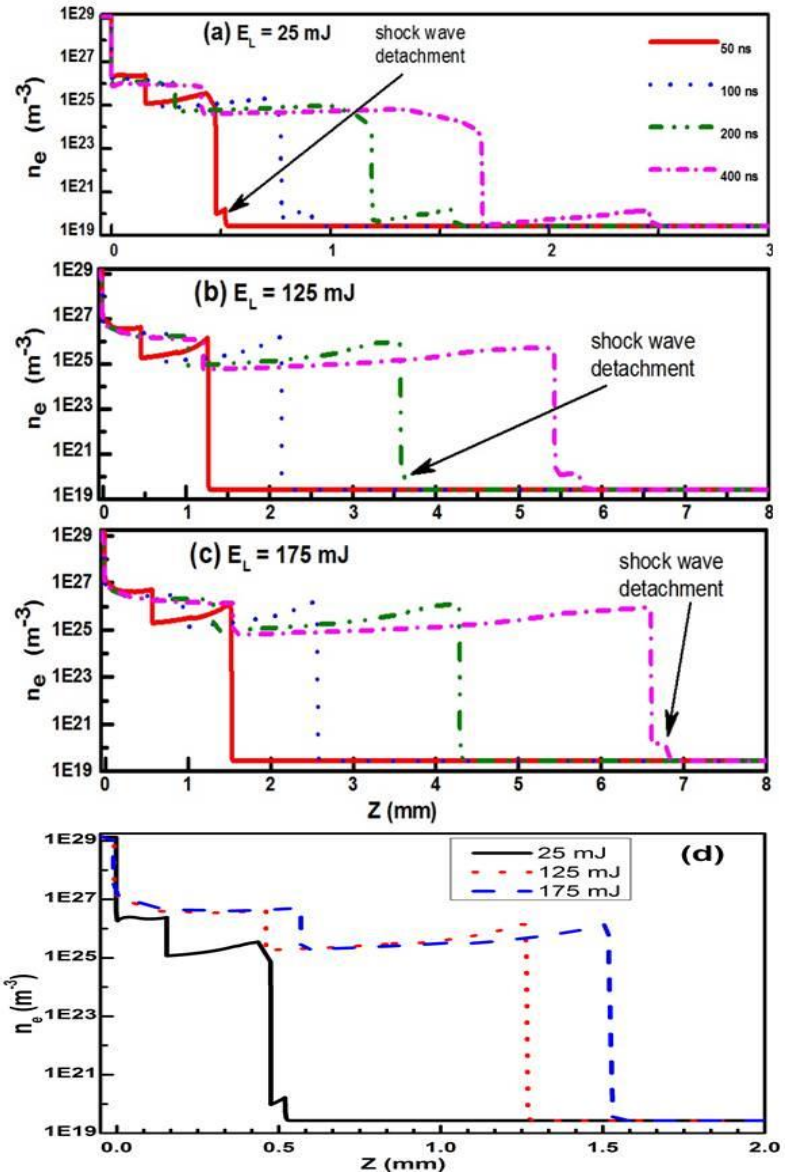

Figure 3.9 Detachment of the SF and CF from ablated plasma and their propagation into ambient air for laser energies of a) 25 mJ, b) 125 mJ and c) 175 mJ using planar geometry with ETR effects taken into consideration and d) comparison of n_e evolution with 25 mJ, 125 mJ and 175 mJ at 50 ns using planar geometry.

The CF gives an insight of the propagation distance of the ejected mass and is known to be a source of SF. The detachments are given for planar geometry with ETR effects considered. At initial timescales, only ablated plasma is observed to expand into ambient air as CF and as the time passed the SF is observed detaching from the

expanding plasma. Before the detachment, the SF accumulates enough energy through collisions of particles from ablated plasma and once detached it moves quickly through ambient air compressing the ambient gas ahead of it. The mass density, ion specific energy and temperatures across the SF will have very high values. The detachment time of the SF was found to be dependent on the input laser energy. At 25 mJ, SF detaches at around 50 ns, at 125 mJ around 200 ns and at 175 mJ around 400 ns. The detachment time is found to increase with increasing laser energy. During the SF formation, simultaneously, the CF is also formed which follows the SF with a lower velocity. The separation between the SF and CF ($Z_{SF} - Z_{CF}$), increases with respect to time and with the increasing laser energy. Fig. 3.10 compares $Z_{SF} - Z_{CF}$ for 25 mJ and 175 mJ laser energies using planar, cylindrical and spherical geometries considering the radiation effects.

Fig. 3.9 (d) gives the comparison of n_e evolution with the three energies at 5 0 ns using planar geometry which shows that the spatial expansion and the peak n_e both in PC and POR increases with increasing laser energy. The plasma expansion and the separation was more in case of planar and least in case of spherical. Insets in fig. 3.10 (a-c) show the separation between $Z_{SF} - Z_{CF}$ at lower timescales upto 1 μs for 25 mJ, 125 mJ and 175 mJ, respectively. With planar geometry, the separation at 25 mJ is found to exist from 50 ns of time whereas, with 125 mJ and 175 mJ the separation could be seen from 200 ns indicating that the SF accumulating more energy from the ablated plasma before the detachment. Similarly, with cylindrical and spherical geometries the separation can be seen from 50 ns of time. Though the detachment with the planar nature starts late, the SF accumulates high energy as a result it cross over the SF generated using cylindrical and spherical geometries.

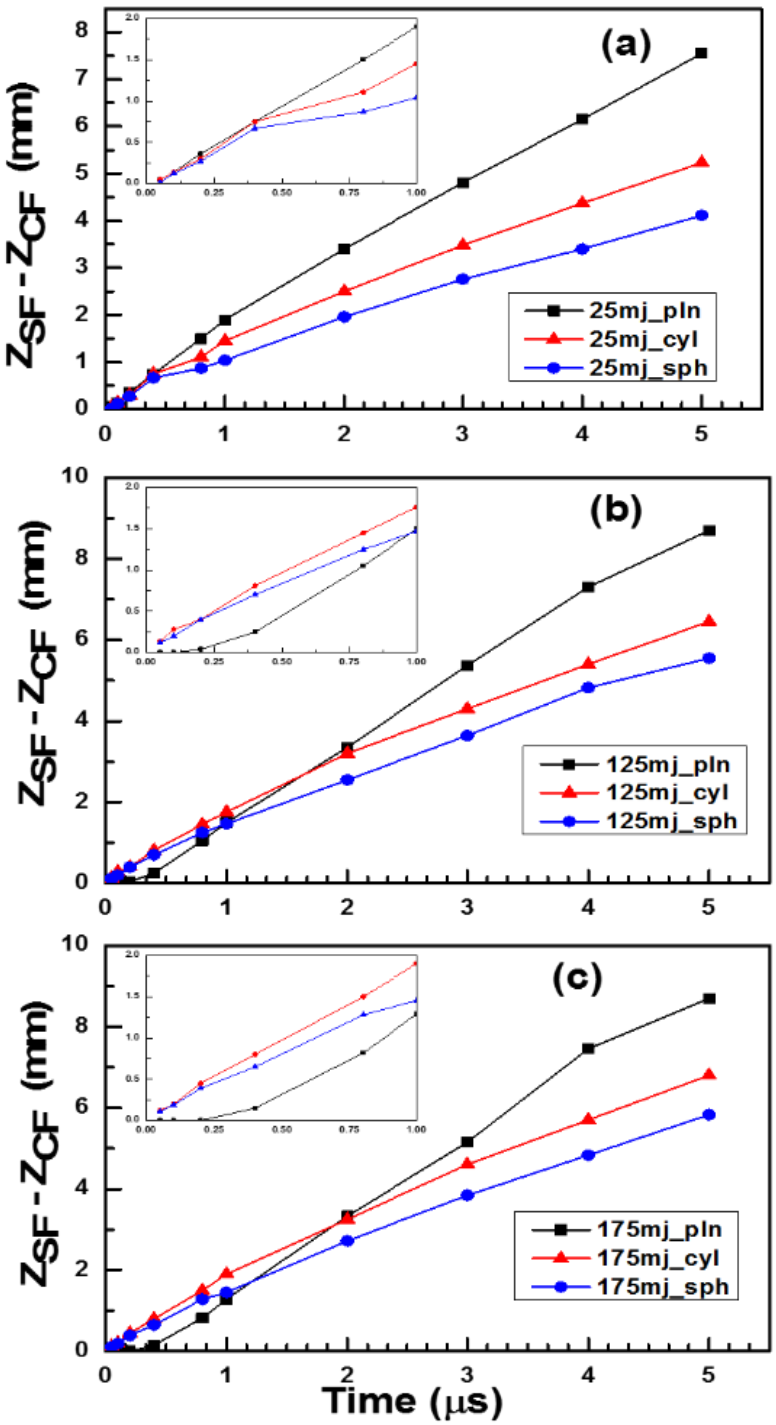

Figure 3.10 Separation between SF and CF with respect to time for planar, cylindrical and spherical geometries for input laser energies a) 25 mJ , b) 125 mJ and c) 175 mJ, respectively with ETR effects. The lines are guide to the eye.

3.6 Temporal Evolution of Plasma Parameters

3.6.1 Comparison of n_e and T_e with and without ETR

The temporal evolution of peak n_e and T_e extracted in the PC region over the time scales of 0.05 - 8.0 μs is given for 25 mJ (fig. 3.11 (a & b)), for 125 mJ (3.11 (c & d)), and for 175 mJ (3.11 (e & f)) laser energies with and without ETR effects.

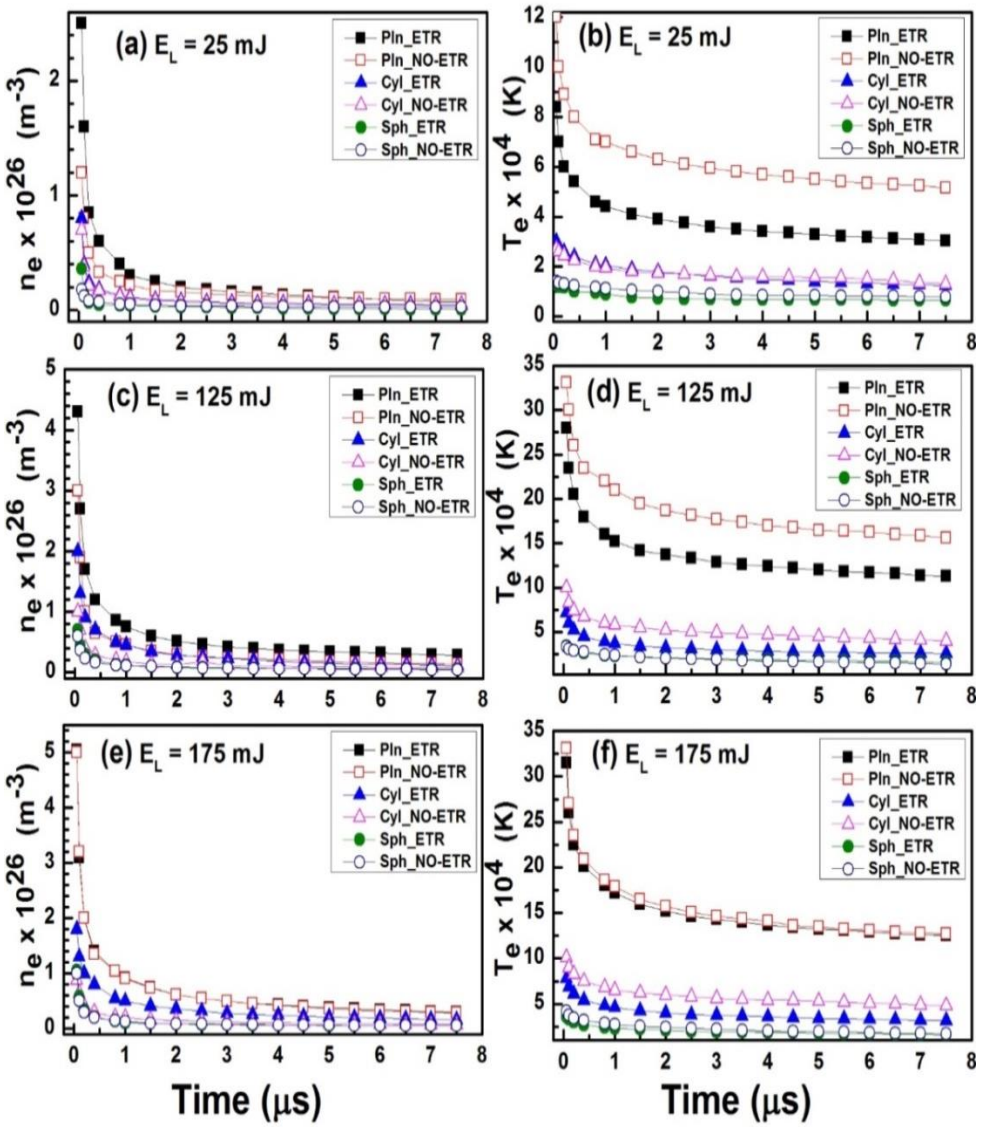

Figure 3.11 Comparison of temporal evolution of n_e and T_e for the input laser energies (a-b) 25 mJ, (c-d) 125 mJ and (e,f) 175 mJ without and without ETR using planar, cylindrical and spherical geometries, respectively. The lines are guide to the eye.

Table 3.6 Peak values of n_e and T_e compared with and without ETR effects at 50 ns.

	Planar		Cylindrical		Spherical		
E_L (mJ)	n_e $\times 10^{26}$ (m^{-3})	T_e $\times 10^4$ (K)	n_e $\times 10^{26}$ (m^{-3})	T_e $\times 10^4$ (K)	n_e $\times 10^{26}$ (m^{-3})	T_e $\times 10^4$ (K)	EFFECT
25	2.5	8.2	0.8	3.0	0.36	1.35	ETR
25	1.2	12.0	0.7	2.7	0.18	1.4	NO-ETR
125	4.4	28.0	2.0	7.2	0.7	3.4	ETR
125	3.0	36.0	1.0	10.0	0.6	3.3	NO-ETR
175	5.0	31.0	1.8	7.8	1.0	3.3	ETR
175	5.0	33.0	0.9	10.0	1.0	4.2	NO-ETR

Variables n_e and T_e with planar geometry have higher values followed by cylindrical and spherical geometries. Table-3.6 summarizes comparison of n_e and T_e at 50 ns with and without ETR for planar, cylindrical and spherical geometries. At 25 mJ and 125 mJ with planar, n_e have higher values with ETR whereas, at 175 mJ n_e is found to have same values compared to without ETR. Similarly, T_e with ETR has lower values with 25 and 125 mJ and slightly lower values with 175 mJ. As discussed previously, due to f-f transitions occurring from the PC region, T_e evolves inversely with n_e. The similar values in n_e at 175 mJ may indicate that the large amount of radiation emissions occurring during the initial plasma formation and expansion. With cylindrical geometry, the difference in n_e, T_e will be small compared to that of planar geometry. With the spherical geometry, n_e and T_e have same values with and without ETR effects. Since n_e have high values with planar nature, the radiation emissions will be dominant in this geometry.

The decay nature of n_e and T_e is same for the three geometries. The sudden fall off of n_e and T_e during the initial times (< 2 μs) is due to the occurrence of simultaneous processes like the radiation emissions and fast expansion of the plasma. Due to these

processes, the electrons recombine with the ions and the plasma cools down quickly resulting in faster decay of n_e and T_e. However, at later times during cylindrical and spherical the plasma expansion slows down and the recombination decreases due to plasma cooling resulting in slower decay or almost constant in n_e and T_e over 2 – 8 μs time scales. During the fast decay process, the nature of the SF is observed to have converted from planar to cylindrical (Pln-Cyl) at lower energies (fig. 3.5 (a & b)) and from cylindrical to spherical (Cyl-Sph) (fig. 3.5 (c & d)) at higher energies for 0.4 – 2 μs time scales.

3.6.2 Mass density comparison in the PC and across the SF with ETR effects

Fig. 3.12 compares the temporal evolution of peak mass density (ρ) in the PC and across the SF during the evolution. The mass density across the SF for all energies and geometries is found to have higher values than at the PC. Since the gas across the SF is highly compressed, ρ have higher values. As seen from fig. 3.12 (a-c) with PN, ρ across SF have higher values compared to cylindrical and spherical nature signifying that the compression is more during the early SF evolution and decreases with time due to decrease in the kinetic energy of the SF by the confinement. The compression of the background gas increases with increasing laser energy that is clearly seen from fig. 3.12 (a-c). Due to the presence of very high temperatures inside the PC, ρ in this region is observed to be small compared to that at the SF. However, due to expansion of the plasma, the ρ values inside the PC decrease with time. As can be seen from fig. 3.12 (a-c) the mass density is observed to reduce with respect to time which follows somewhat, the decay trend of n_e and T_e (fig. 3.12 (a-f)). At lower energy of 25 mJ, with spherical geometry in the PC it is observed that the mass density is increasing with time after > 1 μs. This nature has a physical significance which will be discussed in the next section.

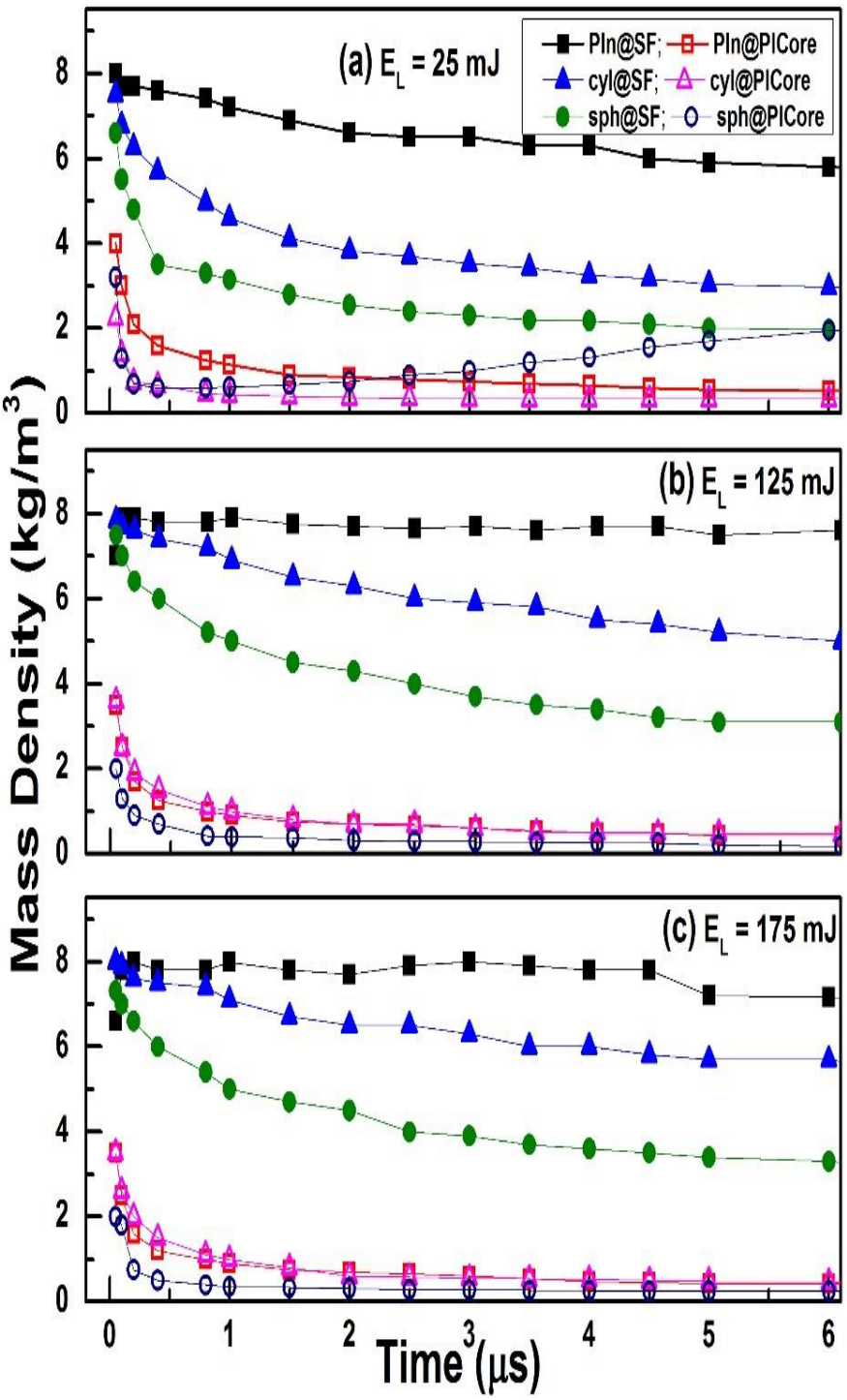

Figure 3.12 Temporal evolution of mass density for laser energies of a) 25 mJ, b) 125 mJ and c) 175 mJ with ETR effects using planar, cylindrical and spherical geometries respectively. The lines are guide to the eye. X-axis scale is the same for all the plots.

3.6.3 Backward growth of the ablated plasma

In fig. 3.13 (a) the spatial evolution of electron number density is given for the spherical geometry for the input laser energy of 25 mJ with ETR taken into consideration. The inset of fig. 3.13 shows the spatial evolution of the ablated plasma core and plasma outer region for the 500 – 2000 ns time scales. As observed initially the PC and POR expands into ambient air and at around 1200 ns the plasma experiences a backward motion due to the pressure gradient existing across the POR and shocked air interface becoming lower than the gradient across the PC and the internal region. The plasma expansion length at 500 ns found to be ~0.145 mm and is slightly increased to ~0.155 mm at 1000 ns and as the time progressed to 1500 ns its length decreased to ~0.151 mm and is further decreases to ~0.141 mm at 2000 ns.

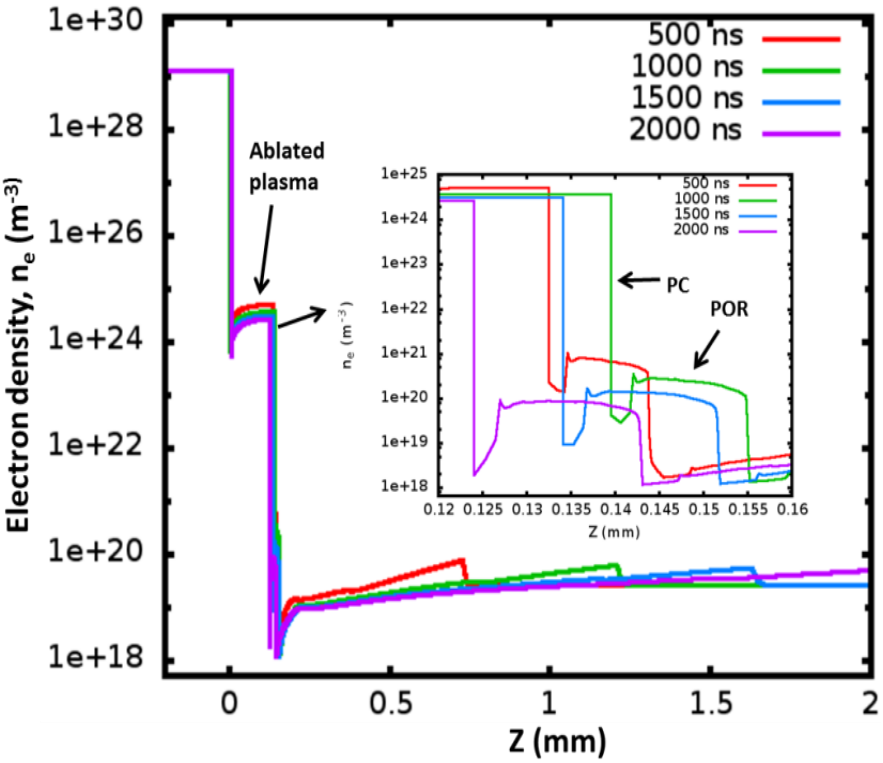

Figure 3.13 Spatial evolution of electron number density for 25 mJ input laser energy using spherical geometry. Inset showing the backward growth of the plasma after 1000 ns.

In fig. 3.4 (b) of Section 3.4, it is seen that in addition to the ablation of the plasma into ambient atmospheric air, the SWs were also launched into the target with pressures ranging between 2000 MPa – 50 MPa for planar, cylindrical and spherical geometries, respectively. The investigations of SW propagating through Al target is useful in the context of understanding the response of the bulk Al target to dynamical loadings. The present chapter focused mainly on the effects of ETR on the ablated plasma and SW dynamics in ambient air. In the next chapter, the focus will be on the effects of ETR on the SW propagating through Al target.

3.7 Summary

Laser ablation of aluminum and the subsequent generation and propagation of shock wave into ambient air was simulated using the 1D radiation hydrodynamic code. The experimentally obtained V_{sw} values from shadowgraphy technique were compared with the numerical simulated data by considering the ETR and non-ETR effects using planar, cylindrical and spherical geometries over the time scales of 0.4 μs – 8.0 μs. The nature of the SF and its evolution was found to be influenced by the radiation emitting from the plasma. The SF was observed to move quickly with ETR effects indicating that the radiation emissions from the ablated plasma drives the SW during its propagation into ambient air. The radiation effects were observed to be dominant typically up to 2 μs depending on the input laser energy. The radiation influence on the SW evolution was observed to be dominant at earlier time scales and decreased with time. So, at times up to 2.0 μs the SW was observed to be driven mostly by the radiation heat transfer mechanism. The simulation results also predicted that the SW will undergo transitions from initial planar to cylindrical (Pln-Cyl) and cylindrical to spherical (Cyl-Sph) for all the laser energies used in our study. During the transition from Pln-Cyl it is observed that the SW has taken certain time to transfer from PN to CN possibly due to the expansion of the plasma and SW. The transition from Cyl-Sph was observed to be instantaneous for all the laser energies considered. After 1.5 μs, the

spherical nature is observed to be dominant. The spatial evolution of different plasma variables (E_e, E_i, T_e, T_i, n_e, and P_e, P_i) is analyzed by considering ETR effects. The analysis showed that due to ETR the internal plasma structure is modified by splitting into two parts: the plasma core (PC) and plasma outer region (POR) whereas, without ETR only one plasma region that is, PC is observed. Due to high absorption of the laser energy by the PC, the plasma variables in that region have very high values compared to that of the POR. The detachment times of the SF was observed to be laser energy dependent. The SF was observed to detach late from the ablated plasma with increasing laser energy. The separation between the SF and CF was observed to increase with time indicating that the SF moves off very quickly from the ambient air. The temporal evolution of n_e and T_e compared with planar, cylindrical and spherical geometries showed that with PN, n_e and T_e have higher values followed by cylindrical and spherical nature. During the early times (< 2.0 μs) n_e and T_e was observed to fall off very quickly due to sudden expansion of the plasma and recombination of large number of electrons to the ions. Due to these processes, the plasma cools down and the number density falls drastically. The decay of n_e and T_e after 2.0 μs was found to be slower indicating negligible emission of radiation from the plasma core. Due to dominance in the radiation emissions upto 2.0 μs, the SF was observed to move quickly (during planar and cylindrical with ETR) however, at later time due to negligible radiation effects the SF is found to move with same velocity (during SN with and without ETR).

References

[1]D. B. Chrisey and G. K. Hubler, *Pulsed Laser Deposition of Thin Films*. (Wiley, 1994).
[2]S. C. Singh and R. Gopal, The Journal of Physical Chemistry C **112** (8), 2812-2819 (2008).
[3]L. J. Radziemski, Spectrochimica Acta Part B: Atomic Spectroscopy **57** (7), 1109-1113 (2002).
[4]H. Chen, *Microscale Laser Shock Peening: Experiment, Modeling and Spatially Resolved Material Characterization*. (2004).
[5]N. K. Bourne, J. C. F. Millett and G. T. Gray, Journal of Materials Science **44** (13), 3319-3343 (2009).
[6]C. Phipps, M. Birkan, W. Bohn, H.-A. Eckel, H. Horisawa, T. Lippert, M. Michaelis, Y. Rezunkov, A. Sasoh, W. Schall, S. Scharring and J. Sinko, Journal of Propulsion and Power **26** (4), 609-637 (2010).
[7]A. Benuzzi-Mounaix, M. Koenig, A. Ravasio, T. Vinci, N. Ozaki, M. R. l. Gloahec, B. Loupias, G. Huser, E. Henry, S. Bouquet, C. Michaut, D. Hicks, A. MacKinnon, P. Patel, H. S. Park, S. L. Pape, T. Boehly, M. Borghesi, C. Cecchetti, M. Notley, R. Clark, S. Bandyopadhyay, S. Atzeni, A. Schiavi, Y. Aglitskiy, A. Faenov, T. Pikuz, D. Batani, R. Dezulian and K. Tanaka, Plasma Physics and Controlled Fusion **48** (12B), B347 (2006).
[8]A. Vogel and V. Venugopalan, Chemical Reviews **103** (2), 577-644 (2003).
[9]A. Caruso and R. Gratton, Plasma Physics **10** (9), 867 (1968).
[10]C. E. Max, C. F. McKee and W. C. Mead, Physical Review Letters **45** (1), 28-31 (1980).
[11]C. E. Max, C. F. McKee and W. C. Mead, Physics of Fluids **23** (8), 1620-1645 (1980).
[12]P. Mora, Physics of Fluids **25** (6), 1051-1056 (1982).
[13]B. Meyer and G. Thiell, Physics of Fluids **27** (1), 302-311 (1984).
[14]D. Batani, H. Stabile, A. Ravasio, G. Lucchini, F. Strati, T. Desai, J. Ullschmied, E. Krousky, J. Skala, L. Juha, B. Kralikova, M. Pfeifer, C. Kadlec, T. Mocek, A. Präg, H. Nishimura and Y. Ochi, Physical Review E **68** (6), 067403 (2003).
[15]D. Marla, U. V. Bhandarkar and S. S. Joshi, Journal of Applied Physics **109** (2), 021101 (2011).
[16]P. Cristian and A. W. David, Journal of Physics D: Applied Physics **42** (15), 155503 (2009).
[17]C. Porneala and D. A. Willis, Applied Physics Letters **89** (21), 211121 (2006).
[18]A. Gragossian, S. H. Tavassoli and B. Shokri, Journal of Applied Physics **105** (10), 103304 (2009).
[19]A. E. Wynne and B. C. Stuart, Appl Phys A **76** (3), 373-378 (2003).
[20]M. Capitelli, A. Casavola, G. Colonna and A. De Giacomo, Spectrochimica Acta Part B: Atomic Spectroscopy **59** (3), 271-289 (2004).
[21]V. I. Mazhukin, V. V. Nossov and I. Smurov, Applied Surface Science **253** (19), 7686-7691 (2007).
[22]F. J. Gordillo-Vázquez, A. Perea and C. N. Afonso, Appl. Spectrosc. **56** (3), 381-385 (2002).
[23]S. Gurlui, M. Agop, P. Nica, M. Ziskind and C. Focsa, Physical Review E **78** (2), 026405 (2008).
[24]S. Mahmood, R. S. Rawat, M. S. B. Darby, M. Zakaullah, S. V. Springham, T. L. Tan and P. Lee, Physics of Plasmas **17** (10), 103105 (2010).
[25]A. K. Sharma and R. K. Thareja, Applied Surface Science **243** (1–4), 68-75 (2005).
[26]Y. Tao, M. S. Tillack, S. S. Harilal, K. L. Sequoia, B. O. Shay and F. Najmabadi, Journal of Physics D: Applied Physics **39** (18), 4027 (2006).
[27]T. Moscicki, J. Hoffman and Z. Szymanski, Archives of Mechanics **63** (2), 18 (2011).
[28]M. Cirisan, J. M. Jouvard, L. Lavisse, L. Hallo and R. Oltra, Journal of Applied Physics **109** (10), 103301 (2011).
[29]A. E. Hussein, P. K. Diwakar, S. S. Harilal and A. Hassanein, Journal of Applied Physics **113** (14), 143305 (2013).

[30]S. Laville, F. Vidal, T. W. Johnston, M. Chaker, B. Le Drogoff, O. Barthélemy, J. Margot and M. Sabsabi, Physics of Plasmas **11** (5), 2182-2190 (2004).
[31]J. J. Yoh, H. Lee, J. Choi, K.-c. Lee and K.-h. Kim, Journal of Applied Physics **103** (4), 043511 (2008).
[32]A. Gomes, A. Aubreton, J. J. Gonzalez and S. Vacquié, Journal of Physics D: Applied Physics **37** (5), 689 (2004).
[33]H. Mohammad and A. W. David, Journal of Physics D: Applied Physics **44** (14), 145501 (2011).
[34]S. S. Harilal, G. V. Miloshevsky, P. K. Diwakar, N. L. LaHaye and A. Hassanein, Physics of Plasmas **19** (8), 083504 (2012).
[35]M. Owens and V. Majidi, Appl. Spectrosc. **45** (9), 1463-1467 (1991).
[36]Y.-I. Lee, K. Song, H.-K. Cha, J.-M. Lee, M.-C. Park, G.-H. Lee and J. Sneddon, Appl. Spectrosc. **51** (7), 959-964 (1997).
[37]F. Rezaei and S. H. Tavassoli, Physics of Plasmas **20** (1), 013301 (2013).
[38]A. Bogaerts and Z. Chen, Spectrochimica Acta Part B: Atomic Spectroscopy **60** (9–10), 1280-1307 (2005).
[39]R. K. Singh and J. Narayan, Physical Review B **41** (13), 8843-8859 (1990).
[40]R. F. Wood, J. N. Leboeuf, K. R. Chen, D. B. Geohegan and A. A. Puretzky, Applied Surface Science **127–129**, 151-158 (1998).
[41]J. R. Ho, C. P. Grigoropoulos and J. A. C. Humphrey, Journal of Applied Physics **78** (7), 4696-4709 (1995).
[42]S. Amoruso, Appl Phys A **69** (3), 323-332 (1999).
[43]S. Amoruso, R. Bruzzese, N. Spinelli and R. Velotta, Journal of Physics B: Atomic, Molecular and Optical Physics **32** (14), R131 (1999).
[44]S. H. Jeong, R. Greif and R. E. Russo, Applied Surface Science **127–129**, 177-183 (1998).
[45]V. I. Mazhukin, V. V. Nossov, I. Smurov and G. Flamant, Journal of Physics D: Applied Physics **37** (2), 185 (2004).
[46]V. I. Mazhukin, V. V. Nossov, G. Flamant and I. Smurov, Journal of Quantitative Spectroscopy and Radiative Transfer **73** (2–5), 451-460.
[47]H. Borchert, K. Darée and M. Hugenschmidt, Journal of Physics D: Applied Physics **38** (2), 300 (2005).
[48]E. A. Ershov-Pavlov, K. Y. Katsalap, K. L. Stepanov and Y. A. Stankevich, Spectrochimica Acta Part B: Atomic Spectroscopy **63** (10), 1024-1037 (2008).
[49]I. B. Gornushkin, A. Y. Kazakov, N. Omenetto, B. W. Smith and J. D. Winefordner, Spectrochimica Acta Part B: Atomic Spectroscopy **59** (4), 401-418 (2004).
[50]R. Ramis, K. Eidmann, J. Meyer-ter-Vehn and S. Hüller, Computer Physics Communications **183** (3), 637-655 (2012).
[51]Y. B. Zel'dovich and Y. P. Raizer, *Physics of Shock Waves and High-Temperature Hydrodynamic Phenomena*. (Dover Publications, 2012).
[52]Y. T. Lee and R. M. More, Physics of Fluids **27** (5), 1273-1286 (1984).
[53]R. M. More, K. H. Warren, D. A. Young and G. B. Zimmerman, Physics of Fluids **31** (10), 3059-3078 (1988).
[54]C. Leela, S. Bagchi, V. R. Kumar, S. P. Tewari and P. P. Kiran, Laser and Particle Beams **31** (02), 263-272 (2013).
[55]C. Leela, P. Venkateshwarlu, R. V. Singh, P. Verma and P. P. Kiran, Opt. Express **22** (S2), A268-A275 (2014).
[56]C. Leela, Ph. D. thesis, University of Hyderabad, India, 2014.
[57]M. Kundu, Physics of Plasmas **21** (1), 013302 (2014).

This page is intentionally left blank

Chapter 4

1D-Numerical study of Laser driven SWs into bulk Al target: Effects of ETR

Numerical investigation of laser driven shock waves (LDSW) launched into bulk Al target of thickness ~2 mm is simulated using the modified 1D-RHD MULTI-fs code over the intensity range 10^{10} – 10^{11} W/cm^2. The characteristics of the SW propagating into Al target over the time scales from the initial launching times to 1000 ns is presented in this chapter. As discussed in the previous chapter, where the ETR emitted from the ablated plasma plays a significant role in affecting the plasma and SW dynamics expanding in ambient air, the role of ETR affecting the propagation of the SW into bulk Al target cannot be neglected. This chapter emphasizes mainly on the effects of the ETR on the SW propagating into bulk Al target. The SWs are driven into the target in order to conserve the momentum created by the sudden expansion of the ablated plasma into ambient air. In the present work, the ETR effects were observed for two extrema of energies 25 mJ and 175 mJ, respectively. The radiation emitting from the plasma was observed to show negligible effects in the case of low laser energy (25 mJ) whereas, it was significantly affecting the propagation at higher laser energy (175 mJ) which was found to be dominant up to 50 ns of time. The observations show that two SWs have been launched onto the target surface: one during the pulse duration (primary SW (PSW)) after the breakdown of the target and the other (secondary SW (SSW)) immediately after the termination of the laser pulse. The effects of ETR were found to be dominant on SSW compared to that on PSW for the higher laser energy (175 mJ). The PSW and SSW found to coalesce at around 30-40 ns and move as a single SW after these time scales. The resultant pressure after coalesce has higher value than the individual ones before coalesce for 175 mJ. The PSW pressures at 25 mJ and 175 mJ were found to be ~1.5 GPa and ~7 GPa, respectively that were launched at 10 ns and 7 ns.

4.1 Introduction

When a laser beam of sufficiently high intensity is focused on to the target surface the breakdown of the medium occurs and subsequently formation of plasma takes place due to coupling of laser energy with the target[1]. The plasma then ablates from the target and expands into background gas by absorbing the remaining incoming laser energy until the termination of the laser pulse. Due to the ablation, the shock wave (SW) or compression wave (CW) is launched into the target in order to conserve the momentum created by the ablated material[2-5]. Due to the transient laser intensity pulse, the SW launched onto the target also has a transient nature making it a very efficient tool to study the dynamic response of materials. Moreover, with the laser driven shock waves (LDSW) very high dynamic pressures over very short durations of time (pulse durations) can be generated[6] unlike that created by the flyer plate impact technique. Due to very high pressures generated at very short times, the impulses will be very high making it an efficient technique to generate the equations-of-state[7] of the material. The response of the material to LDSW loadings can be understood from the shocked parameters such as pressure (P), particle (u_p) and shock velocity (V_{sw}), density (ρ) and specific internal energy (E_{sp}). The SW pressures launched onto the target depends on various parameters such as target properties, incident laser intensity, wavelength, pulse duration, background gas and also on the radiation emitted from the ablated plasma. The effects of ETR on the ablated plasma and SW expanding into the background medium for different laser intensities is investigated[8] and observed that the radiation plays an important role on the plasma and SW dynamics with the effects becoming significant with increasing laser energy. Many efforts have been made on the LDSW propagating into solid targets[4, 7, 9] and found some of the important aspects.

The numerical simulation of LDSW propagation through bulk Al target of thickness ~2 mm is presented. The intensities ranging between 10^{10} – 10^{11} W/cm^2 were used to launch the SW on to the target surface and the SW dynamics were investigated over the

time scales of up to 1000 ns from the initial laser pulse interaction. The simulations have been carried with and without electron thermal radiation effects mentioned as ETR and No-ETR, respectively using planar, cylindrical and spherical geometries. Initially the role of ETR at two extrema of laser energies 25 mJ and 175 mJ used in the study were presented. Later on the role of geometry on SW propagation at 175 mJ, where the effects are dominant are presented using cylindrical and spherical geometries. The numerical simulations are carried out using modified 1D-radiation hydrodynamic code MULTI-fs[8, 10].

4.2 Simulation Methodology

The LDSWs into Al target in the experiments were launched using the Nd: YAG laser with the excitation wavelength of 532 nm and 7 ns pulse duration (FWHM). The detailed setup of the experiments is presented elsewhere[11, 12]. The laser ablative shock waves (LASW) from Al target propagating into ambient air are presented in the previous chapter-3. Figure 4.1 shows the schematic of the laser-Al interaction and the associated processes such as plasma formation and expansion into ambient air, SW propagation simultaneously into the ambient air and into Al target and the influence of ETR from the ablated plasma on SW propagating into Al and air. The ETR is observed to be significantly influencing the SW propagating in ambient air which was observed to be increasing with increasing intensity[8].

In fig. 4.2 the simulated laser-Al interaction, the plasma expansion into ambient air and the corresponding SW launched by the ablated plasma, its propagation into Al is given for the input laser energy of 25 mJ. The origin represented with the dashed vertical line is the Al-Air interface. The laser beam is incident on the Al surface at Z=0. The expansion of the plasma into ambient air and the SW into Al is given over 10 - 16 ns time scales which shows that the pressure of the ablated plasma in air (~0.3 GPa) is small compared to that of the SW in Al (~0.85 – 0.8 GPa). However, the plasma expansion length in air is greater (~110 μm) than the distance travelled by the SW in Al

(~15 μm). The pressure and the expansion length increases with increasing laser intensity.

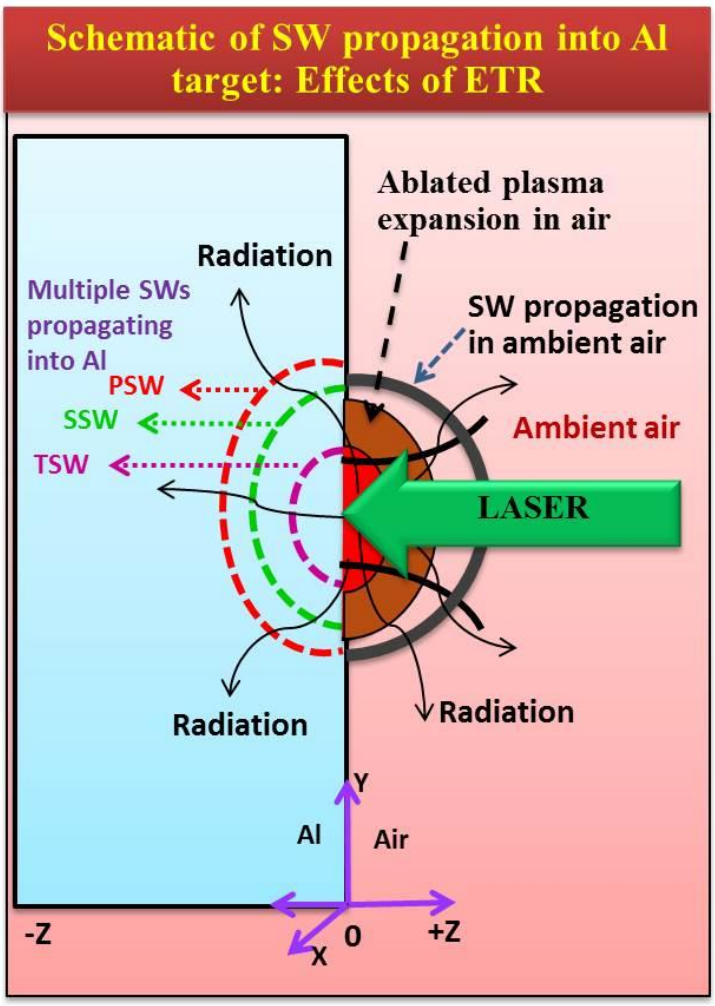

Figure 4.1 Schematic of laser-Al interaction and effects of ETR on SW driven into Al target. Z=0 represents the Al-Air interface, +Z - air medium, -Z – Al target, solid curve represents SW propagation into air, dotted curves represent multiple SWs propagating into Al target.

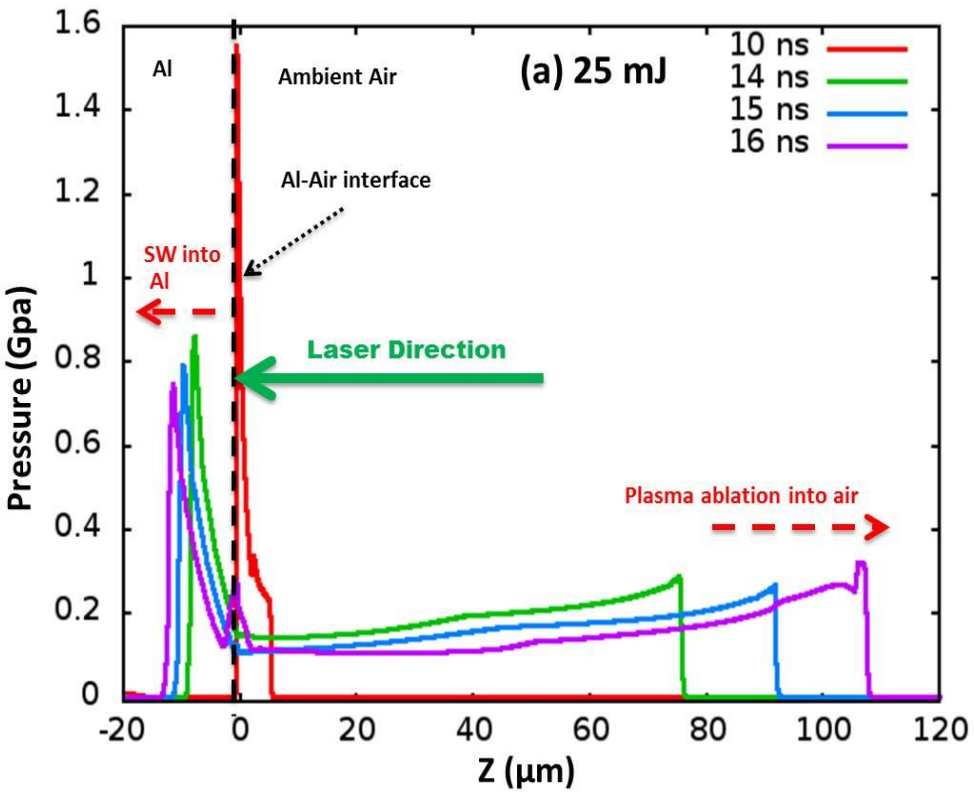

Figure 4.2 Simulated laser-Al interaction, the expansion of the Al ablated plasma into ambient air and the SW driven into Al by the ablated plasma. Z=0 represents the Al-Air interface, +Z - air medium, -Z – Al target.

4.3 Results and Discussion

4.3.1 Origin of Primary and Secondary Shock Wave (PSW and SSW)

Figure 4.3 (a & b) shows the times where PSW and SSW are launched into Al by the ablated plasma in air. The PSW was observed to be launched at 10 ns for 25 mJ and 7 ns for 175 mJ. This wave is originated due to the sudden expansion of the plasma into ambient air after the breakdown of the Al. The fluencies used in the simulations are very high (>300 J/cm^2) compared to the breakdown threshold[13] of Al 3 J/cm^2. This threshold is reached at the very early times of the laser pulse duration during the rising edge. After the breakdown, the absorption of the remaining laser energy by the plasma increases due to the presence of large number of free electrons in the plasma. The free

electrons that are close to the plasma-air interface interact with the air particles leading to the thermal ionization of the surrounding air.

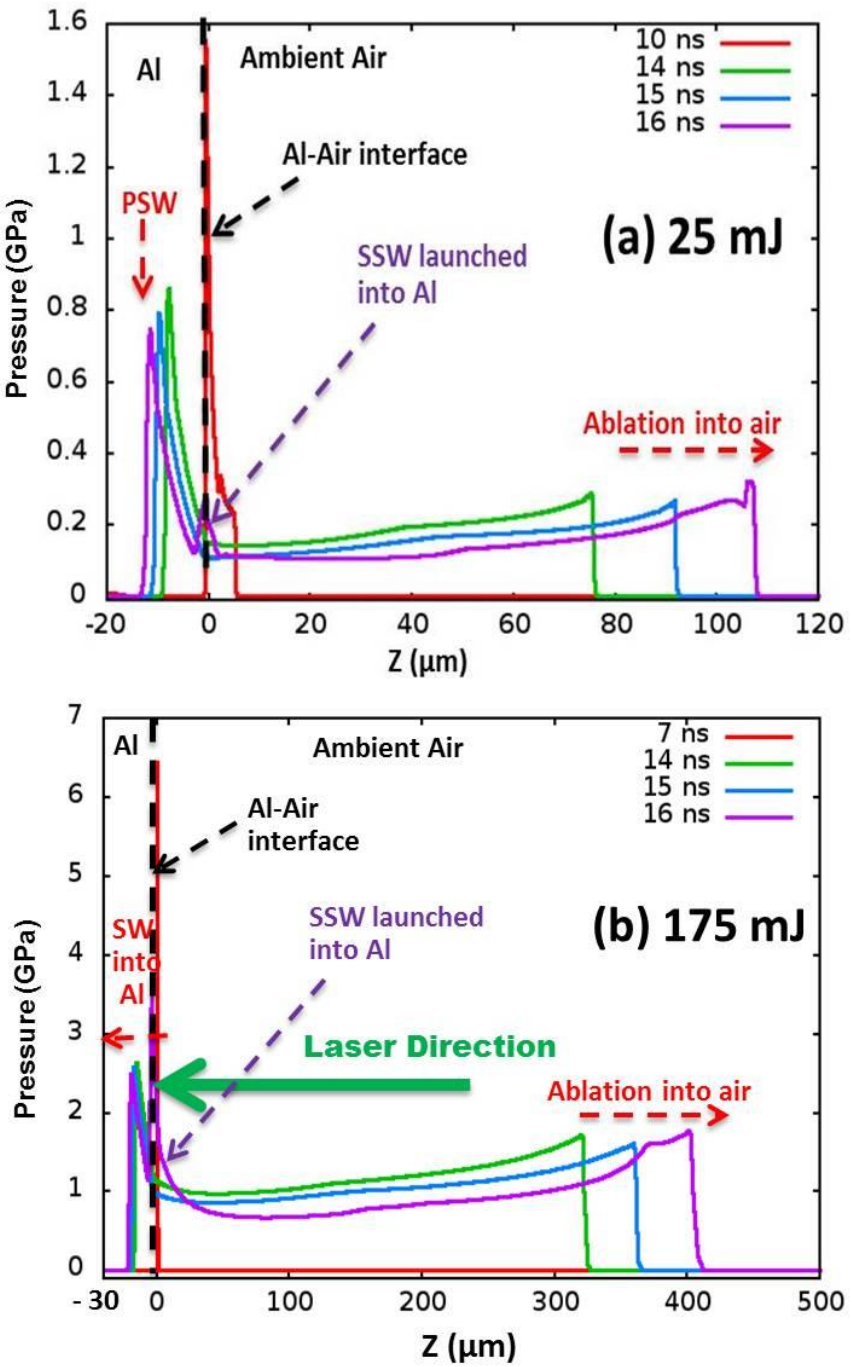

Figure 4.3 Simulated laser driven PSW and SSW into Al for the input laser energies of a) 25 mJ and b) 175 mJ.

The interaction and energy transfer between the particles increases with the rising laser pulse due to increase in the laser absorption and high kinetic energy gained by the free electrons. Simultaneously, the thermal ionization of air also increases as discussed in the previous chapter-3. The ionization of the air happens to be around 10 ns for 25 mJ and 7 ns for 175 mJ. Before these times the plasma expansion was found to be increasing continuously with time and once the air ionization increases a sudden expansion of the plasma into ambient air is observed. Due to this sudden expansion a recoil momentum opposite to the plasma expansion is created into the Al target launching PSW into the target. The time where the PSW had launched decreases with the increasing energy (10ns for 25 mJ and 7 ns for 175 mJ) as the interaction time of the laser pulse with the plasma increases due to breakdown threshold occurring at early time scales.

The times at which the SSW had launched is observed to take place at around 16 ns from the initial laser interaction time. This was observed to be launched immediately after the termination of the laser pulse. In fig. 4.4 (a & b), the Al ablated plasma expanding into ambient air corresponding to fig. 4.3 (a & b) is shown which gives a clear insight into the launching of the SSW into Al. The ablated plasma can be divided as region-I and II where region-I is close to the Al surface and II is slightly away from the surface. The regions are separated with dashed vertical lines in fig. (4.4 (a & b)) at lengths of approximately 40 μm and 180 μm, respectively for 25 mJ and 175 mJ. The pressure gradient (∇P) in region I and II as moved away from the target surface increases over the spatial length (Z). For 25 mJ, the pressure gradients from the target surface to region-I, at 14 ns and 16 ns are found to be ~ 0.06 GPa and ~ 0.03 GPa, respectively. Similarly between region-I and region-II, it is found to be ~ 0.1 GPa and ~ 0.14 GPa, respectively. For 175 mJ, the gradients from target surface to region-I, at 14 ns and 16 ns are found to be ~0.2 GPa and ~0.1 GPa, respectively. Similarly in region-II, it is found to be ~ 0.55 GPa and ~ 1.1 GPa, respectively. The pressure gradient in region-II is higher than in region-I.

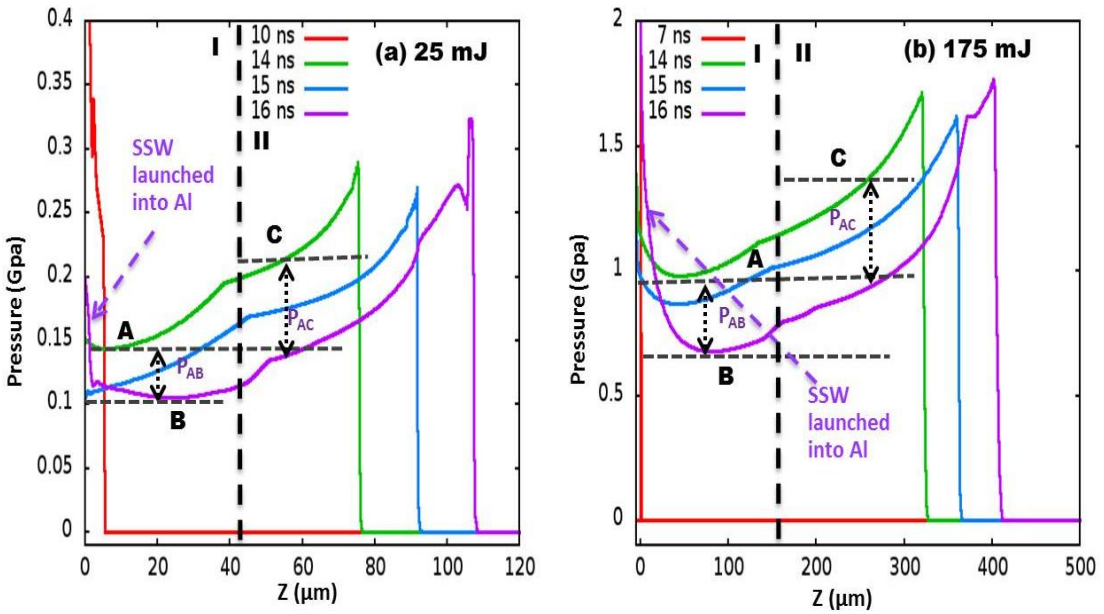

Figure 4.4 Illustration of origin of PSW and SSW launched into Al due to ablated plasma in air for the input laser energies a) 25 mJ and b) 175 mJ.

The pressure drop in the case of 25 mJ, between 14 – 16 ns in region-I is found to be P_{AB} ~0.05 GPa and in region-II, P_{AC} ~0.06 GPa. Similarly, in the case of 175 mJ, it is found to be P_{AB}~0.25 GPa in region-I and P_{AC}~0.5 GPa in region-II. Since the (∇P) in region-II is higher than in region-I the pressure drops are higher in region-II for both the laser energies. Due to higher pressure drop in region-II than region-I, the plasma close to the target surface is exerted a backward motion towards the surface launching SSW into Al. Similarly, due to sudden drop of the pressure the ablated plasma in air also experiences a force resulting in the formation of a small peak behind the shock front. This is observed to be visible at 16 ns, at a spatial length of ~100 μm and ~360 μm, respectively for 25 mJ and 175 mJ. The similar nature of the generation of the SSW was observed by Harilal et al.[14] where the ablation of the plasma is performed at 1 atm argon gas with 1064 nm. The SSW generated in ambient air catches the PSW at later time scales and finally moves as a single wave. The strength of the SSW launched in to the Al target depends on the pressure drop in region-I and II which in turn depends on the input laser intensity and absorbed energy.

4.3.2 Propagation and Coalescence of PSW and SSW in Al target

In fig. 4.5 (a & b) the propagation of PSW and SSW through Al target is clearly visible at 20 ns and 40 ns, respectively. The first or PSW launched at 10 ns and 7 ns for 25 mJ and 175 mJ have peak pressures of ~1.6 GPa and ~6.5 GPa, respectively. These pressures at 20 ns decreased to ~0.6 GPa and ~2 GPa, respectively. The SSW launched at 16 ns (not shown in fig. 4.5) was observed to have peak pressures of ~0.25 GPa and ~3.6 GPa for 25 mJ and 175 mJ, respectively which is observed to have same values at 20 ns. This signifies that the pressure of the SSW is stable during these times. This stability is due to small pressure gradients existing between PSW and SSW resulting in negligible attenuation. The attenuation of the PSW peak pressure is fast compared to SSW due to higher pressure gradient existing between undisturbed Al and PSW front.

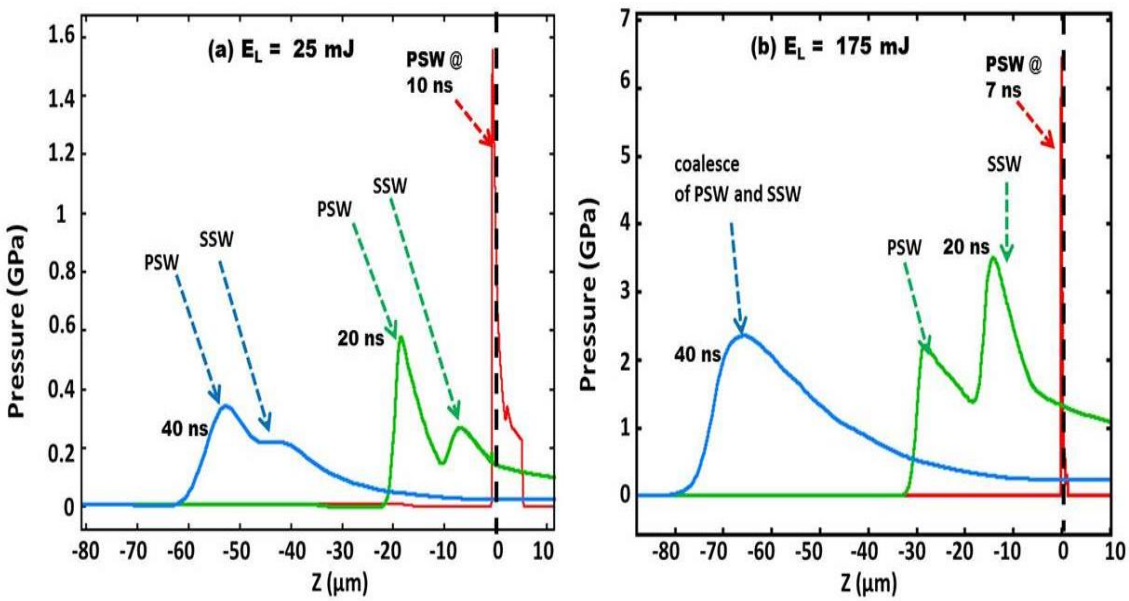

Figure 4.5 Propagation of the primary and secondary shock wave into Al target at a) 25 mJ and b) 175 mJ over the time scales 7 - 40 ns using planar geometry. Z=0 represents the Al-Air interface laser incident from right to left. –Ve Z-axis is the Al target and +Ve Z-axis is the air medium.

With both the energies it is observed that the two SWs (PSW and SSW) coalesce at some point of time during their propagation. In case of 25 mJ, since the strength of SSW is weak compared to PSW, the SWs coalesce weakly at around 40 ns. Similarly, in

case of 175 mJ, since the SSW strength is more than the PSW, the propagation speed of it will be higher than the PSW. Hence the SSW quickly catches the PSW and coalesces at earlier times of around 30 ns. During the coalescence time at 25 mJ, the resultant peak pressure (0.5 GPa) is found to have same value as that of PSW before coalescence (0.5 GPa), whereas at 175 mJ it is found to have higher (2.4 GPa) value than the individual SW (2 GPa) before coalescence (fig. 4.9 (a)).

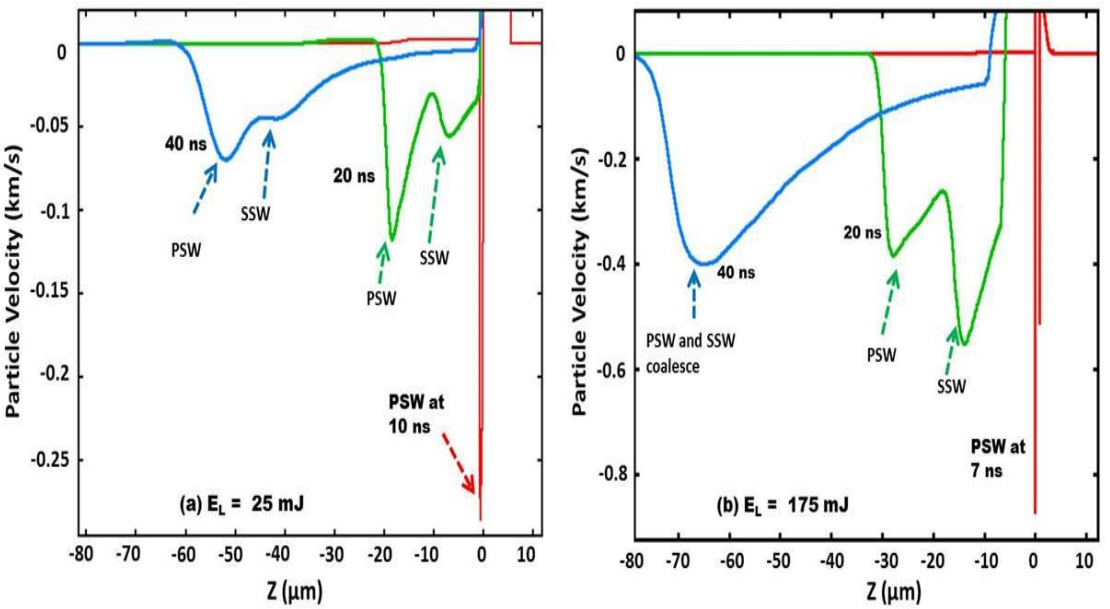

Figure 4.6 Spatial evolution of particle velocity across and behind PSW and SSW at a) 25 mJ and b) 175 mJ over the time scales 7 - 40 ns using planar geometry.

The particle velocities due to the PSW and SSW propagation are shown in fig. 4.6 (a & b) for both energies. The negative particle velocities (u_p) signifies the propagation direction of the SW and particle motion into Al target. It is obvious from fig. 4.6 (a & b) that, as the input laser energy increases, the pressure and in turn the particle velocities increases due to increase in the compression of the undisturbed material present ahead of the SF. Hence the particles gain high velocities as the pressure increases. The particle motion follow similar trend as that of the pressure (PSW and SSW) observed in figure 4.5 (a & b). The peak particle velocities (u_p) in the PSW at 25

mJ (fig. 4.6 (a)) were observed to decrease from ~0.28 - 0.07 km/s over 10 – 40 ns time scales. Similarly, at the SSW decreased from ~0.06 - 0.05 km/s over 20-40ns time scales. At higher input laser energy (175 mJ) (fig. 4.6 (b)) the u_p at the PSW observed to decreased from ~0.85 - 0.4 km/s over 7 – 40 ns and at the SSW from ~0.6 - 0.4 km/s over 20-40 ns.

4.3.3 Effects of ETR on SW propagating into Al

A) Planar geometry

Figure 4.7 (a & b) compares the spatial evolution of the SW pressures propagating into Al target with ETR and No-ETR effects for the input laser energies 25 mJ and 175 mJ, respectively at 14 and 30 ns using planar geometry. The origin, Z=0 in figure represents Al-air interface where the laser is incident onto the target surface from right to left as shown in fig. 4.1. The peak pressures at 25 mJ with ETR and No-ETR found to have same values at both time scales, whereas with 175 mJ, the pressures are observed to differ slightly at 14 ns, but differ largely at 30 ns. The percentage of laser absorption by the ablated plasma increases with increasing laser energy. Due to the increase in the laser energy absorption, the electron number density and electron temperatures increases largely within the ablated plasma, also simultaneously the radiation emitting from the plasma increases due to collisions with the ions. The emitted radiation propagates into ambient air and also into the target. Rezaei et al.[15] reported that the radiation emitted by the plasma close to the target surface is mostly due to free-free transitions. During this transition, the electrons lose their thermal energy without recombining with ions that is emitted in the form of radiation. Since, the temperature in the laser affected region within the target increases the emitted radiation penetrates to over a longer distances of upto few orders of laser wavelength.

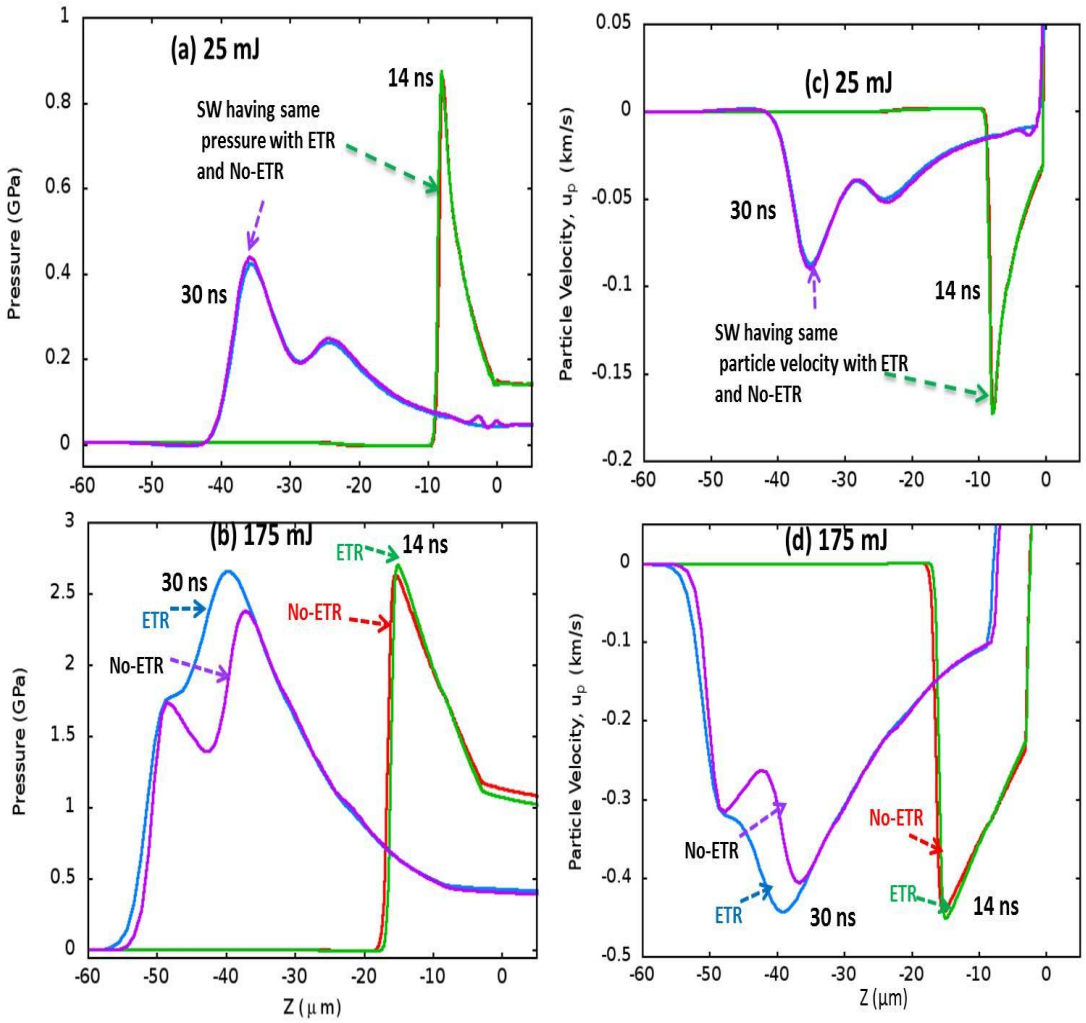

Figure 4.7 Comparison of spatial evolution of pressure and particle velocity with ETR and No-ETR effects using planar geometry for the input laser energies of (a, c) 25 mJ and (b, d) 175 mJ at 14 and 30 ns, respectively.

The probability of emitted photon absorption per unit length at a frequency, ϑ is the measure of the opacity (Rosseland and Planck)[10] which depends on the local temperature and mass density of the material. At higher laser energy (175 mJ), the absorption of the laser energy increases resulting in the higher laser affected region and higher plasma temperatures. The high kinetic energy electrons lose their energy which is emitted as intense radiation due to the f-f transition. As a result, the radiation emitted

by the plasma influences the SW propagation into the target which is observed to become prominent at higher laser energies. This emitted radiation enhances the SW pressure hence the pressures were found to have higher values with ETR (~2.75 GPa) compared to No-ETR (~2.3 GPa) at 30 ns. However, the influence of the radiation diminishes quickly at around 50 ns and the SW pressures become similar with ETR and No-ETR.

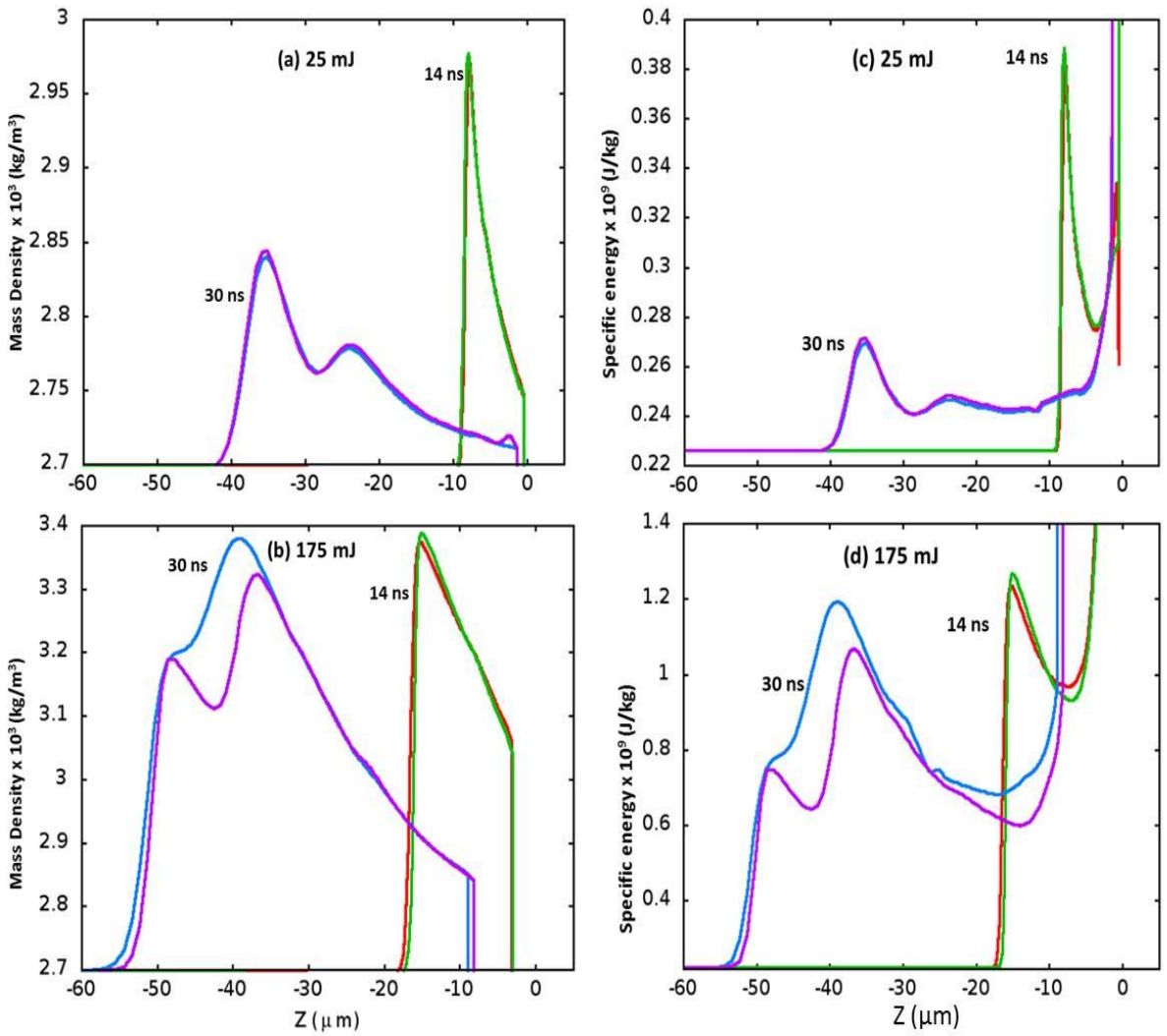

Figure 4.8 Comparison of Mass density and total specific energy with ETR and No-ETR effects using planar geometry for input laser energies (a, c) 25 mJ and (b, d) 175 mJ at 14 and 30 ns, respectively.

In fig. 4.8 (a & b) the spatial evolution of mass density, ρ is compared for the input laser energies of 25 mJ and 175 mJ, respectively at 14 ns and 30 ns. Similarly, in figure 4.8 (c & d) the spatial evolution of total specific internal energy is compared at 14 ns and 30 ns. All the SW parameters across and behind the PSW and SSW were observed to follow the same trend as the pressure in fig. 4.7.

Table-4.1 summarizes the peak SW parameters P, u_p, ρ and E_{sp} compared with ETR and No-ETR effects for 25 mJ and 175 mJ laser energies, respectively at 14 and 20 ns. At 25 mJ, these parameters were found to be same with ETR and No-ETR at both times. Similarly, at 175 mJ the values were found to be same at 14 ns, but differ slightly at 30. A small increment in the values with ETR signifies that the ETR from the ablated plasma also affects the SW parameters in Al target. The probability of ETR affecting the SW parameters may increase at higher laser energies.

Table 4.1 Comparison of peak P, u_p, ρ and E_{sp} with ETR and No-ETR effects at 14 and 30 ns, respectively

E_L (mJ)	t (ns)	P (GPa)	u_p (km/s)	ρ × 10^3 (kg/m^3)	E_{sp}× 10^5 (J/kg)	Effect
25	14	0.9	0.14	3	0.4	Same with ETR and No-ETR
	30	0.4	0.09	2.8	0.25	
175	14	2.6	0.45	3.4	1.3	Approximately same with ETR and No-ETR
	30	2.6	0.44	3.4	1.2	ETR
		2.4	0.4	3.3	1.05	No-ETR

B) Cylindrical geometry

In the previous section-A, the spatial evolution of P, u_p, ρ and E_{sp} of the SW is compared with 25 mJ and 175 mJ, respectively using planar geometry. As observed the ETR effects are negligible in the case of lower input energy of 25 mJ. In this present section, the ETR effects using cylindrical geometry is compared for the higher input laser energy, 175 mJ.

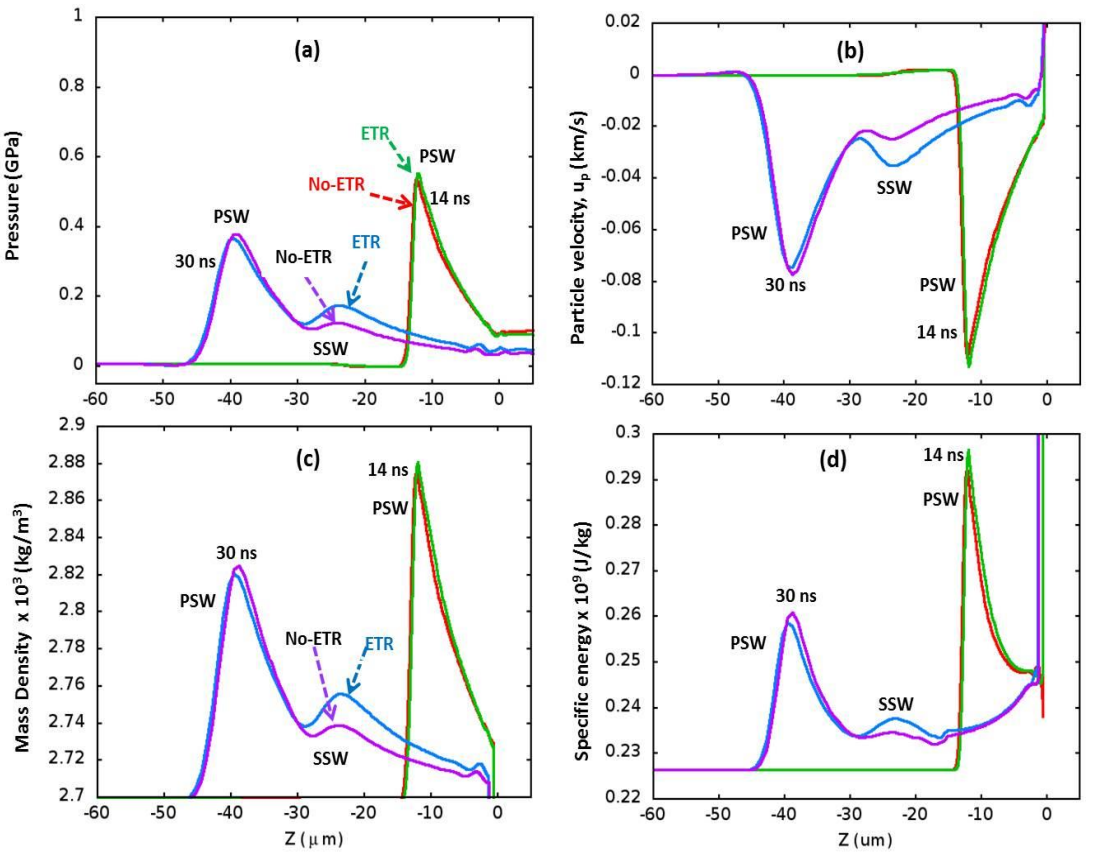

Figure 4.9 Comparison of spatial evolution of a) pressure, b) particle velocity, c) Mass density and d) total specific energy using cylindrical geometry with ETR and No-ETR effects for the input laser energy of 175 mJ at 14 and 30 ns, respectively.

In fig. 4.9 (a – d) the spatial evolution of P, u_p, ρ and E_{sp} is compared with ETR and No-ETR effects, respectively using cylindrical geometry at two instants of time 14 and 30 ns. As seen from the pressure profile (fig. 4.9 (a)), the peak pressure of PSW with ETR and No-ETR is same at 14 ns and very small difference is observed at 30 ns.

However, in the SSW at 30 ns, the pressure with ETR (~0.2 GPa) has slightly higher value than No-ETR (~0.1 GPa). Similar trend is observed with the particle velocity (fig. 4.9 (b)), mass density (fig. 4.9 (c)) and specific energy (fig. 4.9 (d)). Table 4.2 summarizes the peak parameters with ETR and No-ETR across the SSW at an energy of 175 mJ at 30 ns.

The peak values of the PSW and SSW with cylindrical geometry are small compared to that with planar geometry as given in fig. 4.7 (b & d) and fig. 4.8 (b & d). Also, the effects of ETR on the SSW propagation into Al are small with cylindrical geometry compared to that with the planar geometry. The lower peak values is due to the volume occupied and the total mass per unit cell higher than that of planar geometry as discussed in Chapter-3 section-3.4.2.

Table 4.2 Comparison of peak P, u_p, ρ and E_{sp} with ETR and No-ETR effects across the SSW at 30 ns.

E_L (mJ)	t (ns)	P (GPa)	u_p (km/s)	$\rho \times 10^3$ (kg/m^3)	$E_{sp} \times 10^5$ (J/kg)	Effect
175	30	0.2	0.035	2.76	0.24	ETR
		0.1	0.02	2.74	0.23	No-ETR

C) Spherical geometry

In figure 4.10 (a – d) the spatial evolution of the SW pressures, particle velocity, mass density and total specific internal energy propagating into Al target is compared with ETR and No-ETR effects, respectively at two instants of time 14 and 30 ns using spherical geometry. As seen from the pressure profile of fig. 4.10, the peak pressure of PSW with ETR is slightly higher than that of with No-ETR at 14 ns, however this difference is observed to be negligible at 30 ns. Unlike the planar (fig. 4.7 and fig. 4.8) and cylindrical (fig. 4.9) SW evolutions where a steep gradient of the SW parameters is seen across the interface between PSW and the undisturbed Al region, no such sharp gradients is observed with the spherical evolution. Moreover, the spread in the wave is

observed to be flattened. The peak values of the PSW and SSW with spherical are very small compared to that with planar and cylindrical evolutions. The effects of ETR on the SSW propagation with spherical were found to be almost negligible compared to the planar and cylindrical evolutions.

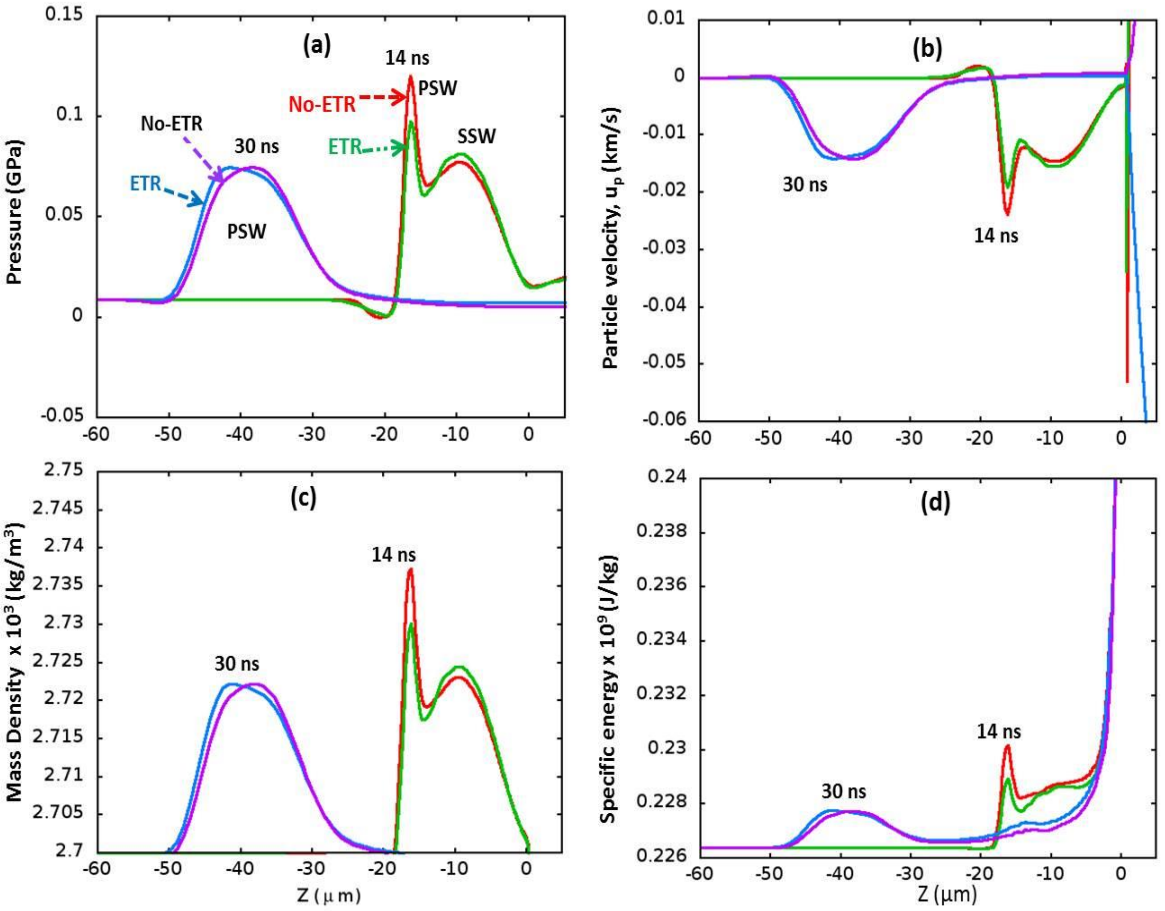

Figure 4.10 Comparison of a) pressure, b) particle velocity, c) Mass density and d) total specific energy using spherical geometry with ETR and No-ETR effects for the input laser energy of 175 mJ at 14 and 30 ns, respectively.

4.4. Temporal evolution of P, u_p, ρ and E_{sp}

In figure 4.11 (a-d) the temporal evolution of the peak pressure, particle velocity, mass density and specific internal energy of the PSW is compared with ETR effects for the input laser energies of 25 mJ and 175 mJ over the time scales of 7 – 1000 ns.

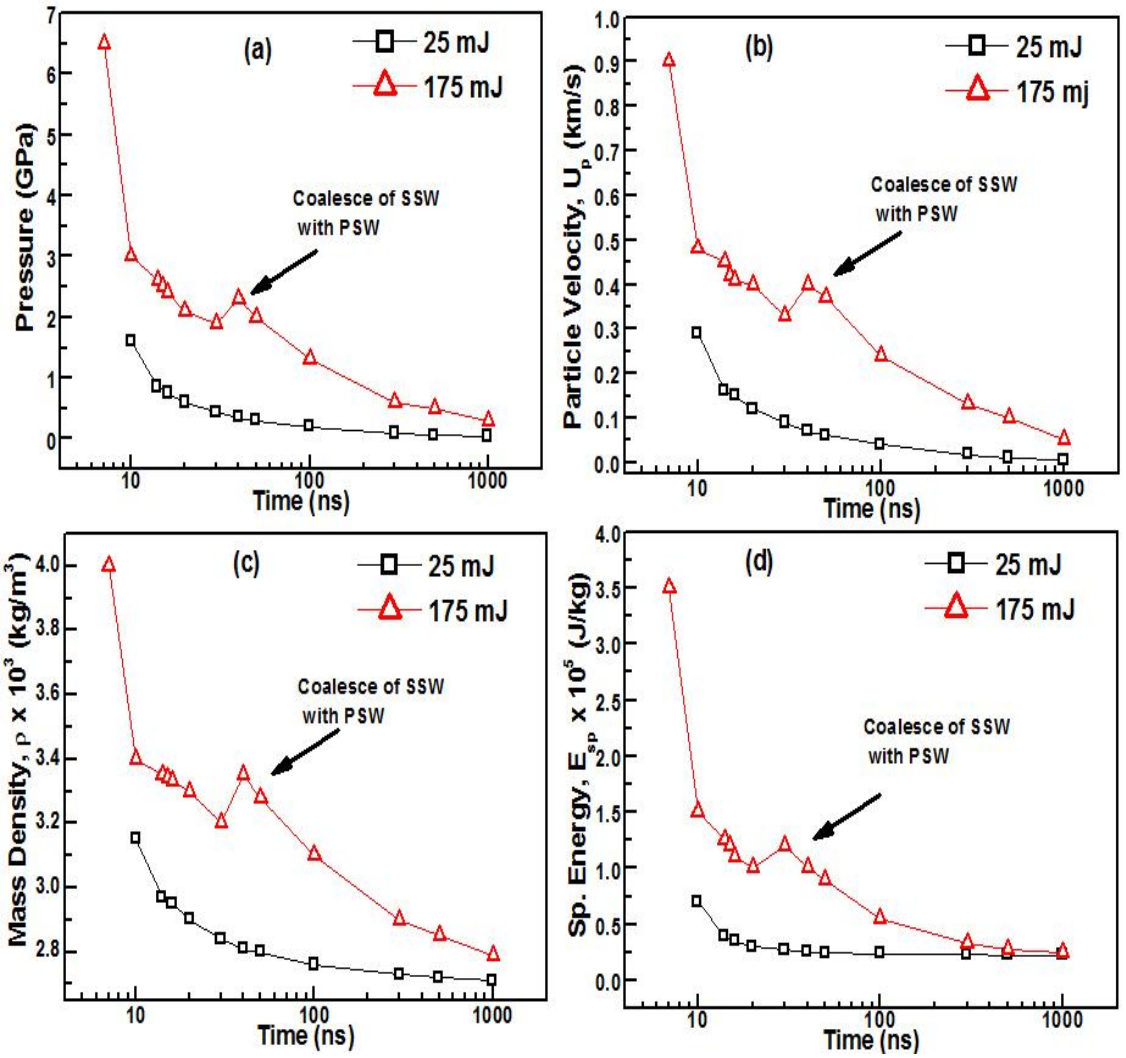

Figure 4.11 Temporal evolution of the peak a) pressure, b) particle velocity, c) mass density and d) specific internal energy of the PSW propagating into Al target using planar geometry for the 25 mJ and 175 mJ.

The peak pressure (fig. 4.11 (a)) in the case of 25 mJ decay from ~1.6 -0.2 GPa over the time scales 10 – 1000 ns due to weak coalescence of PSW and SSW no rise in the pressure is seen in between these time scales. The peak pressure (fig. 4.11 (a)) in the case of 175 mJ decay from ~6.5 -1.8 GPa over the time scales 7 – 30 ns and rises to over ~2.4 GPa at 40 ns due to coalescence of PSW and SSW. The SSW pressure found to

decay from ~3.5 - 2.3 GPa over 16 – 30 ns time scales. After the coalescence the pressure then decrease from ~2.4 - 0.5 GPa over the time scales of 40 – 1000 ns.

Table-4.3 summarizes the peak values of PSW corresponding to pressure, particle velocity, mass density and specific internal energy over the time scales of 7- 1000 ns for the input laser energies of 25 mJ and 175 mJ.

Table 4.3 Peak PSW values corresponding to pressure, particle velocity, mass density and specific internal energy over 7- 1000 ns time scales for the input laser energies of 25 mJ and 175 mJ, respectively.

E_L (mJ)	Time (ns)	P (GPa)	U_p (km/s)	$\rho \times 10^3$ (kg/m^3)	$E_{sp} \times 10^5$ (J/kg)
25	14	1.6	0.3	3.18	0.7
	1000	0.2	0.01	2.7	0.25
175	7	6.5	0.9	4	3.5
	1000	0.5	0.1	2.8	0.25

The peak particle velocities (fig. 4.11 (b)) in the case of 25 mJ decay from ~0.3 -0.01 km/s over the time scales 10 – 1000 ns. In the case of 175 mJ these values decay from ~0.9 - 0.3 km/s over the time scales 7 – 30 ns and rises to over ~0.4 km/s at 40 ns at the coalescence point. The particle velocities behind SSW decay from ~0.58 - 0.4 km/s over 16 – 30 ns and from ~0.4 - 0.1 km/s over 40 – 1000 ns.

The peak mass density (fig. 4.11 (c)) in the case of 25 mJ decay from ~3180 -2700 kg/m^3 over the time scales 10 – 1000 ns. In the case of 175 mJ these values decay from ~4000 - 3200 kg/m^3 over the time scales 7 – 30 ns and rises to over ~3.4 kg/m^3 at 40 ns at the coalescence point and thereafter decreases from 3.4 – 2.8 kg/m^3 over the time scales of 40 – 1000 ns.

The peak specific internal energy (fig. 4.11 (d)) in the case of 25 mJ decay from ~0.7×10^5 -0.25×10^5 J/kg over the time scales 10 – 1000 ns. In the case of 175 mJ these

values decay from ~3.5×10^5 -1.0 $\times10^5$ J/kg over the time scales 7 – 30 ns and rises to over 1.25 $\times10^5$ J/kg at 40 ns at the coalescence point and thereafter decreases from 1.25 $\times10^5$– 0.25×10^5 kg/m^3 over the time scales of 40 – 1000 ns.

Figure 4.12 compares the temporal evolution of the peak pressure of the SW using planar, cylindrical and spherical geometries over the time scales of 7 – 1000 ns. As discussed in section 4.3.3 the peak values with planar is higher followed by the cylindrical and spherical evolutions. With planar geometry the pressure decays from 6.5 – 0.5 GPa, with cylindrical geometry the pressure decays from 0.45 – 0.05 GPa and with spherical it is observed to decay from 0.35 – 0.01 GPa.

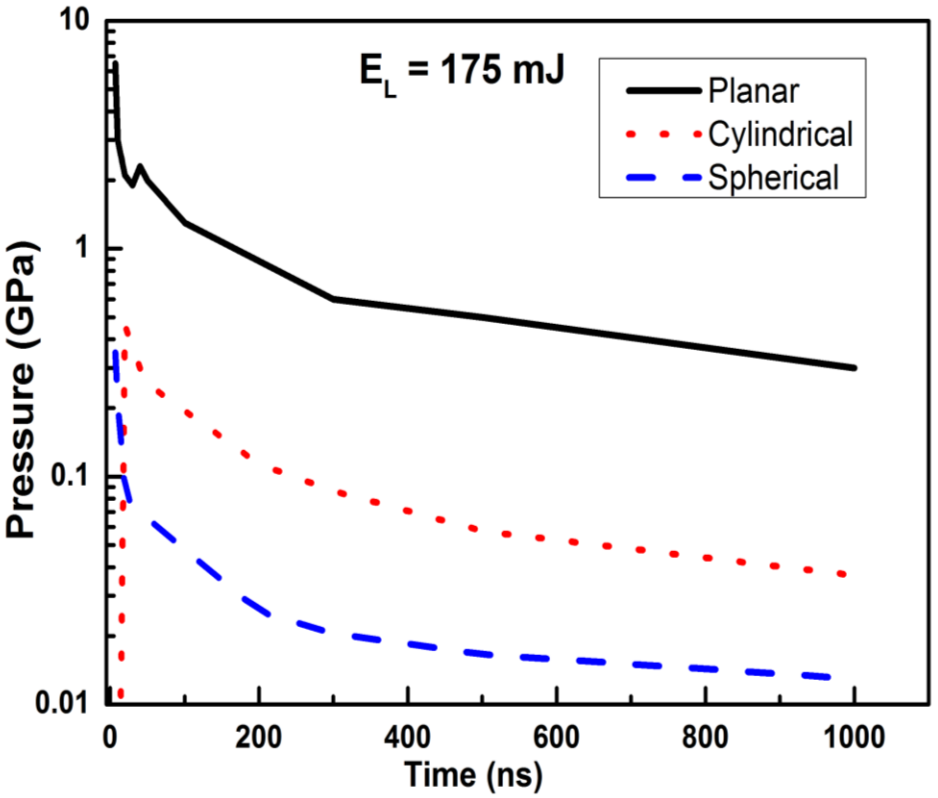

Figure 4.12 Temporal evolution of the peak pressure compared between planar cylindrical and spherical geometries, respectively for the input laser energy of 175 mJ.

4.5 P-u_p and P-V Hugoniots

The information of the Hugoniot curves of a particular material is very important in the fields like laser shock peening, material processing using lasers etc. In the present section, the P-u and P-V Hugoniot curves of the Al target have been constructed for Al target using planar geometry with peak values of pressure, particle velocity and specific volume (inverse of mass density) parameters. Fig. 4.13 (a & b) shows these curves for the input laser energies 25 mJ and 175 mJ, respectively.

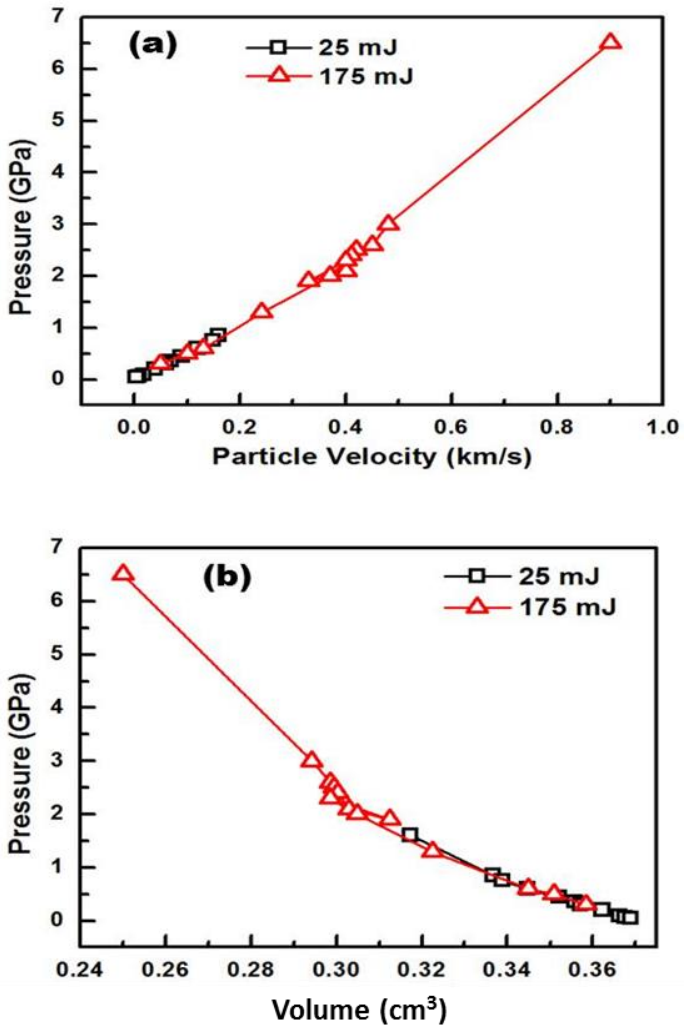

Figure 4.13 Construction of a) P-u_p and b) P-V Hugoniots over the pressure range 6.5 – 0.5 GPa from the shocked parameters obtained using planar geometry for the input laser energies of 25 mJ and 175 mJ, respectively.

P-u_p Hugoniot curve of Al target obtained for two laser energies 25 mJ and 175 mJ, respectively. As observed from figure that as the shock pressure increases the particle velocities also increases. The maximum particle velocity at 1 GPa observed to be ~0.18 km/s (at 25 mJ) similarly, at 6.5 GPa observed to be ~0.9 km/s.

4.6 Summary

Numerical simulations performed with 1D-RHD code show that at low (25 mJ) and high (175 mJ) input laser energies two different shock waves (PSW and SSW) have been launched into Al target during the laser pulse duration and immediately after the termination of the laser pulse. The PSW launched during the laser pulse interaction is due to the increase in the absorption of the input laser energy after the breakdown of the Al target which result in thermal ionization of the background air. Due to increase in the thermal energy transfer between the hot Al and air particles, the temperatures of the surrounding air increases causing the sudden expansion of the plasma into ambient air that creates the equal momentum but propagating into the Al target. Due the momentum the PSW is launched into Al target. The secondary SW (SSW) observed to be launched immediately after the termination of the laser pulse due to the existence of different pressure gradients in the ablated plasma expanding into air. The gradient causes the hydrodynamic instabilities leading to the generation of the SSW. The PSW pressure in case of low laser energy is observed to have higher pressure than the SSW, whereas at higher laser energy the SSW is observed to have higher pressure than the PSW at its launching time. These waves are observed to be emanating through the target separately and found to be coalescing at around 30 - 40 ns and later on moves as a single SW. During the coalescence time the resultant SW is found to have higher pressure than the individual pressures before coalesce for higher input laser energy.

The ETR effects were observed to influence the shock parameters such as the pressure, particle velocity, mass density and specific internal energy during the evolution through Al at higher input laser energies, whereas at lower energies it is found to be negligible. The effects of ETR on SSW evolution were found to be dominant compared to that on the PSW at 175 mJ. This is due to the fact that PSW have launched as soon as the breakdown of the material occurs where the net radiation emissions are low and not much intense to modify the SW propagation. The ETR effects on SSW launched at 16 ns is higher because the plasma formed after the breakdown absorbs the remaining laser energy resulting in raise in the net radiation emissions and intensity due to recombination of the free electrons to the constituent ions in the form of bremsstrahlung free-free, free-bound radiation, and cooling of the ablated plasma due to the expansion. The ETR effects are found to influence the shock parameters up to 50 ns time scales and later on becomes negligible on the SW propagation. The effects were found to be dominant in the case of planar evolution and negligible in the cylindrical and spherical evolutions.

The temporal evolution of the PSW peak pressure, particle velocity, mass density and specific internal energy is presented over time scales from the initial PSW launching times to 1000 ns and compared with 25 mJ and 175 mJ. The P - u_p and P-V Hugoniot of the Al target is constructed for both energies over the pressure range of 6.5 GPa to 0.5 GPa. These studies will help one to get an insight into the laser based material processing and applications like shock peening.

References

[1]L. J. Radziemski, *Lasers-Induced Plasmas and Applications*. (Taylor & Francis, 1989).
[2]A. Caruso and R. Gratton, Plasma Physics **10** (9), 867 (1968).
[3]L. J. Radziemski, Spectrochimica Acta Part B: Atomic Spectroscopy **57** (7), 1109-1113 (2002).
[4]A. Benuzzi-Mounaix, M. Koenig, A. Ravasio, T. Vinci, N. Ozaki, M. R. l. Gloahec, B. Loupias, G. Huser, E. Henry, S. Bouquet, C. Michaut, D. Hicks, A. MacKinnon, P. Patel, H. S. Park, S. L. Pape, T. Boehly, M. Borghesi, C. Cecchetti, M. Notley, R. Clark, S. Bandyopadhyay, S. Atzeni, A. Schiavi, Y. Aglitskiy, A. Faenov, T. Pikuz, D. Batani, R. Dezulian and K. Tanaka, Plasma Physics and Controlled Fusion **48** (12B), B347 (2006).
[5]C. E. Max, C. F. McKee and W. C. Mead, Physics of Fluids **23** (8), 1620-1645 (1980).
[6]S. Atzeni and J. Meyer-ter-Vehn, *The Physics of Inertial Fusion: BeamPlasma Interaction, Hydrodynamics, Hot Dense Matter*. (OUP Oxford, 2004).
[7]B. A. Remington, R. P. Drake, H. Takabe and D. Arnett, Physics of Plasmas **7** (5), 1641-1652 (2000).
[8]S. Sai Shiva, C. Leela, P. Prem Kiran, C. D. Sijoy and S. Chaturvedi, Physics of Plasmas **23** (5), 053107 (2016).
[9]D. Batani, H. Stabile, A. Ravasio, G. Lucchini, F. Strati, T. Desai, J. Ullschmied, E. Krousky, J. Skala, L. Juha, B. Kralikova, M. Pfeifer, C. Kadlec, T. Mocek, A. Präg, H. Nishimura and Y. Ochi, Physical Review E **68** (6), 067403 (2003).
[10]R. Ramis, K. Eidmann, J. Meyer-ter-Vehn and S. Hüller, Computer Physics Communications **183** (3), 637-655 (2012).
[11]C. Leela, Ph. D. thesis, University of Hyderabad, India, 2014.
[12]C. Leela, P. Venkateshwarlu, R. V. Singh, P. Verma and P. P. Kiran, Opt. Express **22** (S2), A268-A275 (2014).
[13]L. M. Cabalín and J. J. Laserna, Spectrochimica Acta Part B: Atomic Spectroscopy **53** (5), 723-730 (1998).
[14]S. S. Harilal, G. V. Miloshevsky, P. K. Diwakar, N. L. LaHaye and A. Hassanein, Physics of Plasmas **19** (8), 083504 (2012).
[15]F. Rezaei and S. H. Tavassoli, Physics of Plasmas **20** (1), 013301 (2013).

Chapter 5

1D-Numerical study of Laser Ablative plasma and SW dynamics in air and their interaction with Al target

The interaction of laser induced under-dense (UD) air plasma with solid targets offers a different plasma and SW dynamics both into the ambient air and into the target. The air plasma created ahead of the target surface at few microns of distance expands into ambient air towards laser propagation direction and towards the target surface. The plasma heading towards the solid target interacts and reflects back to move in the opposite direction. Due to the interaction and reflection a SW is launched into the target to conserve the momentum created by the air plasma on to the surface. The expansion of the plasma into ambient air after the interaction is completely different from the expansion dynamics of the plasma created by direct irradiation of the laser onto the surface as discussed in chapter-4. Similarly, the SW that is launched into Al offers a different dynamics compared to that of the SW launched by direct irradiation of the laser. In the previous case the SW is launched due to the ablation of the plasma from the Al target whereas, in this case the SW is launched by the interaction of air plasma with Al target.

The plasma dynamics and the corresponding SW characteristics behave differently depending on the point of source where the initial plasma breakdown has taken place from the point of target surface. To understand the dynamics of air plasma interaction with Al into ambient air and the SW propagation in Al target is numerically simulated using the modified 1D-RHD

code MULTI-fs. The focusing plane in air is shifted such that the distance between the Al target surface and the initial air breakdown is varied which is mentioned as separation, D over 5 - 40 μm. The simulations have been carried for two different energies 25 mJ and 175 mJ whose corresponding intensities range over 10^{10} – 10^{11} W/cm^2. The model considers the air plasma to behave as an ideal gas hence, the ideal gas charge state EOS is taken, whose ionization is evaluated from the relation given by More et al.[1] and Atzeni et al.[2] Similarly tabulated QEOS[3, 4] data is used for Al target. The radiation effects for both the background air and Al is considered where the Rosseland and Planck opacities corresponding to Al is used from tabulated QEOS data whereas, in the case of air these were obtained from the analytical expressions given by Minguez et al.[5] The absorption of the laser energy is carried by the IB due to e-i as given in MULTI-fs code. This chapter is organized as follows:

1) **In part-I, the laser –air interaction and the formation and expansion of the air plasma is studied.**
2) **In part-II, the interaction of air plasma with Al target and the plasma dynamics in ambient air is studied with varying separation (D) between the Al target and UD air plasma.**
3) **In part-III the SW launched into the Al target by the reflected air plasma is investigated with varying separation (D) between the Al target surface and UD air plasma.**

The simulations have been carried out in planar geometry.

5.1 Introduction

The interaction of the laser plasma created in air with the solid target leads to the launching of multiple shock waves (SWs) into the target. Such studies are very important if the interest is to know how the material behaves to dynamical loadings created by high power lasers[2, 6-8]. In the conventional techniques like flyer plate impact and gas gun[9, 10], the SW are launched into the target where it is standing still at some position is impacted by the other target of the same or different material. Similarly in the direct laser irradiation method the dynamic SW are launched into the target. The SW strength launched into the target by these techniques depends on the impact time, impact material used due to impedance matching[11]. In the present chapter, the investigations of the laser ablative SW created in air and their interaction with the Al target are presented. These studies offer different SW dynamics in to Al target that depends on the distance where the initial air breakdown has created in ambient air.

5.2 Schematic and simulation methodology

Figure 5.1 (a) shows the schematic of laser-air breakdown by the incoming laser beam, the formation and expansion of the plasma both into the ambient air. Fig. 5.1 (b) shows the air plasma expansion towards Al surface and the interacting of air plasma with Al surface followed by launching of SW into Al. The separation, D represents the point where the air breakdown occurs with respect to the target surface which is varied in step of 5, 10, 20 and 40 μm, respectively. The interaction time of the plasma with the target surface and simultaneously the SW propagating into Al will vary with D. In this chapter, the dynamics of the SW propagating into Al by varying separation D is studied for the input laser energies of 25 mJ and 175 mJ. The simulations have been carried out as follows, in section 5.4 laser induced air dynamics is investigated in planar geometry, in section-5.5 laser induced air plasma interaction with Al target is performed. This section has two parts, in the first part the reflected plasma dynamics

from Al target in air is investigated and in the second part the laser driven SWs into Al target is investigated for planar, cylindrical and spherical geometries.

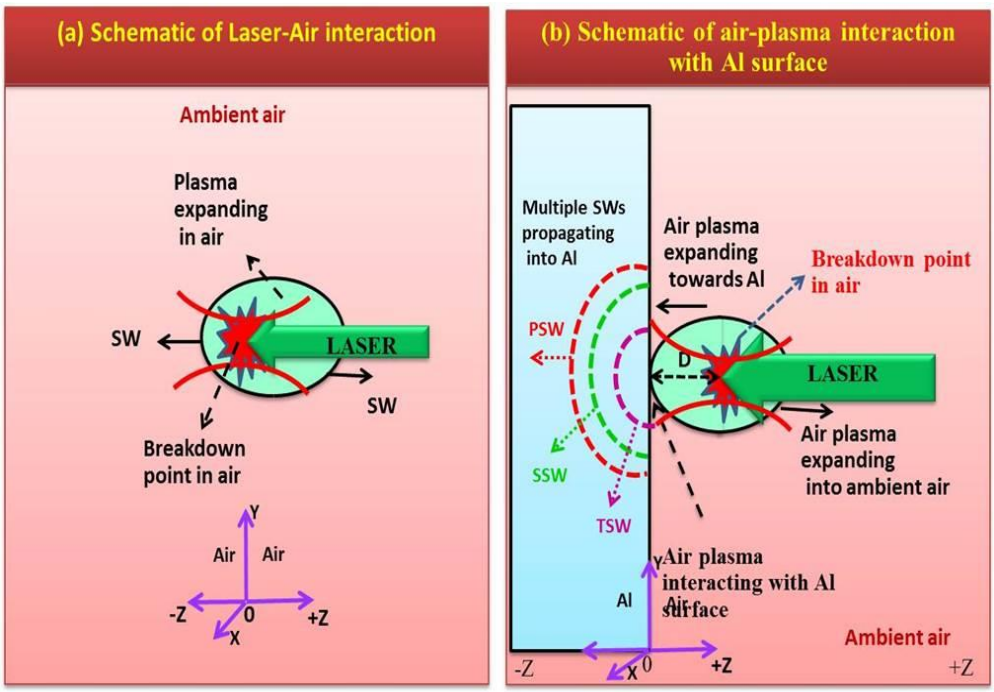

Figure 5.1 Schematic of (a) laser induced plasma in air and b) interaction of air plasma with Al target and launching of SW into target. Z=0 represents the Al-Air interface, +Z - air medium, -Z – Al target. Laser headed from right to left. PSW, SSW and TSW represent the primary, secondary and third SW, respectively.

5.3 Model and Governing Equations

The governing equations for the laser-air interaction and the associated processes such as air-plasma interaction with Al surface is performed by the same equations (3.1) – (3.4) given in Chapter-3. The ideal gas charge state EOS is taken for ambient air where the charge state is evaluated using the analytical expression given by More et al.[1] and Atzeni et al.[2] The electron thermal radiation (ETR) effects are considered where the opacities of air is obtained from the analytical expressions[5]. Similarly, the opacities of Al is taken from the tabulated QEOS data. However it is observed that the radiation effects on the plasma dynamics are negligible. The Gaussian laser pulse with 7 ns (FWHM) and the total pulse duration of 15 ns is used in the simulations.

5.4 Laser Induced Air Plasma and SW Dynamics

5.4.1 Spatial evolution of plasma parameters

Figure 5.2 (a, b) show the total specific energy and fig. 5.2 (c, d) shows the pressure profiles of laser induced plasma expanding into ambient air over the time scales of 5 - 90 ns for the input laser energies of 25 mJ (fig. 5.2 (a & c)) and 175 mJ (fig. 5.2 (b & d)), respectively.

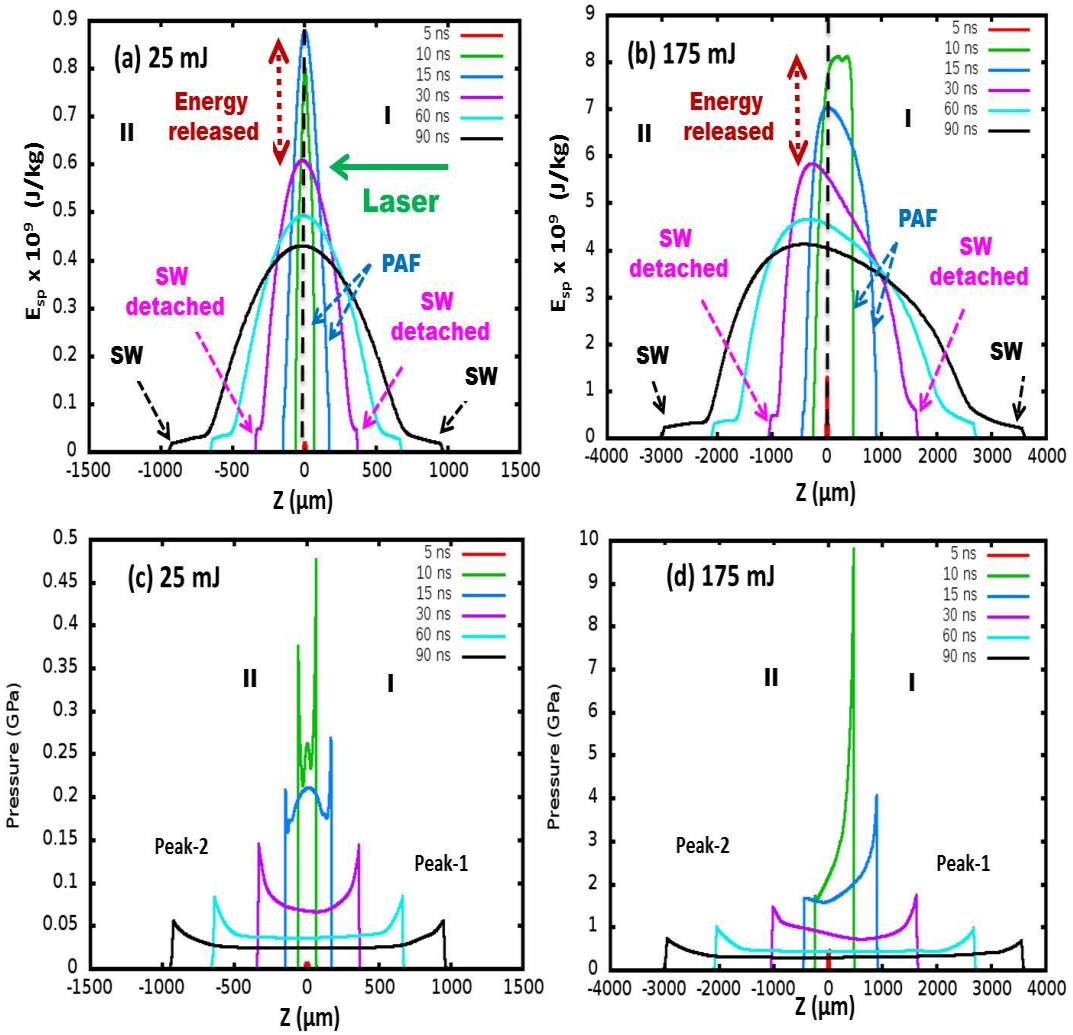

Figure 5.2 Laser induced plasma from air expanding into ambient air for the input laser energy of a) 25 mJ and b) 175 mJ. Bold horizontal arrow indicates the laser propagation direction. Z=0 represents the focal plane of the focusing lens, +Z and –Z - air medium, PAF - Plasma Absorption Front.

The plasma formed is separated into two regions-I and II before and after the focal plane, respectively and the corresponding peak pressures in these regions are represented as peak-1 and peak-2, respectively (fig. 5.2 (c & d)). As observed due to very low absorption of the input laser energy the total specific energy (E_{sp}) and the corresponding total pressure (P) with both the laser energies is observed to have very low values at 5 ns. As the time progress, at 10 ns these values raised to very high value due to the increase in the laser energy absorption by the plasma. The peaks in region-I and II during the laser pulse interaction represents the plasma absorption front (PAF). Since the PAF in region-I interacts first with the incoming laser pulse, the values in this region were observed to be higher than in region-II and this difference is profound at 175 mJ due to the increase of the laser energy absorption by the PAF. The laser energy deposition with 25 mJ is symmetric along the laser axis whereas, with 175 mJ it is asymmetrically distributed due to increase in laser energy absorption by the PAF in region-I. After the termination of the laser pulse, the absorbed energy is released suddenly to the surroundings due to high energy and pressure gradients existing across the PAF and ambient air. Due to these gradients a hydrodynamic motion is set at the interface resulting in the sudden release of the energy. This released energy across the focal plane (region-I and II) may be distributed symmetrically or asymmetrically depending on the nature of the initial laser energy deposition. The asymmetric distribution is clearly seen at 175 mJ, due to the existence of higher gradients in region-I compared to that of region-II. The higher the energy gradient the higher is the energy release thus, resulted in the higher hydrodynamic expansion in this region-I (towards the laser direction) than in region-II. As the energy release is higher, the appearance of peak energy shift is observed in region-I. The energy distribution to the surrounding air continues until the gradients become small along both the directions.

The released specific energy, E_{sp} of the plasma is observed to be ~0.25 × 10^9 J/kg at 25 mJ and ~2 × 10^9 J/kg at 175 mJ over 15 – 30 ns time scales. This released energy is utilized in different processes as fractions such as the generation of the SW that is

expelled through the surrounding, hydrodynamic expansion of the plasma, thermal diffusion and electron thermal radiation (ETR). During the propagation, the SW highly compresses the ambient gas, as a result the temperatures become higher across the shock front. At both the laser energies, the SW is observed detaching from the plasma at around 30 ns. The pressure (strength) of the SW depends on the specific energy released by the plasma (as discussed in chapter 2, section 2.2). The peak-1 and peak-2 represented in region-I and II (fig. 5.2 (c & d)) after 30 ns corresponds to peak pressures of the SW. Table 5.1 summarizes the peak pressure values across the PAF and SW. As observed, the highest peak pressure across the PAF during the laser interaction time is observed at 10 ns which is found to be ~0.47 GPa and ~0.37 GPa at 25 mJ and ~10 GPa and ~2 GPa at 175 mJ in regions-I and II, respectively. Similarly, the peak pressures of the SW at the onset of the detachment that is, at 30 ns in both regions is found to be same ~0.15 GPa at 25 mJ and ~2 GPa and ~1.5 GPa, respectively at 175 mJ. The pressure at latter time scales becomes equal in both regions at 175 mJ.

Since the input laser energy absorption with 175 mJ is higher than that of 25 mJ, the specific energy gradient and the corresponding pressure gradients across the interface is higher. As a result, the hydrodynamic expansion of the plasma and SW is more ~500 - 3500 μm in the case of 175 mJ compared to ~200 - 1000 μm at 25 mJ over 10 – 90 ns time scales.

Table 5.1 Highest peak pressures across the PAF and SW in region-I and II.

Energy (mJ)	Highest peak pressure across PAF (GPa) at 10 ns		Highest peak pressure across SF (GPa) at 30 ns	
	Region-I	Region-II	Region-I	Region-II
25	0.47	0.37	0.15	0.15
175	10	2	2	1.5

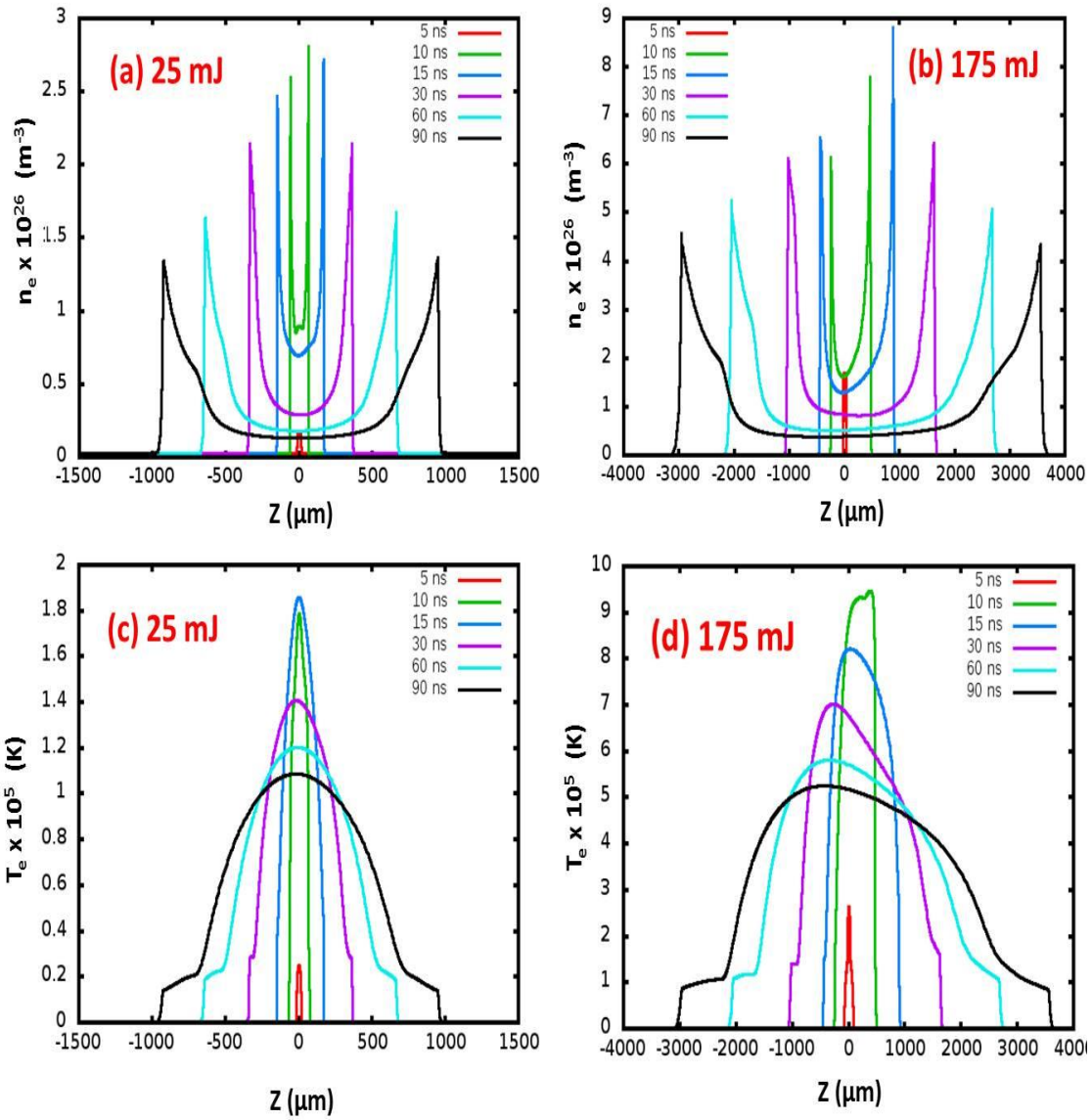

Figure 5.3 Spatial evolution of (a, b) electron number density and (c, d) electron temperature of the air plasma for the input laser energy of 25 mJ and 175 mJ, respectively.

In fig. 5.3 (a & b) and (c & d) the corresponding electron number density (n_e) and electron temperature (T_e) is given for 25 mJ and 175 mJ, respectively. The n_e across PAF have higher values than at the focal point because of the hydrodynamic expansion of the plasma into ambient air that highly compresses the gas across the interface between PAF and ambient air resulting high pressure (peak- 1and -2 in fig 5.2 (c & d)) and mass density (fig. 5.4 (a & b)). The electron temperature (T_e) at the focal point is

higher because of the higher specific energy existing in that region. Though T_e has higher values than that across the front locations, the volume occupied by the front location is very small with respect to the focal region, hence the electron number density is higher across PAF. In gases, the number density normally has the proportionality relation with the pressure hence the electron number density is higher at the PAF. The similar spatial profiles is also observed by Soubacq et al.[12] During the initial plasma formation the laser energy absorption is high at the focal point (central region) which results in high specific energy and electron temperatures in this region.

The peak electron number density decreased from $2.7 \times 10^{26} - 1 \times 10^{26}$ m^{-3} in the case of 25 mJ and from $9 \times 10^{26} - 4.5 \times 10^{26}$ m^{-3} in the case of 175 mJ over the time scales of 10 – 90 ns. Similarly, the peak electron temperatures decreased from $\sim 1.8 \times 10^5 - 1.1 \times 10^5$ K in the case of 25 mJ and from $9.5 \times 10^4 - 5 \times 10^4$ K in the case of 175 mJ over the time scales of 10 – 90 ns.

The mass density in fig. 5.4 (a & b) is found to be more across the PAF and SF and low at the focal point which is due to the existence of high temperatures at the focal point. The mass density (ρ) at 10 ns is found to be same ~4 kg m^{-3} in region-I and II at 25 mJ whereas, at 175 mJ it is found to be more in region-II than in region-I which signifies that the absorption is more at the PAF in region-I. However, ρ in region-I increases abruptly until the detachment of the SF (30 ns), as the PAF expansion is higher in this region. At latter time scales after the SW detachment the density decays gradually.

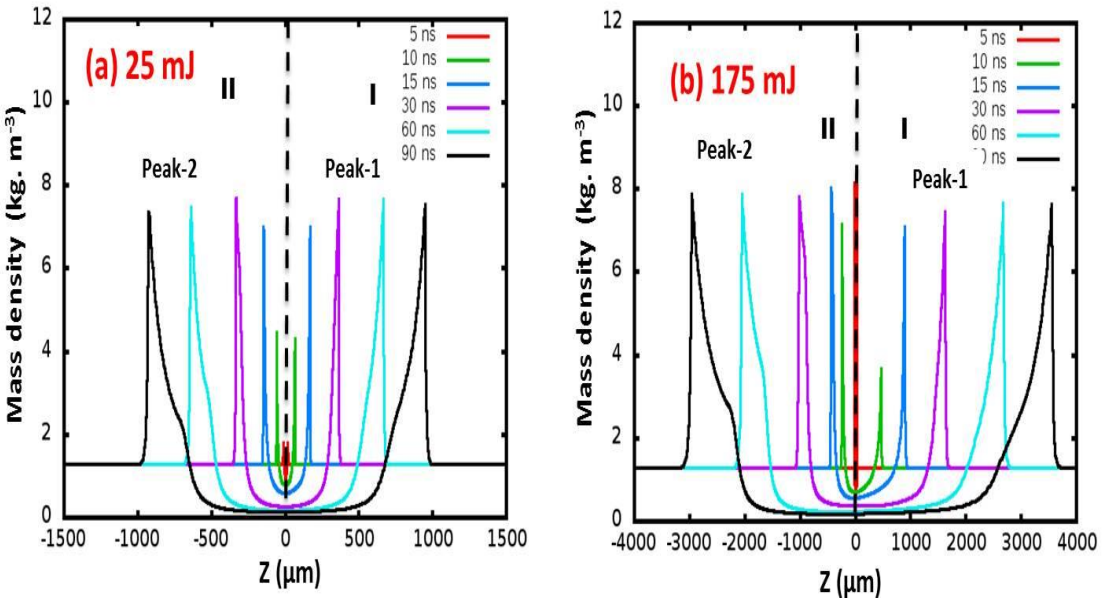

Figure 5.4 Spatial evolution of mass density of the air plasma for a) 25 mJ and b) 175 mJ.

5.4.2 Temporal evolution of peak parameters

In figure 5.5 the temporal evolution of peak plasma variables E_{sp}, pressure, n_e and T_e is compared with 25 mJ and 175 mJ over the time scales from the initial laser interaction time up to 2 µs. The specific energy decreased from $0.3 \times 10^{13} - 4 \times 10^{10}$ J/kg with 25 mJ and $8 \times 10^{13} - 4 \times 10^{11}$ J/kg with 175 mJ. Pressure decreases from 1 – 0.01 GPa in the case of 25 mJ and from 10 – 0.2 GPa in the case of 175 mJ. The n_e in the case of 25 mJ decreases from $3 \times 10^{26} - 0.5 \times 10^{26}$ m^{-3} and with 175 mJ it decreases from $9 \times 10^{26} - 2 \times 10^{26}$ m^{-3}over these time scales. Similarly the T_e in the case of 25 mJ decreases from $10 \times 10^4 - 0.3 \times 10^4$ K and with 175 mJ from $90 \times 10^4 - 2 \times 10^4$ K. As observed during the initial expansion of the plasma that is, upto 250 ns a fast decay in n_e and T_e is observed and later on found to decrease slowly.

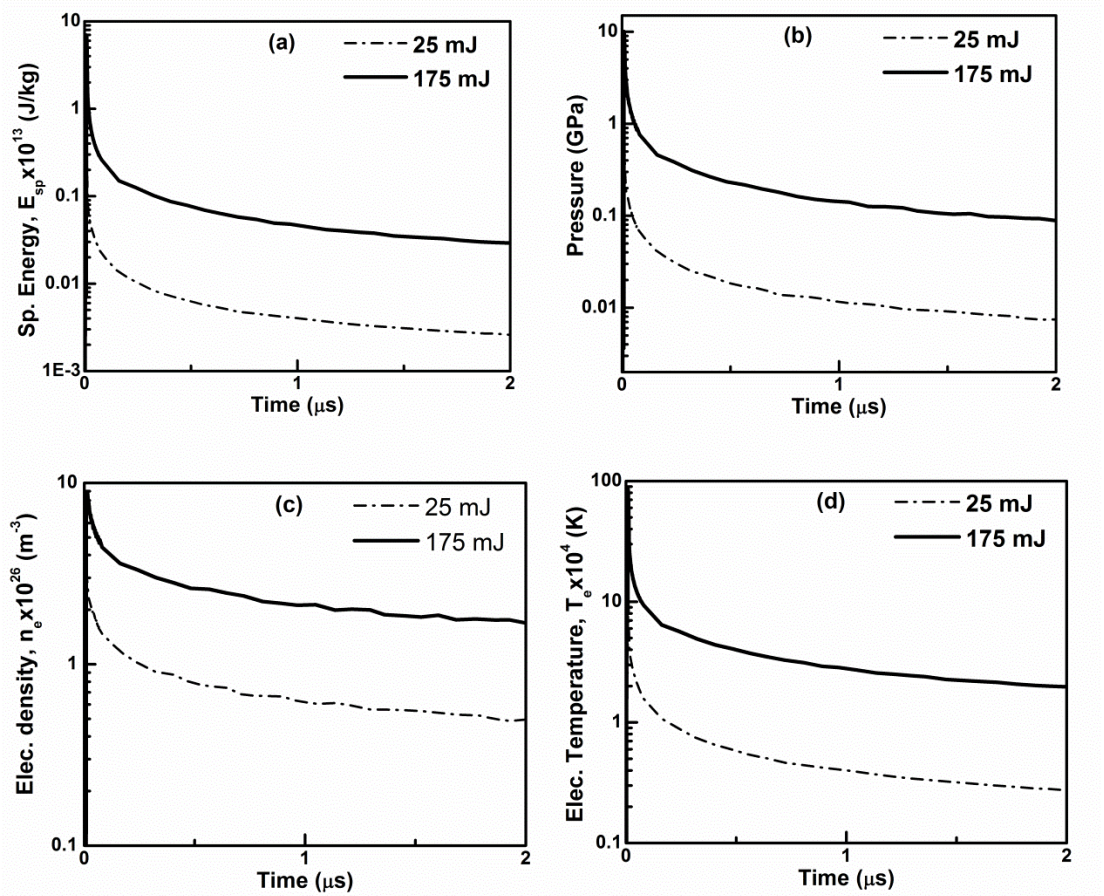

Figure 5.5 Comparison of temporal evolution of a) total specific energy, b) total pressure, c) electron number density and d) electron temperature between 25 mJ and 175 mJ input laser energies up to the time scales of 2 μs from the initial laser interaction time.

5.5 Air plasma interaction with Al and plasma dynamics in air: Effects of shifting focal plane away from Al target

5.5.1 Air plasma expansion before interacting with Al target

In this section the laser induced plasma produced and its interaction with Al surface and the consequent plasma dynamics in ambient air are studied for the input laser energies of 25 mJ and 175 mJ. The initial breakdown point where the air plasma is created by the laser is varied where its separation from the Al surface (D) is taken to be 5 μm, 10 μm 20 μm and 40 μm. In figure 5.6 (a &b) the laser induced air plasma created at a separation, 5 μm is shown for the both laser energies, respectively. The

plasma is expanding in the opposite directions in to ambient air: towards the laser propagation direction and towards the Al surface before interacting with the Al target.

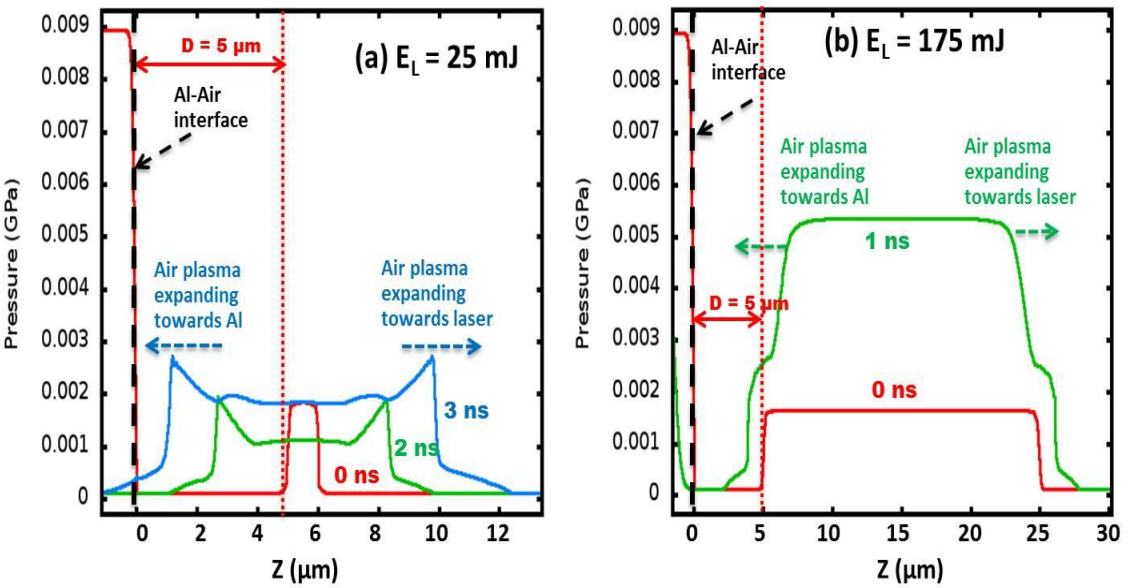

Figure 5.6 Illustration of numerically simulated laser induced air plasma evolution before interacting with Al surface at a) 25 mJ and b) 175 mJ. Z=0 is the Al-air interface, double ended arrow represents the separation (D), dotted vertical line is the initial breakdown point.

5.5.2 Comparison of expansion of Laser induced plasma in air and air plasma after interacting with Al target

In fig. 5.7 the comparison between a) the laser induced plasma (LIP) in air where the Al is not present and b) LIP in air interacting with Al target is shown for 175 mJ input laser energy for the separation, D equal to 5 µm over the time scales of 5 – 15 ns. The plasma pressure at 10 ns within air alone is found to be ~10 GPa, whereas with Al interaction it is enhanced to a slightly higher value of ~11 GPa. Similarly at 15 ns, the peak pressure in ambient air with plasma-Al interaction is found have ~5 GPa compared with air only ~4 GPa. There exist some dis-similarities in the spatial evolution of the plasma and SW evolution with air alone and plasma-Al interaction. As observed in the case of Al interaction, a valley in the pressure at 15 ns is seen behind the PAF which is not observed in the case LIP in air alone. The similar profile is

observed at 30 ns and higher time scales (fig. 5.8). The SSW is observed to be formed with the ablated plasma during the plasma-Al interaction which was found to overtake the PSW at 60 ns (discussed in the next sections) at a spatial length of ~3000 μm (fig. 5.8 (b)). Finally, it is observed that the plasma and SW expansion speeds was enhanced with the Al target placed in front of the LIP produced in air. Moreover, it is seen that, the peak pressure decay rate was observed to be different with both the cases.

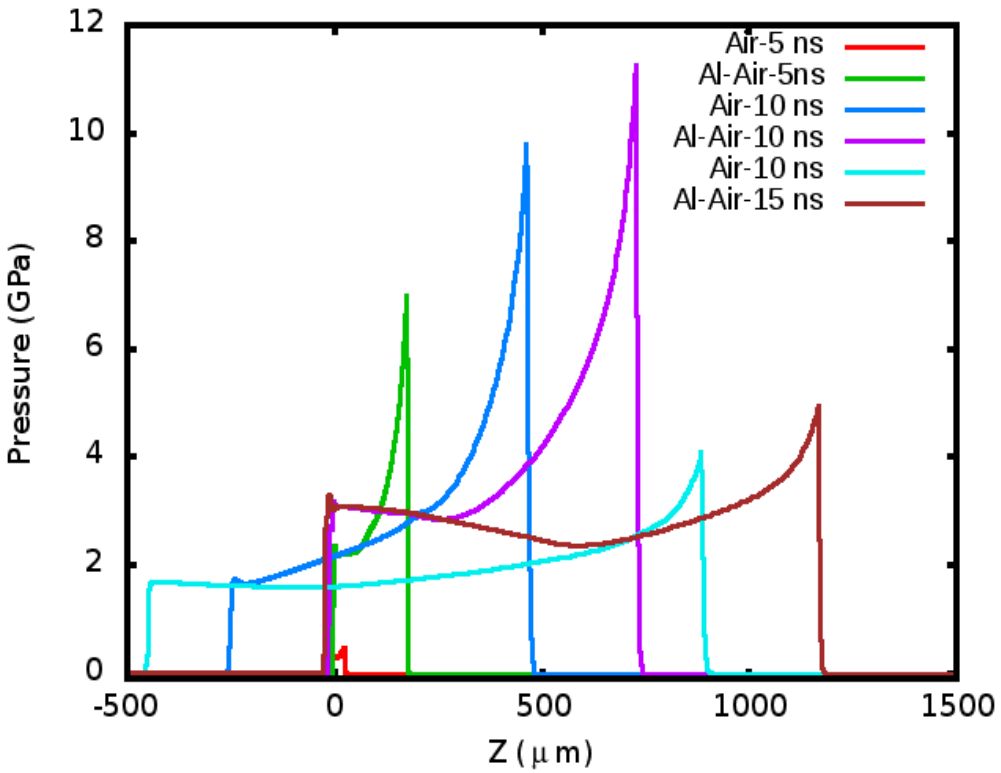

Figure 5.7 Comparison of spatial evolution of pressure from air alone (fig. 5.2 (b)) and after Al-Air interaction in ambient air for the input laser energy of 175 mJ at a separation of 5μm. Z=0 represents the target position of Al-Air interface and focal plane in air.

5.5.3 LIP dynamics in ambient with varying separation, D

Figure 5.8 gives the comparison of plasma dynamics after interacting with Al target for four different separations a) 5 μm, b) 10 μm, c) 20 μm and d) 40 μm for 25 mJ input laser energy.

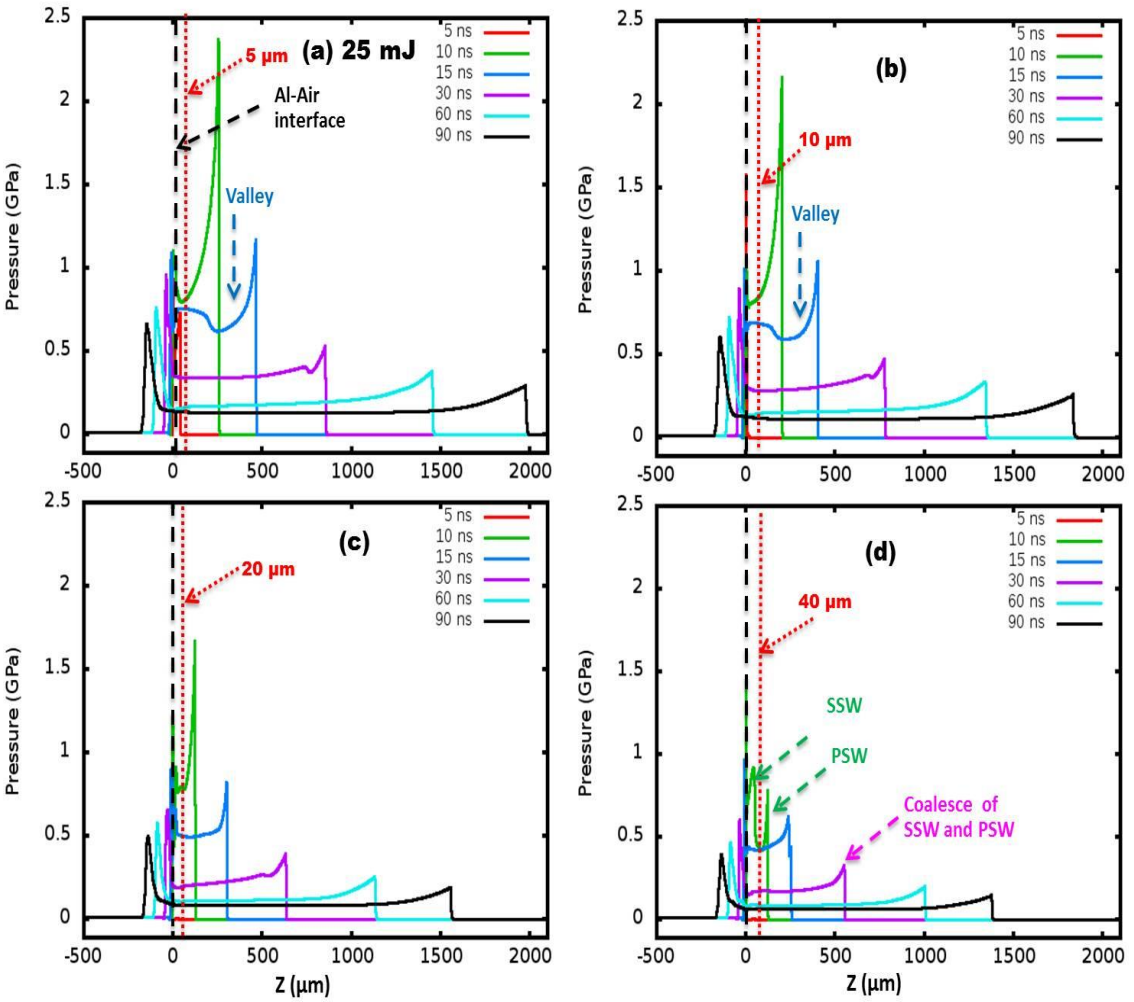

Figure 5.8 Comparison of numerically simulated pressure with varying separation D at a) 5 µm b) 10 µm, c) 20 µm and d) 40 µm for the input laser energy of 25 mJ.

The peak pressure at 5 ns with 5 µm is found to be small ~0.7 GPa and with 10 µm ~1.5 GPa whereas no such pressures were seen with 20 µm and 40 µm. At 10 ns, pressures were observed for all Ds and the values were found to be ~2.4 GPa with 5 µm, ~2.2 GPa with 10 µm, ~1.6 GPa with 20 µm and ~0.7 GPa with 40 µm. Since the air plasma formed interacts early with decreasing D it reflects back as soon as it interacts with the surface. This reflected plasma again absorbs the incoming laser beam resulting in the increase of pressure. At shorter D this reflected pressure encounters the peak laser intensity hence the absorption increases resulting in very high peak pressure.

As the distance increases the reflected plasma interacts with the trailing edge of the pulse resulting in decrease in the peak pressure. This shows with increasing separation the peak pressure decreases to a very small value.

At 15 ns a pressure valley is observed at a distance of ~250 μm from the target surface for the separations 5 μm and 10 μm, respectively. The pressure is found to be increased towards the surface from the valley. This pressure may correspond to the reflected plasma that forms as the second SW (SSW) and propagates through the compressed air in the direction of the first or primary SW (PSW). The SSW overtakes or coalesces with the PSW which found to be occurring in between 30- 60 ns. With 40 μm, reflected plasma formed at 10 ns is observed to coalesce at around 15 ns with the PSW.

Figure 5.9 gives the comparison of plasma dynamics after interacting with Al target for four different separations a) 5 μm, b) 10 μm, c) 20 μm and d) 40 μm for 175 mJ input laser energy. Since the laser energy absorption in air increases with the increasing laser energy the peak pressures were found to have higher values compared to 25 mJ. The peak pressures at 5 ns with increasing D is ~7, ~6.5, ~4.5 and ~5.5 GPa, respectively. The interaction of the plasma with Al occurs at very early times in between 2-4 ns due to high input laser energy absorption as a result the reflected plasma is seen with all the four separations, D. Since the times at which the plasma reflected are smaller than the leading edge of the laser pulse, this reflected plasma has enough time to interact with the remaining laser pulse i.e., some part of the leading edge and full part of the trailing edge. Due to this reason the pressures at 10 ns were found to have approximately same value of 11.5 GPa at four separations. Hence the expansion lengths also found to have the same values of ~700 μm at 10 ns. The plasma expansion dynamics is also observed to behave similarly with all the separations D. The SSW is also observed to form that coalesce with PSW at around 60 ns.

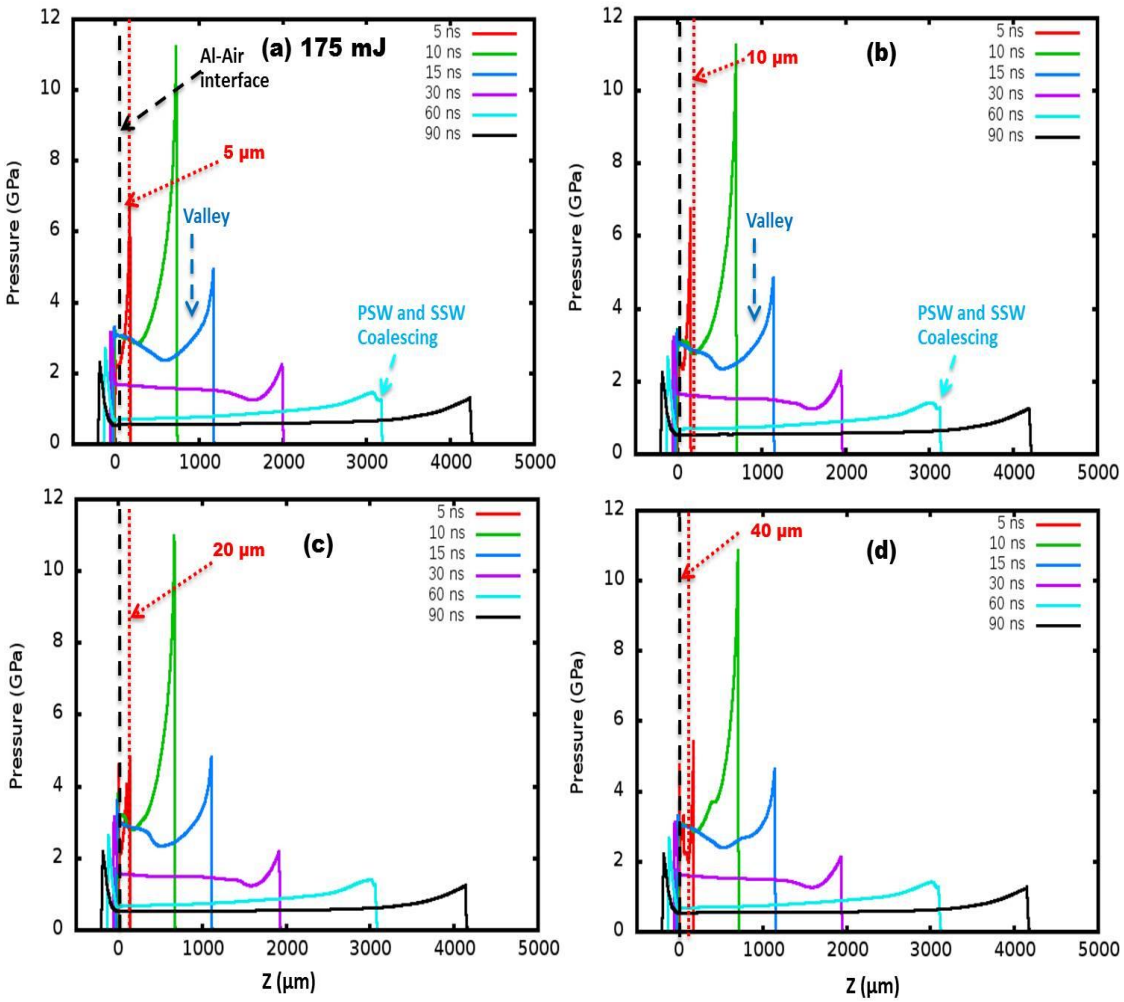

Figure 5.9 Comparison of numerically simulated pressure with varying separation D at a) 5 µm b) 10 µm, c) 20 µm and d) 40 µm for the input laser energy of 175 mJ.

5.5.4 Comparison of temporal evolution of parameters with varying D

The temporal evolution comparison of pressure and total specific energy with four different separations D for the two input laser energies 25 mJ and 175 mJ is shown in figure 5.10 (a-d).

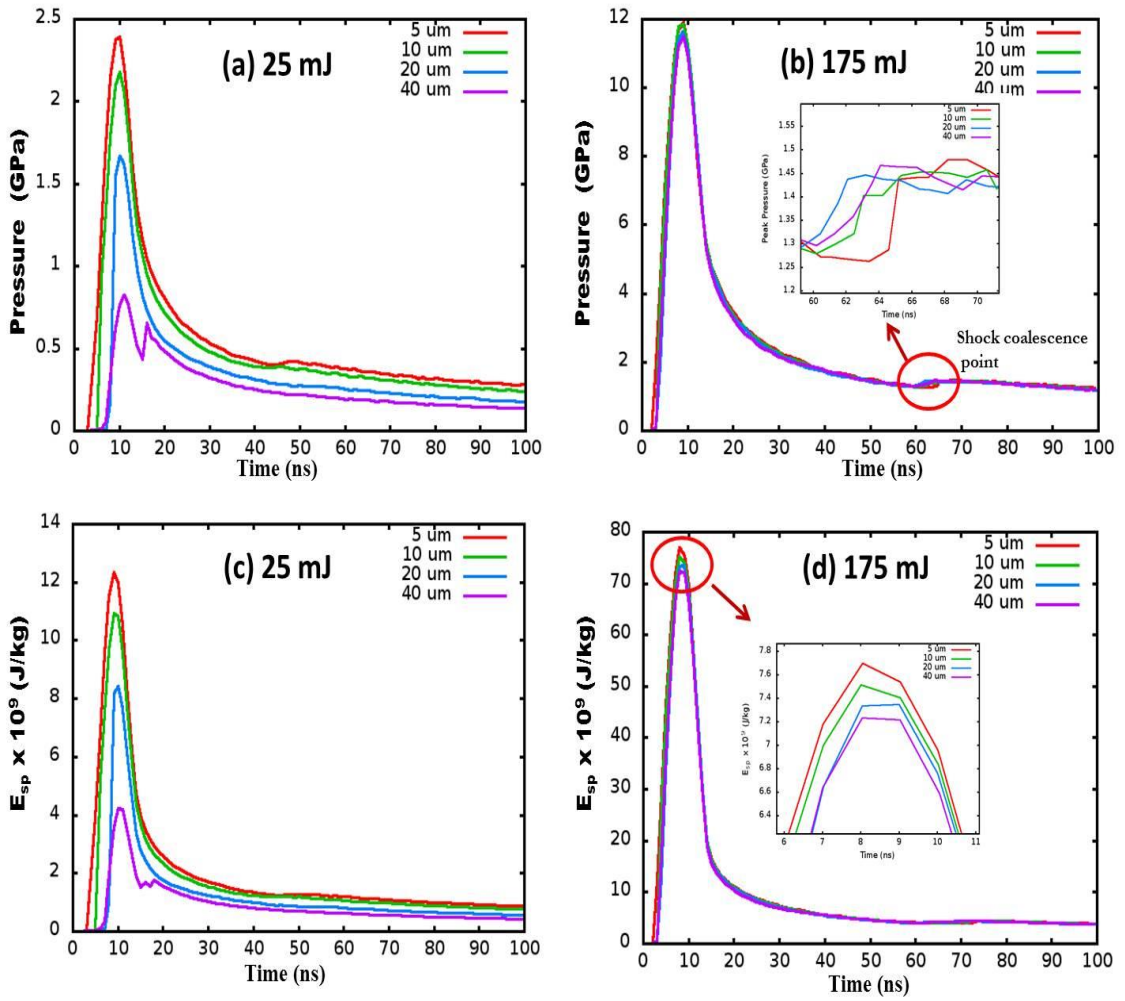

Figure 5.10 comparison of temporal evolution of (a, b) pressure and (c, d) total specific energy with all Ds for the input laser energies of 25 mJ (a, c) and 175 mJ (b, d).

The peak pressure and the total specific energy was observed at ~10 ns from the initial laser interaction for both input laser energies. The first peak pressure appearance time is observed to decrease with increasing D at 25 mJ (fig. 5.10 (a)). The pressure continues to attenuate gradually with time from 10 - 100 ns in the range 2.4 - 0.25 GPa with 5 μm; 2.2 - 0.2 GPa with 10 μm. 1.6 - 0.15 GPa with 20 μm and 0.8 - 0.1 GPa with 40 μm. Similarly the specific energy (fig. 5.10 (c)) is found to decrease from 12 × 10^8 - 1 x 10^8 J/kg with 5 μm, 11 × 10^8 – 0.75 × 10^8 J/kg with 10 μm, 8.0 x 10^8 - 0.5 × 10^8 J/kg with 20 μm and 4 × 10^8 - 0.25 × 10^8 J/kg with 40 μm. The peak pressure (fig.

5.10 (b)) with 175 mJ also found to attenuate in a similar way as 25 mJ and as discussed above the peak values are found to have approximately same values with all Ds. The pressure decreases from 11.5 - 1.5 GPa and the specific energy (fig. 5.10 (c)) decreases from 75×10^8 - 4×10^8 J/kg. A small increase of peak values in pressure and E_{sp} is observed to exist between 60 – 70 ns which indicates that SSW emanating from the ablated plasma coalescing around these time scales. Two small peaks present in the case of 25 mJ at 40 μm is the point where the PSW and SSW coalesce.

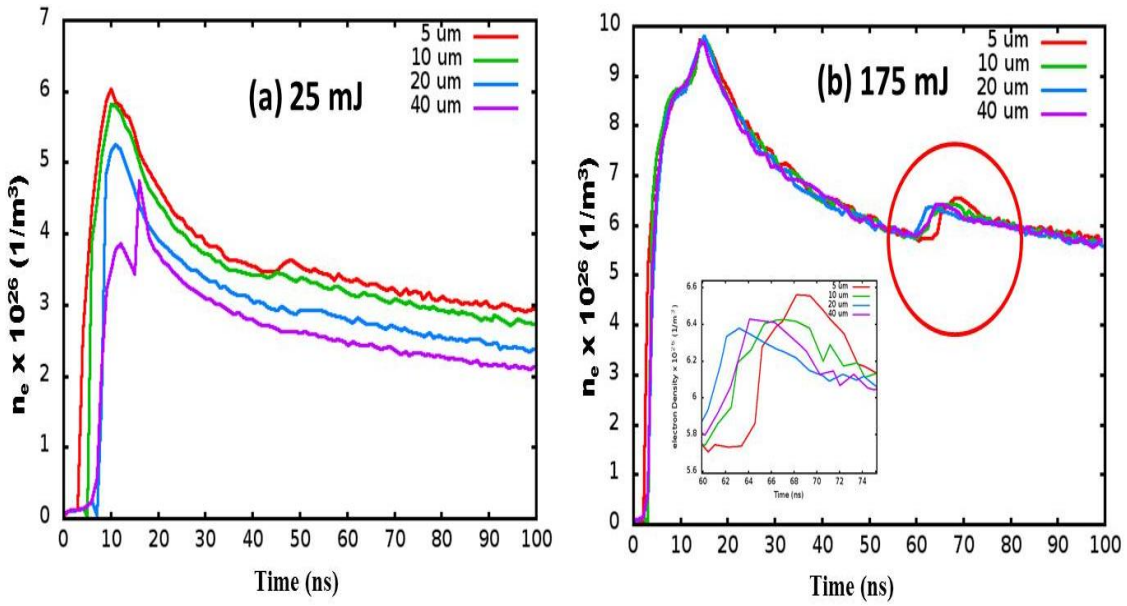

Figure 5.11 Temporal evolution of electron number density for the input laser energy of a) 25 mJ and b) 175 mJ with all Ds for a) 25 mJ and b) 175 mJ.

The electron number density, n_e (fig. 5.11 (a & b)) behaves in a similar way as that of the pressure and E_{sp} as given in fig. 5.10 (a-d). These values decrease from 6×10^{26} - 3×10^{26} m^{-3} with 5 μm, 6×10^{26} – 2.8×10^{26} m^{-3} with 10 μm, 5×10^{26} – 2.2×10^{26} m^{-3} with 20 μm and 4.8×10^{26} - 2×10^{26} m^{-3} with 40 μm. Similarly, n_e with 175 mJ decreases from 9.8×10^{26} - 6×10^{26} m^{-3}. The inset of fig. 5.11 (b) shows the increment in n_e values between 60 – 75 ns due to the coalescence of the SSW with the PSW resulting in the increase in the electron number density by 0.5×10^{26} m^{-3}.

5.6 Air plasma interaction with Al target, launching of SW into Al

5.6.1 Spatial evolution of pressure and particle velocities using planar geometry

A) 25 mJ

In addition to PSW and SSW a third and fourth SWs mentioned as (TSW and FSW) was observed to propagate through the Al target due to the continuous back and forth of the plasma residing close to the Al surface. Fig. 5.12 (a-d) shows the comparison of PSW, SSW and TSW launching times and their propagation into Al target over the time scales from the launch of PSW time to within the pulse duration (<15 ns) for the separations 5, 10, 20, and 40 µm, respectively for the input laser energy 25 mJ.

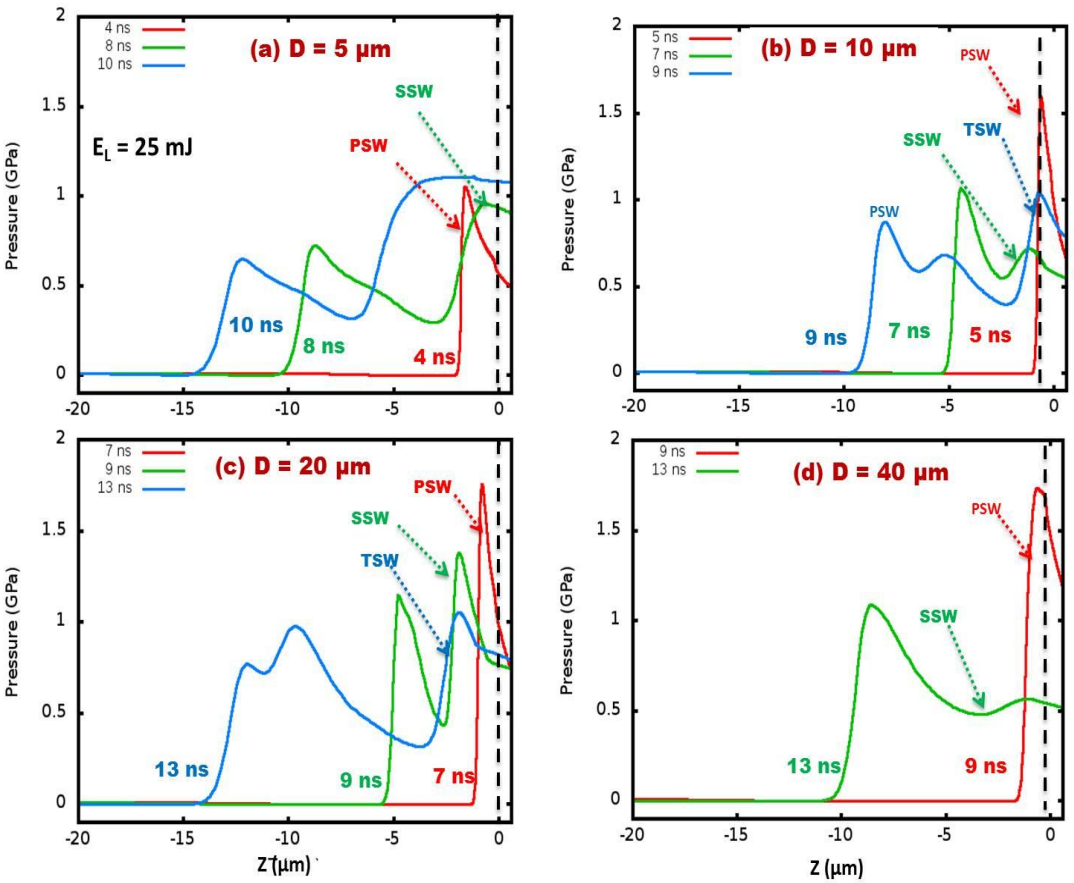

Figure 5.12 Comparison of spatial evolution of the pressure showing the origin times of PSW, SSW and TSW launched into Al target 25 mJ with a) 5 µm b) 10 µm c) 20µm and d) 40 µm.

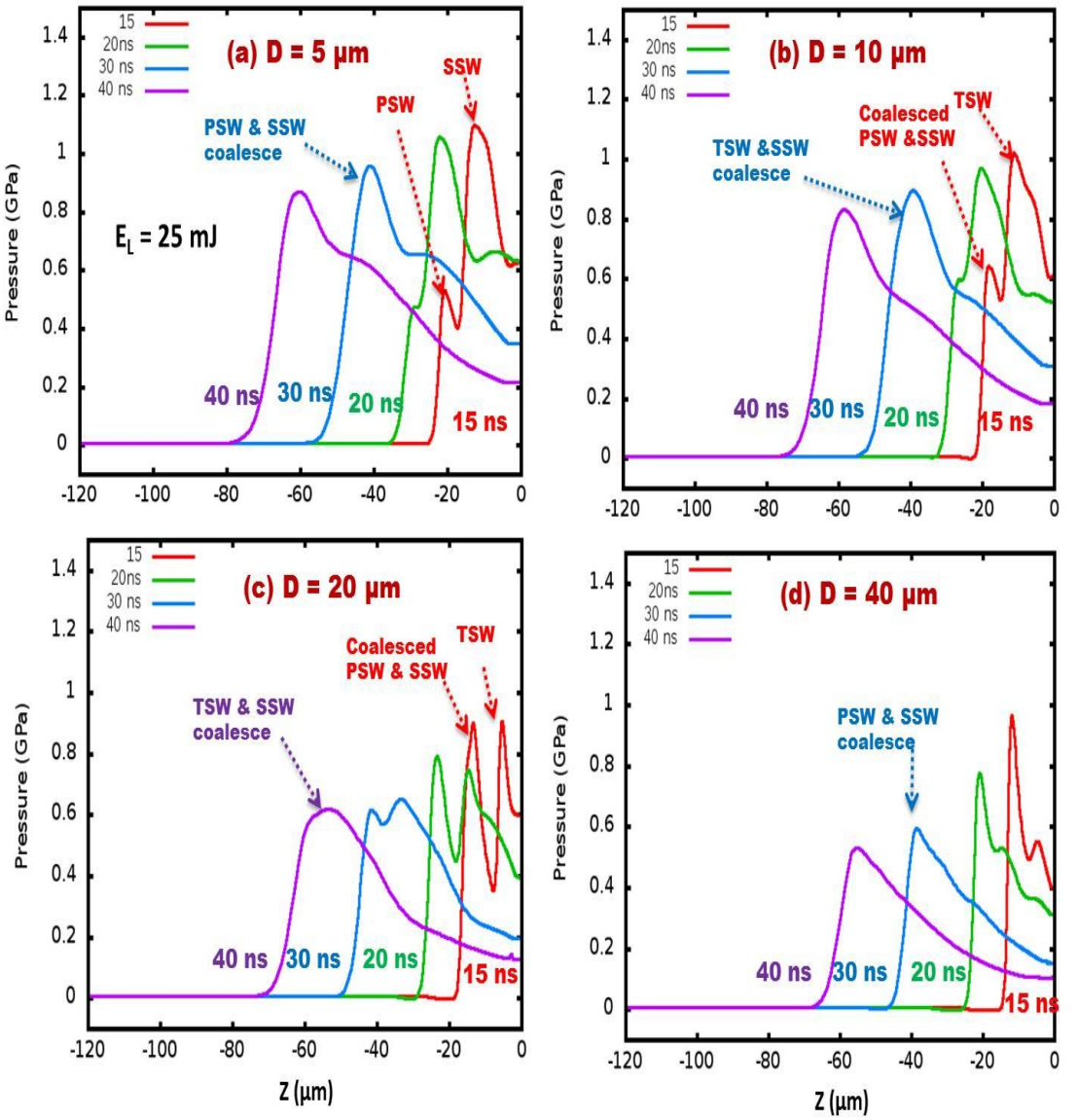

Figure 5.13 Comparison of spatial evolution of the pressures of PSW, SSW and TSW and their coalescence times sat 25 mJ with a) 5 µm b) 10 µm c) 20µm and d) 40 µm, respectively over the time scales of 15 ns to 40 ns.

The initial air plasma-Al interaction is observed to take place at 4 ns and the PSW at 5, 10, 20 and 40 µm is launched at 4 ns, 5 ns, 7 ns and 9 ns, respectively. Table-5.2 summarizes the peak values of the total pressure and the particle velocities at their launch times. The pressure of the PSW were found to be ~1, ~1.6, ~1.7 and ~1.7 GPa, respectively with increasing D. The pressure of the SSW launched at 8 ns, 7 ns, 9

ns and 13 ns, respectively is found to be ~0.9, ~0.7, ~1.4 and ~0.6 GPa. The SSW in the case of 5 μm is observed to increase slightly to ~1.1 GPa. The third shock wave (TSW) is observed only in the case of 10 μm and 20 μm with the pressure of ~1 GPa. The propagation of the SW at longer time scales from 15 – 40 ns is shown in fig. 5.13 for different separations 'D'. The PSW and SSW is observed to coalesce at 30 ns with 5 μm, at ~13 ns with 10 μm, at 14 ns with 20 μm, 30 ns with 40 μm.

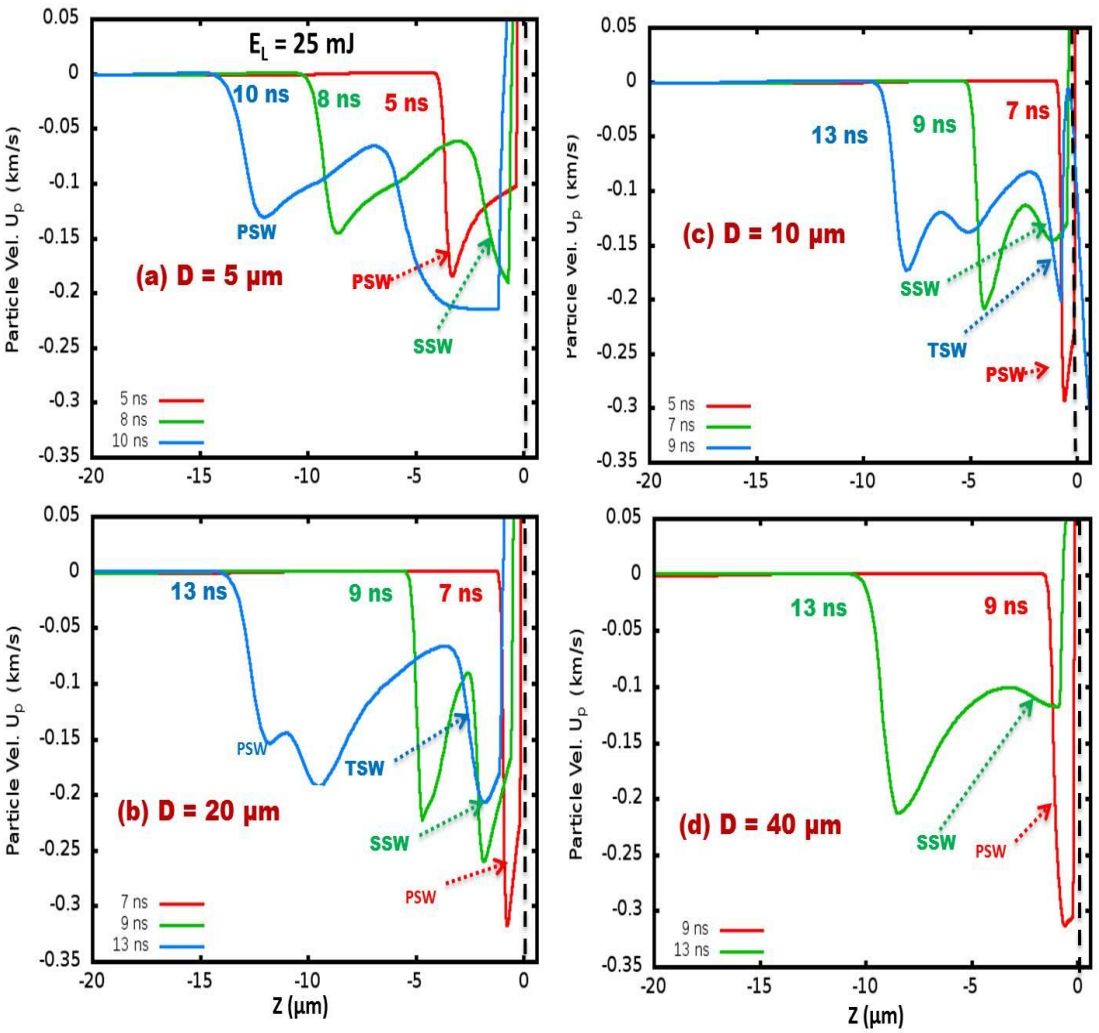

Figure 5.14 Comparison of spatial evolution of the particle velocities across and behind the PSW, SSW and TSW for 25 mJ with a) 5 μm b) 10 μm c) 20μm and d) 40 μm.

Table 5.2 peak pressure and particle values at their respective launch times with 25 mJ.

D (μm)	Peak pressure (GPa)			Particle velocities (km/s)		
	PSW	SSW	TSW	PSW	SSW	TSW
5	1.0	0.9	--	0.18	0.19	--
10	1.6	0.7	1.0	0.3	0.15	0.2
20	1.7	1.4	1.0	0.32	0.25	0.2
40	1.7	0.6	--	0.3	0.22	--

As observed in fig. 5.12 due to the propagation of the SW, the particles of the target set into motion and are accelerated to high velocities depending on the strength or pressure attained by the SW during the launch times. The acceleration is caused due to the high compression and release of the shock pressure acting on the volume. As observed in fig. 5.12 and fig. 5.13 multiple SWs were observed to emanate through the target hence, the particles behind these waves set into motion. In fig. 5.14 and fig. 5.15, the corresponding particle velocities across and behind the SWs are given.

The pressure of the PSW were found to be ~1, ~1.6, ~1.7 and ~1.7 GPa, respectively with increasing D. The pressure of the SSW launched at 8 ns, 7 ns, 9 ns and 13 ns, respectively is found to be ~0.9, ~0.7, ~1.4 and ~0.6 GPa. The SSW in the case of 5 μm is observed to increase slightly to ~1.1 GPa. The third shock wave (TSW) is observed only in the case of 10 and 20 μm with the pressure of ~1 GPa.

B) 175 mJ

Figure 5.15 (a-d) shows the comparison of PSW, SSW, third (TSW) and fourth (FSW) launching times and their propagation into Al target over the time scales from the first SW launch time to within the pulse duration (<15 ns) for the separations 5 μm, 10 μm, 20 μm, and 40 μm, respectively for the input laser energy 175 mJ.

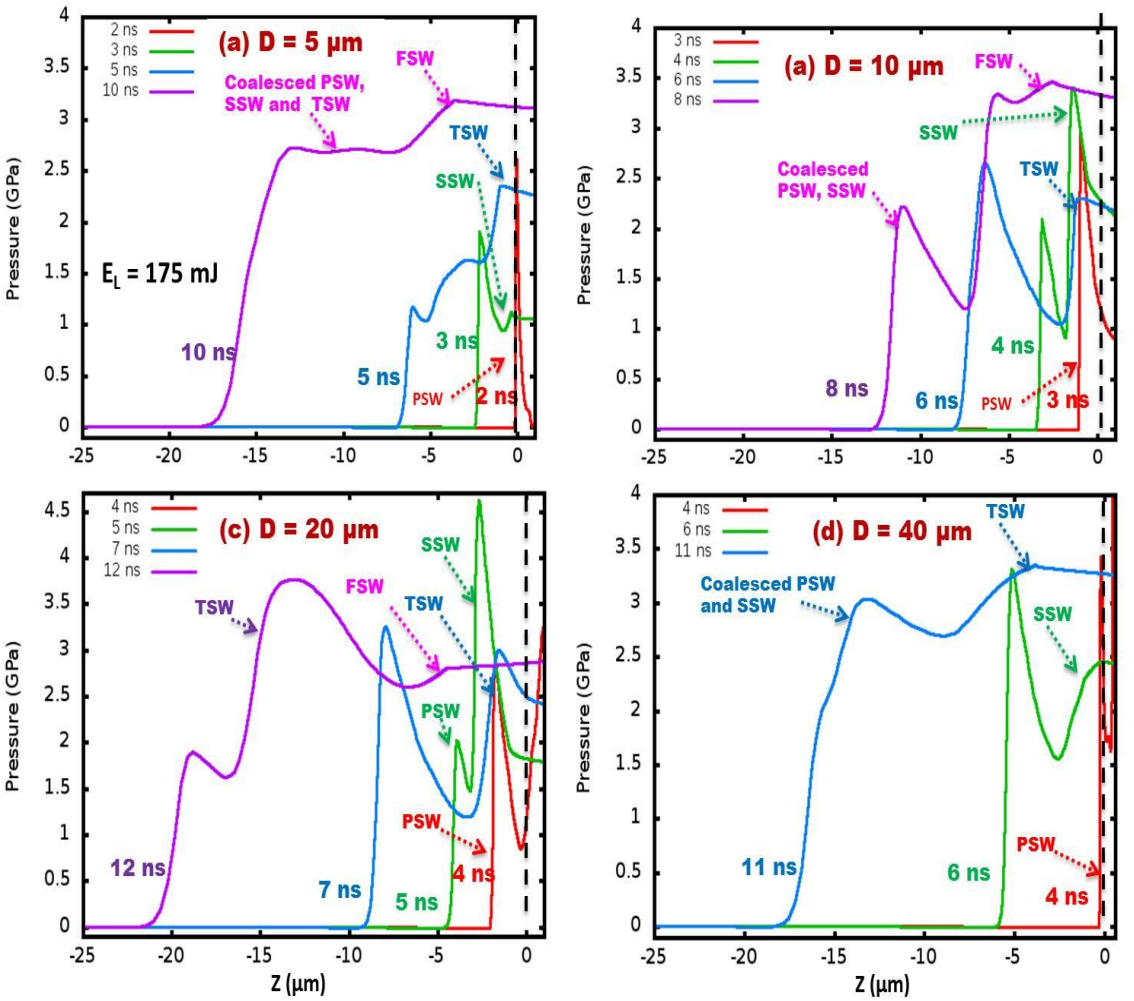

Figure 5.15 Comparison of spatial evolution of PSW, SSW and TSW pressures at 175 mJ with a) 5 μm, b) 10 μm, c) 20μm, and d) 40 μm.

In Figure 5.15 (a-d) the spatial pressure profiles of different SWs: PSW, SSW, TSW and FSW launched into Al target is given at their respective times. The corresponding peak pressures of these SWs are summarized in Table-5.3 for different Ds. In fig. 5.16 the spatial pressure profiles of these SWs emanating through the target is given for higher time scales, that is, from 15-40 ns.

At D=5 μm, the pressure waves were launched at 2 ns, 3 ns, 5 ns and 10 ns where the peak pressures are found to be ~2.6, ~1.2, ~2.4 and ~3.2 GPa, respectively. The PSW and SSW were coalesced at 7 ns (fig. 5.15 (a)) with the resultant peak pressure

reaching ~1.5 GPa. The resultant SSW and TSW were coalesced at 11 ns with the resultant peak pressure reaching ~2.4 GPa. Similarly, the resultant TSW and FSW were coalesced at around 20 - 25 ns (fig. 5.16 (a)) with the resultant peak pressure reaching ~3.2 GPa

At D=10 μm, the waves were launched at 3 ns, 4 ns, 6 ns and 8 ns where the peak pressures found to be ~3, ~3.5, ~2.25 and ~3.5 GPa, respectively. Apart from this another wave represented with fifth SW is observed at 11 ns with peak pressure of ~2.7 GPa. The PSW and SSW were coalesced at 6 ns (fig. 5.15 (b)) with the resultant peak pressure reaching ~2.6 GPa. Similarly, the TSW and FSW were coalesced at 11 ns with the resultant peak pressure reaching ~3.5 GPa. The resultant PSW and SSW and the resultant TSW and FSW were coalesced at 14 ns with the resultant peak pressure reaching ~3.4 GPa. This SW represented with FSW is again coalesced with the fifth SW at 30 ns (fig. 5.16 (b)) with the resultant pressure reaching ~3.2 GPa.

Table 5.3 Peak pressure and particle values of different SWs at the launch times for the input laser energy of 175 mJ.

D (μm)	Peak pressure (GPa)				Particle velocities (km/s)			
	PSW	SSW	TSW	FSW	PSW	SSW	TSW	FSW
5	2.6	1.2	2.4	3.2	0.45	0.2	0.4	0.5
10	3	3.5	2.25	3.5	0.4	0.55	1.2	0.55
20	3	4.5	3	2.8	0.45	0.7	0.5	0.45
40	3.5	2.5	3.2	--	0.55	0.4	0.53	--

At D=20 μm, the waves were simultaneously launched at 4, 5, 7 and 12 ns (fig. 5.15 (c)) where the peak pressures found to be ~3 , ~4.5, ~3 and ~2.8 GPa, respectively. The PSW and SSW were coalesced at 6 ns (fig. 5.15 (c)) with the resultant peak pressure reaching ~1.5 GPa. The resultant SSW and TSW were coalesced at 15 ns (fig.

5.16 (c)) with the resultant peak pressure reaching ~3.6 GPa. Similarly, the resultant TSW and FSW were coalesced at 30 ns (fig. 5.16 (c)) with the resultant peak pressure ~3.2 GPa.

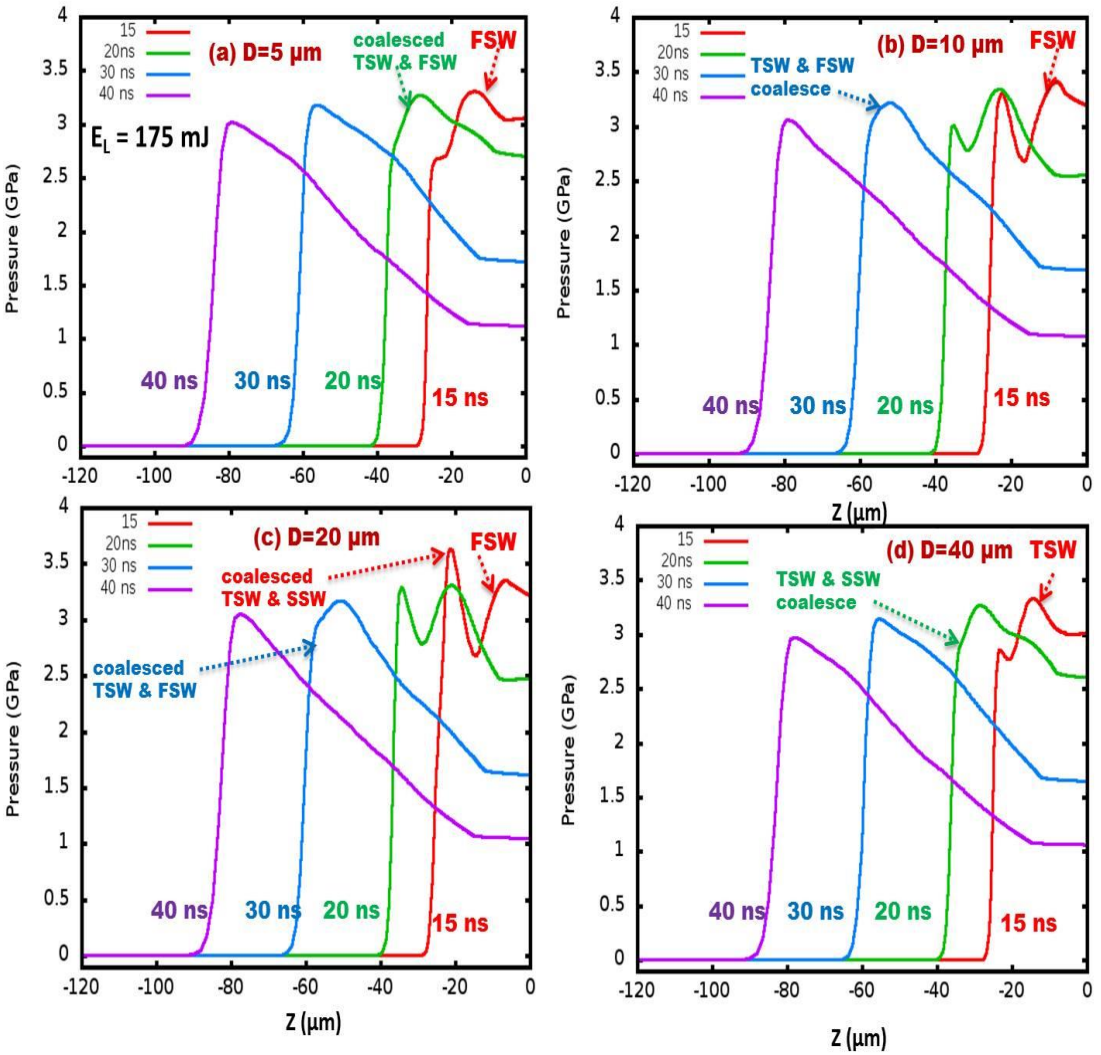

Figure 5.16 Comparison of spatial evolution of pressures of PSW, SSW, TSW and FSW and their coalescence times at 175 mJ with a) 5 µm b) 10 µm c) 20 µm and d) 40 µm, respectively over the time scales of 15 ns to 40 ns.

At D=40 µm, only PSW, SSW and TSW were observed and these were launched at 4 ns, 6 ns, and 11 ns (fig. 5.15 (d) with the peak pressures found to be ~3.5, ~2.5 and ~3.2 GPa, respectively. The PSW and SSW were coalesced at 11 ns with the resultant

peak pressure reaching ~3 GPa. The resultant SSW and TSW were coalesced at 20 ns (fig. 5.16 (d)) with the resultant peak pressure reaching ~3.3 GPa.

The coalesced pressure wave (fig. 5.16 (a-d)) at latter times attenuates gradually during its evolution for all the separations (D). Moreover, it is observed that the distance travelled (90 μm) and the peak pressure (~3 - 3.2 GPa) is found to be same for all D's at 40 ns. At higher all these different SWs: PSW, SSW, TSW and FSW ensure that a constant higher pressure compression wave is launched into Al. This leads to compressive residual stress of the material which is the main principle behind laser shock peening (LSP).

Over all it is observed that as the separation (D) increased, the strength of the PSW launched into the target also increased from 2.6 – 3.5 GPa. This is due to the fact that the initial plasma formed in air reaches the target surface at longer time scales with increasing D, so during this time the laser absorption increases such that the plasma strength also increases thus, the resulting PSW launched into the target also has the higher value. The peak pressure of the SSW at 5 μm, is small compared to that at 10 μm and 20 μm this is because the strength of the air plasma before interacting with Al is small due to very small absorption time of 2 ns. The reflected plasma into ambient air also has small strength and moreover it has to interact with the laser pulse where the FWHM time has not yet reached. Hence the ablation of this reflected plasma absorbs low energy resulting in the small pressure of the SSW. However, with separations 10 μm and 20 μm as the air plasma reflected at the times (5 ns) equal to that where the FWHM of the laser pulse has started (4 ns). Hence, the laser intensity increases resulting in higher absorption of the laser energy by the reflected plasma as discussed in the next section 5.6.2. As a result the sudden expansion takes place into air which creates high momentum in Al target. The TSW is launched between the times where FWHM (4 - 11ns) of the laser pulse exists. However, during this time the absorption front of the plasma in air expands more towards the laser propagation direction, hence the peak pressures launched will have pressures approximately to that of the PSW.

In fig. 5.17 the spatial profiles of the particle velocities, u_p across and behind the PSW, SSW, TSW and FSW are given at their launching times. The peak particle velocities at these times are summarized in Table 5.3.

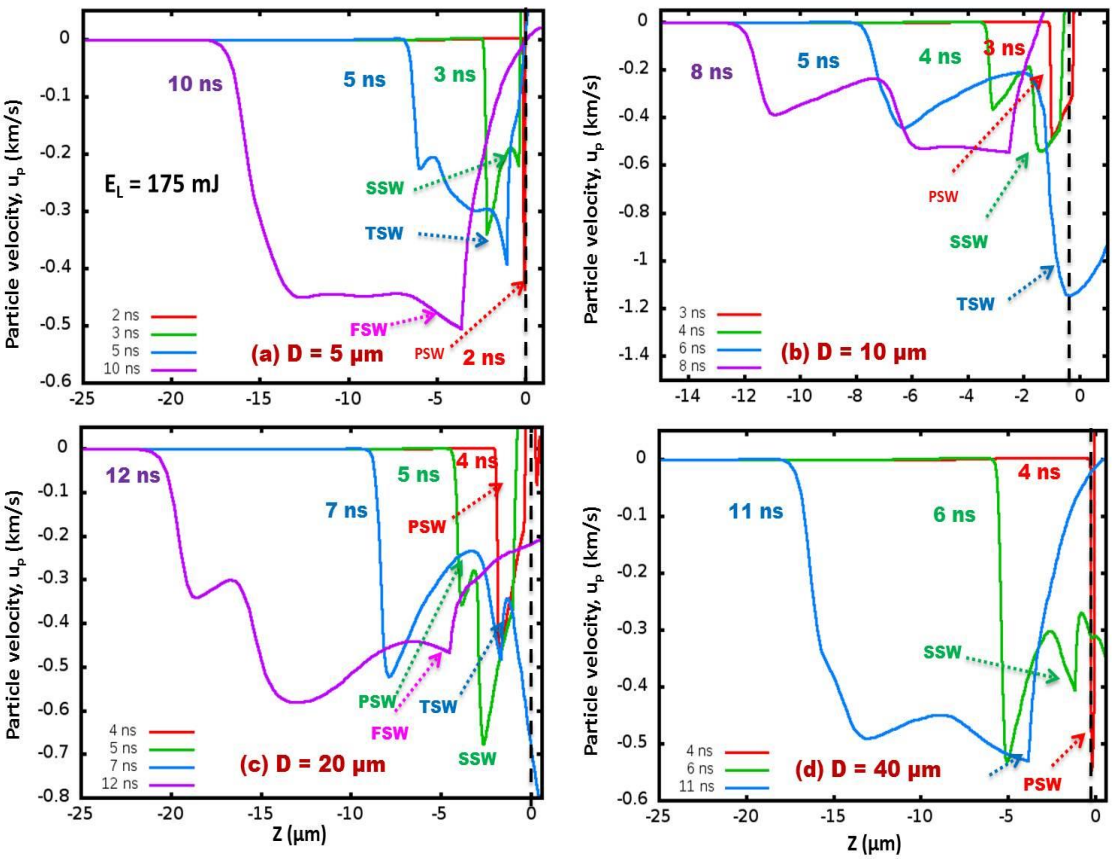

Figure 5.17 Comparison of spatial evolution of particle velocities across and behind the PSW, SSW, TSW and FSW launched at their respective times at 175 mJ with a) 5 μm b) 10 μm c) 20 μm and d) 40 μm, respectively.

In fig. 5.18 (a-d) the spatial evolution of particle velocities over the time scales of 15 ns to 40 ns are given for four separations, D. The velocities, u_p across these SWs at D=5 μm, these values were observed to be ~0.45, ~0.2, ~0.4 and ~0.5 km/s, respectively. At 10 μm, these were found to be ~0.4, ~0.55, ~1.2 and ~0.55 km/s, respectively. At 20 μm, these were found to be ~0.45, ~0.7, ~0.5 and ~0.45 km/s, respectively. Similarly, at 40 μm, only PSW, SSW and TSW were observed and its corresponding

values were found to be ~0.55, ~0.4, ~0.53 km/s, respectively. As observed from the Table-5.3, the particle velocities increase with increasing peak pressures of the SWs.

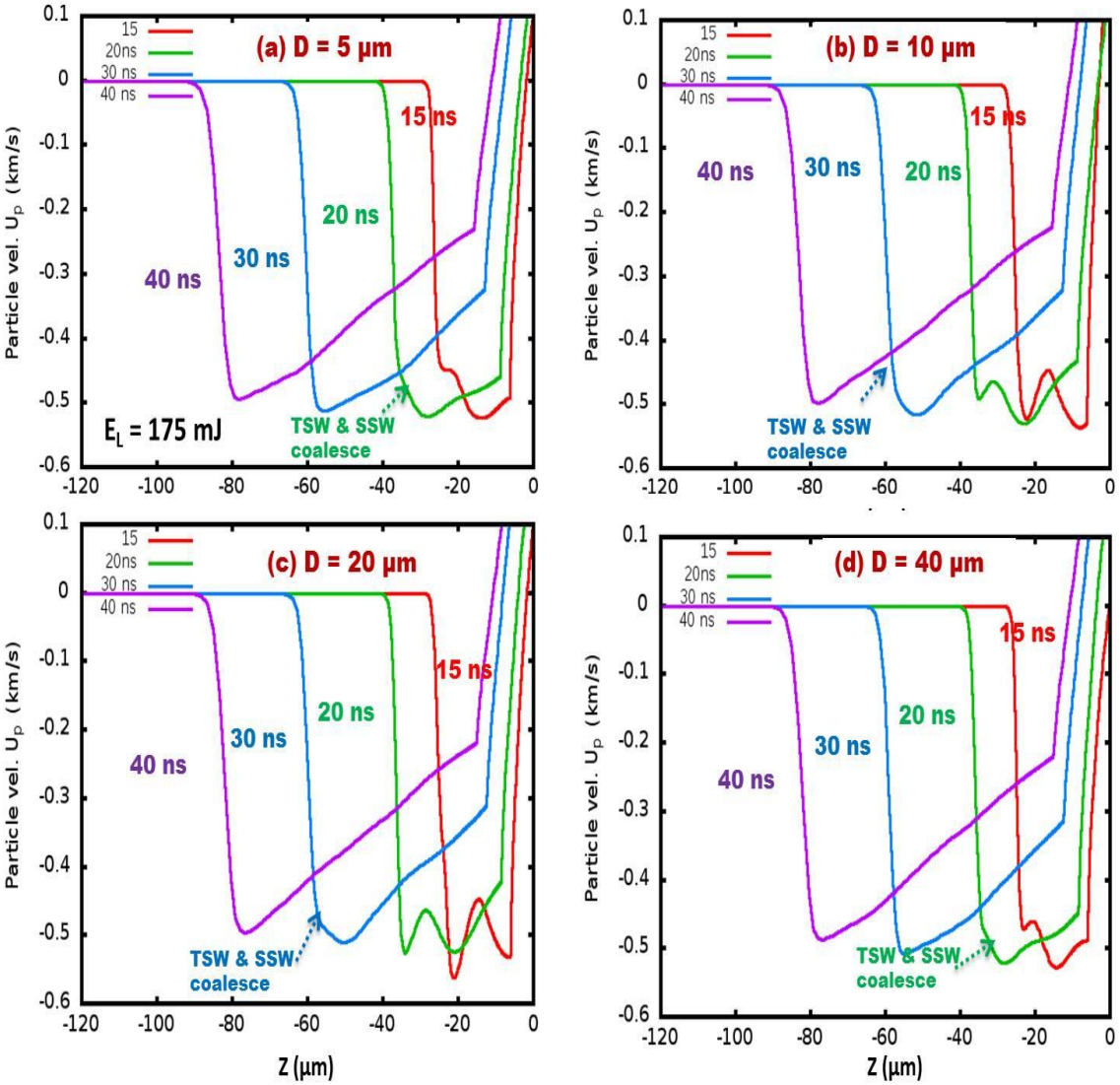

Figure 5.18 Comparison of spatial evolution of particle velocities across and behind PSW, SSW, TSW and FSW at their coalescence times at 175 mJ with a) 5 µm, b) 10 µm, c) 20 µm, and d) 40 µm, respectively over the time scales of 15 ns to 40 ns.

5.6.2 Origin of PSW, SSW, TSW, FSW and fifth SW

Figure 5.19 shows the interaction and reflection of air plasma with Al target and the ablation of the reflected plasma into ambient air for the input laser energy of 25 mJ at a separation 5 μm. The initial air plasma and Al interaction takes place at 5 ns. After the interaction in the reflected plasma there exists a deep valley close to the target surface whose spatial length found to be ~5 μm. Beyond this valley, air plasma which has not interacted with the target is seen mentioned as region-I.

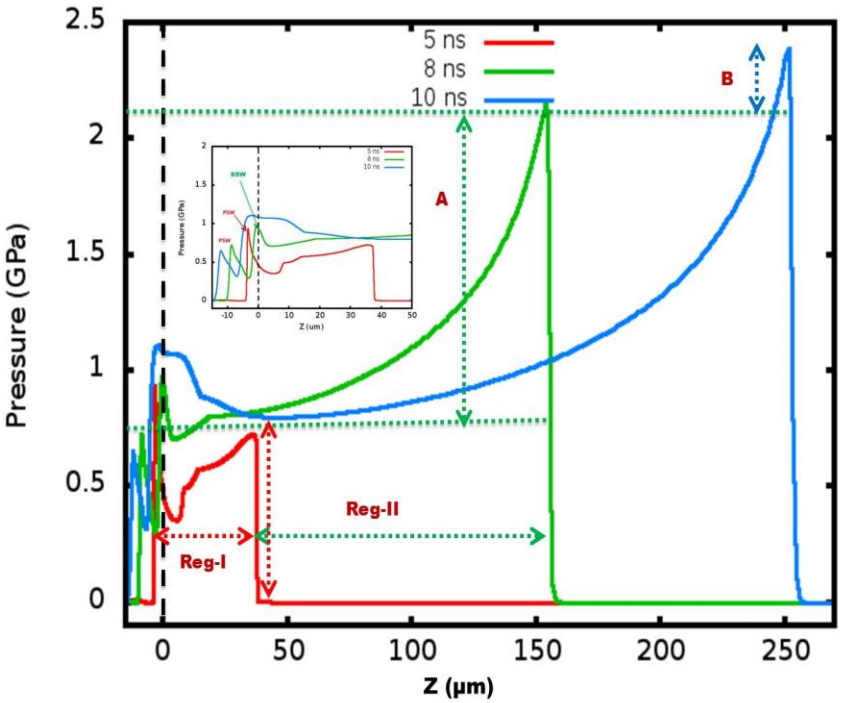

Figure 5.19 Illustration of the origin of the PSW, SSW and TSW launched into the Al target by the ablated plasma for 25 mJ input laser energy with 5 μm. Z=0 represents the air-Al interface.

The air plasma present in region-I absorbs most of the input laser energy due to the interaction of rising edge of the laser pulse. Due to the peak intensity of the laser pulse existing between 4 – 11 ns the absorption is very high in this region. This results in sudden expansion of the plasma into ambient air (region-II in figure) where the plasma has expanded from ~40 μm to ~150 μm and the peak pressure rises from 0.7 GPa to

2.1 GPa over the time scales of 5 ns to 8 ns. Due to this expansion, the momentum with which the plasma has expanded into air simultaneously acts on the target surface but in the opposite direction leading to launching of the SSW into the Al target as shown in the inset of fig. 5.19. The energy of the plasma close to the surface increases due to the absorption of the rest of the laser pulse, thus resulting in increase in the SSW pressure that is launched into the target during the laser air interaction.

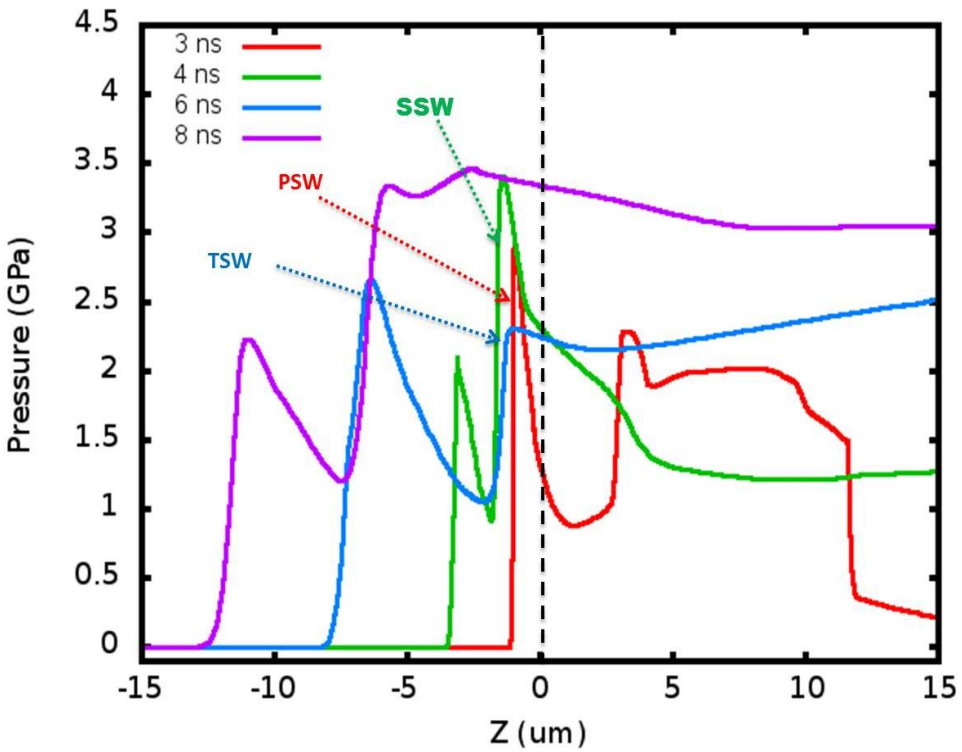

Figure 5.20 Illustration of the origin of the PSW, SSW and TSW launched into the Al target by the ablated plasma for 175 mJ input laser energy with 10 μm.

Figure 5.20 shows the plasma ablation dynamics in ambient air and SW launched by the ablated air plasma in Al target for the input laser energy of 175 mJ for a separation of 10 μm and shows the launching of the TSW into the target. As observed the PSW and SSW were launched at 3 ns and 4 ns, respectively. The TSW observed to be launched at 8 ns is due to the air plasma residing close to the target interacting with the Al target due to absorption of the laser energy. This plasma at later times also launches

the FSW and fifth SW after the termination of the laser pulse due to the pressure gradients existing in the ablated air plasma whose hydrodynamic motion predominantly moves towards the target surface.

5.7 Temporal evolution of the SW parameters into Al target

The ETR effects as explained in the previous chapter are considered on the propagation of SWs through Al. Figure 5.21 (a, b) shows the comparison of temporal evolution of specific energy with four separations is presented for the input energies 25 and 175 mJ, respectively. As observed with 25 mJ the first peak-1 corresponds to coalescence point of the PSW and SSW where the peak energies have reached to ~4.5 × 10^4 J/kg with 5 µm, ~7 × 10^4 J/kg with 10 µm, ~7.8 × 10^4 J/kg with 20 µm and ~7.5 × 10^4 J/kg with 40 µm. These values were observed to decrease with time and reaching values of ~3 × 10^4 J/kg at 20 ns with 5 µm, ~3.1 × 10^4 J/kg at 20 ns with 10 µm, ~3.5 × 10^4 J/kg at 13 ns with 20 µm. These values were observed to increase (represented with peak-2) again due to the coalescence of the PSW and SSW and reaching a value of ~4.5 × 10^4 J/kg with 5 µm, ~4 × 10^4 J/kg with 10 µm, ~4 × 10^4 J/kg with 20 µm. The second peak is not observed with 40 µm separation.

Table 5.4 specific energy, peak pressure, particle velocity and density values at their respective launch times with 25 mJ.

	Peak-1				Peak-2			
D (µm)	**E_{sp} × 10^4 (J/kg)**	**P (GPa)**	**u_p (km/s)**	**ρ (kg/m^3)**	**E_{sp}× 10^4 (J/kg)**	**P (GPa)**	**u_p (km/s)**	**ρ (kg/m^3)**
5	4.5	1.0	0.2	3	4.5	1.0	0.21	3.4
10	7	1.6	0.29	3.15	4.0	1.0	0.19	3.45
20	7.8	1.75	0.32	3.2	4.0	0.9	0.18	3.45
40	7.5	1.75	0.31	3.2	--	--	--	3.75

With 175 mJ the three peaks were observed, the first peak-1 correspond to the coalescence of the PSW and SSW, the second peak-2 correspond to the resultant SSW and TSW and third peak-3 correspond to the resultant TSW and FSW, respectively. As observed the peak-1 values with 5, 10, 20 and 40 μm were observed to be ~0.2 × 10^6, ~2 × 10^6, ~0.15 × 10^6, and ~0.3 × 10^6 J/kg, respectively. These values were observed to vary little at peak-1 and peak-2.

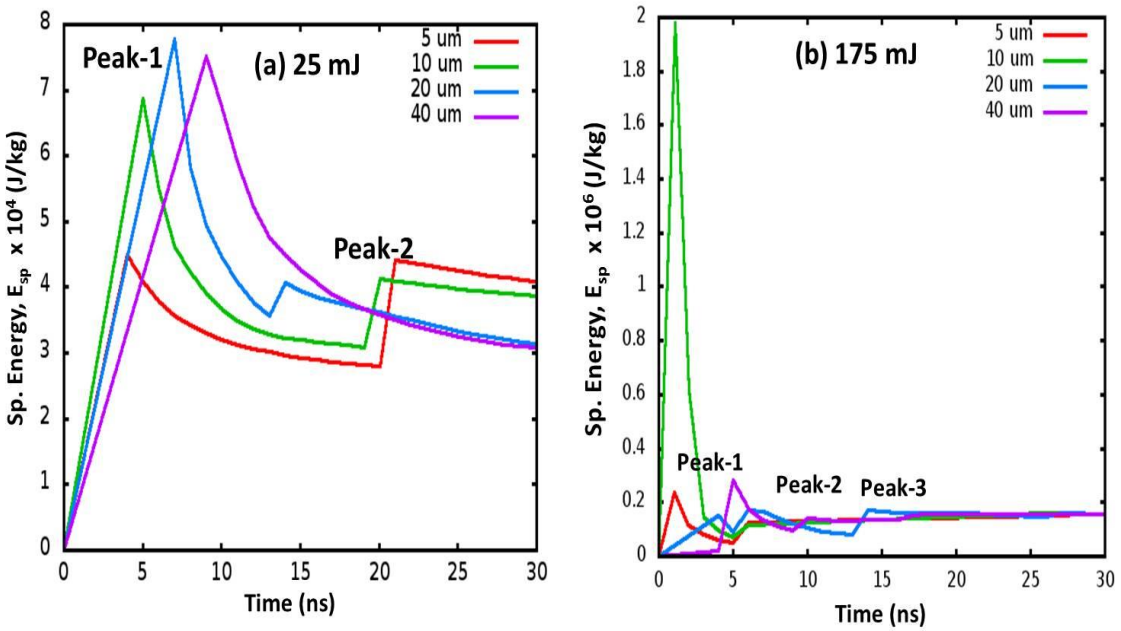

Figure 5.21 Comparison of the temporal evolution of the peak specific energy across the SWs over the time scales of upto 30 ns with 5 μm, 10, 20 and 40 μm for the input laser energies a) 25 mJ and b) 175 mJ, respectively.

Figure 5.22 (a, b) shows the comparison of temporal evolution of peak pressure with four separations is presented for the input energies 25 and 175 mJ, respectively. As observed with 25 mJ the first peak-1 corresponds to coalescence point of the PSW and SSW where the peak energies have reached to ~1 GPa with D=5 μm, ~1.6 GPa with D=10 μm, ~1.7 GPa with D=20 μm and ~1.7 GPa with D=40 μm. These values were observed to decrease with time and reaching values of ~0.5 GPa at 20 ns with 5 μm, ~0.6 GPa at 20 ns with 10 μm, ~0.8 GPa at 13 ns with 20 μm. These values were observed to increase (represented with peak-2) again due to the coalescence of the

PSW and SSW and reaching a value of ~1.0 GPa with 5 μm, ~1 GPa with 10 μm, ~0.9 GPa with 20 μm. The second peak is not observed with 40 μm separation.

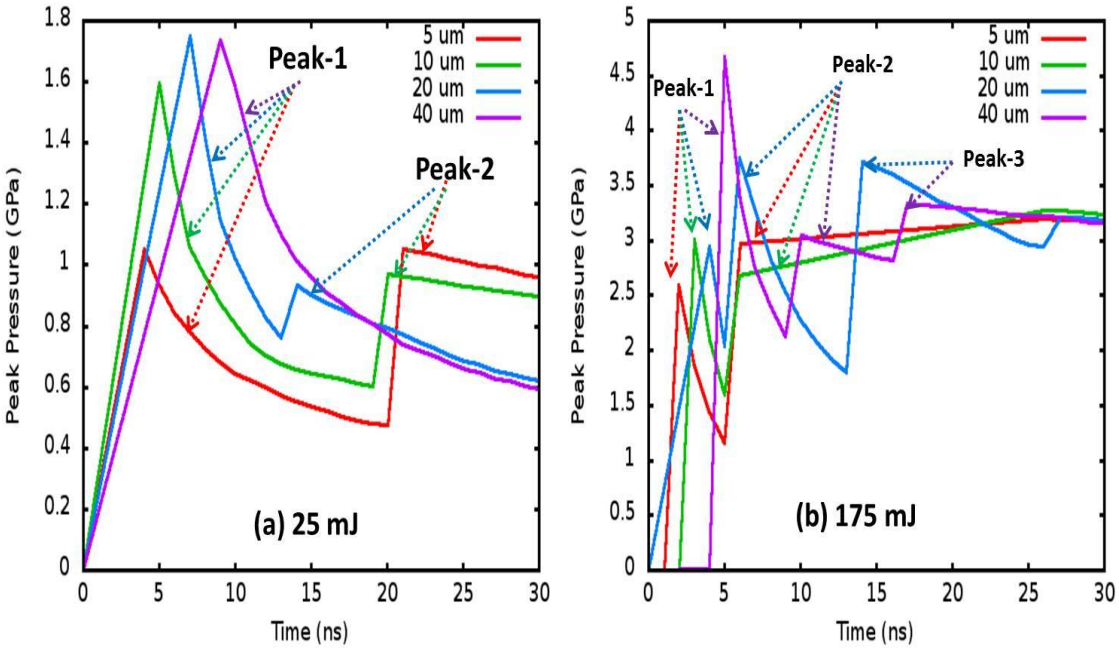

Figure 5.22 Comparison of the temporal evolution of the peak pressure across the SWs over the time scales of upto 30 ns with 5, 10, 20 and 40 μm for the input laser energies a) 25 mJ and b) 175 mJ, respectively.

With 175 mJ of input laser energy the three peaks were observed, the first peak-1 correspond to the coalescence of the PSW and SSW, the second peak-2 correspond to the resultant SSW and TSW and third peak-3 correspond to the resultant TSW and FSW, respectively. As observed the peak-1 values with 5 μm, 10 μm, 20 μm and 40 μm were observed to be ~2.5, ~3, ~2.8, and ~4.6 GPa, respectively. These values decreased to ~1.1 GPa at 5 ns, ~1.6 GPa at 5 ns, ~2 GPa at 5 ns, and ~2.1 GPa at 10 ns, respectively and again increased (represented with peak-2) to ~3, ~2.5, ~3.7 GPa at 6 ns with 5, 10, 20, respectively and ~3 GPa at 11 ns with 40 μm. The third peak-3 is observed be very small in the case of 5, 10 μm which is observed at around 25 ns similarly, with 20 and 40 μm this was observed at 15 ns and 18 ns with pressures ~3.5 and ~3.2 GPa, respectively.

Figure 5.23 (a, b) shows the comparison of temporal evolution of the particle velocity with four separations for the input energies 25 and 175 mJ. As observed with 25 mJ the first peak-1 corresponds to coalescence point of the PSW and SSW where the peak energies have reached to ~0.2 km/s with 5 μm, ~0.29 km/s with 10 μm, ~0.32 km/s with 20 μm and ~0.31 km/s with 40 μm. These values has decreased to ~0.1 km/s at 20 ns with 5 μm, ~0.17 km/s at 20 ns with 10 μm, ~0.14 km/s at 13 ns with 20 μm and again increased (represented with peak-2) due to the coalescence of the PSW and SSW to ~0.22 km/s with 5 μm, ~0.19 km/s with 10 μm, ~0.18 km/s with 20 μm. The second peak is not observed with 40 μm separation.

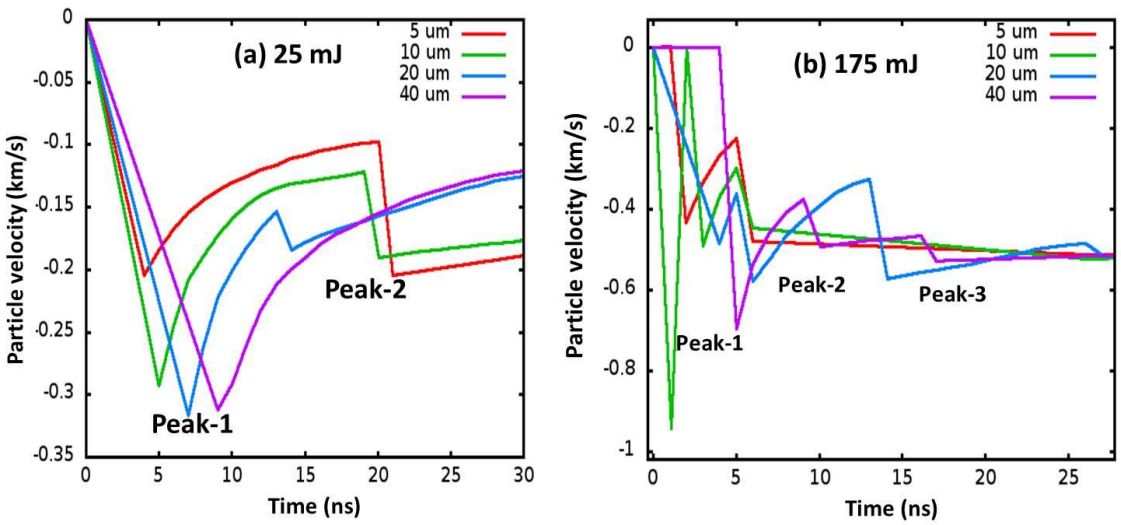

Figure 5.23 Comparison of the temporal evolution of the peak particle velocity across the SWs over the time scales of upto 30 ns with 5, 10, 20 and 40 μm for the input laser energies a) 25 mJ and b) 175 mJ, respectively.

With 175 mJ of input laser energy the three peaks were observed, the first peak-1 correspond to the coalescence of the PSW and SSW, the second peak-2 correspond to the resultant SSW and TSW and third peak-3 correspond to the resultant TSW and FSW, respectively. As observed the peak-1 values with 5, 10, 20 and 40 μm were observed to be ~0.42, ~0.9, ~0.45, and ~0.7 km/s, respectively. These values decreased to ~2, ~3, ~3.8, respectively at 5 ns with 5 , 10, 20 μm and ~4 km/s at 10 ns. At latter times these values were increased (represented with peak-2) to ~4.5, ~4,

~5.8 km/s at 6 ns with 5, 10, 20 μm, respectively and ~5 km/s at 11 ns with 40 μm. The third peak-3 is observed be very small with 5, 10 μm which exists around 25 ns, with 20 μm this is observed at 15 ns with velocity ~6 km/s similarly with 40 μm observed at 18 ns with ~5.5 km/s.

In figure 5.24 (a, b) the comparison of temporal evolution of the mass density with four separations is presented for the input energies 25 and 175 mJ. As observed with 25 mJ the first peak-1 corresponds to coalescence point of the PSW and SSW where the peak energies have reached to ~3 kg/m^3 with 5 μm, ~3.15 kg/m^3 with 10 μm, ~3.2 kg/m^3 with 20 μm and ~3.2 kg/m^3 with 40 μm. These values were decreased to ~2.85 kg/m^3 at 20 ns with 5 μm, ~2.9 kg/m^3 at 20 ns with 10 μm, ~2.95 kg/m^3 at 13 ns with 20 μm and again increased (represented with peak-2) due to the coalescence of the PSW and SSW to ~3.05 kg/m^3 with 5 μm, ~3 kg/m^3 with 10 μm, ~3 kg/m^3 with 20 μm. The second peak is not observed with 40 μm separation.

With 175 mJ the three peaks were observed, the first peak-1 correspond to the coalescence of the PSW and SSW, the second peak-2 correspond to the resultant SSW and TSW and third peak-3 correspond to the resultant TSW and FSW, respectively. As observed the peak-1 values with 5, 10, 20 and 40 μm were observed to be ~3.4, ~3.4, ~3.4, and ~3.75 kg/m^3, respectively. These values decreased to ~3.1, ~3.2 and ~3.3 at 5 ns with 5, 10, 20 μm, respectively and ~3.3 kg/m^3 at 10 ns with 40 μm. The mass density also increased (represented with peak-2) to ~3.4, ~3.4, ~3.6 kg/m^3 at 6 ns with 5, 10, 20 μm, respectively and ~3.4 kg/m^3 at 11 ns with 40 μm. The third peak-3 is observed be very small with 5 μm, 10 μm that is around 25 ns and with 20 μm at 15 ns with ~3.6 kg/m^3 similarly with 40 μm at 18 ns with ~3.5 kg/m^3.

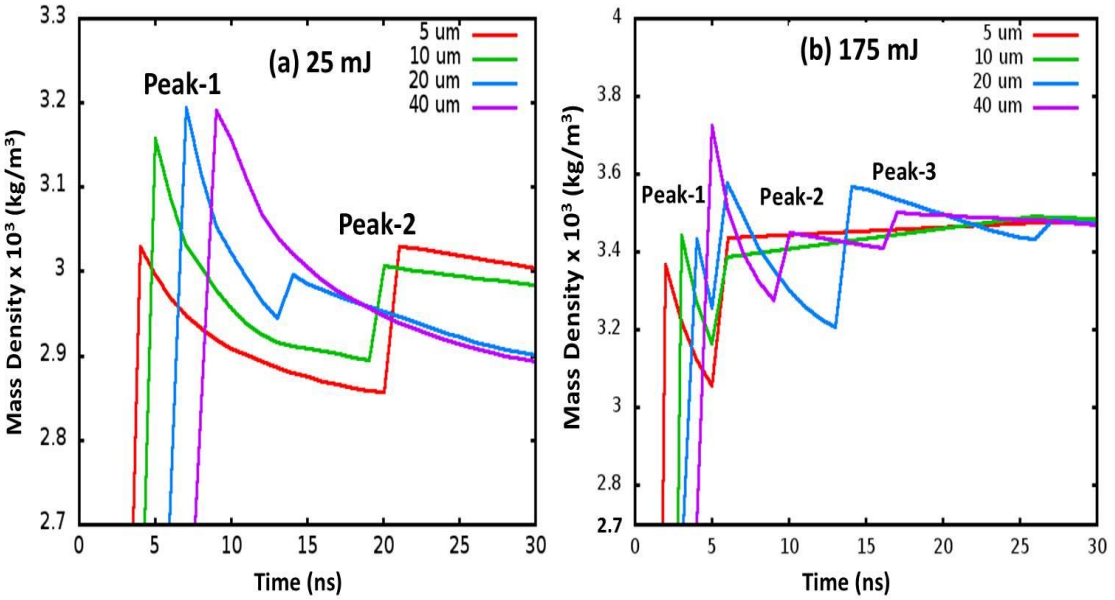

Figure 5.24 Comparison of the temporal evolution of peak mass density across the SWs over the time scales of upto 30 ns with 5, 10, 20 and 40 μm for the input laser energies a) 25 mJ and b) 175 mJ, respectively.

5.8 Summary

The laser induced plasma evolution in air is modelled with modified 1D-RHD code and the expansion dynamics is compared with 25 mJ and 175 mJ energies. The spatio-temporal evolution of the plasma variables such as the electron temperatures (T_e), electron number density (n_e), total specific energy (E_{sp}), total pressure (P) and mass density (ρ) are compared and observed that the peak values increasing with input laser energy. The asymmetric laser energy deposition is observed with 175 mJ laser energy. The sudden release of the deposited energy is expelled in the form of the SW that propagates through the ambient air with very high velocities. The expansion of the plasma and SW with both the energies is observed to be higher towards the laser propagation direction compared to that along the laser direction.

The laser induced air plasma dynamics interacting with the Al target placed in front of the expanding plasma along the laser direction are studied and compared with two input laser energies 25 mJ and 175 mJ with shifting focal plane whose separation (D)

from the Al target is varied from 5 - 40 μm. The laser induced plasma dynamics is observed to behave differently with the increasing separation resulting in the change in the peak variables of the plasma expanding in air is profound with 25 mJ than that of 175 mJ. The temporal evolution of peak plasma variables such as P, E_{sp}, ρ and n_e is compared with four different D for both the laser energies and observed that these variables decreased with increasing D for 25 mJ and found to be same with 175 mJ for all the separations. The coalescence of the SSW with the PSW expanding in ambient air is observed with both the energies and is found to occur around 25 - 30 ns with 25 mJ and between 65 - 75 ns with 175 mJ. The SSW is formed due to the reflection of the plasma at the Al surface.

Due to the variation in the plasma dynamics expanding in air different SW were observed to be launched into the Al target. It is observed that with 25 mJ three different SW named as PSW, SSW and TSW are launched into the target whose launching times were found to be different for four separations. Similarly, with 175 mJ a total of five different SWs named as PSW, SSW, TSW, FSW and fifth SW have launched into the target whose launching times also were found to be different for four separations. The total pressures, particle velocities, total specific energy and mass density of these SW were found to vary with D and the input laser energy used. Moreover, these values were found to be higher in the case of 175 mJ compared to 25 mJ. The PSW, SSW and SSW, TSW and TSW, FSW and FSW with fifth SW were observed to coalesce during the evolution and all were coalesced between the first PSW launched times to the 40 ns. After 40 ns only a single SW is observed to propagate through the Al target. During the coalescing times an increase in the peak variables is observed. The PSW is launched due to the first interaction of the air plasma with the Al target, the second SW is launched due to the opposite momentum created by reflected plasma due to the absorption of the laser energy, the other SW were launched due to the hydrodynamics instabilities occurring in the reflected air plasma expanding in ambient air.

References

[1]R. M. More, in *Advances in Atomic and Molecular Physics*, edited by D. R. Bates and B. Benjamin (Academic Press, 1985), Vol. Volume 21, pp. 305-356.
[2]S. Atzeni and J. Meyer-ter-Vehn, *The Physics of Inertial Fusion: BeamPlasma Interaction, Hydrodynamics, Hot Dense Matter*. (OUP Oxford, 2004).
[3]R. Ramis, K. Eidmann, J. Meyer-ter-Vehn and S. Hüller, Computer Physics Communications **183** (3), 637-655 (2012).
[4]R. M. More, K. H. Warren, D. A. Young and G. B. Zimmerman, Physics of Fluids **31** (10), 3059-3078 (1988).
[5]E. Mínguez, P. Martel, J. M. Gil, J. G. Rubiano and R. Rodríguez, Fusion Engineering and Design **60** (1), 17-25 (2002).
[6]A. Benuzzi-Mounaix, M. Koenig, A. Ravasio, T. Vinci, N. Ozaki, M. R. l. Gloahec, B. Loupias, G. Huser, E. Henry, S. Bouquet, C. Michaut, D. Hicks, A. MacKinnon, P. Patel, H. S. Park, S. L. Pape, T. Boehly, M. Borghesi, C. Cecchetti, M. Notley, R. Clark, S. Bandyopadhyay, S. Atzeni, A. Schiavi, Y. Aglitskiy, A. Faenov, T. Pikuz, D. Batani, R. Dezulian and K. Tanaka, Plasma Physics and Controlled Fusion **48** (12B), B347 (2006).
[7]D. Batani, H. Stabile, A. Ravasio, G. Lucchini, F. Strati, T. Desai, J. Ullschmied, E. Krousky, J. Skala, L. Juha, B. Kralikova, M. Pfeifer, C. Kadlec, T. Mocek, A. Präg, H. Nishimura and Y. Ochi, Physical Review E **68** (6), 067403 (2003).
[8]D. Batani, A. Balducci, D. Beretta, A. Bernardinello, T. Löwer, M. Koenig, A. Benuzzi, B. Faral and T. Hall, Physical Review B **61** (14), 9287-9294 (2000).
[9]B. K. Godwal, S. K. Sikka and R. Chidambaram, Physics Reports **102** (3), 121-197 (1983).
[10]H. C. Pant, M. Shukla, V. K. Senecha, S. Bandyopadhyay, V. N. Rai, P. Khare, R. K. Bhat, B. K. Godwal and N. K. Gupta, CURRENT SCIENCE **82** (2), 149-157 (2002).
[11]P. W. Cooper, *Explosives engineering*. (Wiley-VCH, 1996).
[12]S. Soubacq, P. Pignolet, E. Schall and J. Batina, Journal of Physics D: Applied Physics **37** (19), 2686 (2004).

Chapter 6

Numerical Investigation of Laser Induced Shock Waves (LISW) from air using 2D-radiation hydrodynamic code

A two dimensional (2D) axis symmetric hydrodynamic model was developed to investigate the generation of laser induced plasma and shock wave dynamics in ambient air. The simulations have been performed using laser absorption models viz., inverse Bremsstrahlung (IB), and photoionization (PI) and with two equations of states (EOS) viz., ideal gas and chemical equilibrium applications (CEA) (EOS). The shock wave (SW) generated by ns Nd:YAG laser whose velocities measured experimentally from the shadowgraphy technique over the time scales of 0.4 – 8 μs for the intensities ranging between 2.3×10^{10} to 1.8×10^{11} W/cm^2 was compared with that of numerical models. The plasma features like the initial tear drop shape and the subsequent expansion into the spherical shape, rolling and splitting of the internal plasma, shock wave detachment from the plasma observed experimentally was reproduced with the numerical simulations. The temporal evolution of electron number density, temperature and specific internal energy obtained in the hot core plasma and across the shock front (SF) over the time scales 0.2 - 8 μs were presented. The measured number density, temperatures, and specific energies in the plasma region were observed to decay from 12×10^{19} - 2×10^{19} (cm^{-3}), 14×10^4 - 0.6×10^4 (K), and 1×10^8 - 5×10^6 (J/kg), respectively over 0.2 - 8 μs of time. Similarly, the temperatures carried by the SF after the detachment from the plasma was observed to decay from 3500 - 400 (K) over the same time scales. The compared numerical results show that the velocities along the laser direction found to be reasonably matching with that observed experimentally.

6.1 Introduction

The optical breakdown in gases initiated by intense pulsed lasers has gained many practical applications in different areas over the past few decades like laser-spark ignition of fuel-air mixtures[1, 2], laser propulsion of systems[3] for wave drag reduction in a vehicle, localized flow control of blunt bodies[4], laser thrusters[3], laser triggering of switches[5] and Laser induced breakdown spectroscopy (LIBS)[6] to name a few.

Laser-spark in gases was first reported by Meyerland et al.[7] in 1963 as soon as lasers became available. The initial studies focused mainly on understanding the breakdown phenomenon occurring during the laser interaction[7, 8]. These studies showed that the breakdown phenomenon involves different physical mechanisms such as multiphoton ionization (MPI), cascade ionization by the process of inverse-Bremsstrahlung (IB) due to electron-ion and electron-neutral interactions. The electron generation during these processes was observed to be dependent on various laser parameters[9] such as wavelength, beam size and pulse duration[10]. Claudio[11] reviewed the role of different absorption mechanisms and their dependence on ambient pressure, laser frequencies, energy loss due to diffusion of electrons. Ireland et al.[8] investigated the role of pressure on the breakdown phenomena in Argon and He gases and observed that MPI was dominant mechanism at low pressure regimes and cascade ionization was dominant at high pressures. Gamal et al.[12] investigated the same in Ar, He, N_2 gases considering different wavelengths (694.3 nm, 1064 nm, 532 nm) over the pressure range of 1-10^5 Torr. Young et al.[13] investigated the electron generation in rare gases by considering different loss mechanisms such as diffusion of electrons, recombination and attributed that diffusion contributes to the breakdown in the lighter gases (He, Neon) and recombination contributes in the heavier gases (Argon and Krypton). The breakdown threshold intensity studies in air is performed by Thareja et al.[14] at different background pressure conditions, spot size, and pulse widths using various wavelengths (1064, 532, 355 and 266 nm). It was found that the threshold intensity varies with the wavelength and focal spot size. Simeonsson et al.[15] studied the breakdown thresholds

of air at different wavelengths (1064, 532, 355, 266 and 193 nm) and reported the electron density and plasma temperature ranges measured from the time-resolved emission spectroscopy. Breitling et al.[16] observed that IB to be the dominant absorption mechanism that is responsible for the growth of electrons and breakdown. It is found that the minimum intensity required to optical breakdown of ambient air is of the order of 10^{10} W/cm^2. Breitling investigated the dependence of laser energy absorption on laser wavelengths (532 and 1064 nm). Schwarz et al.[17] investigated the optical breakdown thresholds of air at 1 atm pressure with 532 and 1064 nm wavelengths. The studies were made to improve laser ignition system for internal combustion engines. Magesh et al.[18] investigated the laser induced plasma density and temperature in air over pressure ranges of 1.3×10^{-3} – 5 atm using the UV laser radiation. Various groups[1, 19-32] have performed the studies on the laser induced plasma and shock wave (SW) dynamics in ambient air over the time scales of initial laser interaction up to few milliseconds. These studies gave the spatio-temporal expansion of the plasma, and its structures at different times, plasma relaxation, SW generation from the plasma and its expansion into various ambient atmospheric gas pressures. Though, many physical processes observed from the experiments but a complete understanding of such processes has been one of the challenging tasks. Radiation hydrodynamics (RHD) has gained considerable interest in modelling the essential features of laser produced plasma and its associated processes. The numerical simulation using RHD enables better understanding of the complex phenomenon occur during and after the termination of laser pulse of up to few microseconds of time scales. Hence in the present chapter, the 2D-RHD was used to model the laser induced air plasma and the SW propagation through ambient air.

When a nanosecond pulsed laser is focused into gases, the breakdown of the gas takes place leading to the formation of plasma. The created plasma will strongly absorb the incoming laser energy due to the presence of large number of free electrons. During the incident laser absorption the shielding of the incoming laser beam occurs at

the plasma front resulting in the expansion favouring towards the focusing lens leading to the asymmetric expansion of the plasma[33, 34]. During the laser-plasma interaction the temperature and pressure of the gas increases abruptly and the plasma expands supersonically in to the background atmosphere. This expanding plasma launches a shock wave (SW) in to the ambient gas by highly compressing the background gas.

The electrons generated during the ns laser interaction involve different physical mechanisms[8, 11, 12, 33]. It is observed that the electrons in the focal volume are generated in two different stages. In the first stage, the primary or free electrons that are already present due to impurities in the gas and in the second stage by the collision of high kinetic energy primary electrons with the neutral or excited atoms. In this process, the electrons after gaining sufficient energy from the incoming photons collide with the neutral atoms or ions to generate the secondary electrons. The process of knocking out the electrons by three-body (photon-electron-atom or photon-electron-ion) combination is called the IB absorption. The cascade growth of the secondary electrons leads to the avalanche of electrons resulting in the breakdown of the medium. The photoionization (PI) process also plays a role in the generation of the secondary electrons[33] where these affects are dominant at moderate temperatures. In the PI process, the electrons are knocked out from the excited atoms by a single photon whose energy is higher than the lowest ionization potential of the excited atom. After the breakdown, the material starts absorbing most of the laser energy due to large number of free electrons present in its vicinity. Due to high laser energy absorption, the thermodynamic variables of the plasma such as, the temperature (T), specific internal energy (E_{sp}) and pressure (P) will reach as high as few orders of magnitude greater than the ambient atmosphere[5]. The absorption continues until the laser pulse terminates. Once the laser terminates, due to very large pressure gradients present at the interface between the plasma and the surrounding air, the plasma expands with supersonic speed into the surrounding gas[35] by releasing the absorbed energy. This sudden expansion, launces the SW into the surrounding gas whose pressures ranges

from few MPa – GPa depending on the input laser intensity and ambient gas conditions[29].

Numerous papers on numerical modeling have been presented to support the experimental results. The laser induced breakdown of gases and the SW evolution is understood from the hydrodynamic simulations[4, 5, 36-39]. The simulations enabled to understand the underlying physics of different physical processes observed experimentally. Owing to the complexity of the problem the simulations have been carried out in two different ways. Firstly, starting from the initial laser-induced breakdown to a few microseconds[5, 38, 40] which covers the formation, expansion of the plasma and SW. Secondly starting from the post-laser interaction dynamics[4, 39] where the laser effects are discarded. In the former case, the complexity of the problem increases due to implication of laser energy deposition term and moreover the simulations have to handle large pressure, temperature and specific energy gradients that require fine meshing of the cells to cut down the numerical instabilities. In the latter case, the problem of solving the hydrodynamics is relatively simple as the laser deposition term is neglected by considering the fraction of energy absorbed within the focal volume and the initial conditions of P, T and E_{sp} taken from the experiments[4, 36, 39].

The contribution from both the experiments and simulations has led to understand most of the plasma and SW features produced due to the nanosecond laser interaction, but still there exists few gaps that need to be worked out to bridge in a better way for clear and complete understanding of the whole system. Moreover, most of the studies have been performed on inert gases that are simple and easy to analyze because of single molecular gas. For the gases like quiescent air which is composed of mixture of different molecular gases such as nitrogen (78 %), oxygen (21 %) and others (1 %) makes the system very complex to understand.

In this chapter, we present the numerically simulated laser induced plasma and SW dynamics with different models and compare them with the experimental

observations[23, 24] over the intensity range of 2.3×10^{10} to 1.8×10^{11} W/cm^2. The simulations were performed from the initial laser interaction, that is, 0 ns - 8 μs covering the plasma formation and SW evolution. The behavior of the internal plasma core dynamics (roll-off, plasma splitting) and the plasma relaxation process is investigated. This study is performed by comparing density and temperature contours of simulations with the shadowgrams over the time scales of 0.2 – 8 μs. Apart from this, the temporal evolution of maximum plasma temperature and the corresponding electron number density is presented. The temperature that is carried by the shock front (SF) during its temporal evolution is presented in the context of the laser-spark ignition of gases. Finally, experimentally obtained SW velocities (along and opposite to laser propagation direction) were compared with the simulated results using three different models.

6.2 Experimental Details

The experimental setup used to generate the LISW in quiescent air is described elsewhere[23, 24] where the second harmonic of Q-switched Nd:YAG laser operating at a wavelength of 532 nm with ~7 ns (FWHM) pulse duration is used to create the breakdown of air. The beam was focused using a plano-convex lens in f/10 focusing geometry for the laser energies ranging from 25 mJ – 200 mJ. A focal spot diameter of 140±10 μm was achieved that generated the intensities in the range 2.3×10^{10} - 1.8×10^{11} W/cm^2. The spatio-temporal evolution of SW was captured using the shadowgraphy technique[23, 24].

6.3 Simulation Methodology

6.3.1 Governing equations

The equation of continuity, momentum and energy given by eq. (6.1) – (6.3) are used to numerically simulate the laser absorption process and the subsequent evolution of plasma and SW into ambient air.

$$\frac{\partial \rho}{\partial t} = -\nabla.(\rho \mathbf{u}), \tag{6.1}$$

$$\frac{\partial (\rho \mathbf{u})}{\partial t} = -\nabla.(\rho \mathbf{u}\mathbf{u}) - \nabla P, \tag{6.2}$$

$$\frac{\partial \rho (e+\frac{1}{2}\mathbf{u^2})}{\partial t} = -\nabla.\mathbf{u}\left(\rho e + \frac{1}{2}\rho \mathbf{u^2} + \mathbf{P}\right) - K_{th}\nabla T + k_{abs} I_L \tag{6.3}$$

Here, the variables ρ, u, P, e and T correspond to the mass density, fluid velocity, total pressure, internal energy and temperatures respectively of the gas. K_{th} accounts for the heat conduction coefficient due to electrons and ions (e-i) given by the Spitzer-Harm[41, 42], I_L is the laser intensity having Gaussian profile in spatial and temporal variation. The absorption coefficients and the EOS used in the simulations are given in detail in Model-1, 2 and 3, respectively. k_{abs} is the total laser absorption coefficient simulated using three different models. Model-1 considers absorption by PI and IB due to electron-ion (e-i) collisions given by Zel'dovich et al.[33], Model-2 and 3 consider absorption by IB due to e-i and electron-neutral. The ionization number or charge state number of the gas is obtained by the method proposed by Atzeni et al.[43]. The radiation losses from the air plasma is observed to be small and its influence on the plasma and SW evolution is found to be upto shorter time scales (discussed in Chapter-2) hence, these affects have been neglected.

The system of equations (6.1) – (6.3) is numerically solved using two-dimensional axisymmetric Eulerian radiation hydrodynamic code developed Sijoy et al.[44-47], the numerical technique and the laser deposition process is discussed elsewhere.[44, 47] These equations are closed by considering separately two different equations of states (EOS): ideal gas with ionization effects taken into account[33] and CEA[48]. Using the combination of two EOS and two absorption coefficients, three different models have been used to perform the simulations.

6.2.2 Details of the models used

Model-1: This model takes into consideration the photoionization[33] (PI) (eq. 6.4) and IB[33] (eq. 6.5) absorption coefficients due to electron-ion (e-i) to absorb the incident laser energy in the focal volume

$$k_{PI}(cm^{-1}) = \frac{64\pi^4}{3\sqrt{3}} \frac{q^{10} m_e N Z_i^4}{h^6 c \vartheta^3} \left(\frac{e^{-x_1}}{2x_1}\right)(e^x - 1), \tag{6.4}$$

$$k_{IB_{e-i}}(cm^{-1}) = \frac{64\pi^4}{3\sqrt{3}} \frac{q^{10} m_e N Z_i^4}{h^6 c \vartheta^3} \left(\frac{e^{-x_1}}{2x_1}\right), \tag{6.5}$$

The total absorption coefficient after combining eq. (6.4) and (6.5) becomes,

$$k\ (cm^{-1}) = k_{PI} + k_{IB_{e-i}} = 0.96 \times 10^{-7} \frac{N Z_i^2}{T^2} \frac{e^{\frac{-I_p - h\vartheta}{k_b T}}}{x^3}, \tag{6.6}$$

where $x = \frac{h\vartheta}{k_b T}$, $x_1 = \frac{I_p}{k_b T}$, q - the electro-static charge of the electron, m_e - the electron mass, h - planck constant, c - the speed of light, ϑ - laser frequency, N- total number density (cm^{-3}), Z_i - ionization or charge state number, I_p - the ionization potential in eV of the gas taken to be equivalent to oxygen gas, T - the gas temperature in K, k_b - the Boltzmann constant and n_e is the electron number density (cm^{-3}).

The ideal gas EOS with ionization effects taken into account[33] (eq. 6.6)) is used to close the eqs. (6.1) – (6.3)

$$P = N(1 + Z_i)k_b \mathrm{T}, \tag{6.7}$$

Model-2: In this model, the IB due to e-i and electron-neutral (e-n) absorption coefficient[11] is used for the laser absorption in the focal volume which takes the form

$$k_{IB_{e-i,e-n}}\ (cm^{-1}) = \frac{4}{3} \left(\frac{2\pi}{3}\right)^{\frac{1}{2}} \frac{n_e n_i {Z_i}^2 e^6}{(m_e k_b T)^{\frac{3}{2}} c \vartheta^2} \tag{6.8}$$

The equation after inserting the numerical values becomes

$$k_{IB_{e-i,e-n}} = 1.995 \times 10^{-5} \frac{n_e n_i Z_i^2 \lambda^2}{T^{\frac{3}{2}}}, \quad (6.9)$$

where n_e, n_i - the electron and ion number densities in (cm^{-3}), respectively, λ – laser wavelength.

Model-3: In this model, eq. 6.8 is used for laser absorption and Chemical Equilibrium and Applications[48] (CEA)EOS is used to close the equations. This EOS is generated using CEA code developed by NASA where the ionization and concentration of each species is obtained with respect to the associated temperatures. The pressure of the individual species is obtained from the corresponding rotational, vibrational and electronic states of the molecule. The species concentration is calculated from the temperature and number density of molecules. Based on the temperature and mass density the partial pressure corresponding to each species is calculated from the weight factors. Finally the total pressure of the gas is calculated from the summed partial pressures of each species

$$P = \sum_{i=1}^{N} n_i \mathrm{R} T \rho, \quad (6.10)$$

In all the above models, the charge or ionization state (Z_i) of the gas is evaluated by the method proposed by Atzeni et al.[43]

Table 6.1 Summary of the models utilized in this chapter.

Model	Laser Absorption Coefficients (k_{abs})	EOS
1	PI & IB due to e-i	Ideal charge state
2	IB due to e-i, e-n	Ideal charge state
3	IB due to e-i, e-n	CEA

6.3.3 Methodology for Laser Energy Deposition

Figure 6.1 (a) illustrates the laser energy deposition across the symmetric axis along the laser axis (Z) in the computational domain (R, Z) plane.

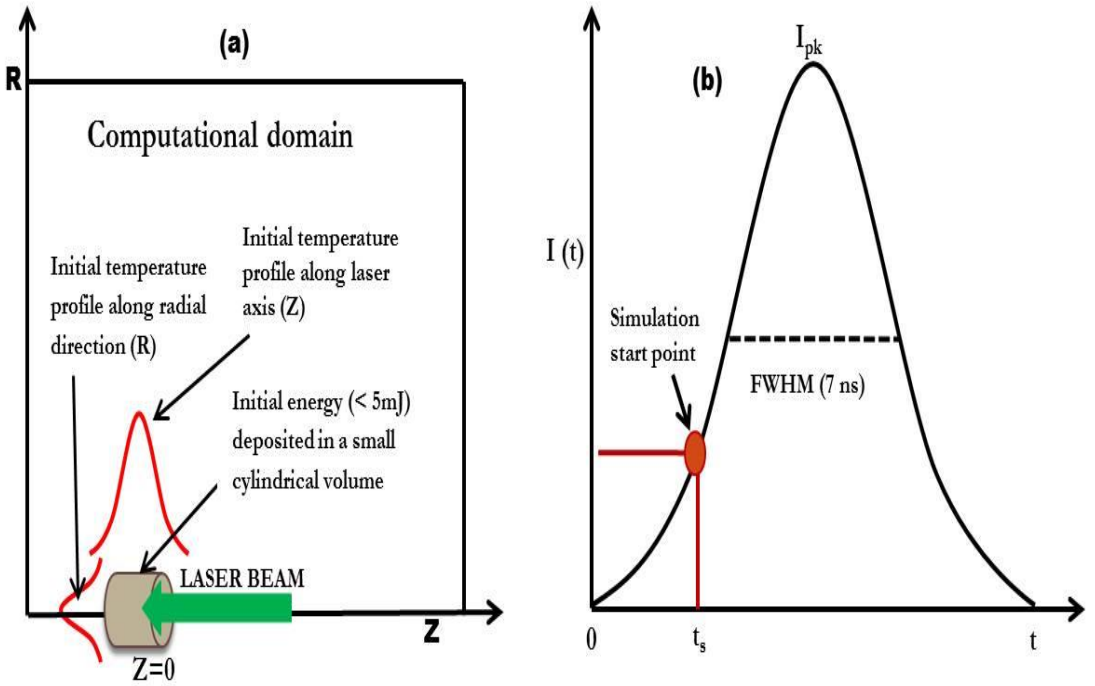

Figure 6.1 Illustration of a) initial laser energy deposition in a cylindrical volume with Gaussian temperature along laser (Z) and radial (R) axis within a computational domain, b) simulation start point within the total pulse duration, τ.

The laser energy deposition within the focal volume of the laser beam is performed by the ray tracing method given by Sijoy et al.[45, 47]. In the code, the routine for laser focusing is not implemented. So initially to start, the Gaussian temperature profile along (R, Z) with peak temperatures ranging from 15000-20000 K is considered in the cylindrical volume. This allows creating seed electrons inside the cylindrical volume resulting in the absorption of the laser energy. This is taken from the breakdown threshold value of 5 mJ/pulse from experiments[23, 24]. The total energy corresponding to these temperatures within the volume is estimated to be < 5 mJ depending on the dimensions and temperatures considered. The dimensions of the cylindrical volume

were taken in the range 70 - 500 μm that is well with the range of the spot diameter and Rayleigh range used in the experiments. Due to the presence of electron number density gradient across the volume and surrounding air interface, the energy deposition takes at this particular point. The initial free electrons act as the initiators for the growth of secondary electrons by absorbing the laser energy during the laser interaction. The minimum energy deposited initially that is, <5 mJ in the focal volume is excluded from the total laser pulse energy.

Fig. 6.1 (b) shows the temporal profile of the laser intensity, I(t) within the total time or pulse duration, τ. The time, t_s is the point where, the laser energy becomes equivalent to the initial energy deposited in the volume. Beyond this time, the laser energy absorption takes place. Hence, the contribution of the laser energy deposition before time, t_s is excluded in the simulations.

6.4 Comparison of Experimental and Numerical Results

6.4.1 Absorption percentage comparison

Figure 6.2 compares the absorption percentages obtained experimentally with the simulation results. In Model-1, the laser absorption coefficient $k \propto Z_i^2 \lambda^3 T$. Similarly, in Model-2 and 3, $k \propto Z_i^2 \lambda^2 T^{-3/2}$. This shows that k always have higher values with Model-1 compared to that of Model-2 and 3. At 50 mJ, the simulated absorptions were found to have lower values (around 35 - 42 %) with all the three models whereas the experimental value is observed to be higher (around 60 %). At 75 mJ, the simulated values (56 - 65 %) observed to be closer to the experimental values (73 %). Similarly, at 150 mJ Model-1 and 2 (78 – 80 %) are able to reproduce the experimental values (80%) whereas, Model-3 was observed over estimating with the experimental values. The variation in the laser energy absorptions with the three models is due to the dependency on the variables such as the charge state, wavelength and temperature. In the next sections, the comparative study of the plasma and SW dynamics with the three models is discussed.

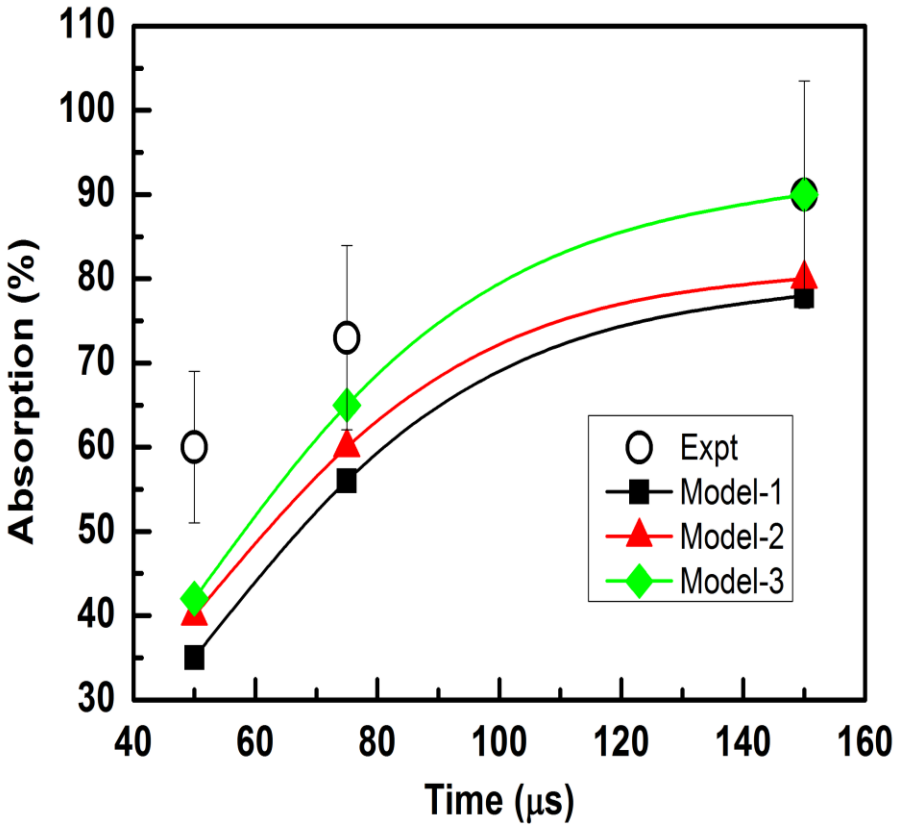

Figure 6.2 Comparison of absorption percentage between experimental values and numerical Models-1, 2 and 3 for the input laser energies 50, 75 and 150 mJ, respectively. The lines are guide to the eye.

6.4.2 Asymmetric laser energy deposition

In figure 6.3 (a) & (b) the shadowgrams corresponding to the evolution of shock waves (SW) at 0.2 and 4 μs, respectively is shown for the input laser energy of 50 mJ. Figure 6.3 (c) shows the self-emission from air for 45 mJ. As observed, the SW evolution is asymmetric at 0.2 μs (fig. 6.3 (a)) and as the time progresses it attains a spherical shape at 4 μs (fig. 6.3 (b)). The asymmetric expansion of the internal core as observed in fic 6.3 (c) is also observed in the laser produced plasmas in gases[49-51].

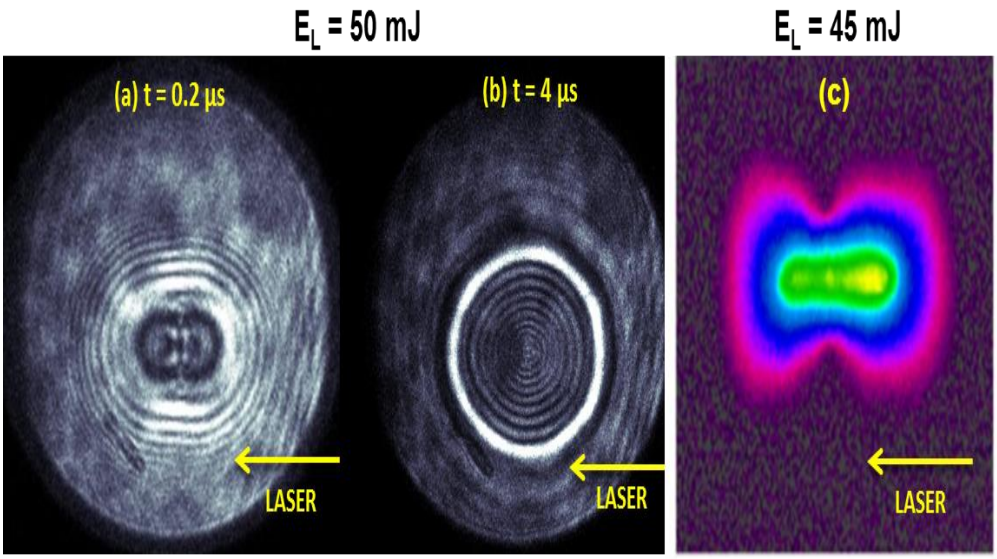

Figure 6.3 shadowgrams of shock wave evolution in ambient air for the input laser energy of 50 mJ a) asymmetric shape at 0.2 µs and b) almost symmetric at 4 µs, c) plasma plume self-emission from air for the input laser energy of 45 mJ. Courtsey: Leela et al.[24]

In experiments, the expansion of the plasma and SW is observed from 0.2 µs. The simulated density contours presented in fig. 6.4 (a & b) shows the appearance of the plasma and SW expansion at early times of 25 ns and 50 ns for the input laser energy of 50 mJ using Model-2. The internal part with black spot corresponds to the hot plasma core (PC) region, where the temperatures are very high (fig 6.5). Similarly the outer region with a thin bright line represents the SW where the mass density is very high ~5 - 6 kg/m^3 at 25 ns compared to the PC. During 25 ns and 50 ns times, the SW is in contact with the plasma. As observed from figure 6.4 (a), the expansion at 25 ns and 50 ns appears to be mostly along laser axis (Z) than the radial (perpendicular to laser) axis. However, at latter times the expansion in the radial direction also becomes comparable. These density contours confirm that the deposition of the laser energy happens asymmetrically across the focal plane of the lens (Z=0 in fig. 6.5), resulting in the asymmetric expansion of the plasma and SW at early time scales.

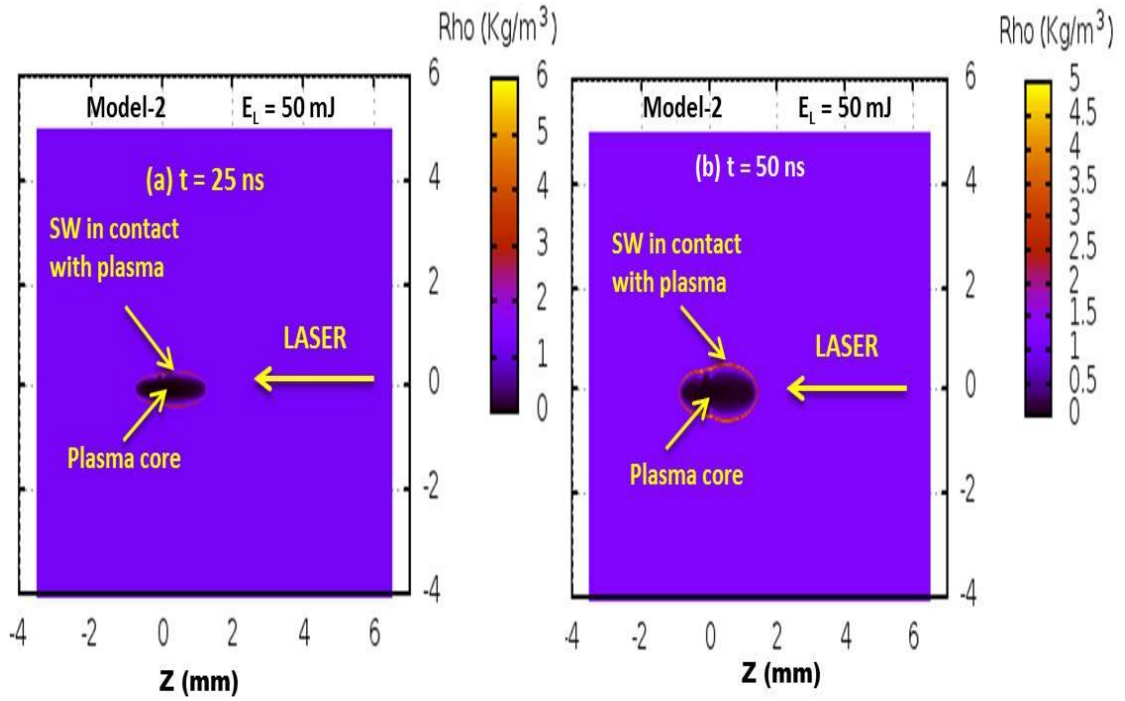

Figure 6.4 Density contours of the plasma and SW evolution in ambient air at a) 25 ns and b) 50 ns for 50 mJ using Model-2.

Figure 6.5 shows the temperature profile along the laser axis (Z) over 50 ns – 4 μs time scales using Model-2 for the input laser energy of 50 mJ. As observed at the early expansion of 50 ns, the temperature is asymmetric over the spatial region and is continued at all the time scales of upto 4 μs. At 50 ns, peak temperature of ~15×10^4 K exists over the region 1 mm along the laser direction in the negative Z-axis. At latter time scales due to the heat transfer to the surroundings, the temperature distribution within the PC changes continuously and the peak shifts from one point to other over time. The plasma and the SF expands together with time upto 0.1 μs. At around 0.4 μs SW detaches from the plasma and quickly moves through the surrounding air.

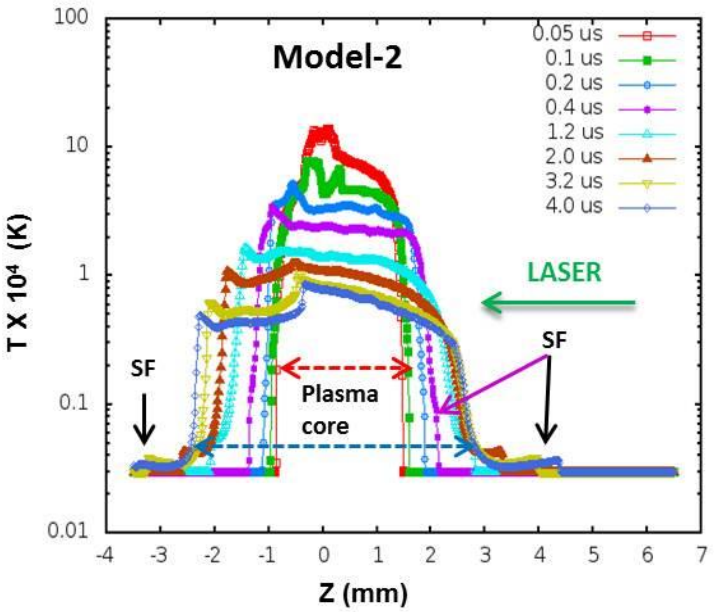

Figure 6.5 Plasma temperature profiles for 50 mJ along the laser axis (Z) simulated numerically over the time scales 50 ns to 4 μs using Model-2 showing the plasma core and SW expansion in ambient air. Z=0 represents the focal plane of the lens.

6.4.3 Internal and external plasma structure comparison with density contours

The experimentally obtained shadowgram (fig. 6.3 (a)) and self-emissions (fig. 6.3 (c)) shows that the external and internal air plasma structures appear like a tear drop and dumbbell, respectively at 0.2 μs. With time, the shape in both internal and external regions appears as oblate and becomes spherical at latter time scales (6.3 (b)) as observed in the experiments[23].

In figure 6.6 (a) a series of shadowgrams (top to bottom) corresponding to the evolution of SW over the time scales of 0.2 – 2 μs is shown for 50 mJ input laser energy. These were compared with the mass density (ρ) contours simulated using Models-1, 2 and 3 (fig. 6.6 (b), (c), (d)), respectively. The arrow in the picture represents the laser propagation direction. The contours in fig. 6.6 (b & c) with Model-1 and 2 also show the similar flow fields as observed in the experiments, but with Model-3 (fig. 6.6 (d)) the shape appears mostly spherical.

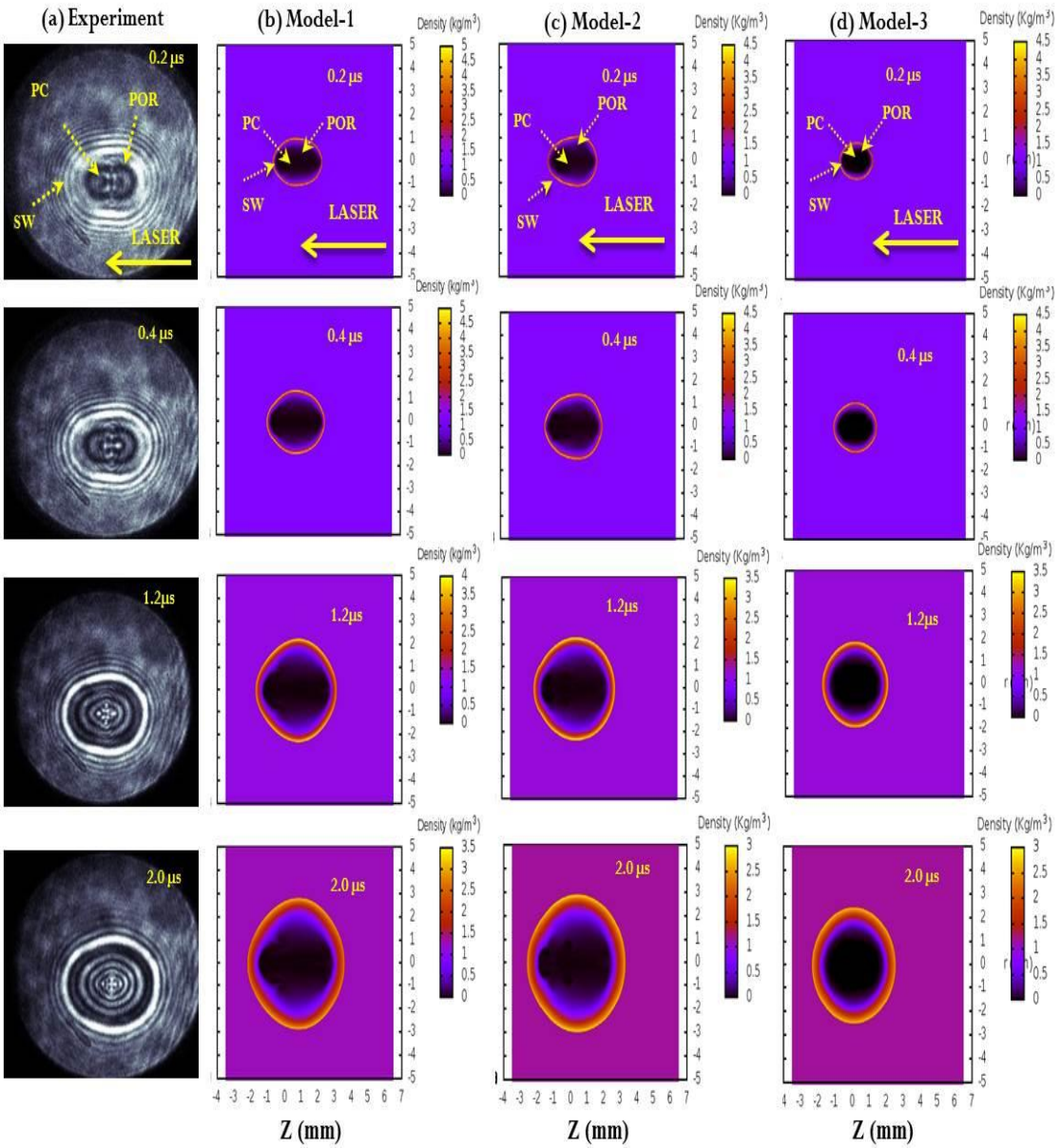

Figure 6.6 Comparison of internal and external flow structures a) shadowgrams obtained from experiments and (b-d) density contours simulated using Models -1, 2 and 3 at times 0.2, 0.4, 1.2 and 2 µs, respectively for the input laser energy of 50 mJ.

At initial times < 0.4 µs, the ionization front (IF) of the plasma and the SW are almost together and move with same velocity. However, at latter times (>0.4 µs) the SW starts detach from the IF and moves away outward direction leaving the plasma field.

After the termination of the laser pulse, the plasma region normally has two different regions: the PC which is very hot and the plasma outer region (POR), where the temperatures are low compared to the PC. Due to this, mass density in the PC region is very low which is increased as moved away from the PC to POR and becomes high at the interface between the POR and the surrounding gas due to high pressure gradient. Due to high pressures acting across the interface, accumulation of mass takes place within a small region from the POR very rapidly which results in the formation of the SW (fig. 6.6 (b-d)). Since the accumulation occurs within a small region the resulting density is few orders greater magnitude than the PC or POR. The higher in the density (ρ) across the SF implies high compression of the ambient gas. The accumulation of mass starts from the early expansion of the plasma and continues to increase resulting in the formation of SW. During the time evolution, the density (ρ) across the SW decreases because of the opposing forces acting on it similarly in the PC and POR, ρ increases as the temperatures attain the normal ambient conditions.

Figure 6.7 & 6.8 shows the comparison between the shadowgrams and simulated density contours for 75 and 150 mJ energies, respectively over the time scales of 0.2 – 2 μs. The tear drop shape is seen to be retaining up to longer times with the increased laser energy. At 75 mJ this nature is observed up to 0.8 μs, whereas at 150 mJ this is observed up to 1.2 μs. For all laser energies considered (fig. (6.6) - fig (6.8)) the expansion is observed to be asymmetric along the laser axis and moreover, it is pronounced along the direction opposite to the laser propagation. Similarly, the extent to which the plasma and SW expanded is also observed to be increasing with increasing laser energy.

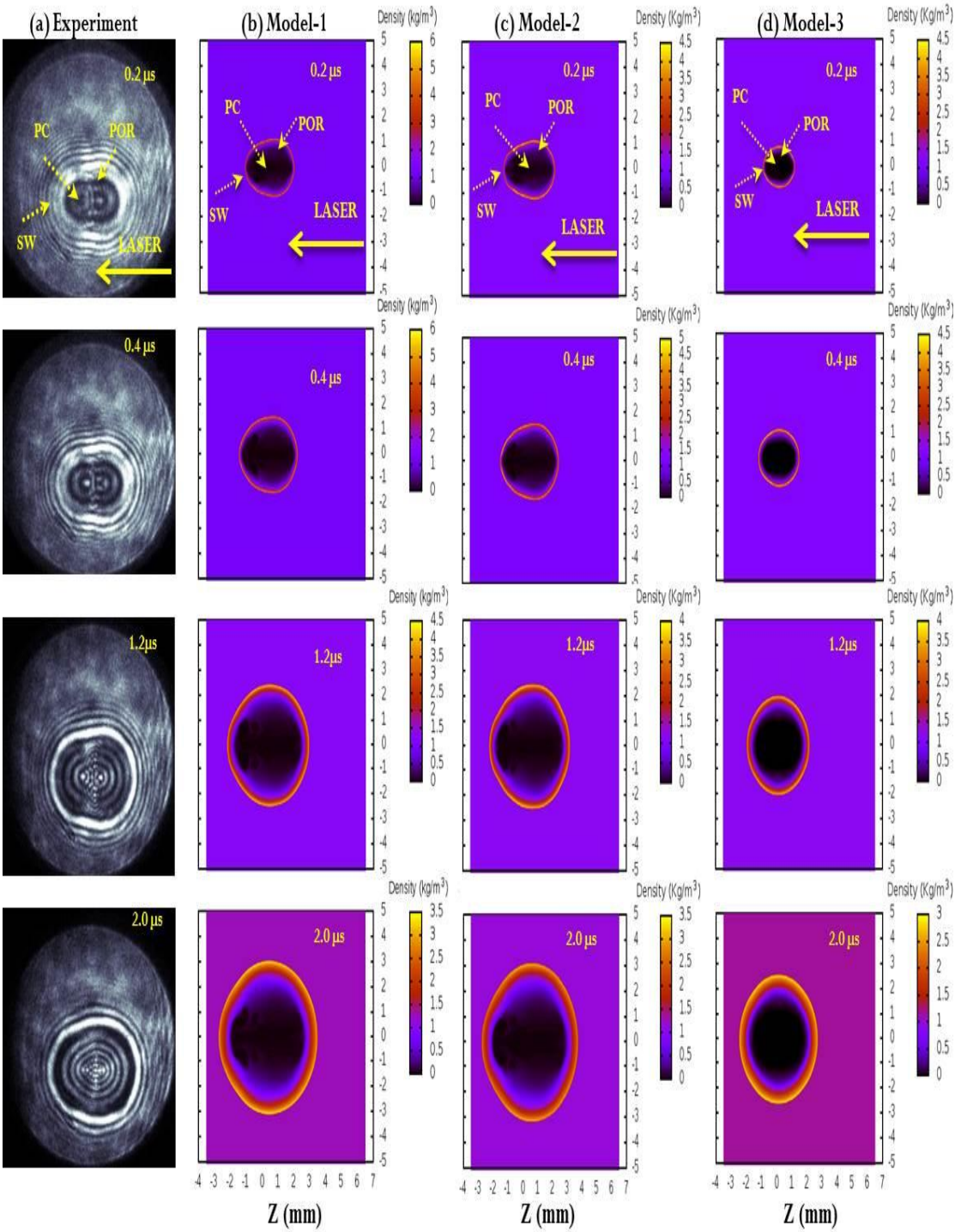

Figure 6.7 Comparison of internal and external flow structures a) shadowgrams obtained from experiments and (b-d) density contours simulated using Models -1, 2 and 3 at times 0.2, 0.4, 1.2 and 2 µs, respectively for the input laser energy of 75 mJ.

The asymmetric nature and the elongation towards the laser direction occur due to asymmetric deposition of the laser energy during the laser pulse in action. Raizer et al.[33, 34] had proposed three different mechanisms: shifting of the absorption front (AF) location, radiation driven shock wave (RDSW) and laser supported detonation wave (LSDW) for explaining the asymmetric expansion of the plasma and SW during the evolution. In the simulations with all the three models, the radiation effects are assumed to be negligible therefore, the asymmetric expansion observed here is due to the shifting of AF location or due to LSDW mechanism. During the early interaction of the laser pulse with ambient air, the absorption normally takes place at the focal point, but once the breakdown is achieved the absorption starts occurring at the front location due to shielding of the laser energy. As a result, the deposition takes place at the front location which moves continuously towards the laser propagation direction until the laser pulse terminates.

As the input laser energy increases the energy deposition also increases (see fig. 6.2) as a result, the AF location moves with higher velocities. Hence the elongation towards the laser direction is observed to increase more by increasing the laser energy. Due to increase in the laser energy absorption the asymmetric behaviour (tear drop) can be seen to retain even up to longer times scales (see fig. 6.6(b-d), 6.77 (b-d) & 6.8 (b-d) at 1.2 μs). For 75 mJ, the ionization front and SW are in contact with each other up to ~0.8 μs, similarly for 150 mJ it is observed up to ~1.0 μs. As can be seen from fig. 6-8, during the early expansion the plasma and SW expands more opposite to the laser propagation direction. Once the SW detaches from the plasma it expands supersonically quickly outwards in all directions. Overall the expansion along the laser axis, that is, along and opposite to the laser propagation (towards the laser direction) direction is more compared to that along the lateral direction (radial) for few time scales depending on the laser energy.

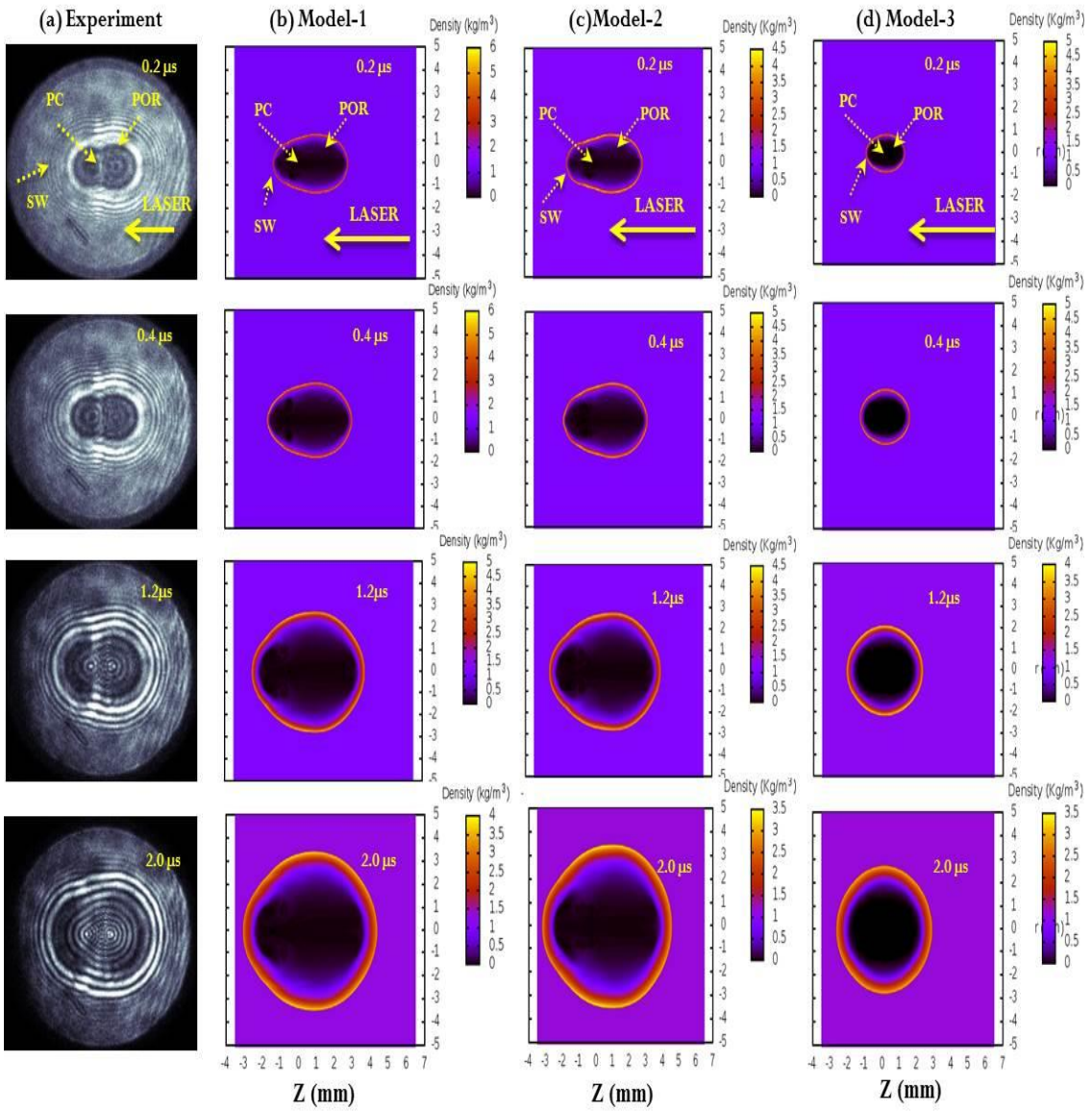

Figure 6.8 Comparison of internal and external flow structures a) shadowgrams obtained from experiments and (b-d) density contours simulated using Models -1, 2 and 3 at times 0.2, 0.4, 1.2 and 2 µs, respectively for the input laser energy of 150 mJ.

The expansion with time becomes symmetric in all the directions except along the laser propagation direction which can be observed upto ~2 µs for all the energies (fig. 6.7-6.8) with Model-1 and 2. However, at times >2 µs the expansion in all directions become similar leading to the attainment of the spherical expansion. During this nature the expansion will be symmetric.

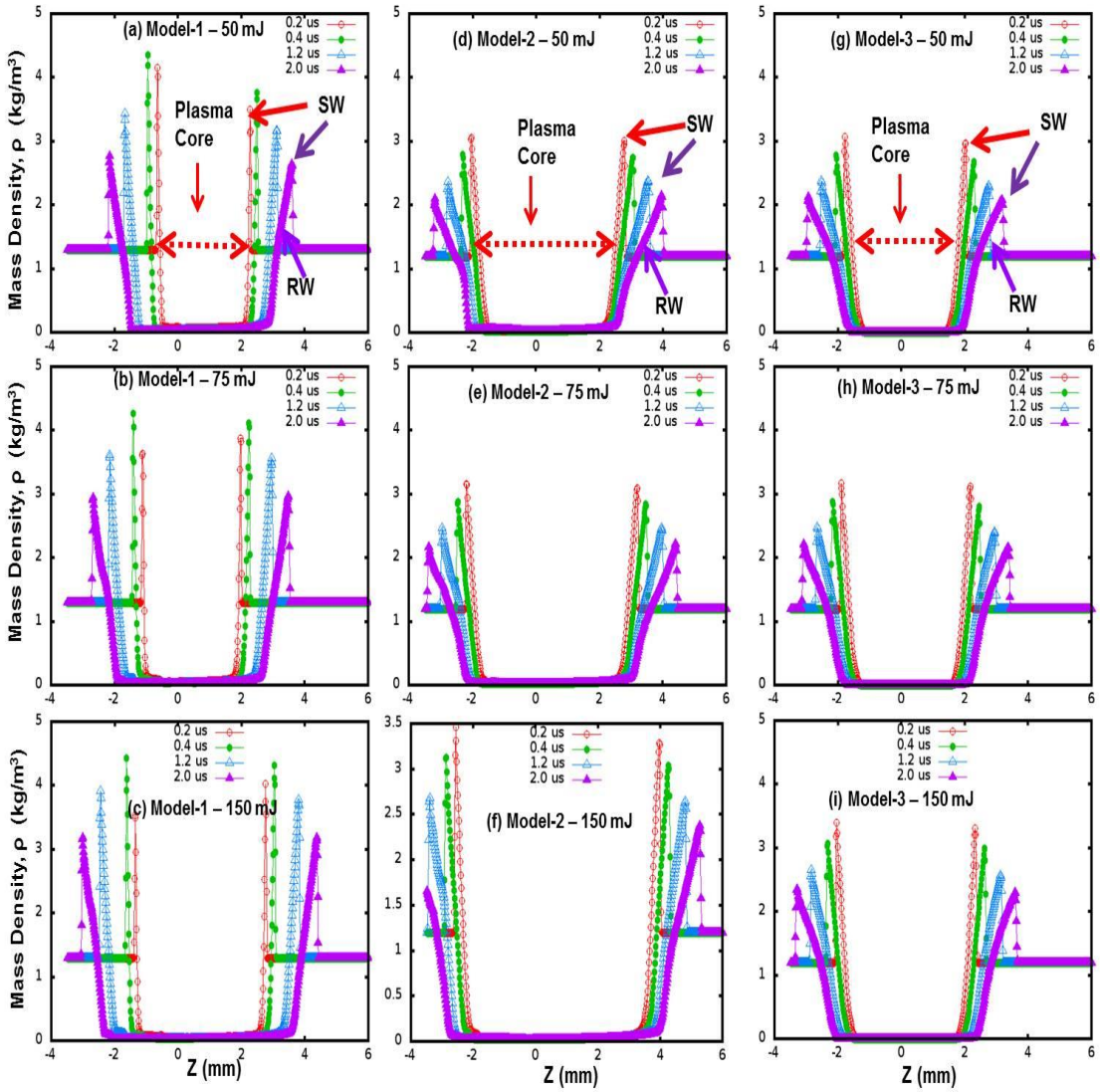

Figure 6.9 Comparison of mass density along the laser axis (a-c) Model-1, (d-f) Model-2 and (g-i) Model-3 for the input laser energies of 50, 75 and 150 mJ, respectively at times 0.2, 0.4, 1.2 and 2 μs.

One interesting feature observed in the internal structure of the plasma in the case of experiments is the appearance of two distinct point sources separated over a small distance which is varied with respect to time and the input laser energy deposited[23, 24]. In the density contours presented (fig. 6.6 (b-d)-6.8 (b-d)) using Models-1, 2 and 3, the signs of the two distinct points is faintly visible due to dark region in the PC. This is observed clearly in the temperature contours from simulations. In all the density

contours (figure (6.6), (6.7) and (6.8)) the plasma and SW expands asymmetrically during the initial times, but as soon as the SW detaches the plasma, it expands quickly outwards to attain the symmetric expansion. So during the evolution, the SW converts from asymmetric to symmetric expansion.

In figure 6.9 the mass density along the laser axis is compared for 50, 75 and 150 mJ using Models-1, 2 and 3, respectively for time scales 0.2, 0.4, 1.2 and 2 μs. In the density line profiles (fig. 6.9), the peak points represent the SW where the density (ρ) is higher compared to the PC. Behind the SW, a rarefaction wave (RW) is generated that relieves the pressure created by the SW on the surrounding air. The pressure behind the SW decreases linearly up to POR and beyond this region a sudden fall in ρ is observed. The profiles are observed to be similar with all the models. However, the peak density across the SF with Model-1 is observed to be higher than with Models-2 and 3. The peak density in Model-1 is observed to be higher at 0.4 μs compared to 0.2 μs which represents the SW detachment taking place at this point.

6.4.4 Plasma splitting and roll-off comparison with temperature contours

The shadowgrams in fig. 6.10 (a), 6.12 (a) and 6.14 (a) clearly shows the appearance of two distinct point sources(two spots) for the input laser energies 50, 75 and 150 mJ, respectively. This nature was observed to exist between 0.4 – 1.0 μs at 50 mJ, 0.4 – 1.8 μs at 75 mJ, 0.8 – 2.4 μs at 150 mJ. The times at which the two points occur and their existence time was observed to increase with the input laser energy. In the present section, a detailed discussion of the internal plasma core dynamics and its comparison with the temperature contours is presented.

i) 50 mJ

Figure 6.10 compares the internal and external flow structures of shadowgrams with temperature contours using Model-1, 2 and 3, respectively over the time scales 0.2 – 2.0 μs.

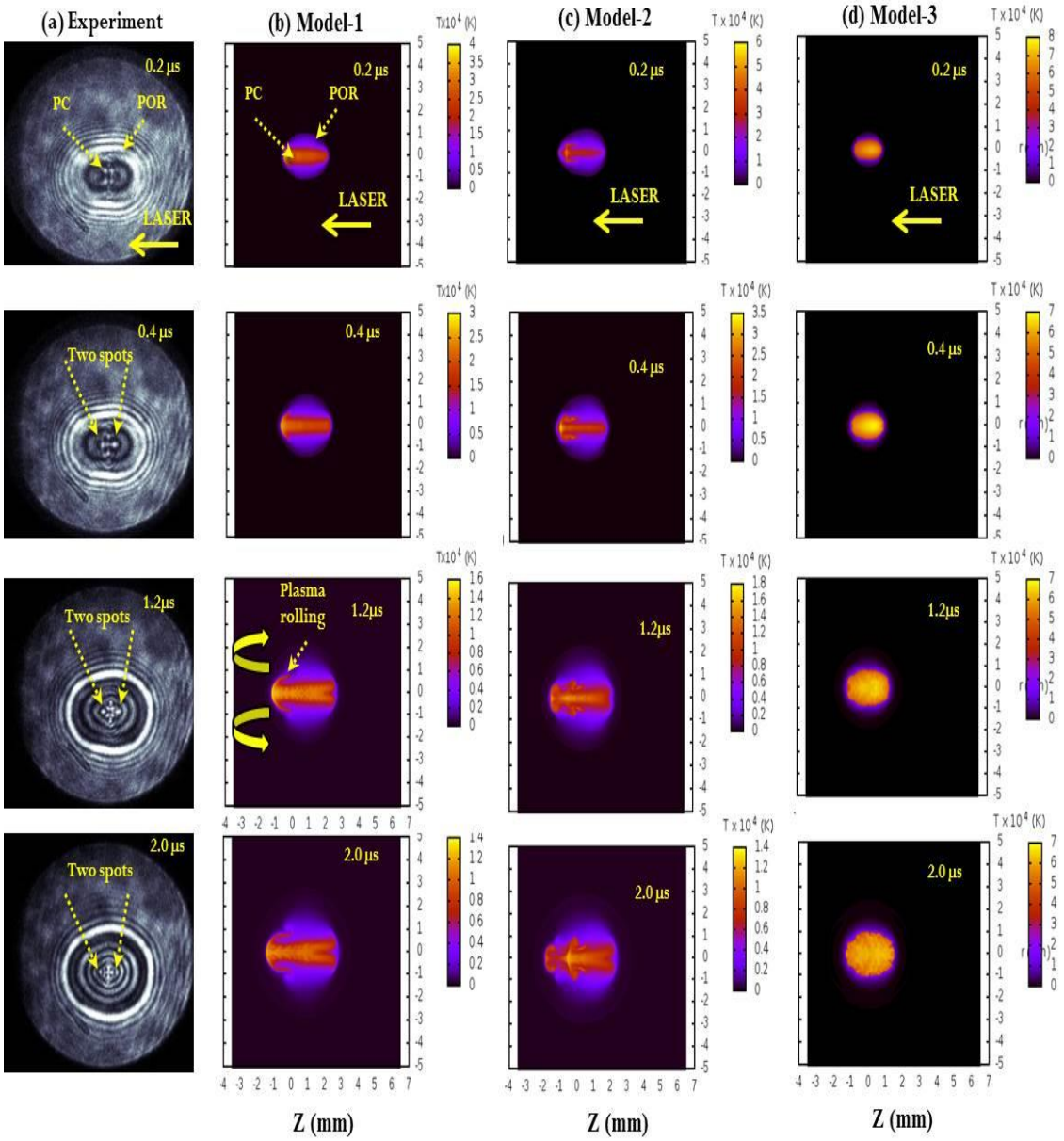

Figure 6.10 Comparison of internal and external flow structures of (a) shadowgrams with (b-d) simulated temperature contours using Models -1, 2 and 3 for the input laser energy of 50 mJ.

The central spot in the contours corresponds to the PC where the temperatures are very high of the order of 10^4 K which is shielded by the plasma outer region (POR) as moves away towards the radial direction where the temperatures have decreased to over few thousands of kelvins. Along the laser axis the decrement in the temperatures

is small compared to towards radial direction. The internal PC is observed to be asymmetric at all the times as can be seen from fig. 6.10 (b-d), respectively. The spatial distribution of the temperature with Model-1 and 2 is observed to be more asymmetric than with Model-3. Due to localized hot spots existing within the plasma region, the core experiences hydrodynamic instabilities internally. Hence, the plasma collapses wherever the temperature gradients become high compared to respective residing regions. Since the temperature and pressure gradients along the laser and radial direction are different, the plasma collapse will be different. Similarly the spreading (the length) of the plasma along the laser axis is more which confirms that the laser energy deposition occurs mostly along the laser axis. The asymmetric distribution of the temperature along this axis is due to shifting of the AF during the laser interaction process that causes the localized hot spots at different regions[33, 34]. With Models-1 and 2, the peak temperature (T_{max}) along the laser axis (-ve Z-axis) is found to appear at the left portion of the plasma and is decreased over a distance towards the +ve Z-axis. This was not observed with Model-3.

Table 6.2 Temperature range observed along laser and radial directions for 50, 75 and 150 mJ input laser energy.

E_L (mJ)	t (μs)	T × 10^4 (K) along laser axis			T × 10^4 (K) along radial axis		
		M-1	**M-2**	**M-3**	**M-1**	**M-2**	**M-3**
50 mJ	0.2	4.0-2.0	6.0-3.0	8.0–3.0	2.0-0.5	3.0-1.0	4.0 – 1.0
	2.0	1.4-1.0	1.4-1.0	7.0-3.0	0.8-0.2	1.0-0.2	3.0-1.0
75 mJ	0.2	6.0-3.0	6.0-3.0	8.0-3.0	3.0-1.0	3.5-1.0	4.5-1.0
	2.0	1.4-0.6	1.4-0.6	7.0-3.0	1.0-0.2	1.0-0.2	3.5-1.0
150 mJ	0.2	8.0-3.0	8.0-3.0	9.0-4.0	5.0-1.0	5.0-1.0	6.0-1.0
	2.0	1.6-0.6	1.8-0.8	8.0-4.0	1.2-0.2	1.4-0.2	5.0-1.0

M-1, M-2, M-3 represents Model-1, 2 and 3, respectively.

Table 6.2 summarizes the temperature range existing along the laser and radial axis for the time scales of 0.2 and 2 μs. At 0.2 μs, the temperatures along the laser axis falls over the range 40,000-20,000K with Model-1; 60,000-30,000K with Model-2, and 80,000-30,000K with Model-3. Similarly, at 2 μs the temperatures fall over the range 14,000-10,000 K with Model-1 and 2, and 70,000-30,000K with Model-3. T_{max} at 0.2 μs can be seen to reside on the left side with respect to the origin and is observed to exist at a distance of ~0.5 mm.

Along the radial direction with respect to the origin, the temperatures at 0.2 μs falls from 20,000 – 5,000 K with Model-1; 30,000 – 10,000 K with Model-2 over a distance of approximately 0.8 mm. Similarly, with Model-3, it falls from 40,000 – 10,000 K over a distance of approximately 0.4 mm. As the time progresses, at 2 μs the temperatures fall from 8,000 – 2,000 K over a distance of 1.4 mm with Model-1, 10,000 – 2,000 K over a distance of 1.2 mm with Model-2, and 30,000 – 10,000 K over a distance of approximately 1.0 mm. Since the absorption of the laser energy with Model-1 is low (30%) compared to that of Model-2 and 3 (40%), the corresponding temperature ranges are also small. Though the absorption is same with Model-2 and 3, but the temperatures with Model-3 are high due to low energy distribution to the surroundings. The temperature along the laser axis observed to decay quickly compared to that along the radial axis. Due to very high temperature gradients the corresponding pressure gradients will also be high along the laser axis. So the energy and momentum transfer along this axis will be high compared to that along the radial axis as a result the expansion is found to be asymmetric during the time scales < 2 μs. Due to the spatio-temporal gradient of temperature both along the laser and radial axis, the internal plasma core encounters hydrodynamic instabilities during the relaxation process[4, 29]. The process continues even at longer time scales where the plasma experiences collapsing, bubble and jet formations, which is observed experimentally[23, 24] over the times scales of few milliseconds. Assuming the plasma is divided into parts with respect to the origin (focal plane of the lens) one can observe the initial rolling of the

plasma taking place at 0.4 μs at the left corner with respect to the origin (fig. 6.10 (b)). As time progress at 1.2 μs (fig. 6.10), the rolling becomes significant at this point. Moreover, this process also starts at other places like the center and right end of the plasma also. As observed from the density contours (fig. 6.6 (b-c)) at 0.2 μs, a sharp curve existing at the left side of the plasma core (with respect to the origin) this is the point where the maximum temperature exists (left portion of the plasma in fig. 6.9 at 0.2 μs). So the first rolling of the plasma occurs at a point where the plasma attains maximum temperature with respect to the surrounding atmosphere. In fig. 6.10 (b, c) the rolling of the plasma can be seen at 0.4 μs with Model-1 and 2, respectively. A similar process is also observed at 1.2 μs on the right corner with Model-1 and at the right and center with Model-2. No such plasma rolling is observed with Model-3.

In fig. 6.11 the same temperature contours presented in fig. 6.10 with 50 mJ, is viewed at 45^0 angle. This angle clearly shows the splitting of the plasma. The splitting of the plasma is observed after 0.8 μs (not shown in fig. 6.11) of time which can be seen only in the case with Model-1. However, with Model-2, the splitting is observed from very early time scales at 0.2 μs and become dominant with time. No such plasma splitting is observed with Model-3. The points where the splitting occurs is indicated with two arrows at 1.2 and 2 μs. The splitting of the plasma corresponds to the two distinct sources or points observed in case of experiments. The splitting of the plasma appearing in simulations and the two distinct sources appearing in shadowgrams are observed to occur between 0.4 – 0.8 μs after the laser pulse termination. The two sources observed in the experiments correspond to the peak temperatures of plasma after the splitting has taken place. The spots were observed to exist along the left and right portions of the focal plane.

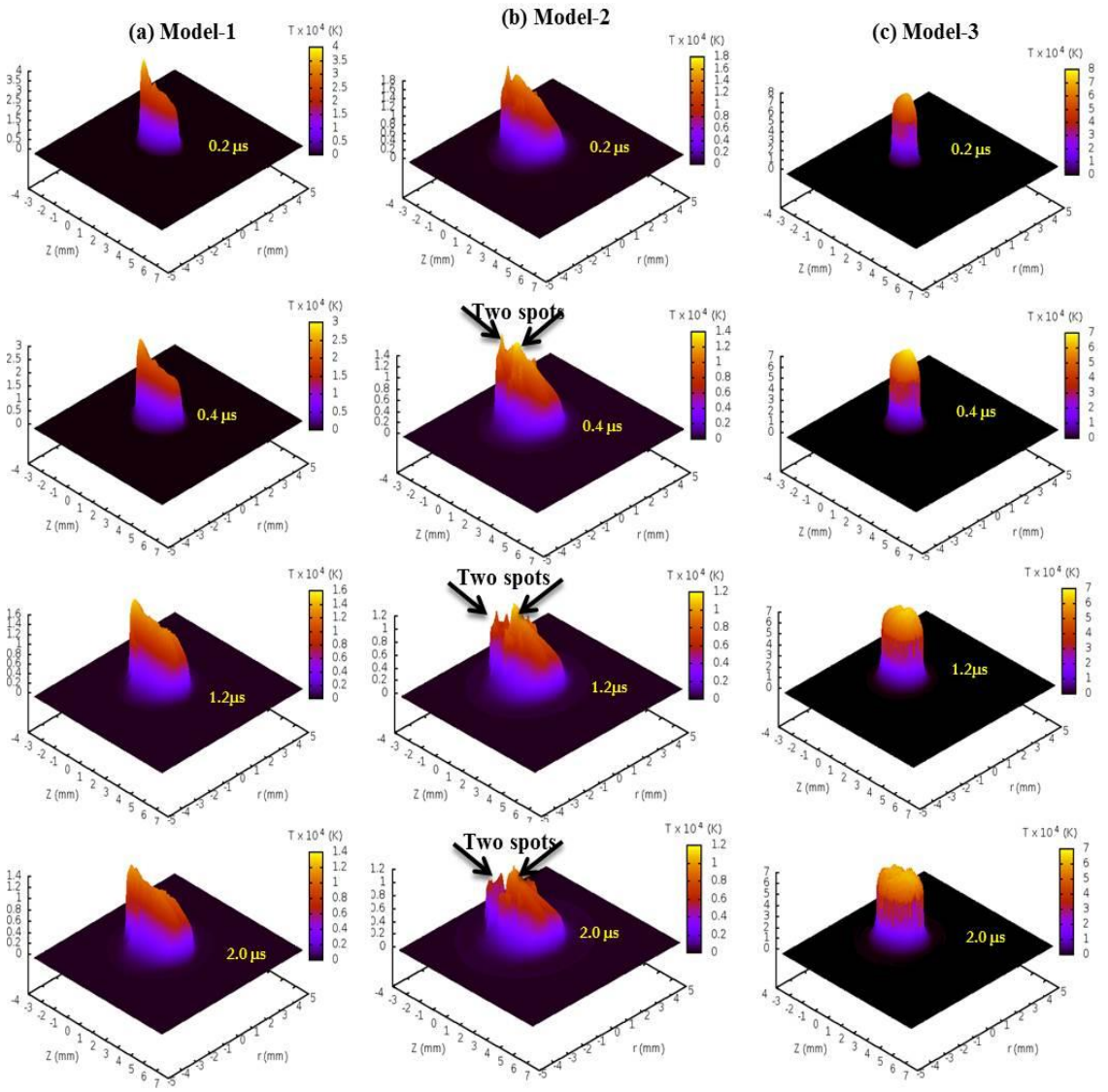

Figure 6.11 Temperature contours viewed with 45^0 angle with respect to the plane of the paper and compared between Model-1, 2 and 3 for the input laser energy of 50 mJ.

ii) 75 mJ

Figure 6.12 compares the internal flow structures at 75 mJ of input laser energy over the time scales 0.2 – 2 µs. The maximum temperature (T_{max}) in this case also exists at the left portion of the plasma with respect to the origin and is found to decrease over a distance towards the laser propagation direction. Due to increase in the laser energy absorption the plasma temperature along the laser and radial axis increases.

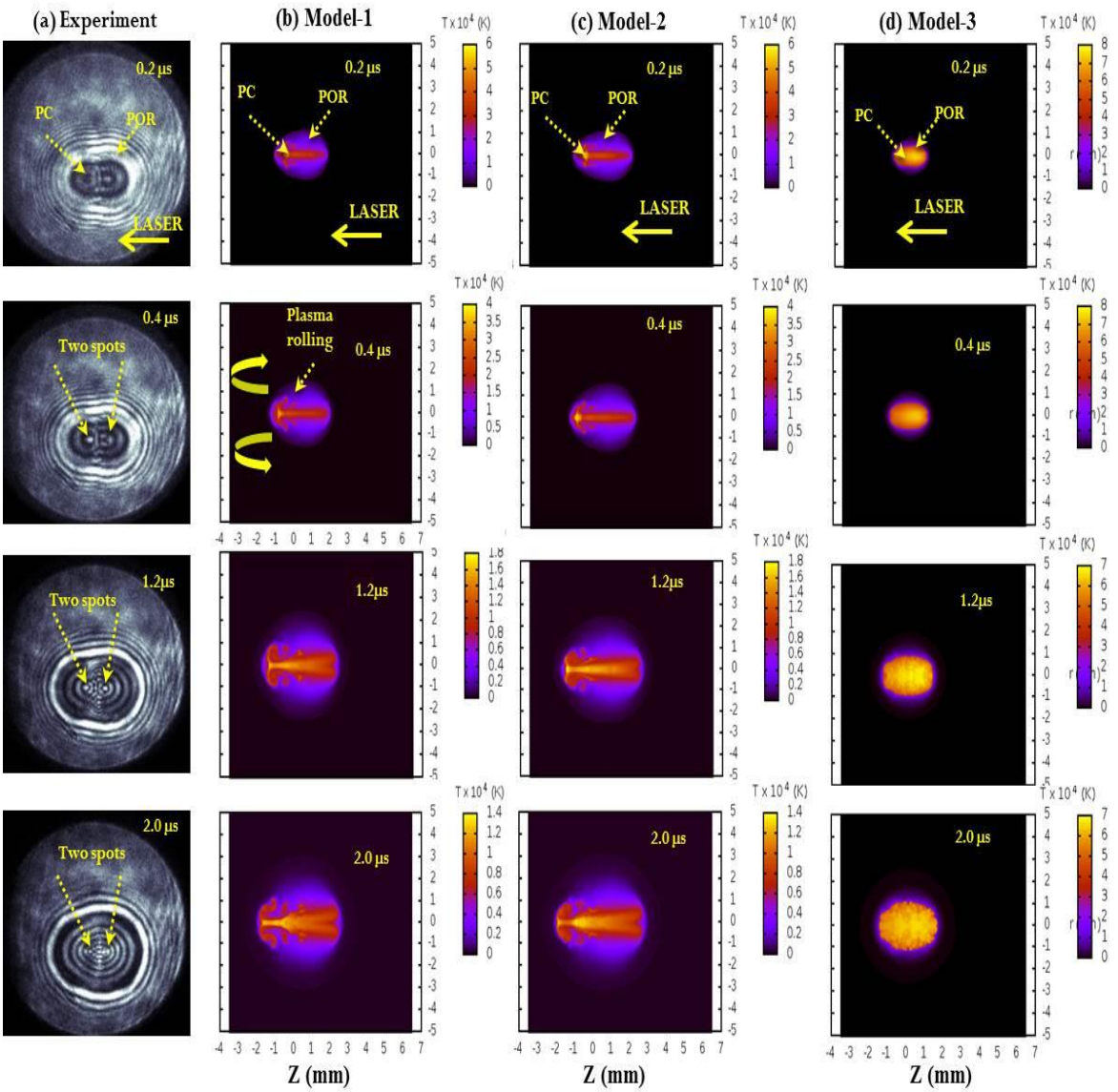

Figure 6.12 Comparison of internal and external flow structures from shadowgrams with temperature contours simulated using Models -1, 2 and 3 for the input laser energy of 75 mJ.

Table 6.2 summarizes the temperature range existing along the laser and radial axis for the time scales of 0.2 and 2 µs, respectively for the input laser energy of 75 mJ. At 0.2 µs, the temperature along the laser axis falls over the range 60,000-30,000 K with Model-1 and 2, respectively and 80,000-30,000 K with Model-3. Similarly, at 2 µs the temperatures exist over the range 14,000-6,000 K with Model-1 and 2, and 70,000-

30,000K with Model-3. The T_{max} at 0.2 μs exists on the left side of the plasma with respect to the origin at a distance of ~0.5 mm. The spreading of the plasma at 0.2 μs is slightly higher with Model-1 compared to other two models. The temperature range in case of 75 mJ is observed to decay quickly along the laser axis. At 2 μs, the plasma temperature along the laser axis and across focal plane (left and right portion) was not thermal equilibrium as compared to that at 50 mJ. Due to increase in the temperatures with respect to laser energy, the plasma will take longer times to come to the thermal equilibrium state.

Along the radial direction, the temperatures at 0.2 μs, falls from 30,000 – 10,000 K with Model-1; 35,000 – 10,000 K with Model-2 over a distance of approximately 1.0 mm. Similarly, with Model-3, it falls from 45,000 – 10,000 K over a distance of approximately 0.5 mm. At 2 μs, the temperatures fall from 10,000 – 2,000 K over a distance of 1.5 mm with Model-1 and 2; and 35,000 – 10,000 K over a distance of approximately 1.0 mm with Model-3. Due to different range of temperatures existing within the hot core plasma over few millimetres along the laser and radial directions the asymmetric nature in the temperature arises within the plasma. Due to this nature the plasma core remains unstable during its evolution. The rolling of the plasma occurs at ~0.4 μs (fig. 6.12) at the left corner of the plasma and at the right corner occurs at ~1.2 μs with respect to the origin. Apart from these points, the rolling is also observed at other locations near to the origin. However, these rolling were not seen to be dominant as compared to that existing at the corners. This may be due to small temperature gradients existing with respect to the surrounding gas.

Figure 6.13 show the temperature contours shown in fig. 6.12 with 75 mJ viewed at 45^0 angles. As observed, the splitting of the plasma starts at ~1.2 μs and is observed with Model-2 only. The splitting can be seen even more clearly at 2 μs. With Model-1, the splitting was observed only after 4 μs that is not shown in the contours presented here, whereas with Model-3, this nature is not observed at any of the simulated time

scale (up to 8 μs). The existence of two point sources at the plasma core in the experiments (from shadowgrams of fig. 6.12) was observed within the time scales of 0.4 - 1.8 μs. This time range coincide with the plasma splitting observed with Model-2. Hence, one may conclude that the two point sources existing in experiments is due to the splitting of the plasma.

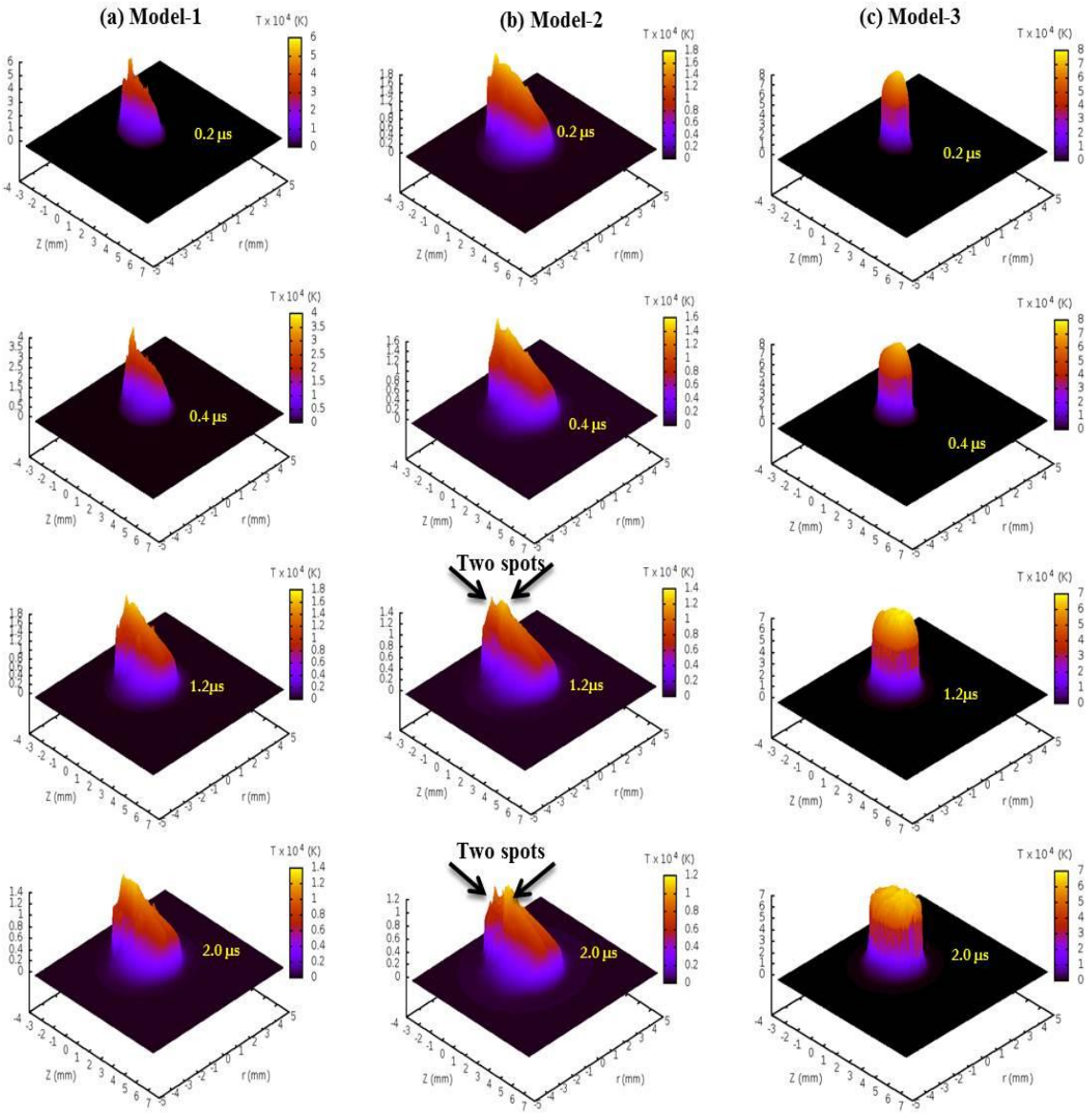

Figure 6.13 Temperature contours viewed with 45^0 angle with respect to the plane of the paper and compared between Model-1, 2 and 3 for the input laser energy of 75 mJ.

iii) 150 mJ

Figure 6.14 shows the temperature contour comparison at 150 mJ laser energy over the time scales 0.2 – 2 µs. The T_{max} in this case also exists at the left portion of the plasma with respect to the origin along the laser axis and is found to decrease over a distance towards the right portion. Due to increase in the laser energy absorption the plasma temperature along the laser and radial axis increases.

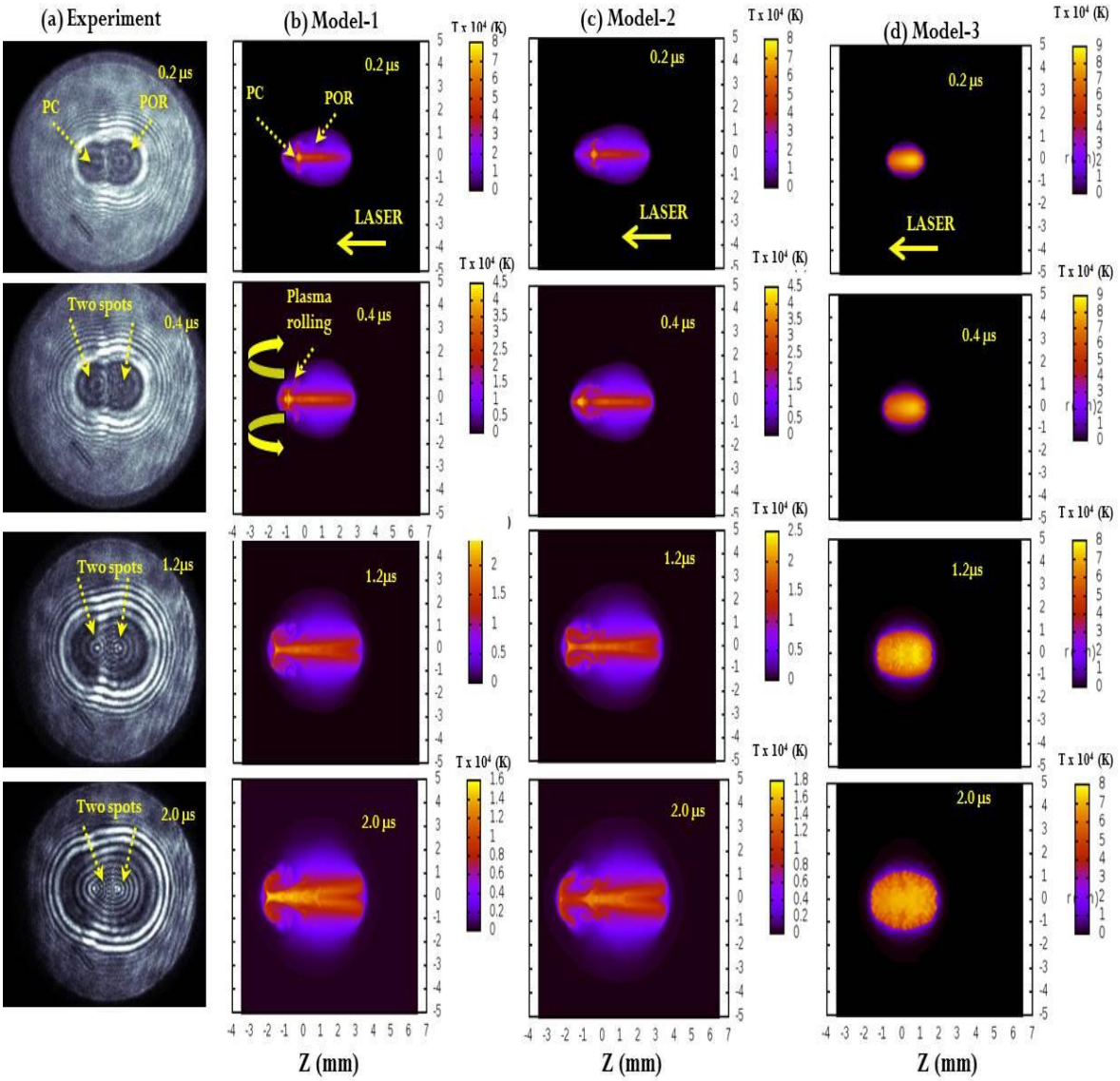

Figure 6.14 Comparison of internal and external flow structures from shadowgrams with the simulated temperature contours of Model-1, 2 and 3 for the input laser energy of 150 mJ.

Table-6.2 summarizes the temperature range existing along the laser and radial axis for the time scales of 0.2 and 2 μs for the input laser energy of 150 mJ. At 0.2 μs, the temperature along the laser axis falls over the range 80,000 – 30,000 K with Model-1 and 2 and 90,000-40,000K with Model-3. Similarly, at 2 μs the temperature falls over the range 16,000-6,000 K with Model-1; 18,000-8,000 K with Model-2, and 80,000-40,000K with Model-3. The T_{max} at 0.2 μs is observed to exist at a distance of ~0.8 mm at the left side from the origin. Along the radial direction, the temperature at 0.2 μs, falls over the range from 50,000 – 10,000 K with Model-1 and 2 over a distance of ~1 mm and 60,000 – 10,000 K with Model-3 over a distance of approximately 0.6 mm. At 2 μs the temperatures fall from 12,000 – 2,000 K over a distance of 2 mm with Model-1, 14,000 – 2,000 K over a distance of 2 mm with Model-2, and 50,000 – 10,000 K over a distance of approximately 1.2 mm with Model-3. The rolling of the plasma starts at ~0.4 μs at the left corner of the plasma and at ~1.2 μs at the right corner of the plasma (fig. 6.14). Like 75 mJ, the rolling in case of 150 mJ is observed to exist at multiple locations. The rolling is observed to occur around 0.4 μs (fig. 6.14) with Model-1 and 2.

The temperature contours presented of fig. 6.14 with 150 mJ is viewed at 45^0 as shown fig. 6.15 where the splitting of the plasma starts appearing at ~1.2 μs which is observed in the case of Model-2 only. The splitting of the plasma becomes more clearly visible as the time increases that is, at 2 μs. Like 75 mJ, the splitting of the plasma with Model-1 was also observed after 4 μs, whereas with Model-3, this nature is not observed at any of the simulated time scale (up to 8 μs).

The existence of two point sources at the plasma core in the experiments (from shadowgrams shown in fig. 6.14 (a)) was observed within the time scales of 0.8 - 2.0 μs. At latter times this phenomena were not seen from the shadowgrams. As observed with the simulated temperature contours, the plasma splitting with Model-2 occurs at ~1.2 μs (fig. 6.14). This time scale exists with the time range (0.8 - 2.0 μs) where

actually the existence of two sources occur in case of experiments. The clear visibility of the two sources at later time scales in case of experiments may be due the presence of very small temperatures (~10,000 K) existing in the PC region.

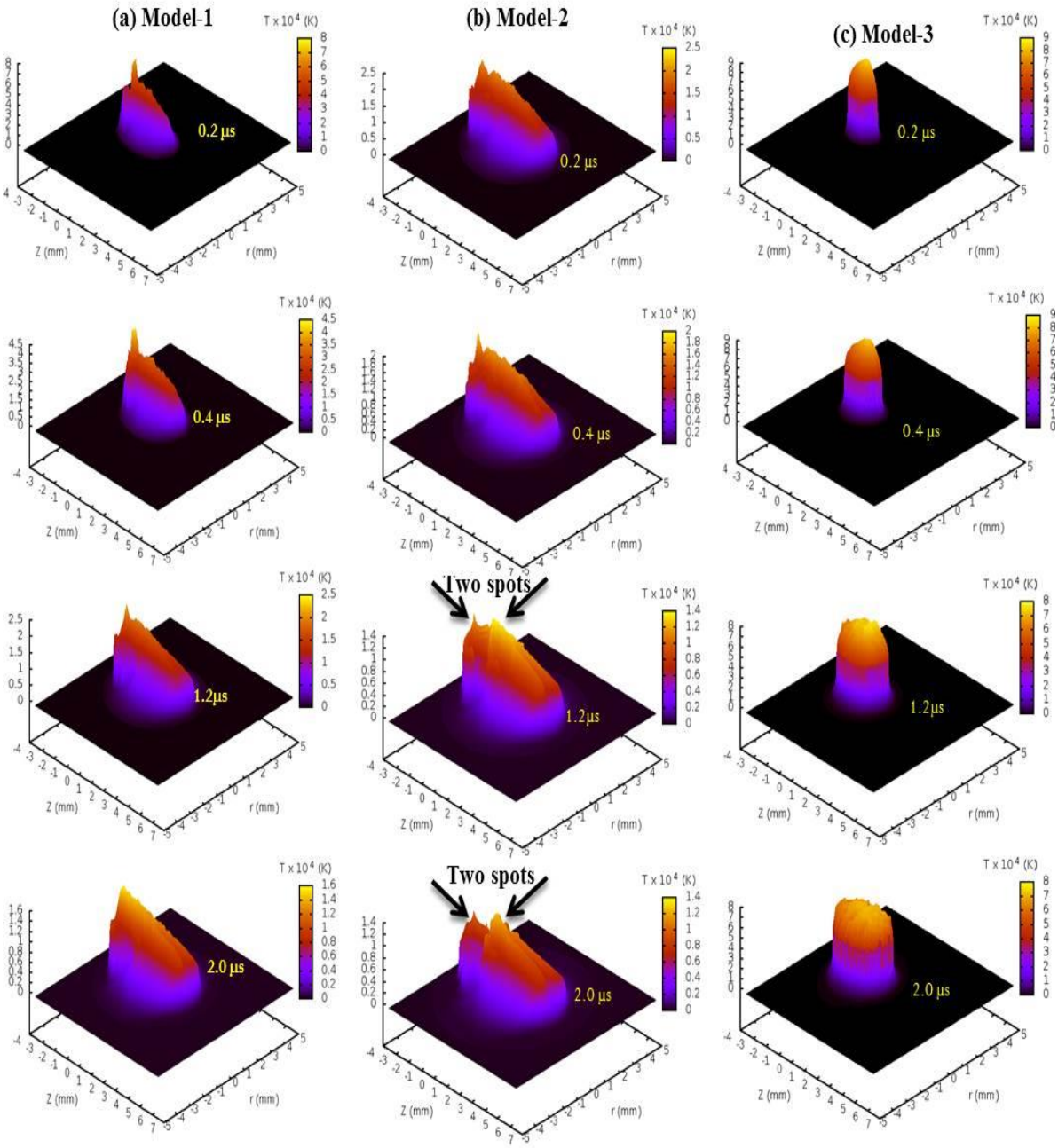

Figure 6.15 Temperature contours viewed with 45^0 angle with respect to the plane of the paper and compared between Model-1, 2 and 3 for the input laser energy of 150 mJ.

6.4.5 Temporal evolution of electron number density and temperature

In fig. 6.16 (a-c) the temporal evolution of the peak plasma electron number density, n_e is compared with the three Models -1, 2 and 3 over the time scales of 0.2 – 7 μs for the input laser energies of 50, 75 and 150 mJ, respectively. Similarly, the corresponding peak plasma temperatures, T are compared in fig 6.16 (d-f).

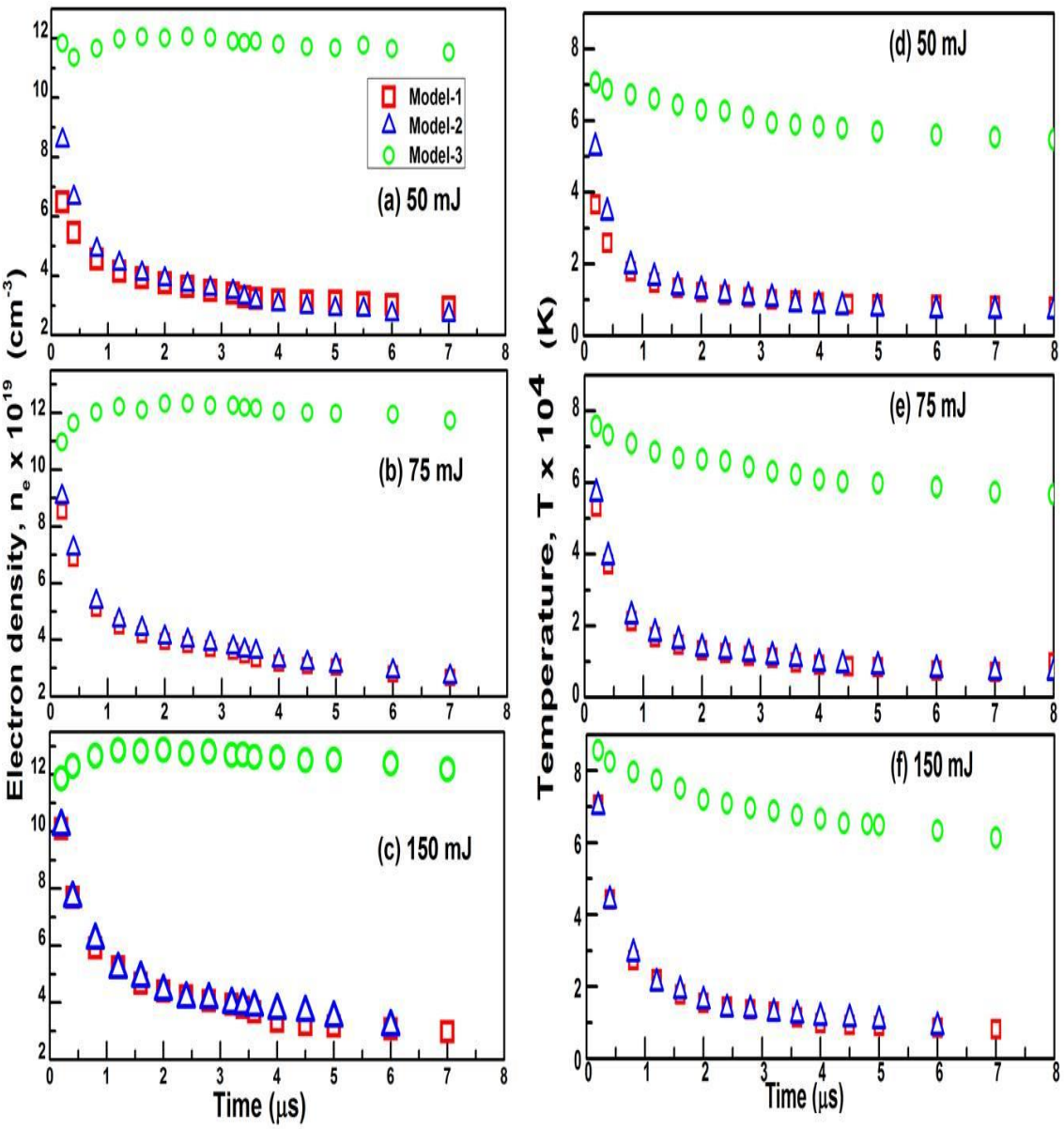

Figure 6.16 Comparison of temporal evolution of electron number density between Models -1, 2 and 3, respectively for the input laser energies a) 50 mJ, b) 75 mJ and c) 150 mJ

With Model-3, for all the laser energies taken, n_e and T have higher values compared to Model-1 and 2. The n_e was observed to be almost constant over all the time of 0.2 – 7 μs, whereas T is found to decay slowly with time. However, with Model-1 and 2, n_e and T observed to decay exponentially over these time scales and these were found to have a direct correlation with respect to each other. The similar trend is observed for all the laser energies considered.

At 50 mJ, with Model-1, n_e is observed to decrease from 8.5 -3×10^{19} (cm^{-3}) over the time scales of 0.2 – 7 μs. Similarly, with Model-2, it is observed to decrease from 6.2 - 3×10^{19} (cm^{-3}). At 75 mJ, with Model-1 n_e is observed to decrease from 9.0 - 2.5×10^{19} (cm^{-3}), with Model-2, it is observed to decrease from 8.5 – 2.5×10^{19} (cm^{-3}) over the time scales of 0.2 – 7 μs. At 150 mJ, n_e is observed to decrease from 10.0 - 3.0×10^{19} (cm^{-3}) with Model-1 and 2, respectively. As seen from the values, the electron number density increases with the increasing laser energy. The decay is fast during the initial times up to 2 μs and thereafter, falls slowly for longer times. The T values in the plasma core at 50 mJ, decay from 40,000 – 10,000 K with Model-1; 55,000 – 10,000 K with Model-2, and 70,000 – 60,000 K with Model-3 over the given time scales. Similarly, at 75 mJ they decay from 55,000 – 10,000 K with Model-1; 60000 – 10,000 K with Model-2 and 80,000 – 60,000 K with Model-3. At 150 mJ, the decay was observed to be from 70,000 – 10,000 K which was similar with Model-1 and 2 and 85,000 – 70,000 K with Model-3.

In figure 6.17 the temperatures across the SF during its evolution into ambient air is compared. The extraction of these values is very essential in the context of laser ignition of fuel-air mixtures as it gives the information of how the temperatures vary across the SW with time. At 50 mJ, the temperatures were observed to decay from 1,500-500 K with Model-1; 2,000-500 K with Model-2. At 75 mJ they decay from 2,000-400 K with Model-1; 1,800-400 K with Model-2. Similarly, at 150 mJ they decay from 3,500-500 K with Model-1; 1,500-500 K with Model-2. With Model-3, the shock

detachments were observed from 0.6 μs. The values decay almost similarly for all the three energies which found to decay from 600-500 K.

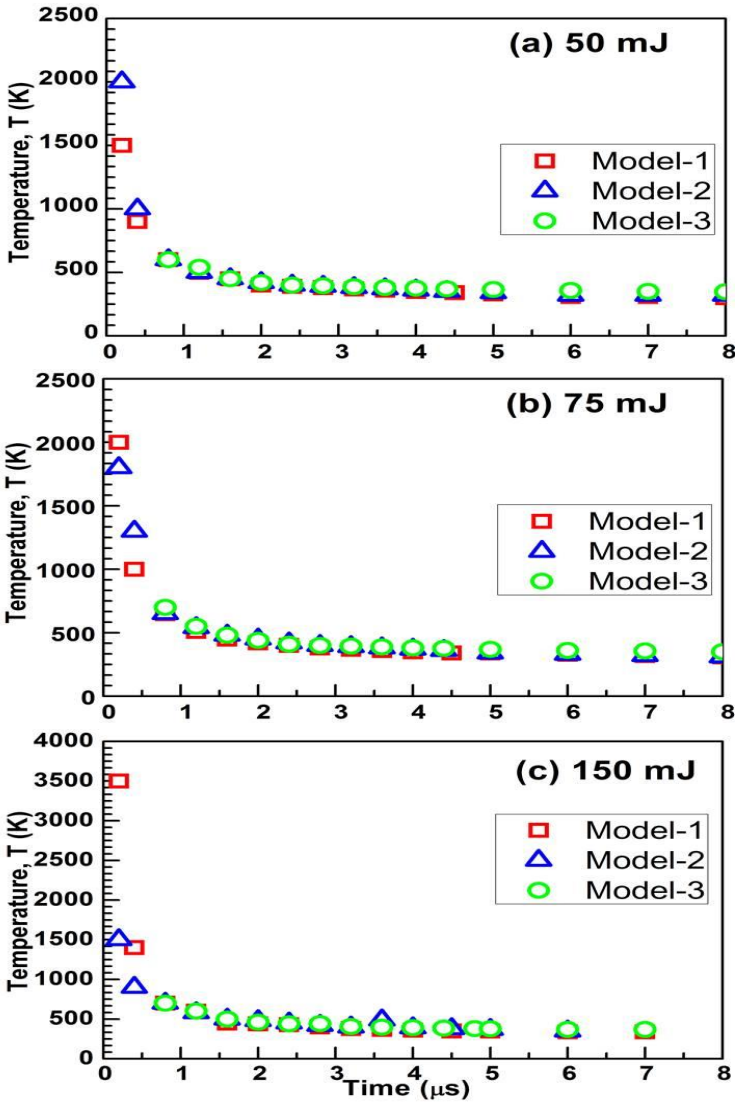

Figure 6.17 Comparison of temporal evolution peak plasma temperature existing across the SF between Models -1, 2 and 3, respectively for the input laser energies of a) 50 mJ, b) 75 mJ and c) 150 mJ.

6.4.6 Temporal evolution of specific internal energy, E_{sp}

The temporal evolution of the specific internal energy, E_{sp} existing in the PC is compared with the three models for energies 50 mJ (fig. 6.18 (a)), 75 mJ (fig. 6.18 (b))

and 150 mJ (fig. 6.18 (c)), respectively over the time scales 0.2 – 7 μs. Similarly, the temporal evolution of E_{sp} across the SF is compared for the same time scales in fig. 6.18 (d)-(f).

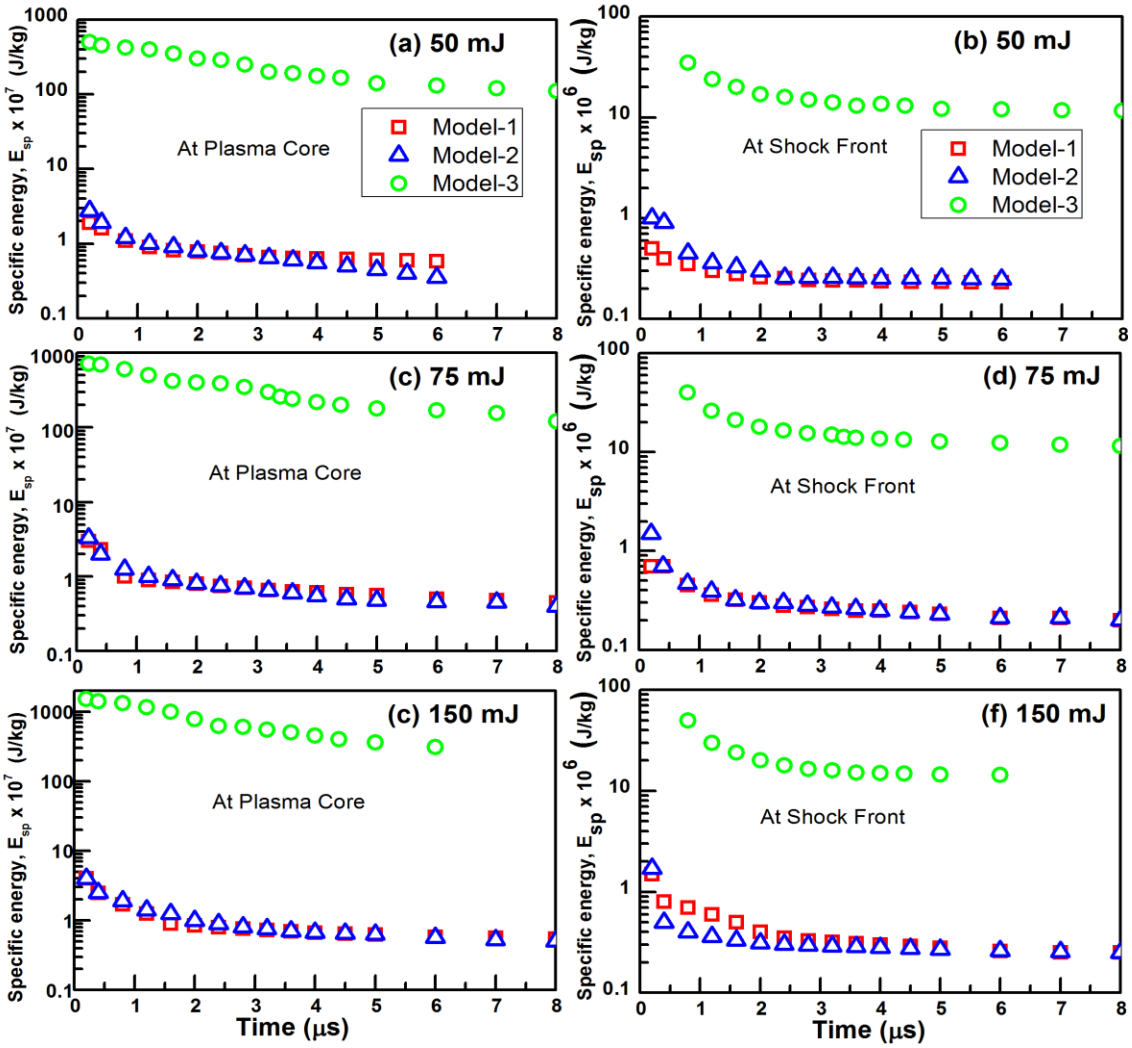

Figure 6.18 Comparison of temporal evolution of peak specific internal energy existing at the (a-c) PC and (d-f) across the SF between Models -1, 2 and 3, respectively for the input laser energies of 50, 75 and 150 mJ.

Table 6.3 summarizes the peak specific energy values in the plasma core region comparison with the three energies and three models over the time scales of 0.2 -7.0 μs for 50, 75 and 150 mJ, respectively. As observed since the PC temperatures observed

to be high with Model-3 (fig. 6.16 (d-f)) the corresponding E_{sp} is also found to be high which decay from 4×10^{9} - 1×10^{9} at 50 mJ, 9×10^{9} - 2×10^{9} at 75 mJ and 2×10^{10} - 4×10^{9} at 150 mJ. These values are of the order 2-3 times higher than that of with Models-1 and 2. The decay was observed to be similar with Models-1 and 2 from 3×10^{7} - 0.3×10^{7} at 50 mJ, 3×10^{7} - 0.4×10^{7} at 75 mJ, 4×10^{7} - 1×10^{7} at 150 mJ.

Table 6.3 Peak specific internal energies in the PC and across the SF compared with 50, 75 and 150 mJ over the time scales 0.2 - 7.0 μs.

E_L (mJ)	t (μs)	Peak $E_{sp} \times 10^7$ (J/kg) in PC			$E_{sp} \times 10^6$ (J/kg) at SF		
		M-1	**M-2**	**M-3**	**M-1**	**M-2**	**M-3**
50	0.2-7.0	3.0-0.3	3.0-0.3	400-100	0.5-0.3	1.0-0.3	40.0-10.0
75	0.2-7.0	3.0-0.4	3.0-0.4	900-200	0.7-0.2	1.5-0.2	40.0-10.0
150	0.2-7.0	4.0-1.0	4.0-1.0	2000-400	2-0.3	4.0-1.0	50.0-20.0

M-1, M-2 and M-3 represent Model-1, 2 and 3, respectively

In figure 6.18 (d-f), the E_{sp} across the SF shows that the SW carries the fraction of plasma energy which is found to approximately one order less than the plasma energy. Table 6.3 summarizes the specific energy values across the SF compared with the three energies and three models over the time scales of 0.2 - 7.0 μs. The E_{sp} at 50 mJ, was observed to decay from 0.5×10^{6} - 0.3×10^{3} with Model-1; 1×10^{6} - 0.3×10^{6} with Model-2 and 40×10^{6} - 10×10^{3} with Model-3. At 75 mJ, it is decayed from 0.7×10^{6} - 0.2×10^{6} with Model-1; 1.5×10^{6} - 0.2×10^{3} with Model-2 and 40×10^{6} - 10×10^{6} with Model-3. Similarly at 150 mJ these values decayed from 2×10^{6} - 0.3×10^{6} with Model-1 and 2, respectively and 50×10^{6} - 20×10^{6} with Model-3.

6.4.7 Shock velocity comparison

The shock velocities obtained along the laser propagation direction (right shock wave, RSW) and opposite to the laser direction (left shock wave, LSW) from the

shadowgrams is compared with the simulations using Model-1, 2 and 3 for 50, 75 and 150 mJ laser energies, respectively.

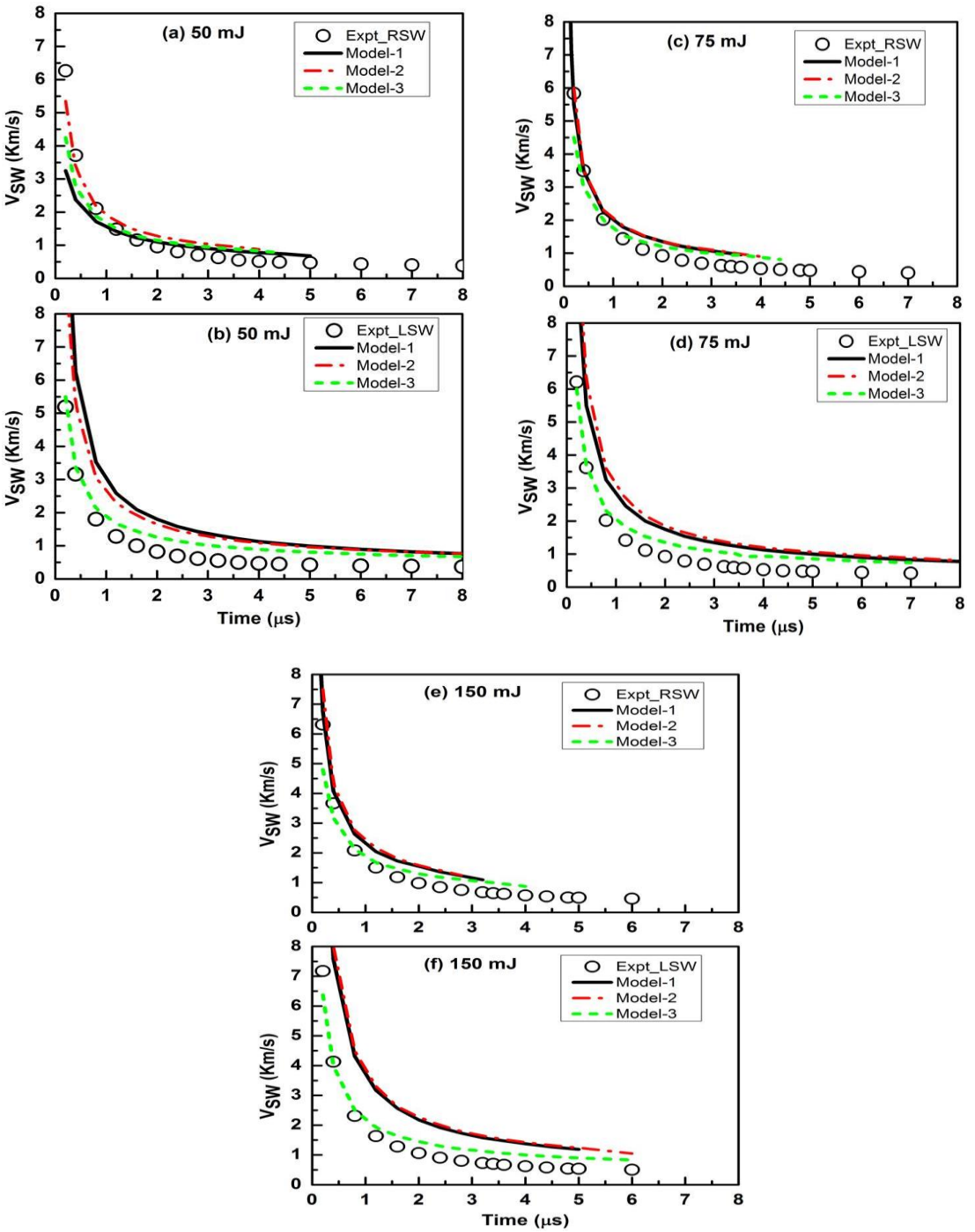

Figure 6.19 Comparison of LSW and RSW velocity between experiments and numerical Model-1, 2 and 3 at (a, b) 50 mJ, (c,d) 75 mJ (e, f) 150 mJ, respectively.

As discussed previously due to asymmetric deposition of the laser energy, the elongation of the plasma opposite to the laser propagation direction will be more than that along the laser propagation direction due the laser absorption occurring mostly in the +ve Z-axis. As a result, the SF propagates with higher velocities in the opposite direction than along the laser direction which was found to occur with all the laser energies and with all the models presented.

In fig. 6.19 (a & b) the shock velocities along RSW and LSW is compared for 50 mJ over the time scales of 0.4 - 8 µs. The RSW in the simulations has crossed the simulation box at times < 5 µs which was observed for all the laser energies. Similarly, in the case of 150 mJ, LSW was also crossed the box at 6 µs. Hence the RSW and LSW were compared up to these time scales.

Table 6.4 Shock velocity comparison at 0.4 µs for 50, 75 and 150 mJ input laser energies.

Energy (mJ)	V_{SW} (km/s)	Experiment	Model-1	Model-2	Model-3
50	RSW	6.2	3.2	5.4	4.2
	LSW	5.0	10	10	5.0
75	RSW	6.0	5.6	5.6	4.5
	LSW	6.2	10	10	6
150	RSW	6.3	7	7	5
	LSW	7.0	>10	>10	6

Table. 6.4 summarizes the shock velocity obtained at 0.4 µs is compared between the experimental values and the simulated Model-1, 2 and 3, respectively. As observed, at 0.4 µs, the RSW velocity, V_{RSW} (fig. 6.19 (a)) with experiments is found to be ~ 6.2 km/s, whereas with Model-1, 2 and 3 it is found to be ~3.2, ~ 5.4 and 4.2 km/s, respectively. However at latter time scales these values were matching well with the

experimental data. The LSW velocity, V_{LSW} with experiments is found to be ~ 5 km/s, whereas with Model-1 and 2 it is found to be higher ~10 km/s and with Model-3 it is found to be ~ 5 km/s which was found to be close to the experimental data. The propagation speed with Models-1 and 2 is found to be higher at all the time scales.

In fig. 6.19 (c, d), RSW and LSW velocities are compared for 75 mJ and the values at 0.4 μs is summarized in Table 6.4. As observed, V_{RSW} with experiments at 0.4 μs is found to be ~6.0 km/s, whereas with Model-1, 2 it is found to be ~5.6 km/s, with Model-3 ~4.5 km/s. Similarly, V_{LSW} with experiments is found to be ~6 km/s, whereas with Model-1 and 2, it is found to be ~10 km/s, respectively and ~6 km/s with Model-3.

In fig. 6.19 (e, f), RSW and LSW velocities are compared for 150 mJ and the values at 0.4 μs is summarized in Table 6.4. As observed, V_{RSW} with experiments is found to be ~6.2 km/s, whereas with Model-1, 2 found to be ~7.0 km/s, with Model-3 ~5.0 km/s. Similarly, V_{LSW} with experiments is found to be ~ 7 km/s at 0.4 μs, whereas it is found to be >10 km/s with Model-1 and 2 and ~6 km/s with Model-3.

6.5 Summary

A two-dimensional numerical simulation of laser-air breakdown, subsequent formation of plasma and its expansion in air launching a shock wave into ambient atmospheric air for the input laser energies ranging over 50 -150 mJ is performed up to the time scales of 8 μs. The experimental results were compared with three different models that take into consideration photoionization and inverse Bremsstrahlung absorption coefficients and two EOS namely, ideal gas EOS and CEA EOS separately. The asymmetric expansion of the plasma and SW during the initial times (<2 μs) is explained from the simulated density contours. The asymmetric expansion of the plasma during the laser interaction was observed to be occurring due to the shifting of the AF opposite to the laser direction (towards lens). Due to this mechanism, the energy deposition was observed to localize at different points leading to asymmetric distribution of density,

temperature, and pressure. The internal plasma processes such as the plasma expansion, splitting, rolling were explained from the temperature contours. The investigation shows higher temperature, pressure gradients along the laser axis than that along the radial axis. It is also observed that the plasma temperature decays quickly along the laser direction due to the presence of larger gradients. The rolling of plasma occurs at points where the higher temperature gradients exist. The splitting of the plasma occurs due to presence of localized hot spots existing within the plasma core leading to hydrodynamic instabilities inside the core region. The existence of two point sources observed from the shadowgrams occurring due to the splitting of the plasma core into two regions. The splitting times were observed to be coming in the range of the experimental one. The internal plasma dynamics was observed to depend on the laser absorption coefficients and the EOS considered. The temporal evolution of electron number density and temperature was observed to decay exponentially with Models-1 and 2 whereas, with Model-3 it is observed to be almost constant. Finally, the shock velocity comparisons show that towards the laser direction the simulations were over estimating, whereas along the laser direction the values were found to match decently. Overall the asymmetric plasma expansion and internal plasma dynamics (splitting, rolling) were found to be explained with Model-2 for all the laser energies and with Model-1 for 75 and 150 mJ energies. Similarly, the asymmetric expansion and internal plasma features could not reproduced with Model-3, but the shock velocities were found to be decently matching both along and opposite to the laser direction. Hence the importance of a proper combination of the laser absorption models and the EOS is verified in this chapter.

References

[1]T. X. Phuoc, Optics and Lasers in Engineering **44** (5), 351-397 (2006).
[2]M. Lackner, S. Charareh, F. Winter, K. F. Iskra, D. Rüdisser, T. Neger, H. Kopecek and E. Wintner, Opt. Express **12** (19), 4546-4557 (2004).
[3]C. Phipps, M. Birkan, W. Bohn, H.-A. Eckel, H. Horisawa, T. Lippert, M. Michaelis, Y. Rezunkov, A. Sasoh, W. Schall, S. Scharring and J. Sinko, Journal of Propulsion and Power **26** (4), 609-637 (2010).
[4]S. GHOSH and K. MAHESH, Journal of Fluid Mechanics **605**, 329-354 (2008).
[5]S. Soubacq, P. Pignolet, E. Schall and J. Batina, Journal of Physics D: Applied Physics **37** (19), 2686 (2004).
[6]L. J. Radziemski, Spectrochimica Acta Part B: Atomic Spectroscopy **57** (7), 1109-1113 (2002).
[7]R. G. Meyerand and A. F. Haught, Physical Review Letters **11** (9), 401-403 (1963).
[8]C. L. M. Ireland and C. G. Morgan, Journal of Physics D: Applied Physics **6** (6), 720 (1973).
[9]N. Glumac and G. Elliott, Optics and Lasers in Engineering **45** (1), 27-35 (2007).
[10]D. C. Smith, Applied Physics Letters **19** (10), 405-408 (1971).
[11]C. DeMichelis, IEEE Journal of Quantum Electronics **5** (4), 188-202 (1969).
[12]Y. E.-D. Gamal and M. A. Harith, Journal of Physics D: Applied Physics **14** (12), 2209 (1981).
[13]M. Young and M. Hercher, Journal of Applied Physics **38** (11), 4393-4400 (1967).
[14]R. Tambay and R. K. Thareja, Journal of Applied Physics **70** (5), 2890-2892 (1991).
[15]J. B. Simeonsson and A. W. Miziolek, Applied Physics B **59** (1), 1-9.
[16]D. Breitling, H. Schittenhelm, P. Berger, F. Dausinger and H. Hügel, Appl Phys A **69** (1), S505-S508.
[17]E. Schwarz, S. Gross, B. Fischer, I. Muri, J. Tauer, H. Kofler and E. Wintner, Laser and Particle Beams **28** (01), 109-119 (2010).
[18]M. Thiyagarajan and J. Scharer, Journal of Applied Physics **104** (1), 013303 (2008).
[19]T. X. Phuoc and C. M. White, Optics Communications **181** (4–6), 353-359 (2000).
[20]T. X. Phuoc, Optics and Lasers in Engineering **43** (2), 113-129 (2005).
[21]T. X. Phuoc, Optics Communications **175** (4–6), 419-423 (2000).
[22]H. Sobral, M. Villagrán-Muniz, R. Navarro-González and A. C. Raga, Applied Physics Letters **77** (20), 3158-3160 (2000).
[23]C. Leela, S. Bagchi, V. R. Kumar, S. P. Tewari and P. P. Kiran, Laser and Particle Beams **31** (02), 263-272 (2013).
[24]C. Leela, Ph. D. thesis, University of Hyderabad, India, 2014.
[25]I. B. Gornushkin, A. Y. Kazakov, N. Omenetto, B. W. Smith and J. D. Winefordner, Spectrochimica Acta Part B: Atomic Spectroscopy **59** (4), 401-418 (2004).
[26]M. Capitelli, A. Casavola, G. Colonna and A. De Giacomo, Spectrochimica Acta Part B: Atomic Spectroscopy **59** (3), 271-289 (2004).
[27]J.-L. Beduneau and Y. Ikeda, Journal of Quantitative Spectroscopy and Radiative Transfer **84** (2), 123-139 (2004).

[28]B. Pokrzywka, A. Mendys, K. Dzierżęga, M. Grabiec and S. Pellerin, Spectrochimica Acta Part B: Atomic Spectroscopy **74–75**, 24-30 (2012).
[29]S. S. Harilal, Appl. Opt. **43** (19), 3931-3937 (2004).
[30]K. Mori, K. Komurasaki and Y. Arakawa, Journal of Applied Physics **95** (11), 5979-5983 (2004).
[31]S. Kohei, M. Keisuke, W. Bin, K. Kimiya and A. Yoshihiro, in *49th AIAA Aerospace Sciences Meeting including the New Horizons Forum and Aerospace Exposition* (American Institute of Aeronautics and Astronautics, 2011).
[32]M. H. Mahdieh, M. Nikbakht and M. Sobhani, Optics Communications **284** (19), 4828-4835 (2011).
[33]Y. B. Zel'dovich and Y. P. Raizer, *Physics of Shock Waves and High-Temperature Hydrodynamic Phenomena*. (Dover Publications, 2012).
[34]Y. P. Raizer, V. I. Kisin and J. E. Allen, *Gas Discharge Physics*. (Springer Berlin Heidelberg, 2011).
[35]R. K. Singh and J. Narayan, Physical Review B **41** (13), 8843-8859 (1990).
[36]I. G. Dors and C. G. Parigger, Appl. Opt. **42** (30), 5978-5985 (2003).
[37]K. Ramnath and C. Graham, in *33rd Plasmadynamics and Lasers Conference* (American Institute of Aeronautics and Astronautics, 2002).
[38]H. Yan, R. Adelgren, M. Boguszko, G. Elliott and D. Knight, AIAA Journal **41** (10), 1988-1995 (2003).
[39]R. Joarder, G. C. Gebel and T. Mosbach, International Journal of Heat and Mass Transfer **63**, 284-300 (2013).
[40]S. Sai Shiva, C. Leela, P. Prem Kiran, C. D. Sijoy, V. Ikkurthi and S. Chaturvedi, in *(Manuscript under preparation)*.
[41]L. Spitzer, *Physics of fully ionized gases*. (Interscience Publishers, 1962).
[42]C. D. Sijoy, S. Chaurasia, V. Mishra, P. Leshma, N. Sakthivel, S. Chaturvedi, S. M. Sharma and S. Basu, High Energy Density Physics **11**, 36-44 (2014).
[43]S. Atzeni and J. Meyer-ter-Vehn, *The Physics of Inertial Fusion: BeamPlasma Interaction, Hydrodynamics, Hot Dense Matter*. (OUP Oxford, 2004).
[44]C. D. Sijoy and S. Chaturvedi, Journal of Computational Physics **229** (10), 3848-3863 (2010).
[45]C. D. Sijoy and S. Chaturvedi, European Journal of Mechanics - B/Fluids **53**, 85-100 (2015).
[46]C. D. Sijoy and S. Chaturvedi, Computer Physics Communications.
[47]C. D. Sijoy and S. Chaturvedi, Computer Physics Communications **190**, 98-119 (2015).
[48]S. Gordon; and B. J. McBride, 1-58 (1994).
[49]F. Cornolti, A. Giulietti, D. Giulietti, M. Lucchesi and M. Vaselli, Optics Communications **57** (4), 249-253 (1986).
[50]M. Gatti, V. Palleschi, A. Salvetti, D. P. Singh and M. Vaselli, Optics Communications **69** (2), 141-146 (1988).
[51]A. A. Malyutin, V. A. Podvyaznikov and V. K. Chevokin, Quantum Electronics **41** (1), 38 (2011).

Chapter 7

Summary and Future Scope

This thesis explores some of the key issues involved in the nanosecond laser ablative shock waves (LASW) driven mainly from Al target and air medium into ambient atmospheric air. In the LASW from Al target particularly, we have emphasized on the effects of electron thermal radiation (ETR) emitting from Al ablated plasma on the SW propagation into ambient air and into target material. These studies gave an insight of how the radiation influencing the SW propagation and the typical time scales upto which the propagation is influenced by the radiation. The ETR effects were found to be dominating with increasing laser intensity. These studies also revealed that the plasma dynamics is significantly modified with ETR effects taken into consideration. The ablated plasma is observed to split into two regions as: plasma core (PC) and plasma outer region during its evolution. The knowledge of spatio-temporal evolution of laser ablated plasma and SW dynamics in air and SW propagation into solid target is very important. In the laser shock peening technique the surface modulation and pressure enhancements play a key role in the strengthening of the material. The studies carried out in this thesis such as direct irradiation of laser onto the target and varying the focusing plane away from the target surface (indirect irradiation) at different separations enabled to understand how the plasma and SW dynamics varies both in ambient air and SW propagating through Al target. The simulations enabled to monitor simultaneously the ablative plasma dynamics in ambient air and SW propagation through Al target that showed couple of interesting dynamics of the SWs into Al target. We particularly observed that the direct irradiation on to the target leads to the launching of two SWs: primary SW (PSW) and secondary SW (SSW) where these SW coalesced inside the target leading to enhanced SW pressures. Similarly in the

indirect irradiation process, multiple SWs (PSW, SSW, third, fourth and fifth SW) were observed to be propagating through the target that maintained the constant pressures into the target for a longer time. The maintenance of constant pressure into the target is very useful in the context EOS studies of different materials. It is also observed that the SW pressure in ambient air is enhanced by placing the Al target close to the air plasma (indirect irradiation). In the future work, these studies are proposed to be extended to other targets like Cu, brass, stainless steel.. In the experimental studies carried by our group, it is explored that the SW pressures can be enhanced by using the structured targets. Hence the future work will be carried with these targets.

The modelling of laser-air interaction is a challenging task as it involves complex phenomenon due to the presence of different concentration present. The knowledge of laser energy deposition at the focal plane and the associated air spark dynamics and SW evolution is very important in the applications like the ignition of fuel air-mixtures and micro-thrusters. In the LASW from air medium a particular interest have be made on the modelling of laser-air interaction and the associated plasma and SW dynamics is taken up. We particularly stressed on the modelling of the laser-air interaction using 2D-RHD code that enabled to understand the essential features of spatio-temporal evolution of the air spark dynamics such as initial plasma evolution, plasma splitting and rolling and SW evolution over the intensity range 10^{10} – 10^{11} W/cm^2 up to time scales of 8 μs. However the intensity range used in this particular studies are limited but, the numerical work can be extended to high intensities (> 10^{14} W/cm^2) where particularly this range of intensities are used in the study of fuel-air mixtures and thrust generation. In the future work, the modelling of laser interaction of different mixtures of gases will be carried out.

List of Publications

1. **S. Sai Shiva,** Ch. Leela, P. Prem Kiran, C. D. Sijoy and S. Chaturvedi, *"The effects of electron thermal radiation on laser ablative shock waves from aluminum plasma into ambient air",* Phys. Plasmas **23**, 053107 (2016).
2. **S. Sai Shiva,** Ch. Leela, S. Chaturvedi, C. D. Sijoy, P. Prem Kiran, *"Development of Numerical Model to Investigate the Laser Driven Shock Waves from Aluminum Target into Ambient Air at Atmospheric Pressure and its comparison with Experiment",* APS - Conference Proceedings of Shock Compression and Condensed Matter (SCCM), W1.42-15-1330, June-2015.
3. E. Manikanta, P. Venkateshwarlu, **S. Sai Shiva,** V. Rakesh Kumar, Ch. Leela, Surya P. Tewari, G. Manoj Kumar, P. Prem Kiran, *"Dynamic Response of metals and alloys to laser-induced shock waves",* Proc. SPIE 8433, Laser Sources and Applications, 84331Z 1-6, 2012.

Manuscripts Communicated/Under Preparation

1. **S. Sai Shiva,** C. Leela, P. Prem Kiran, C. D. Sijoy, and S. Chaturvedi, *"Radiation effects of the laser ablative shockwaves on aluminum under atmospheric conditions"* 10th APFA Conference Proceedings, (2015) Communicated to IOP: Conference Serics, 2016.
2. **S. Sai Shiva,** Ch. Leela, P. Prem Kiran, C. D. Sijoy, V. I. Ikkurthi and S. Chaturvedi, *"2D-Numerical simulations of laser induced shock waves from ambient air",* (Manuscript Under preparation).
3. **S. Sai Shiva,** C. Leela, P. Prem Kiran, C. D. Sijoy, V. Ikkurthi, and S. Chaturvedi, *1D-Numerical investigation of laser induced air plasma and SW evolution into ambient air: Effects of radiation",* (Manuscript under preparation).
4. **S. Sai Shiva,** C. Leela, P. Prem Kiran, C. D. Sijoy, V. Ikkurthi, and S. Chaturvedi, "*1D-Numerical investigation of laser induced air plasma and aluminum interaction and SW evolution into ambient air and Al target: A comparative study",* (Manuscript under preparation).

List of Conference Presentations

1) **S. Sai Shiva,** Ch. Leela, P. Prem Kiran, C. D. Sijoy, V. I. Ikkurthi and S. Chaturvedi, *"Testing of different models for expansion of laser induced plasma into ambient air",* Recent Advances in Optical Sciences (RAOS), 6-7th, May-2016.
2) **S. Sai Shiva,** Ch. Leela, C. D. Sijoy, S .Chaturvedi, P. Prem Kiran, "*Radiation Effects On The Laser Ablative Shock waves From Aluminum Under Atmospheric Conditions", 10th Asia Plasma and Fusion Association (APFA) Conference-2015, December 14 – 18th, 2015, Gandhinagar, India.*
3) **S. Sai Shiva,** Ch. Leela, S. Chaturvedi, C. D. Sijoy, P. Prem Kiran *"Development of Numerical Model to Investigate the Laser Driven Shock Waves from Aluminum Target into Ambient Air at Atmospheric Pressure and its comparison with Experiment",* 19th Biennial Conference on Shock Compression of Condensed Matter (SCCM), June 14-19th, 2015, Tampa, Florida.
4) **S. Sai Shiva,** Ch. Leela, C. D. Sijoy, S .Chaturvedi, P. Prem Kiran, "*Development Of Numerical Models For Laser Driven Shocks In Air And Its Comparison With Experiment",* 29th National Symposium On Plasma Science & Technology PLASMA-2014 and International Conference on Plasma and Nanotechnology, Kottayam, Kerala, India.
5) E. Manikanta, P. Venkateshwarlu, **S. Sai Shiva,** V. Rakesh Kumar, Ch. Leela, Surya P. Tewari, G. Manoj Kumar, and P. Prem Kiran, "*Dynamic response of metals and alloys to laser induced shock waves",* Laser Sources and Applications, SPIE – Photonics – Europe, Brussels, Belgium, 16 – 18 April 2012;
6) *Ch. Leela, E. Manikanta,* **S. Sai Shiva,** *P. Venkateshwarlu, V. Rakesh Kumar, G. Manoj Kumar, Surya P. Tewari, and P. Prem Kiran, "Investigation of laser induced acoustic shock waves and vibrations from solids",* 8th International high energy material Conference and exhibit, HEMCE-2011,TBRL, Chandigarh, India .